

UNIVERSITÀ DEGLI STUDI DI PADOVA

DOCTORAL THESIS

---

# Magnetic gears numerical modelling and optimization

---

*Author:*  
Mattia FILIPPINI

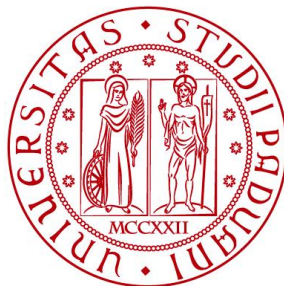
*Supervisor:*  
Prof. Piergiorgio ALOTTO  
*Coordinator:*  
Prof. Roberto TURRI

*A thesis submitted in fulfilment of the requirements  
for the degree of Doctor of Philosophy*

*in the*

Computational Electromagnetic Lab.  
Department of Industrial Engineering  
Electrical Energy Engineering Curriculum, XXXI cycle

November 26, 2018



UNIVERSITÀ  
DEGLI STUDI  
DI PADOVA



# Declaration of Authorship

I, Mattia FILIPPINI, declare that this thesis titled, “Magnetic gears numerical modelling and optimization” and the work presented in it are my own. I confirm that:

- This work was done wholly or mainly while in candidature for a PhD degree at the University of Padova.
- Where I have consulted the published work of others, this is always clearly attributed.
- Where I have quoted from the work of others, the source is always given. With the exception of such quotations, this thesis is entirely my own work.
- I have acknowledged all main sources of help.
- Where the thesis is based on work done by myself jointly with others, I have made clear exactly what was done by others and what I have contributed myself.

Signed:



---

Date: November 26, 2018

---



# Hyperlinks

In order to improve the thesis readability and to provide the reader an easy access to all the papers in literature, in this thesis hyperlinks have been used. The equation, citation and figure numbers in the text are linked to the respective objects and the DOI codes in the references paragraph to the correspondent web pages.



# *Abstract*

Electrical Energy Engineering Curriculum, XXXI cycle  
Department of Industrial Engineering

Doctor of Philosophy

## **Magnetic gears numerical modelling and optimization**

by Mattia FILIPPINI

The main focus of this thesis is to provide efficient modelling and optimization strategies for a certain electro-magnetic device known as magnetic gear. In particular, magnetic, thermal and mechanical models are discussed and the non-linear material models are examined, including permanent magnets demagnetization algorithms and hysteresis models in laminated sheets.

From the magnetic modelling point of view, an analytic approach for the initial simplified gear design is presented. A special focus is given to the computational burden of the method that is especially tailored for stochastic optimization procedures.

For the detailed analysis of magnetic gears, an algorithm based on Finite Element / Boundary Element coupling is proposed, including ferromagnetic non-linearities, mechanical ordinary differential equations, eddy currents and circuit equations.

Detailed models are introduced and discussed to analyze the effects of soft material hysteresis and permanent magnets magnetization, demagnetization and recoil.

Loss mechanisms in magnetic gears are also investigated, and the transmission losses at varying rotational speeds and load angles are analyzed.

A simplified mechanical model of the magnetic gear is presented and formulated as a set of inequality constraints, thus giving a direct link to optimization strategies. The mechanical constraints include the iron poles displacements and stresses and the limitations on the rotational speed due to excessive stresses, resonances and vibrations. A simplified analysis based on an equivalent thermal network is also presented, where the axial cooling flux is also considered.

Stochastic optimization techniques are discussed for a multi-physic optimized machine design, and the analytic model is embedded in a Differential Evolution scheme.

Finally, the optimized results are discussed and compared to commercial mechanical gear-boxes. A solution based on the stiffness rods connection is also proposed and analyzed to provide a damping effect when the gear operation becomes asynchronous.

During the PhD, there has been a constant effort aimed at building a prototype for the validation of the numerical models but, for different reasons, none of the manufacturers finalized the project. Thus, all the algorithms have been validated by comparing their output with commercial codes or, when possible, with data from experiments retrieved from literature. Because of this reasons and since the major objective of this thesis regards the numerical techniques for magnetic gears simulation, different magnetic transmissions have been adopted as numerical test cases for the validation of the algorithms.





## *Acknowledgements*

I would like to thank my supervisor Prof. Piergiorgio Alotto for the support and motivation during these three years of PhD. His advices and knowledge have been precious in both research and writing activities.

My sincere thanks also goes to Prof. Kay Hameyer, who provided me an opportunity to join his research group as intern, and who gave access to the laboratory and research facilities.

I thank my labmates all for the fun we had in the last three years and for the inspiring discussions we shared.

Finally, I would like to thank my family and friends: my parents Giancarlo and Paola, my brother Luca and my girlfriend Serena for the patience and unceasing moral and economical support. Thanks to my friends, who have always been at my side, for all the adventures that made me forget about disappointments and bad periods.



# Publications and submissions

## Published journal papers

- **M. Filippini**, P. Alotto, "An optimization tool for coaxial magnetic gears", *COMPEL - The international journal for computation and mathematics in electrical and electronic engineering*, Vol. 36 Issue: 5, pp.1526-1539, 2017, doi:<https://doi.org/10.1108/COMPEL-02-2017-0068>;
- **M. Filippini** and P. Alotto, "Coaxial Magnetic Gear Design and Optimization," in *IEEE Transactions on Industrial Electronics*, vol. 64, no. 12, pp. 9934-9942, Dec. 2017, doi: <https://doi.org/10.1109/TIE.2017.2721918>;
- **M. Filippini**, P. Alotto, "Multi-objective optimization of coaxial magnetic gears", *International Journal of Applied Electromagnetics and Mechanics*, vol. 56, no. S1, pp. 45-59, 2018, DOI: <https://doi.org/10.3233/JAE-172280>;
- G. Bavendiek, K. Hameyer, **M. Filippini**, P. Alotto, "Analysis of impulse-magnetization in rare-earth permanent magnets", *International Journal of Applied Electromagnetics and Mechanics*, vol. 57, no. S1, pp. 23-31, 2018, doi: <https://doi.org/10.3233/JAE-182301>;
- **M. Filippini**, P. Alotto, G. Glehn, G., K. Hameyer, (2018). Magnetic transmission gear finite element simulation with iron pole hysteresis. *Open Physics*, 16(1), pp. 105-110. Retrieved 26 Jul. 2018, doi: <https://doi.org/10.1515/phys-2018-0017>;

## Submitted journal papers

- **M. Filippini**, P. Alotto, "Permanent magnet modelling in finite element codes considering magnetization, demagnetization and recoil phenomena" submitted to: *IET Electric Power Applications*;

## Published proceedings

- **M. Filippini**, P. Alotto, V. Cirimele, M. Repetto, C. Ragusa, L. Dimauro, E. Bonisoli, "Power loss identification in coaxial magnetic gears", 2017 International CAE Conference, url=[http://www.compumag.org/CMAG2017/\[PB-A6-13\]\\_404.pdf](http://www.compumag.org/CMAG2017/[PB-A6-13]_404.pdf)
- **M. Filippini** and P. Alotto, "Coaxial magnetic gear design" 2016 IEEE Conference on Electromagnetic Field Computation (CEFC), Miami, FL, 2016, pp. 1-1. doi: <http://dx.doi.org/10.1109/CEFC.2016.7815939>;
- Y. Wang, **M. Filippini**, N. Bianchi, P. Alotto, "A Review on Magnetic Gears: Topologies, Computational Models and Design Aspects", 2018 XIII International Conference on Electrical Machines (ICEM), doi: <http://dx.doi.org/10.1109/ICELMACH.2018.8507204>;
- Y. Wang, **M. Filippini**, G. Bacco, N. Bianchi, "Parametric Design and Optimization of Magnetic Gears with Differential Evolution Method", 2018 XIII International Conference on Electrical Machines (ICEM), doi: <http://dx.doi.org/10.1109/ICELMACH.2018.8507160>.

## Accepted proceedings

- **M. Filippini**, P. Alotto, “Anderson acceleration for electromagnetic nonlinear problems”, presented at IGTE 2018 conference.
- **M. Filippini**, P. Alotto, “Transient analysis of magnetic gear asynchronous operation with damping effects”, presented at CEFC conference and accepted for inclusion in IEEE Xplore.

## Patents submission

- **M. Filippini** (UniPd), P. Alotto (UniPd), M. Repetto (Polito), E. Bonisoli (Polito), V. Cirimele (Polito), “Sistema di trasmissione con differenziale magnetico” (“Transmission system with magnetic differential”), patent proposal funded by the University of Padova (approved by Ufficio Valorizzazione della Ricerca), currently awaiting for first deposit.

# Contents

<b>Declaration of Authorship</b>	<b>iii</b>
<b>Abstract</b>	<b>vii</b>
<b>Acknowledgements</b>	<b>ix</b>
<b>1 Motivation</b>	<b>1</b>
1.1 Mechanical gears: causes of failure . . . . .	1
1.2 The magnetic counterpart . . . . .	3
<b>2 Magnetic gears quick overview</b>	<b>5</b>
2.1 Magnetic gear topologies . . . . .	5
2.1.1 Conventional non-modulated magnetic gears . . . . .	5
2.1.2 Modulated magnetic gears . . . . .	6
2.2 Working principle . . . . .	8
2.2.1 Conventional non-modulated magnetic gears . . . . .	8
2.2.2 Modulated magnetic gears . . . . .	8
2.3 Computational models . . . . .	9
2.4 Gear design aspects . . . . .	9
2.4.1 Gear ratio . . . . .	9
2.4.2 Iron pole pieces design . . . . .	10
2.4.3 Transmission losses . . . . .	10
2.4.4 Cogging torque . . . . .	10
2.4.5 Dynamic operation . . . . .	11
<b>3 Magnetic transmissions basics</b>	<b>13</b>
3.1 Permeances network formulation . . . . .	13
3.2 Modulation effect and harmonic analysis . . . . .	15
3.3 Periodicity . . . . .	17
3.4 Torque ripple . . . . .	21
3.5 Overload protection . . . . .	22
3.5.1 Speed control . . . . .	23
3.5.2 Torque control . . . . .	26
<b>4 Magnetic modelling</b>	<b>31</b>
4.1 Analytic modelling . . . . .	31
4.1.1 Modelling in low permeability regions . . . . .	32
4.1.2 Implementation and remarks . . . . .	33
4.1.3 Problem conditioning . . . . .	34
4.1.4 Modelling in high permeability regions . . . . .	36
4.1.5 Simplified iron saturation model . . . . .	37
4.1.6 Model validation . . . . .	38
4.2 2D Finite Element / Boundary Element in Julia . . . . .	40
4.2.1 Julia features . . . . .	40
4.2.2 FEM/BEM algorithm for magnetic gears . . . . .	41
Finite element formulation . . . . .	41
Boundary element formulation . . . . .	42
FEM/BEM coupling . . . . .	42
Torque computation . . . . .	43

4.2.3	Motion and time domain problem . . . . .	44
4.2.4	Julia implementation . . . . .	45
	Mesh import . . . . .	45
	Useful packages . . . . .	45
4.2.5	Acceleration methods for nonlinear problems . . . . .	46
4.2.6	Model validation . . . . .	46
4.3	Anderson acceleration for electromagnetic nonlinear problems . . . . .	48
4.3.1	Fixed point for the magnetostatic problem . . . . .	48
4.3.2	Anderson acceleration . . . . .	50
4.3.3	Test case validation: geometry . . . . .	51
4.3.4	FEM/BEM acceleration . . . . .	51
4.3.5	Harmonic Balance FEM acceleration . . . . .	52
4.3.6	Acceleration results . . . . .	53
4.3.7	FEM/BEM case with hysteresis . . . . .	56
4.4	Hysteresis in soft magnetic materials . . . . .	56
4.4.1	FEM implementation . . . . .	58
4.4.2	Magnetic gear test case . . . . .	59
4.4.3	Model results . . . . .	60
4.4.4	Discussion and remarks . . . . .	60
4.5	Hysteresis and modelling of hard magnetic materials . . . . .	63
4.5.1	Nonlinear formulation . . . . .	64
	Finite element formulation . . . . .	64
	Method 1 . . . . .	65
	Method 2 . . . . .	65
	Time dependent problem . . . . .	65
	PM measurements . . . . .	66
	PM algorithm . . . . .	66
4.5.2	Comsol implementation and results . . . . .	68
4.5.3	Temperature dependence . . . . .	69
4.5.4	Model validation . . . . .	69
	Two-step post assembly magnetization . . . . .	70
	Axisymmetric PM magnetizer . . . . .	70
4.5.5	Magnetic gear test case . . . . .	72
4.5.6	Demagnetization in magnetic gears . . . . .	74
4.6	Losses in ferromagnetic materials . . . . .	76
4.6.1	Theoretical formulation . . . . .	77
4.6.2	Lamination effect . . . . .	77
4.6.3	Generalized Steinmetz's equation model . . . . .	79
4.6.4	2D Rotational loss model . . . . .	80
4.7	Losses in PMs . . . . .	81
4.8	2D vs. 3D simulations . . . . .	83
4.9	Losses vs. speed . . . . .	87
<b>5</b>	<b>Mechanical and thermal modelling</b> . . . . .	<b>93</b>
5.1	Rotational speed limit for magnetic gears . . . . .	93
5.1.1	Rotor speed limit without retaining sleeve . . . . .	94
5.1.2	Rotor speed limit with retaining sleeve . . . . .	94
5.1.3	Skin depth . . . . .	97
5.1.4	Vibrations modes . . . . .	97
5.2	Variable speed . . . . .	98
5.3	Magnetic forces on iron poles . . . . .	100
5.4	Mechanical deformations . . . . .	102
5.4.1	Solid poles case . . . . .	102
5.4.2	Stiffness rods case . . . . .	102
5.4.3	Displacements and stresses . . . . .	103
5.5	Thermal model . . . . .	105
5.5.1	Air flow distribution . . . . .	106

5.5.2	Thermal resistance . . . . .	107
5.5.3	Capacitance . . . . .	110
5.5.4	Matrix notation . . . . .	110
5.5.5	Thermal model validation . . . . .	111
<b>6</b>	<b>Optimized gear design</b>	<b>113</b>
6.1	Complexity definition . . . . .	114
6.2	Differential Evolution strategy . . . . .	114
6.2.1	Mutation and crossover . . . . .	115
6.2.2	Constraints handling . . . . .	115
	NSGA-II directly constrained . . . . .	116
	NSGA-II indirectly constrained . . . . .	118
6.3	Optimization problem statement . . . . .	118
6.4	Example of single gear optimization . . . . .	118
6.5	Multi-stage gears . . . . .	120
6.6	Comparison between magnetic and mechanical gears . . . . .	125
<b>7</b>	<b>Damping effects in magnetic gears</b>	<b>127</b>
7.1	Magnetic gear geometry . . . . .	127
7.2	Problem formulation . . . . .	127
7.3	Model validation . . . . .	129
7.4	Damping effect . . . . .	129
<b>8</b>	<b>Conclusions and future work</b>	<b>137</b>
<b>A</b>	<b>Julia code</b>	<b>139</b>
A.1	Methods . . . . .	139
A.2	Call external code . . . . .	139
A.3	Parallelism . . . . .	139
A.4	Memory profiling . . . . .	140
A.5	Finite element matrices assembly . . . . .	140
A.6	BEM matrices assembly . . . . .	141
A.7	Torque calculation . . . . .	142





# Chapter 1

## Motivation

Mechanical gears have been known before Christ: first prototypes are described in Aristotle's writings (330 B.C.) but according to [1] even some chariots in the Yellow Emperor were equipped with primitive gears (over 4500 years ago).

Nowadays gears represent a well consolidated way to convert torque and speed and are manufactured for a wide speed and power ranges, covering almost all the applications that involve rotating parts. Wind turbines are normally equipped with gearbox stages to match the low-speed power input with the high-speed electrical generator. Helicopters power-trains use gearboxes to convert power from the high-speed turbine to the low-speed rotor blades. The power take-off systems of wave energy plants have to convert the small linear motion of buoys into possibly wide displacements of linear or conventional generators through mechanical transmissions. In general, all applications where two non-coaxial shafts have to be connected adopt a mechanical device that allows the transmission. Potentially, all these applications could benefit from magnetic contact-less solutions.

In Sec. 1.1, the main causes of failure of mechanical gears are briefly presented, while in Sec. 1.2 the magnetic gear is introduced.

### 1.1 Mechanical gears: causes of failure

Gears have a limited life and after this time period they have to be substituted. Apart from the materials aging, multiple factors influence the gear life: load, alignment, materials, temperature, lubricant film, geometrical and surface properties are the most common. Pitting is a well known phenomenon that affect gears and it is one of the main failure reason. Every time there is contact between two radius, contact stresses occur: this generally happens for gears and bearings. In case of two spheres in contact, the entire load will be imparted into a theoretical point. Due to elastic properties of the materials, this point will deform into a contact area. The deformation that occurs will produce high tensile and compressive stresses in the materials and even if the load is lower than the static limit, several effects related to fatigue, overload or failure in the teeth lubrication can damage the gear. The most common effects are abrasive wear, corrosive wear, pitting, spalling and scoring [2].

Pitting is usually classified in initial and progressive categories: the former is also called corrective pitting and his severity decreases with the number of cycles, the latter is the most harmful because it grows his intensity and severity increasing the number of cycles till the surface is completely destroyed. Some examples of pitting are depicted in Figs. 1.1, 1.2 and 1.3, while other failures are shown in Figs. 1.4 and 1.5.

In [3], an extensive survey of the Swedish wind power systems showed that gearboxes failure cover around 10% of the overall number of failures, while the downtime due to gearboxes failure is close to 20% of the overall downtime (see Figs. 1.6, 1.7).

According to [4], the gearbox is the largest contributor to wind turbine downtime and the costliest damage to repair. Among the 257 records of the database, 26% of the faults are due to the gears, while 70% to the bearings.

Mechanical gears have several advantages such as the relative low price and high torque to weight ratio, however vibrations have to be compatible with the application, safety factors and clutches have to be adopted in case of overloads and the lubrication must always be guaranteed

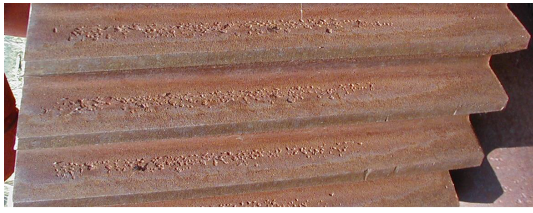


FIGURE 1.1: Corrective pitting example.



FIGURE 1.2: Dedendum wear of a hardened gear.

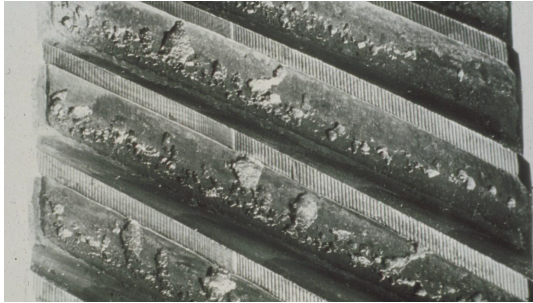


FIGURE 1.3: Destructive pitting example.

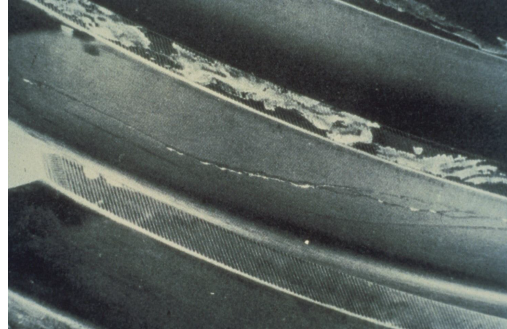


FIGURE 1.4: Overload crushing.

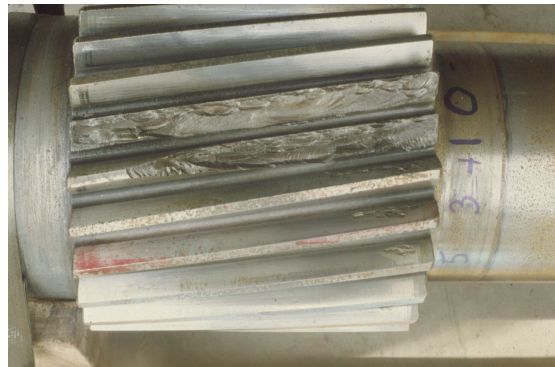


FIGURE 1.5: Misalignment failure.

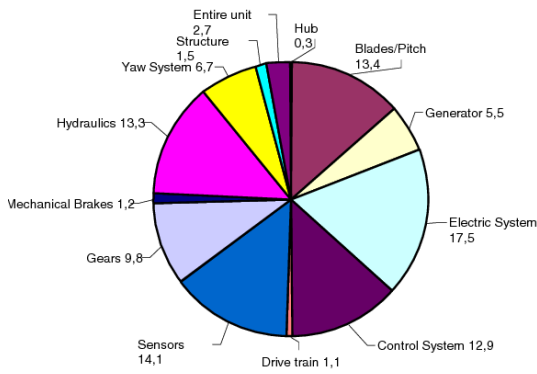


FIGURE 1.6: Swedish wind power system failure statistics in % [3].

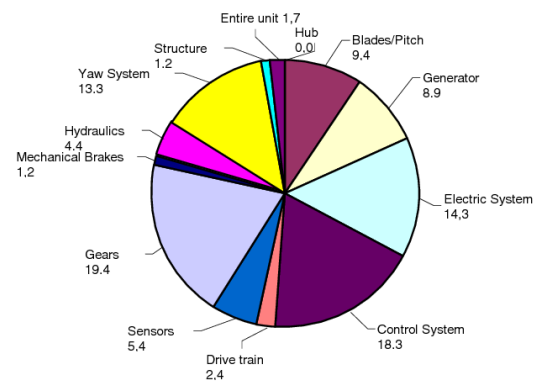


FIGURE 1.7: Swedish wind power system downtime statistics in % [3].

Model	Power (kW)	$rpm_{out}$	ratio	$rpm_{in}$	weight (kg)	Nm/kg	kW/kg
oh58A	220.5	350	95	33250	70	86	2.56
ch47D	5512	225	68	15300	1850	126.46	43.6
UH60	2205	258	81	20898	680.4	119.95	18.38
tp400d6	8085	860	9.5	8170	$\simeq 450$	200	18
UL	44.1	550	110	60500	59	12.98	0.75

TABLE 1.1: Typical gearboxes values for aircraft applications. The weight of the lubrication oil is included.

in order to avoid premature failures. The temperature is another key factor that affect the probability of gear failure as explained in [5].

[6, 7, 8] describe three cases of failure in a vehicle gearbox, in power plant and for an helicopter drivetrain respectively, just to name a few.

## 1.2 The magnetic counterpart

Because of these reasons, a device equivalent to the mechanical gearbox but with less requirements in terms of maintenance would be highly competitive on the market. Magnetic gears could be the candidates to substitute the conventional gearboxes in all the applications where maintenance-free operation is required, since they do not need lubrication systems and they intrinsically guarantee overload protection. A coaxial magnetic gear schematic example is shown in Fig. 1.8, where the tree main components are depicted.

Several comparisons between mechanical and magnetic transmissions have been carried out in the recent years. A comparative study is reported in [9], where the authors show that the mechanical torque density in Nm/L is strictly dependent on the safety factors adopted and rapidly decreases increasing the gear ratio, while the volumetric torque density achievable by magnetic gears is generally higher than the mechanical transmissions.

[10] and [11] compare both volumetric and mass torque densities. According to [10], there is a great potential for magnetic gears in the micro-electro-mechanical systems where mechanical gears suffer from low mass torque densities due to friction forces. In [11], the mass torque density of magnetic gears is still lower than the one of conventional transmissions, but further improvements are expected since the number of magnetic gear prototypes is still limited. According to [12], a coaxial magnetic gear can reach up to  $200 \text{ kNm}/\text{m}^3$ ,  $5.47 \text{ Nm}/\text{kg}$  and  $86.8 \text{ Nm}/\text{kg}$  even if the best prototype reached a torque density of  $17 \text{ Nm}/\text{kg}$  according to [13]. A recent paper [14] proposed a gear with an outer dual flux modulator that reached a torque density above  $21 \text{ Nm}/\text{kg}$ , but further improvements may be expected since the the geometry was not optimized.

In literature, several research groups have discussed the possible application of magnetic gears (e.g. [15]) and are currently developing prototypes or advanced level commercial solutions [16, 17, 18].

In this thesis, detailed numerical models are presented to analyze magnetic, thermal and mechanical physics of magnetic gears for a complete gear simulation package. The models range from analytic-based procedures for the first magnetic gear design, to advanced nonlinear models for hysteresis and permanent magnet simulations.

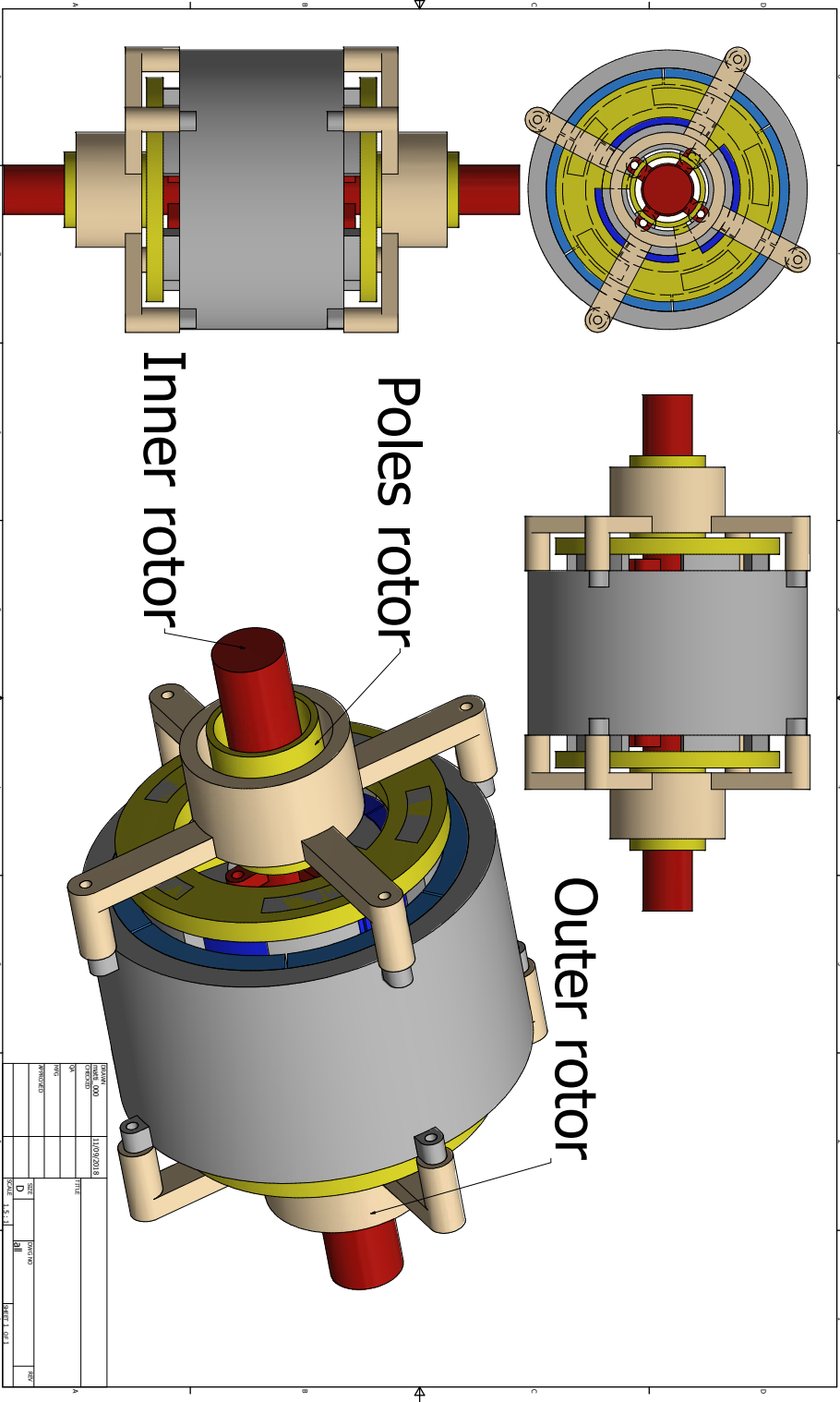


FIGURE 1.8: Schematic example of magnetic transmission. Inner, poles and outer rotors are highlighted. Apart from the end bearings that keep the three rotors coaxial, there is no contact in the torque-transmission area.

## Chapter 2

# Magnetic gears quick overview

Electrical machines play key roles in industrial applications. Since the machine size is inversely proportional to its operating speed, high speed machines achieve higher power density and it is always desirable to use high speed machines whenever possible. Looking for example at direct-drive systems, they suffer from large size and material usage in case of high torque demand due to their low speed. A good alternative option is to combine a high speed machine with a gear transmission system, leading to an effective solution in terms of cost and weight. Geared devices are commonly used to match the operating speed and torque of the power source with the second-mover. Such conventional geared devices are usually mechanical gears of different topologies, including, among others, spur gears, planetary gears, worm gear, spiral gears, hypoid gears, harmonic gears, cage gears and strain wave gearing. Although some of them achieve quite high torque density, mechanical gears usually suffer from the disadvantages of noisy, potential limited reliability, required lubrication and regular maintenance.

Magnetic gears (MGs), on the other hand, are becoming promising devices. This is mainly due to several inherent merits, such as physical detachment between moving parts, no gear lubrication, overload protection and reduced maintenance. The first ideas of magnetic gears date back as early as the 1900s. A patent proposed by Armstrong introduced a power-transmitting device by means of magnetic force, even if the magnetism is produced by coils instead of permanent magnets (PMs) [19]. The magnetic gear, which initially adopted only PMs, was invented in 1941 [20]. In 1964, a patent concerning a coaxial magnetic gear was proposed by Martin [21]. Many different magnetic gear topologies appeared at that period, however, the torque density was quite poor due to the low performance and utilization of magnets. With the development of high-energy rare-earth magnets, magnetic gears revive the researchers' attention. Since 2001, when a novel coaxial magnetic gear equipped with NdFeB magnets was proposed by Atallah [22], magnetic gears have been gaining interest among researches.

This Section will provide an overview on the development of magnetic gears, especially over the last 20 years. It will cover the key publications related to magnetic gears. Several articles have been published to review magnetic gears [23, 24, 25, 26, 27, 28], whereas they show either limited topologies or focus on specified applications. In this Chapter, a general review on magnetic gears is presented, with special attention on coaxial transmission gears. The most common and recent discovered topologies are presented in Sec. 2.1. The working principle of these devices is described in Sec. 2.2. Sec. 2.3 focuses on the computational strategies that have been proposed and finally in Sec. 2.4 the key design aspects are discussed.

From the overview presented in this Chapter a contribution has been published in [29].

## 2.1 Magnetic gear topologies

### 2.1.1 Conventional non-modulated magnetic gears

Conventional magnetic gears are related to the basic non-contact magnetic gears in which PMs on different arrangements interact magnetically. Generally speaking, the ideas of conventional MGs stem from mechanical gears, such as spur gear [30] (Fig. 2.1(a)), worm gear [31] (as shown in Fig. 2.1(b)), skew gear [53], perpendicular gear [32] (as shown in Fig. 2.1(c)) and magnetic screw [33] (as shown in Fig. 2.1(d)). Although they are quite simple, the poor utilization of magnets and the resulting low torque density make them unattractive for industrial applications [27, 25].

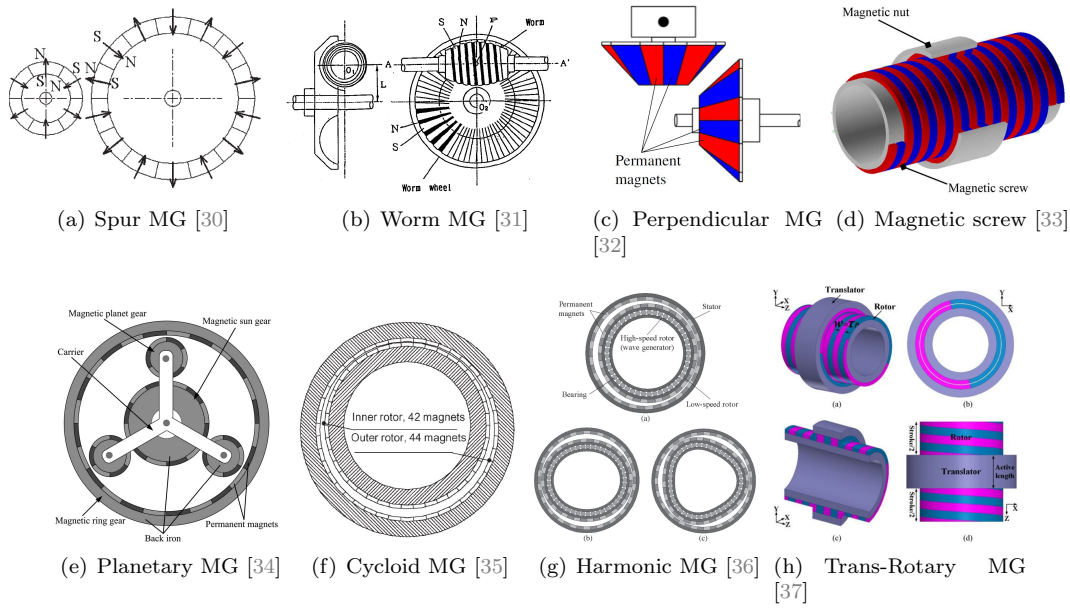


FIGURE 2.1: Schemes of various conventional magnetic gears.

On the contrary, some other conventional topologies exhibit fairly high torque density but complex structures. A magnetic planetary gearing arrangement (counterpart of the mechanical planetary gear) was simulated and fabricated in [34] (as shown in Fig. 2.1(e)). It was shown that torque density of this magnetic gear is close to  $100 \text{ kNm}/\text{m}^3$  with six magnetic planet gears, and less than  $50 \text{ kNm}/\text{m}^3$  with the three-planetary-gear. In [35], a cycloid permanent-magnet gear (as shown in Fig. 2.1(f)), based on the cycloid gearing principle was described. The cycloid action is utilized to modulate the air gap between the two magnetic rings, achieving a significant gear-reduction ability and a torque density close to  $107 \text{ kNm}/\text{m}^3$  was demonstrated experimentally. A magnetic harmonic gear (counterpart of the mechanical harmonic gear, as shown in Fig. 2.1(g)), which is particularly suitable for high-gear-ratio applications, was analyzed in [36]. It was shown that the transmitted torque is ripple-free and a torque density of up to  $150 \text{ kNm}/\text{m}^3$  can be achieved at relatively high gear ratios. A trans-rotary magnetic gear was investigated in [37] (as shown in Fig. 2.1(h)), which is used to convert linear motion to rotation.

### 2.1.2 Modulated magnetic gears

Among the magnetic gear topologies, the modulated type seems to be the most promising, since it exhibits both high efficiency and high torque density. The key merit of this configuration is that all the PMs contribute to torque transmission, achieving a torque density comparable with that of mechanical gears.

The coaxial magnetic gear using rare-earth magnets was initially proposed in [22] (as shown in Fig. 2.2(a)), while its design and performance analysis were given in [22, 54]. PMs are used on both inner and outer rotors, and steel pole-pieces are placed between these two rotors. The yokes of both rotors and steel pole-pieces are composed of silicon steel laminations. It was shown that a transmitted torque density exceeding  $70 \text{ kNm}/\text{m}^3$  was achieved in a prototype [54].

In [38], a coaxial magnetic gear with a spoke type inner rotor was presented (as shown in Fig. 2.2(b)). A torque density of  $54 \text{ kNm}/\text{m}^3$  was achieved in the experiment. It was also advised that a surface-mounted PM rotor seems to be preferable to a spoke one with the same volume.

In [39], a low-cost flux-focusing magnetic gear using ferrite magnets was investigated (as shown in Fig. 2.2(c)), which resulted a relatively high torque density from experimental setups.

In [40], a new stator arrangement, interior permanent magnet design were utilized in a coaxial magnetic gear (as shown in Fig. 2.2(d)). Three ways of connecting stator pole-pieces were also investigated.

In [41], a new topology of coaxial magnetic gear with interior-magnet outer-rotor configuration was designed and implemented (as shown in Fig. 2.2(e)). The inserted PMs are with the same polarity along the circumference of the outer rotor, making it much easier to manufacture. The achieved torque density of the prototype was around  $53 \text{ kNm/m}^3$ .

In [42], a coaxial magnetic gear with Halbach PM arrays was proposed and a complete analysis was performed (as shown in Fig. 2.2(f)). It was verified that a 13 % higher torque density, 67 % reduction in cogging torque and 28 % reduction of the total iron losses over a conventional one were achieved.

In [43], a new coaxial magnetic gear with optimal stationary pole piece shape and Halbach magnetic arrangement was developed (as shown in Fig. 2.2(g)). Using the proposed pole-piece, the torque density could be increased by 15 % or more, as compared to a conventional one.

In [44], a novel reluctance magnetic gear for the high speed transmission was proposed (as shown in Fig. 2.2(h)). Salient poles are utilized in the high speed rotor constructed by only iron core, resulting a very simple and robust structure. Besides, the proposed magnetic gear achieves high efficiency since the magnet eddy current loss is removed. The achieved torque density from simulation was  $29.4 \text{ kNm/m}^3$ .

In [45], a bearingless solution is proposed, with levitation windings embedded between the iron pole-pieces (as shown in Fig. 2.2(i)). Through a proper current control, radial forces can be produced to provide additional levitation capabilities, while the torque density is not affected by the suspension winding.

An interesting solution for applications where the shafts to couple are not intersecting is the one shown in [46], where the topology is equivalent to the conventional coaxial one but the flux modulators are bent (as shown in Fig. 2.2(j)). The torque density of the topology was limited to  $5.4 \text{ kNm/m}^3$  due to the bulky modulators and the flux leakages.

In [47], an axial-field magnetic gear was described (as shown in Fig. 2.2(k)), with a torque density around  $70 \text{ kNm/m}^3$  achieved in simulation.

In [55], the Halbach PM arrays for an axial-field magnetic gear was proposed, achieving a higher torque density compared to the conventional axial-field MG.

In [48], a novel axial-flux magnetic gear with L-shaped modulators and spoke-type magnet arrangement was presented (as shown in Fig. 2.2(l)). Due to the geometrical complexity, a 3D printing process was adopted. It was shown that the reduction of flux leakages and improvement of torque density are both achieved. According to the 3D FEM simulations, the torque density reaches  $74 \text{ kNm/m}^3$  with NdFeB magnets.

In [49], an axial-transverse-flux magnetic gear with T-shape flux modulators was proposed (as shown in Fig. 2.2(m)). The saturation level of iron pole-pieces is decreased in comparison to the standard axial topology considering the same device size and flux leakages are limited. A significant higher torque density (up to  $280 \text{ kNm/m}^3$ ) was obtained by 3D simulations.

In [50], a hybrid transverse-axial magnetic gear where additional PMs are employed on the flux modulator side was proposed (as shown in Fig. 2.2(n)). The torque density found through 3D finite element method (FEM) simulation was  $181.2 \text{ kNm/m}^3$  which is around 20 % improvement over the axial-flux magnetic gear.

A high-performance linear magnetic gear was proposed in [51] (as shown in Fig. 2.2(o)), achieving a thrust force density of  $1.7 \text{ MN/m}^3$ . The principle of operation is similar to that of the coaxial magnetic gear.

A new tubular linear magnetic gear utilizing high temperature superconductor (HTS) bulks for field modulation was proposed in [52] (as shown in Fig. 2.2(p)). The thrust force transmission capacity is significantly improved compared to the conventional one.

The comparison of magnetic gears in literatures is shown in Tab. 2.1. The numbers with stars are verified by prototypes. It is demonstrated that the modulated gears offer compatible torque densities as the mechanical ones.

Gear type	Gear ratio	Torque density ( $kNm/m^3$ )
Mechanical gear [25]	1–18000	100–600
Planetary MG [34]	3:1	97.3
Cycloid MG [35]	21:1	142 (107*)
Harmonic MG [36]	360:1	(75*)
Coaxial MG [54]	5.75:1	117 (72*)
Spoke MG [38]	5.5:1	92 (54*)
Spoke Ferrite MG [39]	3.25:1	40
IPM MG [40]	5.5:1	64 (42*)
Homopolar IPM MG [41]	7.33	(53*)
Halbach MG [42]	4.25	124
Reluctance MG [44]	8:1	29
Axial MG [47]	5.75:1	70
L-shaped axial MG [48]	3.17:1	280
T-shaped axial MG [49]	3.17:1	74
Hybrid-flux MG [50]	5.5:1	181

TABLE 2.1: Comparison of magnetic gears from data in literature. Values with \* refer to prototypes measurements.

## 2.2 Working principle

### 2.2.1 Conventional non-modulated magnetic gears

Generally speaking, the operating principle of conventional magnetic gears is based on the magnetic force interaction between permanent magnets. Usually, the magnetic poles work as the teeth of mechanical gears, thus the torque is transmitted. In order to operate analogously, some requirements should be taken into account [30, 56]:

- 1) the magnetic ratio  $P_1 : P_2$  is analogous to the mechanical ratio  $N_1 : N_2$  (where  $N_1$  and  $N_2$  are the number of teeth, and  $P_1$  and  $P_2$  are the number of poles of the two rings, respectively);
- 2) the total number of poles of each rotor should be even.

Concerning the cycloid and harmonic magnetic gears, the working principles are again based on the force acting between magnets. For further details, the reader is referred to [35, 36].

### 2.2.2 Modulated magnetic gears

In this kind of magnetic gear, which is the main topology under investigation in this thesis, the number of poles of inner and outer rotors are different. The working principle is based on the flux modulation effect of the ferromagnetic pole-pieces (see Secs. 3.1 and 3.2). Due to their modulation effect, from the field distribution produced by the PMs of one rotor, an appropriate space harmonic component, corresponding to the number of pole pairs of the other PM rotor, is generated. Therefore, quasi-constant torque transformation is achieved by the interaction of the harmonics with the same order. In order to achieve the highest torque transmission capability, the number of the steel pole-pieces ( $q$ ) needs to obey the following relationship [54]:

$$q = Pi + Po \quad (2.1)$$

where  $Pi$  and  $Po$  are the number of pole-pairs on the inner and outer rotor, respectively. The rotational speed of each parts then related by:

$$Pi\omega_{in} + Po\omega_{out} = q\omega_{poles} \quad (2.2)$$

where  $\omega_{in}$ ,  $\omega_{out}$  and  $\omega_{poles}$  are the mechanical speeds of the inner, outer rotors and the modulator, respectively. As far as the gear ratio is concerned, three operating modes can be obtained (depending on which part is fixed), corresponding to three different gear ratios. The gear ratios



are given by:

$$G_{os} = \frac{q}{P_o} \quad G_{io} = -\frac{P_o}{P_i} \quad G_{is} = \frac{q}{P_i} \quad (2.3)$$

where  $G_{os}$ ,  $G_{io}$ ,  $G_{is}$  are gear ratios when the inner ring, middle ring and outer ring are fixed, respectively. For further details, the reader is referred to [54, 57].

## 2.3 Computational models

Several models have been proposed for the simulation of magnetic gears, following three main approaches: analytic models based on equivalent networks, analytic models based on the mathematical solution of the field equations and purely numerical models.

The first method is based on machine modelling through reluctance networks as shown in [58], [59] and in Sec. 3.1. The machine domain is discretized through nodes that are connected through magnetic reluctances: this is equivalent to solving the integral form of the magneto-static equations (eddy currents are neglected) on a very coarse mesh with appropriate boundary conditions. If the reluctances depend on the unknowns, a nonlinear problem is obtained and magnetic saturation can be taken into account. The accuracy of this method depends on the number of nodes adopted for the discretization and generally this scheme is used for an initial design because of its simplicity.

The analytic approaches based on the solution of the field equations are formulated starting from the exact solution of the Laplace or Poisson equations in the case of linear ideal materials (iron with infinite permeability) and negligible eddy currents. Using the variables separation technique, the mathematical problem becomes the well known periodic Sturm-Liouville case. The gear domain is divided into several regions that communicate through a proper set of boundary conditions. The exact solution is written as a truncated Fourier series and all the unknown Fourier coefficients are computed to find the solution of the whole system of equations (see Sec. 4.1). For coaxial magnetic gears this approach has been followed in [60] adopting the 2D scalar potential formulation and in [61] adopting the 2D vector potential formulation. In [62] the same approach of [61] is adopted for axial gears. In [63] the analytic method is introduced for the case of spur gears and in [64] the approach is extended to arbitrary magnetization (e.g. Halback pattern). The efficiency of these techniques with respect to purely numerical approaches depends on how many harmonics are needed to accurately represent the field behavior.

FEM has been used since 1997 for studying magnetic transmissions [65] and is still the main tool when accurate nonlinear simulations have to be performed (Sec. 4.2). The analytic methods provide a fast analysis tool that can be as accurate as FEM in case of linear materials [66]. When the machines being studied are slightly saturated, the results still match the FEM ones; in deep saturation conditions or when eddy currents cannot be neglected, the analysis has to be performed numerically [67]. In [68], the comparison between the 2D and 3D FEM results is discussed: 2D simulations can overestimate up to 40% the torques because the end effects and the 3D flux leakages are neglected, especially when the machines are axially short (see Sec. 4.8). As pointed out in [27], in most cases the transmission gears do not exhibit any symmetry for ripple limitations (see Sec. 2.4.4), thus 3D FEM modelling can be computationally very demanding.

Recently several papers discussed the optimized gear design procedure adopting either finite element [69],[70] or analytic approaches [71]. As described in [71], the design procedures are moving towards multi-physic stochastic approaches.

## 2.4 Gear design aspects

### 2.4.1 Gear ratio

The choice of the gear ratio has a significant influence on the maximum torque transmission capability, torque ripple and efficiency [54, 72]. As a consequence, its selection is one of the key points in gear design procedures (see Secs. 3.3 and 3.4). An interesting feature of magnetic gears is the possibility to obtain variable gear ratios, in analogy to the mechanical planetary gear

set. According to Eq. (2.2), if the iron poles are kept fixed, the gear ratio is  $G_{io}$  otherwise the gear ratio changes accordingly to  $\omega_{poles}$ . In [73] and [74] the operation as continuously variable transmission was explained and validated through scaled prototypes.

A different approach for varying the gear ratio is to combine the concepts of flux-switching machines and magnetic gears: the ratio in this case can take discrete values by changing the number of pole pairs of the PMs. This solution is proposed in [75] and [76]. Another complex solution to obtain discrete variable gear ratios is the one shown in [77]: PMs are divided in small rod-shaped geometries that can rotate with respect to their axis and the flux modulators are composed by segments that can be moved and grouped in different numbers of flux modulators.

### 2.4.2 Iron pole pieces design

The geometry of the modulator is one of the crucial aspects of MG design, since it influences the torque transmission capabilities and the iron losses [43]. Mechanical stiffness and thermal dissipation properties should be given more consideration due to the large forces and rich harmonics in the iron pole-pieces [54, 71]. In [43], the effect of different shapes on the transmission torque was analyzed. In [78], the effect of connection bridges was considered from the electromagnetic and mechanical point of view and in [79] a prototype with inner bridges was designed with 3D FEM tools. According to [78], the inner bridge has the best performance when compared to the middle or outer bridge solution concerning average torque and torque ripple, but the iron losses are higher than the other two cases. The outer bridges solution provides the best structural stiffness.

The iron poles losses, forces, and displacements are analyzed in Secs. 4.9, 5.3, and 5.4 respectively.

### 2.4.3 Transmission losses

One of the key aspects of a gearbox is its efficiency. The losses in magnetic gears are mainly due to iron loss and eddy current loss in the permanent magnets (see Secs. 4.6 and 4.7). Modulated magnetic gears differ from conventional electrical machines because of the modulation effect of the pole pieces: several sub-harmonics are introduced as explained in [80], which cause eddy current losses in the PMs and rotational flux loci in the iron parts [81]. In order to compute the iron losses, the main approaches are the Bertotti's equation adopted in [81] and [82], or the Steinmetz one adopted in [80] and [83]. In [84] an alternative procedure is proposed in the frame of the loss separation method considering the rotational behavior of the flux loci. Normally yokes and flux modulators are laminated in magnetic gears thus the eddy currents in the iron regions can be neglected. According to [80]-[84], the highest iron losses are produced in the outer yoke and the losses due to eddy current in PMs are generally higher than the iron losses. Therefore, PMs segmentation should be adopted to achieve high efficiency in modulated magnetic gears.

### 2.4.4 Cogging torque

Based on the simplified approach of magnetomotive forces and the Fourier expansions of the reluctances, [85] predicted the cogging torques on the inner and outer rotors of a coaxial magnetic gear (see Sec. 3.4). The predicted harmonics were validated through 3D FEM modelling and through a prototype. A common practice is to introduce a cogging factor  $C_f$  as proposed in [86, 54]:

$$C_f = \frac{2pn_s}{N_c} \quad (2.4)$$

where  $p$  is the number of rotor pole pairs,  $n_s$  is the number of flux modulators and  $N_c$  is the least common multiple between  $2p$  and  $n_s$ . It was found that the smaller the factor  $C_f$  the lower will be the cogging torque. Thus normally gears are designed to be aperiodic with fractional gear ratios.

Some classical approaches adopted for electrical machines can also be used for ripple reduction. For example in [87], step skewing was shown to be effective for the low speed rotor.

### 2.4.5 Dynamic operation

Magnetic gears suffer from transient oscillations due to the low torsional stiffness [40]. Since gear operating principle is similar to a synchronous machine, passive damper windings were proposed by [40]. [88] discussed the beneficial effect of cage rotor bars on the torque ripples and on the static torque. In [89], the transient operation of an axial magnetic gear was shown through analytic calculations and through a prototype. In particular, the asynchronous operation due to overload was also discussed. In Sec. 7, a solution is proposed to avoid over-speed in asynchronous operation of magnetic gears that can also be adopted, with a proper control system, to damp the oscillations.

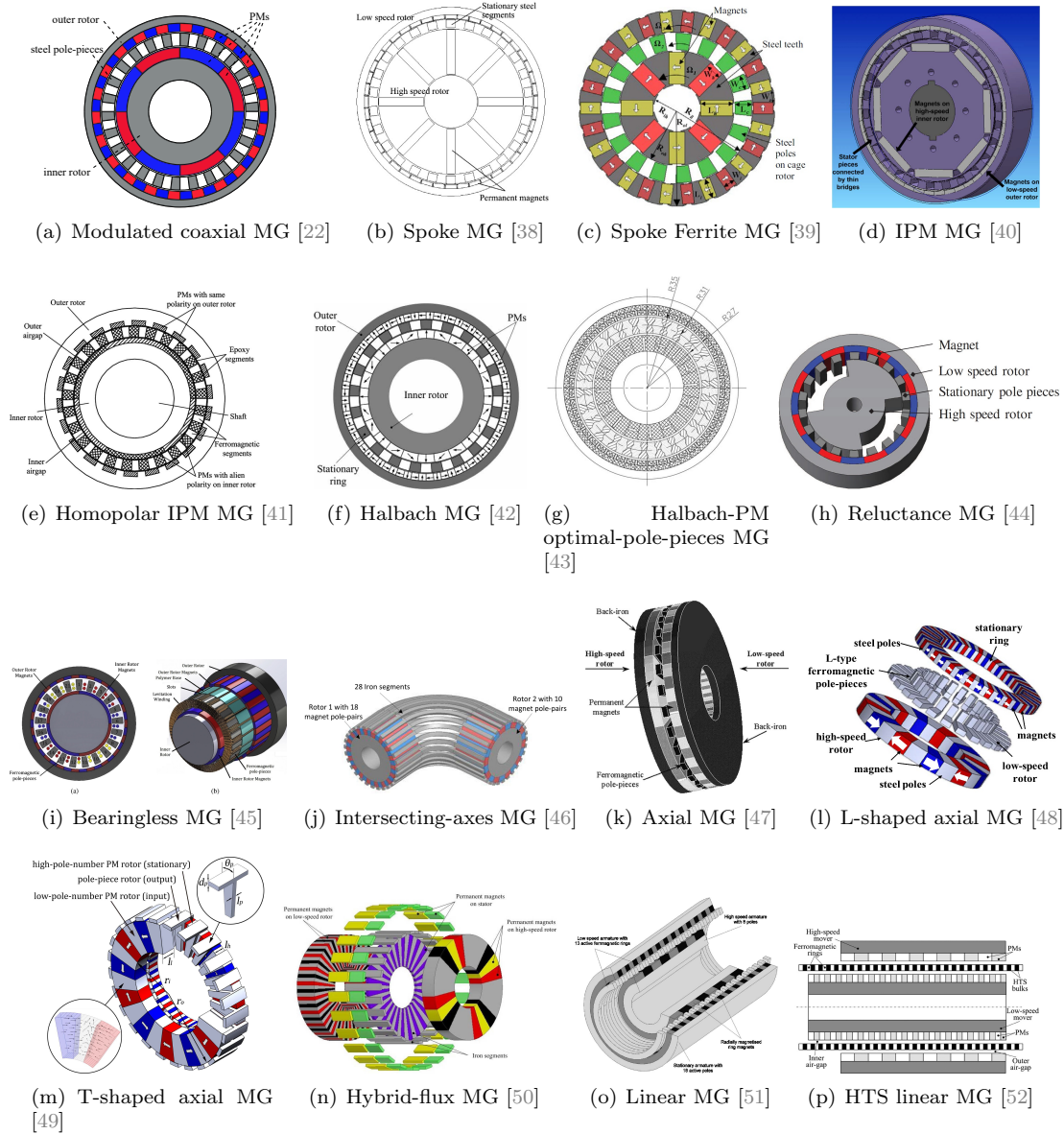


FIGURE 2.2: Schemes of various modulated magnetic gears.

## Chapter 3

# Magnetic transmissions basics

As briefly introduced in Sec. 2.2.2, the operation principle of the most diffused magnetic transmissions is based on the modulation of the magnetic fields produced by two PM rotors using ferromagnetic pole pieces. Unlike different topologies such as spur gears (see Fig. 2.1), since all the magnets contribute to the torque an high torque density can be reached. This Chapter focuses on the main aspects that characterize a magnetic transmission, ranging from the modulation effect, which is the basic principle on which magnetic transmission relies, to the peculiar overload protection.

In Sec. 3.1 a qualitative explanation is given based on a simplified model.

In Sec. 3.2, the general case with three moving rotors is analyzed and the theoretical predictions are validated through a Finite Element simulation.

Secs. 3.3, 3.4 and 3.5 deal with the machine periodicity, the torque ripple analysis and the intrinsic overload protection of magnetic transmissions respectively. From the theoretic point of view, a magnetic gear could have the low speed rotor outside and the high speed rotor inside and vice-versa. For mechanical and manufacturing reasons that will be clarified in the next Chapters, normally the topology adopted is the one with the fast rotor inside: this is the standard configuration adopted in all the thesis ( $P_i < P_o$ ).

### 3.1 Permeances network formulation

In order to find a simple relation between torque and geometrical parameters of a magnetic gear, the Fourier's analysis is applied and the first harmonic is considered in the following calculations. The magneto motive force  $F$  due to both inner and outer rotor can be expressed as:

$$F = \frac{4}{\pi} \cdot N \cdot I \left( \sin(P_i \cdot (\theta + \alpha)) + \sin(P_o \cdot (\theta + \beta)) \right) \quad (3.1)$$

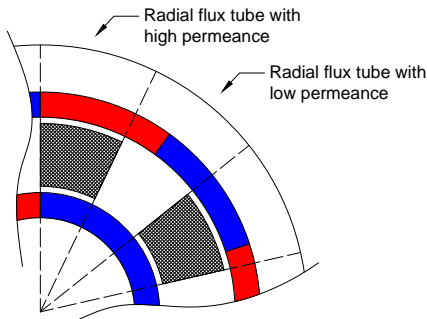


FIGURE 3.1: Approximation of radial flux tubes.

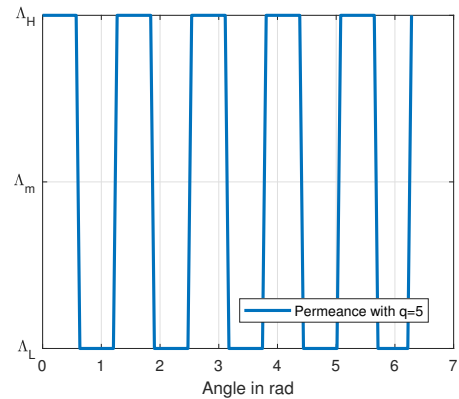


FIGURE 3.2: Permeance square wave with number of iron poles  $q = 5$ .

where  $NI$  are the equivalent ampere-turns that model the magnets and  $\alpha$  and  $\beta$  are the displacement angles of the inner and outer magneto-motive forces (MMFs) referred to a reference position. In Fig. 3.1 the inner and outer magnets are considered to have the same equivalent  $NI$ .  $F$  represents the sum of the first harmonic of inner and outer rotor, with periodicities  $Pi$  and  $Po$  respectively.

For the following development in this Section, the magnetic gear end-effects and flux leakages are neglected and the iron permeability is assumed as infinite. Under these hypothesis, the machine permeance can be approximated to a square wave moving along the angular coordinate according to Fig. 3.1: the permeance wave is shown in Fig. 3.2 as functions of the angular coordinate  $d\theta$ .  $\Lambda_L$  and  $\Lambda_H$  are the low and high permeances respectively, thus the differential permeances read:

$$d\Lambda_L = \frac{\mu_0 L \cdot r_{poles} \cdot d\theta}{g} \quad (3.2)$$

$$d\Lambda_H = \frac{\mu_0 L \cdot r_{poles} \cdot d\theta}{(g + l_{poles})} \quad (3.3)$$

where  $g$  is the total gap size (sum of inner and outer airgap dimension),  $l_{poles}$  is the pole radial size,  $r_{poles}$  is the pole barycentre radius and  $L$  is the machine axial length. Expanding the reluctance square wave through the Fourier's series, the differential mean and first harmonic permeances  $d\Lambda_m$  and  $d\Lambda_1$  are:

$$d\Lambda_m = \mu_0 L \cdot r_{poles} \cdot d\theta \cdot \frac{2 \cdot g + l_{poles}}{2 \cdot g \cdot (g + l_{poles})} \quad (3.4)$$

$$d\Lambda_1 = \frac{4}{\pi} \cdot \frac{\Delta d\Lambda}{2} = \frac{\mu_0 L \cdot 2 \cdot r_{poles} \cdot l_{poles} \cdot d\theta}{\pi g \cdot (g + l_{poles})} \quad (3.5)$$

$$d\Lambda = d\Lambda_m + d\Lambda_1 \cdot \cos(Ps \cdot (\theta + k_p)) \quad (3.6)$$

where  $q$  is the number of iron poles and  $k_p$  is the angular shift of the permeance waveform. If the permeance is set as the reference system,  $k_p$  is nil and the magnetic flux density calculated at the iron poles mean radius  $r_{poles}$  is:

$$\begin{aligned} B = F \cdot \frac{d\Lambda}{r_{poles} \cdot d\theta \cdot L} = \frac{4}{\pi} \cdot NI \cdot \mu_0 \cdot 2 \cdot \left( \frac{2g + l_{poles}}{2g \cdot (g + l_{poles})} \right) \cdot \left( \sin Pi(\theta + \alpha) + \sin Po(\theta + \beta) \right) + \\ + \frac{4}{\pi} \cdot NI \frac{2\mu_0 l_{poles}}{g \cdot (g + l_{poles})} \cdot \left( \frac{1}{2} \sin((q + Pi)\theta + Pi \cdot \alpha) + \frac{1}{2} \sin((q - Pi)\theta - Pi \cdot \alpha) + \right. \\ \left. + \frac{1}{2} \sin((q + Po)\theta + Po\beta) + \frac{1}{2} \sin((q - Po)\theta - Po\beta) \right) \end{aligned} \quad (3.7)$$

and the approximated magnetic flux density inside the inner magnet can be calculated using the radius ratio. From (3.7), the effect of the modulation pole pieces is clear: the permanent magnet MMFs with spatial periodicities  $Pi$  and  $Po$  are modulated, resulting in four MMFs with periodicities  $q + Pi$ ,  $q - Pi$ ,  $q + Po$ ,  $q - Po$ .

The magnetic energy stored into the device airgaps, is:

$$W(\alpha, \beta, \theta) = \int_0^{2\pi} \frac{1}{2} F^2 \Lambda d\theta \quad (3.8)$$

and the torques on the rotors are computed as  $T_{in} = \frac{\partial W(\alpha, \beta, \theta)}{\partial \alpha}$  and  $T_{out} = \frac{\partial W(\alpha, \beta, \theta)}{\partial \beta}$ . According to [57], a device with steady characteristics is obtained only when:

- $Pi = Po$ ,  $q \neq 2Pi$

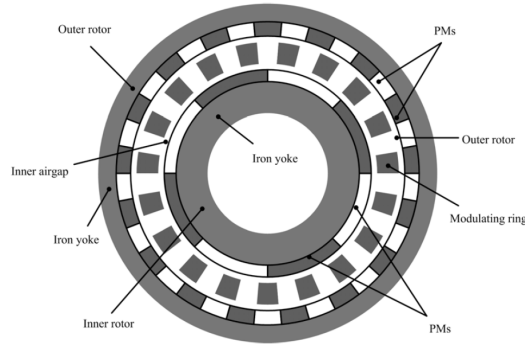


FIGURE 3.3: Coaxial magnetic gear structure, similar to the one proposed in [22].

- $P_i \neq P_o, q = P_o \pm P_i$

The former case is the one of unitary ratio transmissions, normally adopted in all applications where mechanical insulation is requested but the rotational speed of the inner and outer rotors is the same. The torque has an expression:

$$|T_{in}| = |T_{out}| = \pi P_i (NI)^2 \Lambda_m \sin(P_i(\alpha - \beta)) \quad (3.9)$$

The latter case is the most interesting one:

$$\begin{cases} T_{in} = \mp 0.5\pi P_o (NI)^2 \Lambda_1 \sin(P_i\alpha - P_o\beta) \\ T_{out} = -0.5\pi P_o (NI)^2 \Lambda_1 \sin(P_i\alpha - P_o\beta) \end{cases} \quad (3.10)$$

These torque equations are derived only to understand the physical principle beyond the gear modulating effect. In the next Chapters it will be clear that (3.10) is too simplified for being adopted for real calculations.

## 3.2 Modulation effect and harmonic analysis

In Sec. 3.1 the basic idea of the modulation effect has been given. In the current Section the general case with three moving rotors is analyzed. For the sake of clarity, an example of modulated coaxial magnetic gear is shown in Fig. 3.3.

In [54] the radial and tangential flux density distribution produced by either permanent magnet rotors are written, in analogy to the procedure in Sec. 3.1, as:

$$\begin{aligned} B_r(r, \theta) = & \left( \sum_{m=1,3,5\dots} b_{rm}(r) \cos(mp(\theta - \omega_r t) + mp\theta_0) \right) \\ & \times \left( \Lambda_{r0}(r) \sum_{j=1,3,5\dots} \Lambda_{rj}(r) \cos(jq(\theta - \omega_s t) + mp\theta_0) \right) \end{aligned} \quad (3.11)$$

$$\begin{aligned} B_\theta(r, \theta) = & \left( \sum_{m=1,3,5\dots} b_{\theta m}(r) \sin(mp(\theta - \omega_r t) + mp\theta_0) \right) \\ & \times \left( \lambda_{\theta 0}(r) \sum_{j=1,3,5\dots} \lambda_{\theta j}(r) \cos(jq(\theta - \omega_s t) + mp\theta_0) \right) \end{aligned} \quad (3.12)$$

Parameter	Value
High speed rotor pole pairs	4
Low speed rotor pole pairs	22
Iron pole pieces	26
Remanence NdFeB	1.25 T
m coefficient	1
k coefficient	-1

TABLE 3.1: Parameters adopted in [22].

where  $p$  is the generic number of pole pairs on the permanent magnet rotor (since (3.11) and (3.12) can be applied for both inner and outer rotors),  $\omega_r$  and  $\omega_s$  are the rotational speeds of the permanent magnet rotor and pole-pieces respectively,  $b_{rm}$  and  $b_{\theta m}$  are Fourier coefficients of the flux density distribution without pole pieces. In particular, (3.11) and (3.12) have the same structure of (3.7) without Fourier series truncation. Developing the equations further as in [22], the number of pole pairs in the space harmonic flux density distribution can be computed as follows:

$$p_{m,k} = |mp + kq| \quad (3.13)$$

$$m = 1, 3, 5, \dots \infty \quad (3.14)$$

$$k = 0, \pm 1, \pm 2, \pm 3, \dots, \pm \infty \quad (3.15)$$

Eq. (3.13) can be applied to find the inner rotor modulated field (when  $p = Pi$ ) or the outer rotor modulated field (when  $p = Po$ ). Clearly (3.13) defines the link between the number of poles of the inner rotor, outer rotor and the number of ferromagnetic pole pieces. Once the couple  $(m,k)$  is defined,  $Pi$ ,  $Po$  and  $q$  are linked according to (3.13). The rotational velocity of the flux density space harmonics is given as:

$$\omega_{m,k} = \frac{m \cdot p}{m \cdot p + k \cdot q} \cdot \omega_r \quad (3.16)$$

Eq. (3.16) proposed in [22] is valid in the case of stationary pole pieces and can be also found starting from (3.7) if the inner or outer rotors are rotated by  $\alpha = \Delta\theta$  or  $\beta = \Delta\theta$ .

According to Eqs. (3.13) and (3.16), the effect of the pole pieces is well understandable. Considering the inner rotor with  $Pi$  pole pairs, the number of pole pairs seen by the outer rotor is different from  $Pi$  (as already demonstrated with the simple model in (3.7)). The speed of the modulated space harmonic also differs from the one of the rotor which is producing it by the factor in Eq. (3.16).

From (3.11) and (3.12), developing the products with  $\omega_s \neq 0$ , Eq. (3.16) reads:

$$\omega_{m,k} = \frac{m \cdot p}{m \cdot p + k \cdot n_s} \cdot \omega_r + \frac{k \cdot n_s}{m \cdot p + k \cdot n_s} \cdot \omega_s \quad (3.17)$$

Using the couple  $m = 1, k = -1$  that gives the maximum torque contribution, if the iron poles are kept stationary the nominal gear ratio  $G_n$  becomes:

$$G_n = \frac{n_s - p}{p} \quad (3.18)$$

otherwise if the outer rotor is kept stationary, the gear ratio becomes:

$$G_n = \frac{n_s}{p} \quad (3.19)$$

If all the three parts are free to move and the rotational speed of the iron poles can be modified, the gear ratio is continuously variable.



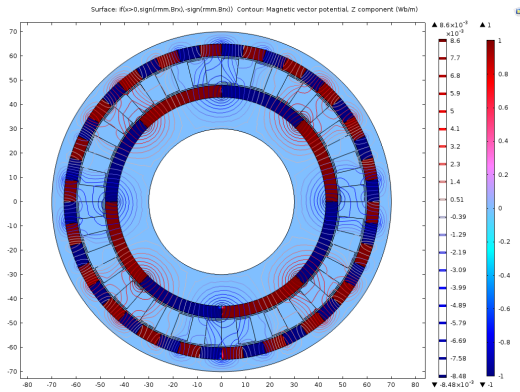


FIGURE 3.4: Test case geometry adopted for the Finite Element simulation.

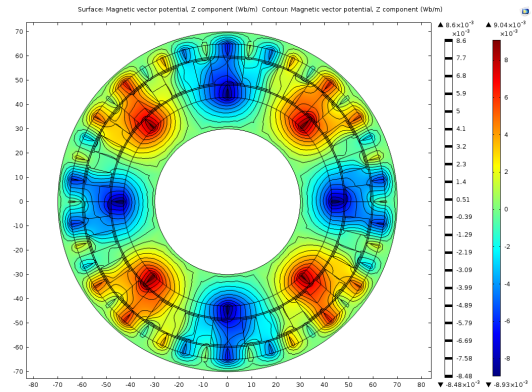
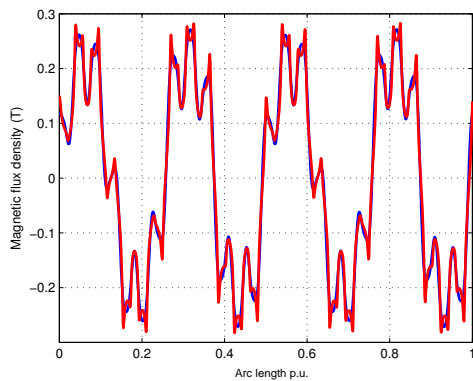
FIGURE 3.5: Magnetic vector potential  $A_z$  color map and contour lines.

FIGURE 3.6: Inner magnets active, outer air gap magnetic flux density. Arc length is in p.u.

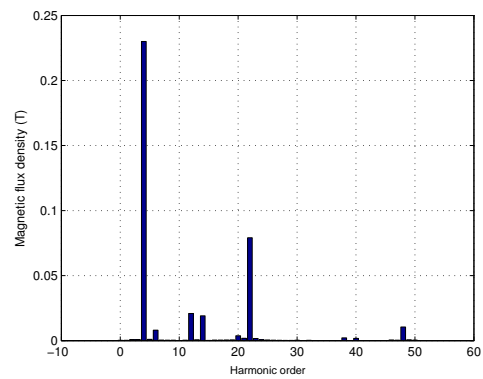


FIGURE 3.7: Inner magnets active, outer air gap magnetic flux density harmonics.

Using the same geometry adopted in [22] reported in Tab. 3.1 but changing the residual flux density  $B_r$  to  $B_r = 0.4$  T (ferrite magnets), the radial magnetic flux density has been computed enabling the inner magnets and the outer magnets. The results are reported in Figs. 3.6 and 3.8. As visible in the bar plots in Figs. 3.7 and 3.9, the iron poles affect the flux density waveform: considering the inner rotor with 4 pole pairs, in the outer air gap the 22<sup>th</sup> harmonic has a considerable amplitude. The same happens with the outer magnets that cause a 4<sup>th</sup> harmonic in the inner air gap. The bar plots also indicate that the couple  $m = 1, k = -1$  gives the maximum torque contribution. A different set for the parameters could be used but the torque density of the magnetic gear wouldn't be the optimal one.

In Fig. 3.10 the magneto-static simulations of the torque ripple has been reported. In this case the device losses are neglected and the rotors are supposed to rotate with a constant speed. Since in steady state operation the magnetic fields must rotate at the same speed, the iron losses affects the output torque that is lower than the loss-less case.

### 3.3 Periodicity

The rotor magnets MMFs and iron poles permeances can be thought as trigonometric space functions in order to find periodicities. The relations are:

$$\begin{cases} y_{in} = \cos(Pi(x - \omega_{in} \cdot t + \phi_i)) \\ y_{out} = \cos(Po(x + \omega_{in} \cdot \frac{P_i}{P_o} \cdot t + \phi_o)) \\ y_{pole} = \cos(q \cdot x) \end{cases} \quad (3.20)$$

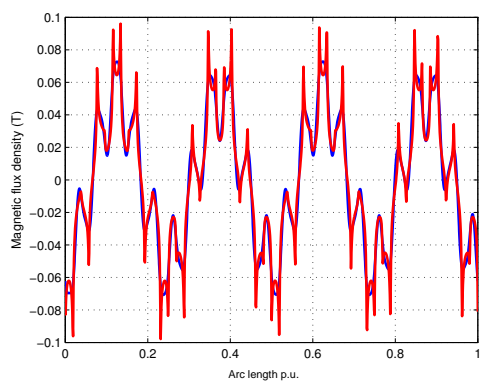


FIGURE 3.8: Outer magnets active, inner air gap magnetic flux density. Arc length is in p.u.

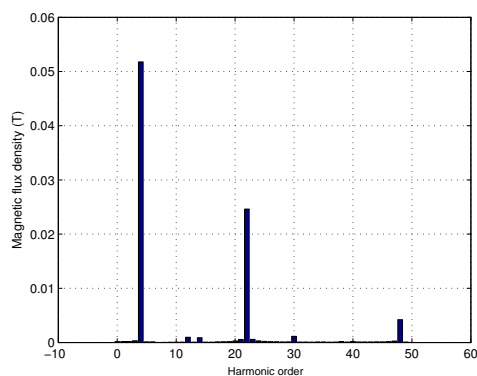


FIGURE 3.9: Outer magnets active, inner air gap magnetic flux density harmonics.

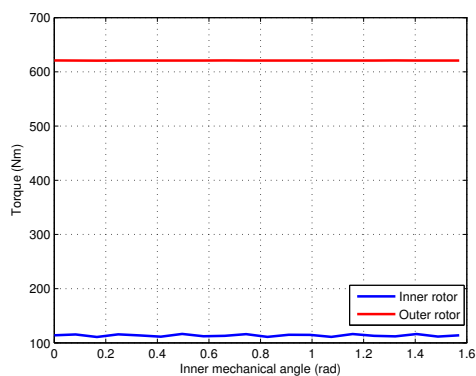


FIGURE 3.10: Stall torques of the inner and outer rotors. The simulation is a magneto-static parametric sweep of angular positions.

Order	Harmonic	From FEM
Pi	4	✓
Po	22	✓
q+Pi	30	✓
q-Pi	22	✓
q+Po	48	✓
q-Po	4	✓

FIGURE 3.11: Magnetic flux density expected harmonics from Eq. (3.7) and comparison with the obtained results in Figs. 3.8 and 3.9.

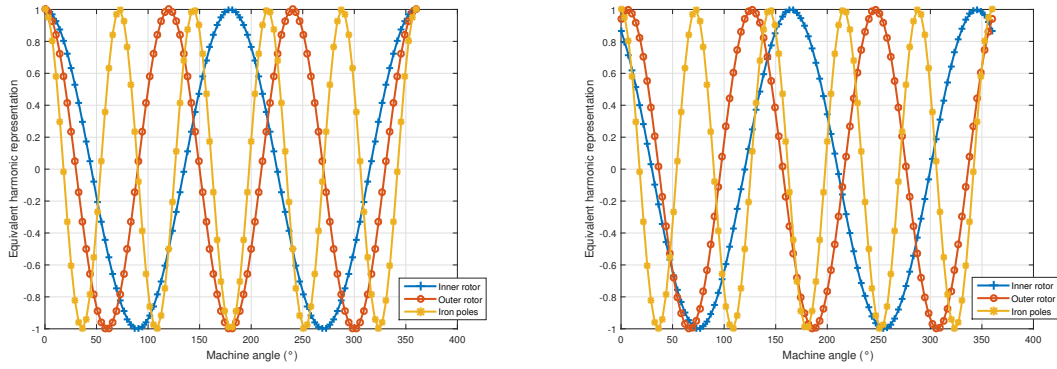


FIGURE 3.12: Periodicity detection for  $P_i = 2$ ,  $P_o = 3$ ,  $q = 5$ . The solution is not periodic for rational gear ratios.

where  $x$  is the angular coordinate referred to the iron poles fixed system,  $\phi_i$  and  $\phi_o$  are spatial shifts,  $\omega_{in}$  is the inner rotor speed. The field distribution has a periodicity  $p = \text{GCD}(P_i, P_o, P_i + P_o)$ . The parameter  $p$  is greater than zero if the gear ratio is integer; in this case only a sector  $\frac{2\pi}{p}$  could be studied reducing the computational effort. As already introduced in Sec. 2.4.4, the integer gear ratio geometry suffers from poor performance in terms of cogging torque therefore generally a full machine simulation is required. When adopting Finite Element Method (FEM) magneto-static position sweeps, the parameter that needs to be set is the angle span  $\Delta\theta_{in}$ , referred to the inner rotor. In order to study the entire fields distribution, an immediate choice is  $\Delta\theta_{in} = \frac{2\pi}{2 \cdot P_i}$  since the inner rotor electrical angle is  $2\pi$  and the outer rotor is consequently shifted by  $\Delta\theta_{out} = \frac{2\pi}{P_o}$  mechanical degrees equivalent to  $2\pi$  electrical degrees.

In order to understand how magnetic fields evolve rotating both inner and outer rotor, the solution of the system (3.20) has to be analyzed. The angles  $\phi_i$  and  $\phi_o$  are considered zero therefore at time  $t = 0$  both the rotors are aligned with the iron poles and  $y_{in} = y_{out} = y_{pole} = 0$ . By imposing  $y_{in} = y_{out} = 1$ , the spatial positions where the inner and outer rotor are aligned as in the initial condition are found. In particular the solutions are:

$$\begin{cases} y_{in} = 1 \rightarrow x_i = \omega_{in} \cdot t + \frac{2k_1\pi}{P_i} \\ y_{out} = 1 \rightarrow x_o = -\frac{\omega_{in} \cdot t \cdot P_i}{P_o} + \frac{2k_2\pi}{P_o} \end{cases} \quad (3.21)$$

where  $k_1$  and  $k_2$  are integers. Searching for the condition  $y_{in} = y_{out}$ , the solution becomes:

$$\omega_{in} \cdot t \cdot \left(1 + \frac{P_i}{P_o}\right) = 2\pi \cdot \left(\frac{k_2}{P_o} - \frac{k_1}{P_i}\right) \rightarrow \omega_{in} t = \frac{k_2 \cdot P_i - k_1 \cdot P_o}{P_i \cdot (P_i + P_o)} \quad (3.22)$$

The solutions of Eq. (3.22) are the angles referred to the inner rotor for which the inner and outer rotors are aligned in at least one point. The graphical representations in Figs. 3.13 and 3.14 allow to find the parameters  $k_1$  and  $k_2$  easily. Assuming the case of Fig. 3.13,  $k_1 = \{0 : (P_i - 1)\}$  and  $k_2 = \{0 : (P_o - 1)\}$ . By ordering the terms  $\omega_{in} t$ , the sweep of  $k_1$  and  $k_2$  gives the sequences  $(K1) = k_1^1 \dots k_1^{P_i-1}$  and  $(K2) = k_2^1 \dots k_2^{P_o-1}$ . These vectors represent the sequences of alignments increasing the inner (and outer) rotor angles in the inner and outer rotor material frame reference respectively.

If the frame is changed to the poles one, the sequence  $(Kp) = \left(\frac{\omega_{in} t (K1, K2)}{2\pi} + \frac{K1}{P_i}\right) \cdot (P_i + P_o)$  gives the iron poles order. For example, Fig. 3.15 shows the radial forces acting on the iron poles of a gear with  $P_i = 2$ ,  $P_o = 7$ ,  $q = 9$ . The periodicity condition allows to study an angular sweep  $\Delta\theta = \frac{2\pi}{18}$ . Rearranging (3.22) the real waveform can be built as shown in Fig. 3.16.

If  $\text{LCM}(P_i, P_o) = P_i \cdot P_o$ , the term  $P_i(P_i + P_o) = P_i \cdot q$  is the number of alignments when the inner rotor is rotated by an angle equal to  $\delta = 2\pi$ . Otherwise if  $P_i$  and  $P_o$  have common factors, the number of periodic angular positions decreases to  $\frac{P_i(P_i + P_o)}{f}$  where  $f$  is the product of the common factors between  $P_i$  and  $P_o$ .

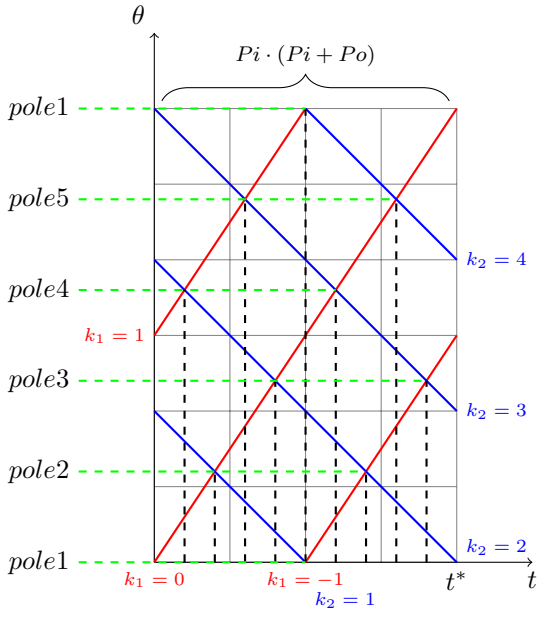


FIGURE 3.13: Periodicity diagram,  $P_i = 2$ ,  $P_o = 3$ ,  $q = 5$ . Red lines represent the inner rotor peaks positions, the blue lines the outer rotor peaks, the dashed lines the alignments between the MMF's peaks.

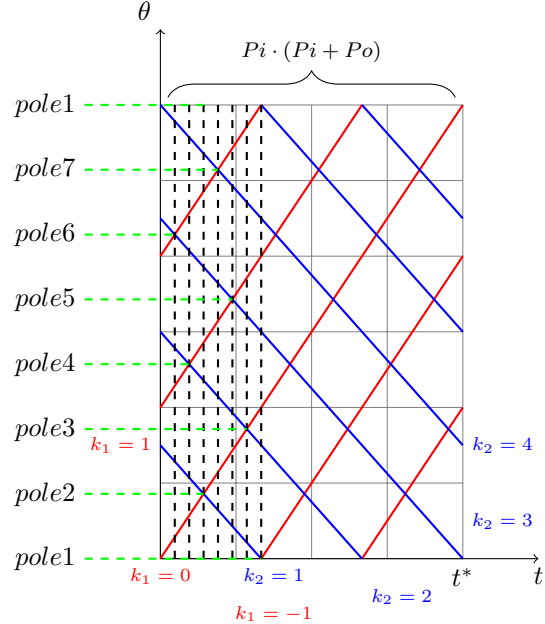


FIGURE 3.14: Periodicity diagram,  $P_i = 3$ ,  $P_o = 4$ ,  $q = 7$ . Red lines represent the inner rotor peaks positions, the blue lines the outer rotor peaks, the dashed lines the alignments between the MMF's peaks.

$P_i$	$P_o$	$q$	$K_1$	$K_2$	$K_p$
2	3	5	0, 1	0, 2, 1	1, 4, 2, 5, 3
3	5	8	0, 1, 2	0, 2, 4, 1, 3	1, 4, 7, 2, 5, 8, 3, 6

TABLE 3.2: Example of sequences.

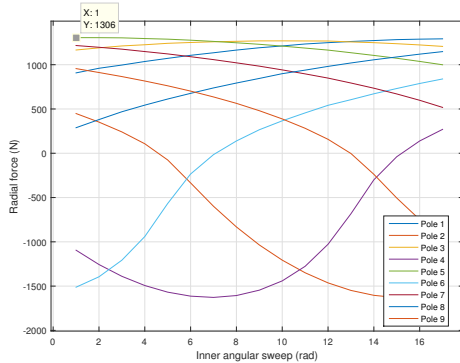


FIGURE 3.15: Radial forces acting on ferromagnetic poles calculated according to Sec. 5.3. The gear geometry considered has  $P_i = 2$ ,  $P_o = 7$ ,  $q = 9$  and the angular sweep is therefore  $\Delta\theta = \frac{2\pi}{18}$ .

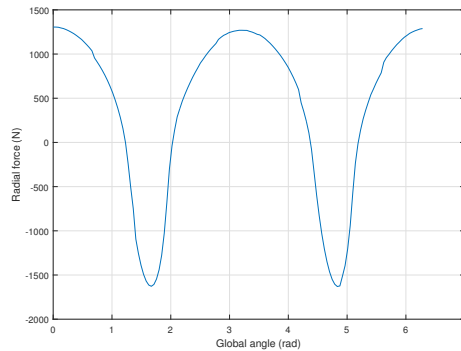


FIGURE 3.16: Radial forces acting on one ferromagnetic pole. The waveform is built for an entire rotation of the inner rotor combining the data from Fig. 3.15 according to Eq. (3.22).

Inner rotor	$LCM(2 \cdot Pi, q)$
Outer rotor	$LCM(2 \cdot Po, q)$

TABLE 3.3: Estimated torque ripple harmonics.

### 3.4 Torque ripple

Mechanical gears, as all electrical machines in general, should be designed in order to transmit a torque with the lowest possible ripple. Magnetic gears suffer from torque ripple because of the intrinsic operating principle: some rotor angle combinations are described by a high energy states and therefore a cogging torque naturally tries to minimize this energy. The torque equation already introduced in Sec. 3.1 is:

$$T(\theta) = -\frac{\partial W(\theta)}{\partial \theta} \quad (3.23)$$

where  $T(\theta)$  can represent an inner or outer torque, while  $W$  is the magnetic energy. Adopting the hypothesis of magnetic energy stored mainly in the air gap with low magnetic permeability, the energy expression becomes:

$$W(\theta) = \frac{1}{2\mu_0} \int_V B^2 dV \quad (3.24)$$

This behaviour is generally shown when studying permanent magnet machines. The cogging torque depends mainly on the gear geometry.

The inner rotor rotation angle is expressed by  $\delta$ . According to [85], the air volume  $dV$  can be expressed as:

$$dV = L \cdot g \cdot r_{gap} \cdot d\delta \quad (3.25)$$

where  $L$  is the axial machine length,  $g$  is the airgap thickness and  $r_{gap}$  is the middle airgap radius.  $F(\delta)$  is the MMF Fourier's series and  $\Lambda(\delta - \theta)$  is the iron poles permeance where  $\theta$  denotes the angular shift between inner rotor and pole pieces, the magnetic flux density is:

$$B = \frac{F(\delta) \cdot \Lambda(\delta - \theta)}{2\pi r_{gap} L} \quad (3.26)$$

The energy expression is therefore:

$$W(\theta) = \frac{g}{8\mu_0 r_{gap} L \pi^2} \int_0^{2\pi} F^2(\delta) \Lambda^2(\delta - \theta) d\delta \quad (3.27)$$

In [85] the Fourier's series are developed and the global harmonic content of the torque ripple is shown in Tab. 3.3. This method only gives informations about the expected harmonic content but the torque ripple amplitude is unknown because of the difficult evaluation of the permeance  $\Lambda$ . The exact calculation of the amplitude requires nonlinear FEM simulations.

In the hypothesis of MMF with a square wave shape, the Fourier's series coefficients are:

$$a_n = \frac{4}{n\pi} K \quad n = 1, 3, 5... \quad (3.28)$$

This means that higher harmonics will have lower values. Based on this law, a general cogging factor  $C_{factor}$  is normally adopted to describe the magnetic gear behaviour in terms of torque ripple, as briefly introduced in Sec. 2.4.4:

$$C_{factor} = \frac{2Pi \cdot q}{lcm(Pi, q)} \quad (3.29)$$

The lower cogging factor the lower torque ripple is expected. The gears that guarantees the lowest cogging factor are the one with the highest least common multiple between  $Pi$  and  $q$ , therefore fractional gear ratios are preferred. In particular with higher number of poles  $Pi$  for

the low pole pairs rotor there are more combinations to obtain fractional ratios but also the outer magnets pole pairs  $P_o$  are harder to be manufactured.

The choice of the pole pairs is therefore a trade off between the device complexity (several magnets with reduced size on the outer rotor) and the torque ripple requirements. Generally the pole pairs of the low speed rotor is at least fixed to  $P_i \geq 2$ .

### 3.5 Overload protection

Mechanical gearboxes must be sized for the maximum expected torque. If the torque exceeds the limit and there are no mechanical frictions, the gear is irreversibly damaged because of the tooth plastic deformation and needs to be replaced. Instead, magnetic gears are synchronous machines: if the torque exceeds the maximum limit, the operation becomes asynchronous and the device is no longer capable of transmitting torque. In this operational condition, the average transferred torque is nil while the torque ripple effects remain. Considering the input shaft to be torque controlled, when the operation becomes asynchronous the input rotor accelerates till a new equilibrium is reached (at much higher rotational speed). Once the transmitted torque goes again below the limit, the magnetic gear starts its normal operation.

In applications such as wind power generation, gearboxes are mandatory in order to keep the generators size small. Since the wind load is variable, the gearboxes have to operate in safe conditions: the device sizing takes into account the maximum estimated overload.

Adopting magnetic gears for the wind turbine case, the overload protection would be automatically guaranteed. In order to understand what happens when the torque exceeds the design threshold, the mechanical equations of the two rotors are implemented as well as the magnetic gear magneto-static equations in the simplifying hypothesis of negligible eddy current effects.

$$\begin{cases} J_{in} \cdot \frac{d\theta_{in}^2}{dt^2} + b_{in} \cdot \frac{d\theta_{in}}{dt} = T_{injected} - T_{in} \\ J_{out} \cdot \frac{d\theta_{out}^2}{dt^2} + b_{in} \cdot \frac{d\theta_{out}}{dt} = T_{out} - T_{extracted} \\ J_{poles} \cdot \frac{d\theta_{poles}^2}{dt^2} + b_{poles} \cdot \frac{d\theta_{poles}}{dt} = T_{poles} - T_s \end{cases} \quad (3.30)$$

The system (3.30) represents the mechanical equations when the input rotor is the inner one, the output rotor is the outer one and the iron poles rotor is not held stationary.  $T_{in}$ ,  $T_{out}$  and  $T_s$  are the torques due to the couplings between the rotors.  $T_{injected}$  is the input torque on the high speed inner rotor,  $T_{poles}$  is the torque injected through the iron poles rotor and  $T_{extracted}$  is the load torque applied on the low speed rotor. In particular  $T_{poles}$  can be positive or negative depending on the effect of the middle rotor on the reduction rate; when negative power is extracted from the rotor and vice-versa.  $T_{extracted}$  is generally the sum of a constant, a damping and an acceleration term:

$$T_{extracted} = T_L + b_{load} \cdot \frac{d\theta_{load}}{dt} + J_{load} \cdot \frac{d\theta_{load}^2}{dt^2} \quad (3.31)$$

where all the contributes could be functions of both time  $t$  and space  $\theta_{load}$ .

In order to simplify the control structure, the output torque is fixed to  $T_{extracted} = b_{load} \cdot \frac{d\theta_{load}}{dt}$  and two cases are considered:

- speed regulation input rotor;
- torque regulation of the input rotor.

The former regulation requires the modelling of a PI controller: a speed error is calculated at each time instant as difference between the reference and current speed. Through a PI the torque applied to the inner rotor becomes:

$$\left( Kp + \frac{Ki}{s} \right) \cdot \omega_{err} = \frac{Ki \cdot (1 + s\tau_c)}{s} \omega_{err} \quad (3.32)$$

Inner pole pairs	$P_i$	2	–
Outer pole pairs	$P_o$	13	–
Iron poles	$q$	15	–
Gear ratio	$G_n$	6.5	–
Inner inertia	$J_{in}$	0.0063	$kgm^2$
Outer inertia	$J_{out}$	0.0447	$kgm^2$
Poles inertia	$J_{poles}$	0.02	$kgm^2$
Load inertia	$J_{load}$	10	$kgm^2$
Inner friction	$b_{in}$	0.05	$\frac{Nm \cdot s}{rad}$
Outer friction	$b_{out}$	0.05	$\frac{Nm \cdot s}{rad}$
Poles friction	$b_{poles}$	0.05	$\frac{Nm \cdot s}{rad}$
Load friction	$b_{load}$	10	$\frac{Nm \cdot s}{rad}$
Control rise time	$t_r$	1	s
Control time const	$\tau_c$	0.4	s

TABLE 3.4: Mechanical parameters adopted for the transient simulations.

where  $T = \frac{K_p}{K_i}$  is the regulation time constant introduced by the controller. The coefficients  $K_p$  and  $K_i$  can be the ones adopted in the electronic controller (if the prime mover is a synchronous electric motor) or they can model a physical principle (for example in an induction motor without frequency regulation the torque can be considered proportional to the slip).

The latter regulation is easier to be implemented numerically because  $T_{injected}$  is directly applied in (3.30).

Generally the control in real applications is more complicated: for example if an asynchronous electric motor is connected as input source, the regulation is similar to a speed regulation but the target velocity changes according to the load because of the machine slip. If a gas turbine is considered as input, the controlled variable is the fuel mass flow which is related to the current power of the turbine. If the rotational speed is variable, the control becomes intrinsically non-linear (the product between torque and speed is involved). In order to keep the analysis simple these general solutions are not implemented.

In the test case here reported, mechanical transients are performed on the geometry depicted in Fig. 3.17. The parameters are reported in Tab. 3.4. The equivalent time constant of the the gear can be calculated as:

$$\tau_g = \frac{J_{eff}}{B_{eff}} = \frac{J_{in} + \frac{J_{load} + J_{out}}{G_n^2}}{b_{in} + \frac{b_{load} + b_{out}}{G_n^2}} \quad (3.33)$$

where the low speed rotor parameters have been reported at the high speed rotor using the nominal ratio  $G_n$  as well as the electric transformer case. The same procedure can be used to write the overall gear transfer function reporting the low speed parameters on the high speed side. The gear mechanical transfer function is:

$$E_{gear} = \frac{1}{J_{eff} \cdot s + b_{eff}} \quad (3.34)$$

### 3.5.1 Speed control

When speed control is adopted, the system overall transfer function (open loop) becomes:

$$E_r = \frac{K_i \cdot (1 + \tau_c \cdot s)}{b_{eff} \cdot s \cdot (1 + \frac{J_{eff}}{b_{eff}} \cdot s)} \quad (3.35)$$

In Fig. 3.18 the rotor speeds have been depicted during a start up. The PI parameters causes a visible overshoot and then the rotational speed of the inner rotor is fixed to  $V_{in} = 600 \text{ rpm}$ . The overshoot is strictly related to the PI controller coefficients: substituting the parameters in Tab. 3.4 into Eq. (3.35) and then calculating the Laplace anti-transform of the closed loop function, an overshoot of  $\Delta = 6.8\%$  is found, in accordance to the one obtained solving the ODE.

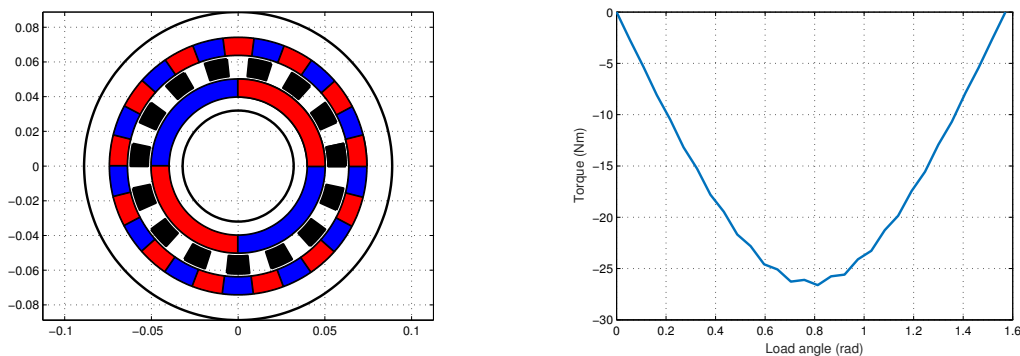


FIGURE 3.17: Gear geometry and inner rotor torque at varying load angle. The torque limit capability is approximately  $C_{in-lim} \simeq 26$  Nm on the inner rotor.

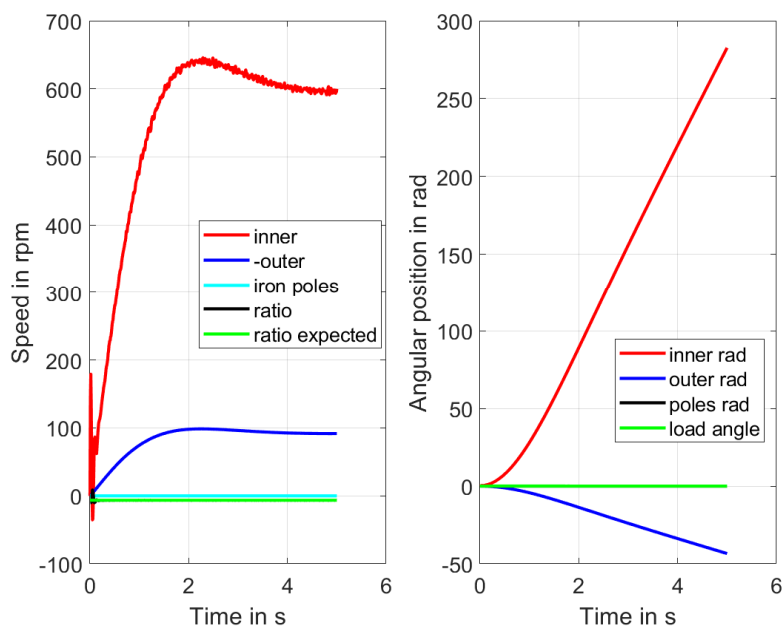


FIGURE 3.18: Speed regulation control: speed waveforms (left) and mechanical angles (right). The rotor speed reaches the steady state condition after a visible overshoot due to the PI controller.



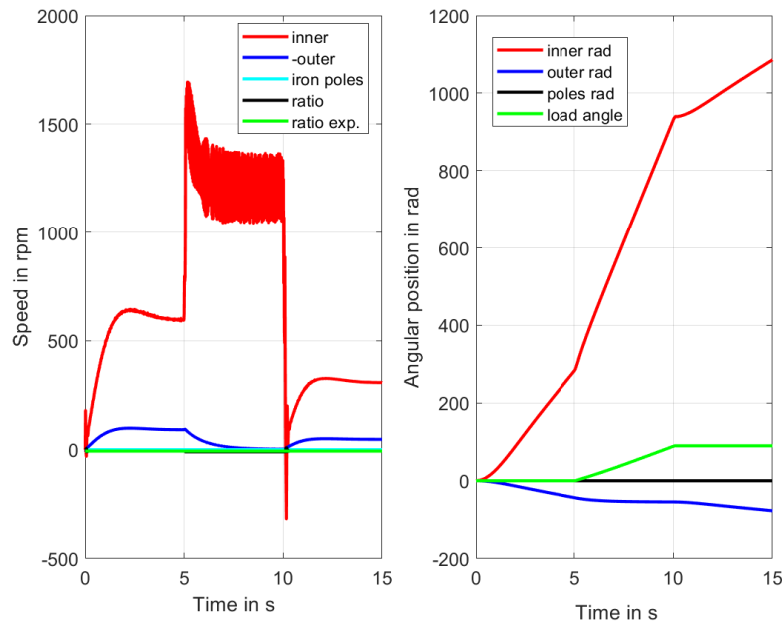


FIGURE 3.19: Speed regulation control when the torque exceeded the limit: speed waveforms (left) and mechanical angles (right). Between  $t = 5$  s and  $t = 10$  s the gear operation becomes asynchronous since the torque capability is exceeded. The transmission goes back to the normal operation when  $t > 10$  s.

When the speed control is implemented, the maximum speed of the inner rotor is:

$$V_{in-lim} = \frac{C_{in-lim}}{\frac{(b_{load}+b_{ext})}{G_n^2} + T_{load}} \cdot \frac{60}{2\pi} = \frac{25}{\frac{(10+0.05)}{6.5^2} + 0} \cdot \frac{60}{2\pi} = 1000 \text{ rpm} \quad (3.36)$$

where  $C_{in-lim}$  is the maximum torque that the magnetic transmission can transmit.

In Fig. 3.19 the reference speed is fixed to 3 different values:

$$\begin{cases} V_{in} = 600 \text{ rpm} & \text{if } 0 < t < 5 \text{ s} \\ V_{in} = 1200 \text{ rpm} & \text{if } 5 < t < 10 \text{ s} \\ V_{in} = 300 \text{ rpm} & \text{if } 10 < t < 15 \text{ s} \end{cases} \quad (3.37)$$

Therefore when the rotational speed is fixed to  $V_{in} = 1200 \text{ rpm}$  the gear is not be capable to drive the low speed rotor according to (3.36). In Fig. 3.19, the rotor speeds and mechanical angles are depicted. When the torque exceeds the maximum limit, the outer rotor speed tends to decrease following a mechanical transient given by the rotor inertia and friction. When the transient is extinguished the torque ripple effects are still visible while the mean torque tends to zero.

When the speed reference value is decreased below the limit speed, the gear should be able to restore the synchronous operation. When  $V_{in} = 300 \text{ rpm}$  in Fig. 3.19, the outer rotor starts to increase its speed according to his mechanical transient.

An important factor that is worth to be considered is the speed of the inner rotor during the asynchronous operation: the PI effect leads to an average speed equal to the reference value, but speed oscillations are clearly visible in Fig. 3.19. In fact the gear transfer function is changed when the synchronism is lost:

$$E_{gear} = \frac{1}{J_{in} \cdot s + b_{in}} \quad (3.38)$$

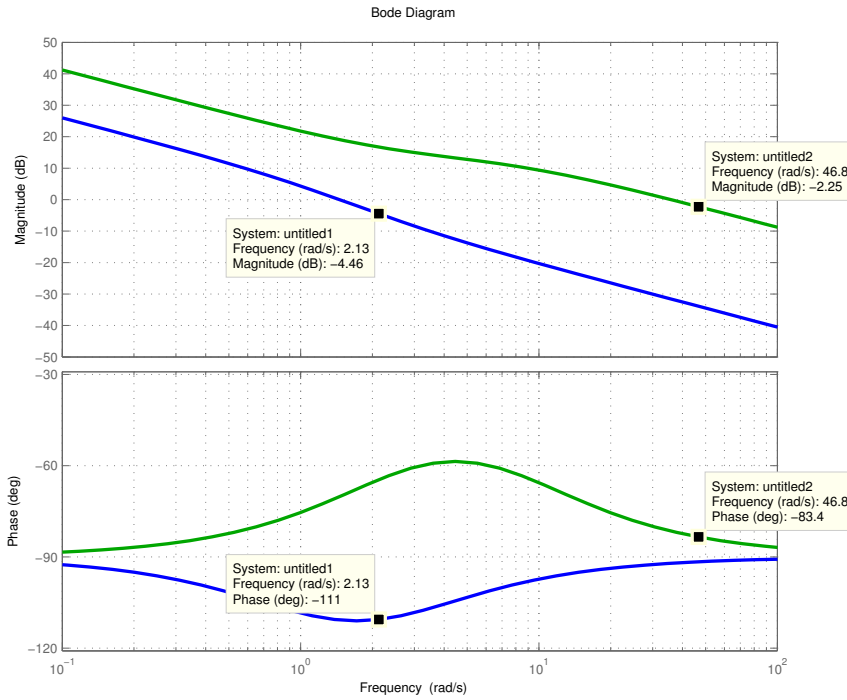


FIGURE 3.20: Bode diagrams of open loop transfer functions: synchronous case (blue) and asynchronous case (red).

and the open loop transfer function is modified as:

$$E_r = \frac{K_i \cdot (1 + \tau_c \cdot s)}{b_{in} \cdot s \cdot (1 + \frac{J_{in}}{b_{in}} \cdot s)} \quad (3.39)$$

Comparing Eqs. (3.35) and (3.39), the gear cut-off frequency is shifted and also the constant term  $\frac{K_i}{b}$  changes by a factor  $\frac{b_{eff}}{b_{in}} > 1$ . This means that all the transfer function is shifted upwards as visible in Fig. 3.20. If from the phase margin point of view the asynchronous operation is better, the system bandwidth is much increased. The relation between bandwidth and rise time is:

$$T_{rise} = \frac{\ln(10)}{Bandwidth} \quad (3.40)$$

and therefore the controller operates much faster. The torque noise produced by the outer combined with the lower rise time produces the oscillations of Fig. 3.19. If these oscillations are too large, the outer rotor may not be able to restart even if the medium inner speed value is lower than the speed limit  $V_{in-lim}$ . This is related to the control loop instability. Therefore, in order to acquire again synchronism, the speed level can be lower than the limit calculated in (3.36); an example is shown in Fig. 3.21.

The asynchronous operation mode can also be caused by a sudden variation of the load torque. The key is to estimate the maximum load level in the worst condition and to set a reference speed that allows the gear to work for all load levels.

### 3.5.2 Torque control

Similarly to the speed control, the torque control can be implemented. If the torque level is set on the inner rotor, if the transmitted torque is set to a value lower than the maximum gear capability the safe operation is ensured, as shown in Fig. 3.22 where the friction factor  $b_{out}$  is changed. Even if a step load torque is applied, the gear operation remains synchronous. On the

other side, if the torque reference is suddenly increased to a value above the maximum value for the current speed, the magnetic gear will operate in asynchronous mode. If there is no source limit on the maximum rotational speed, the torque balance will be reached at a speed much higher than the nominal one, causing mechanical failures. Therefore when torque control is implemented asynchronous operations must be avoided. As soon as the operation turns to asynchronous the torque has to be heavily reduced in order to keep the input rotor speed lower than the limit speed that guarantees the synchronous operation. In Fig. 3.23 the asynchronous mode is shown when  $5\text{ s} < t < 10\text{ s}$ . When  $t > 10\text{ s}$ , the initial reference torque is fixed but the synchronism is lost.

Another factor to consider is related to the gear start-up phase. If a step torque is applied as reference, the dynamical equations are:

$$T_{ref} = J_{in} \frac{d\omega_{in}}{dt} + b_{in}\omega_{in} + J_2 \frac{d\omega_{out}}{dt} + b_{out}\omega_{out} \quad (3.41)$$

where the speed terms  $\omega_{in}$  and  $\omega_{out}$  are nil at the initial instants. The torque repartition is only based on the rotor inertias and this may lead to asynchronous operation as shown in Fig. 3.24. Using ramps instead of steps can avoid loss of synchronism during start-up.

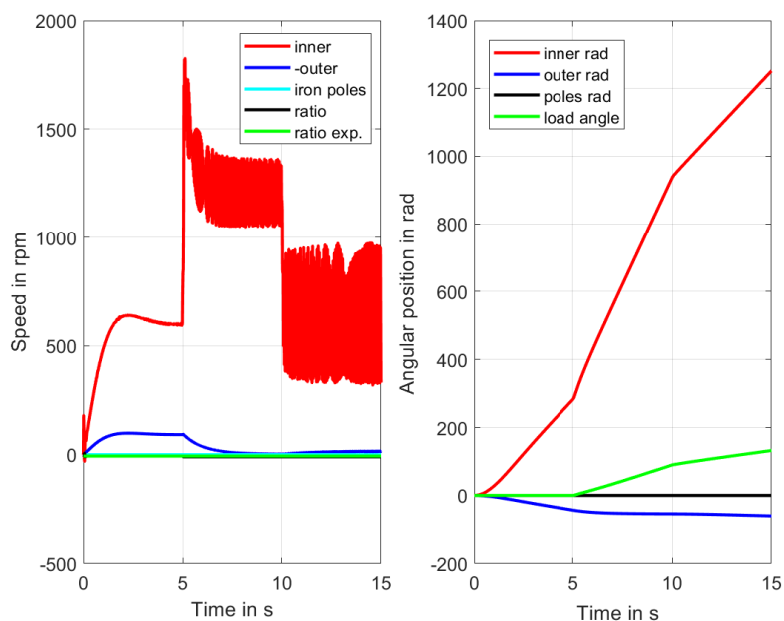


FIGURE 3.21: Speed regulation control. Speed (left) and angular position (right). The reference speed is  $V_{in} = 1200 \text{ rpm}$  when  $5 \text{ s} < t < 10 \text{ s}$  and  $V_{in} = 600 \text{ rpm}$  when  $t > 10 \text{ s}$ .

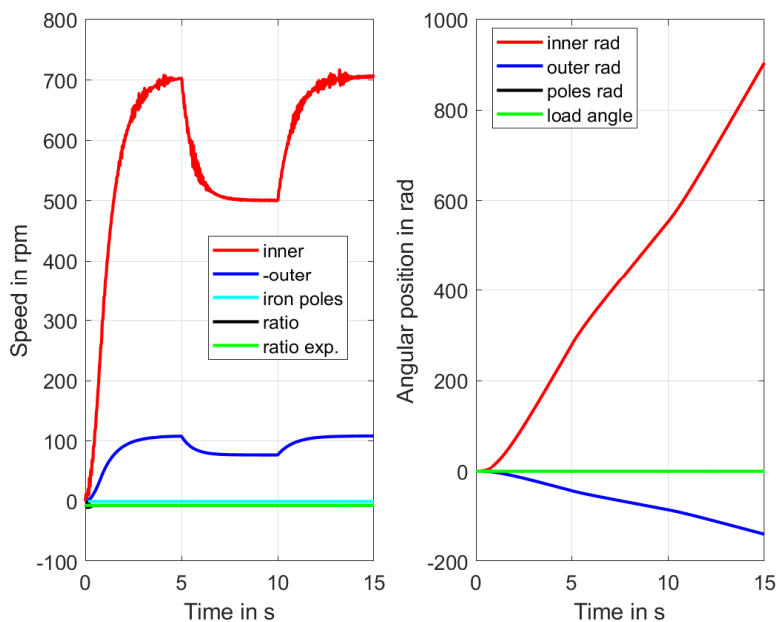


FIGURE 3.22: Torque regulation when the friction term has a step change. Speed (left) and angular position (right). The transmission exhibits synchronous operation even when the damping value is changed.

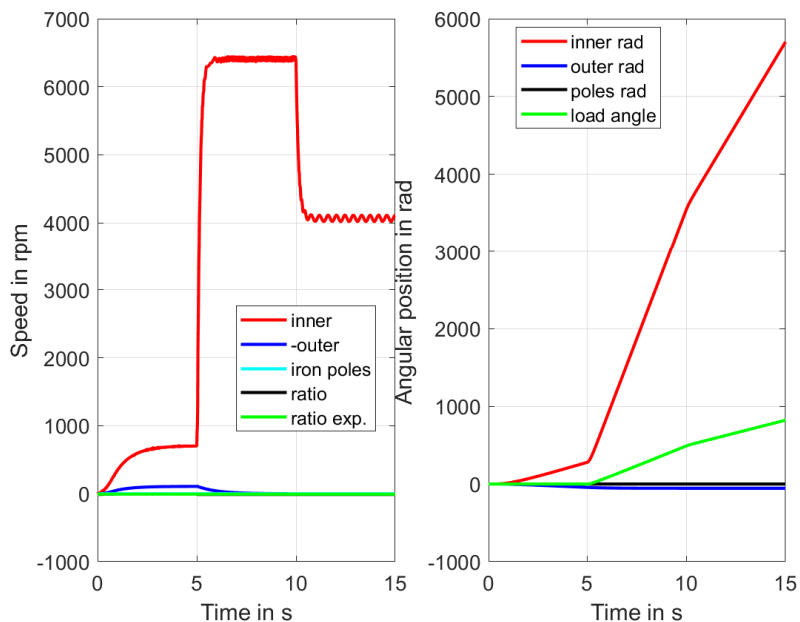


FIGURE 3.23: Torque control when the reference exceeds the limit. Speed (left) and angular position (right). When  $t > 10$  s the previous value is set, but the operation remains asynchronous.

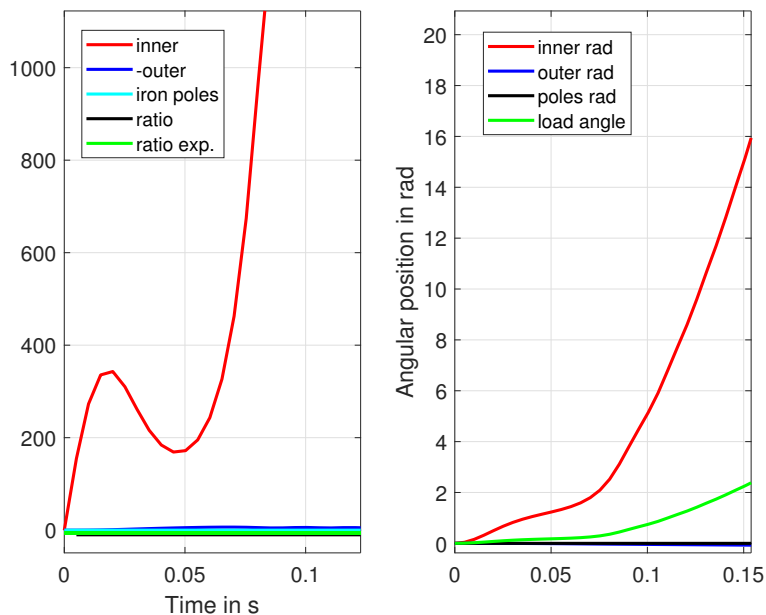


FIGURE 3.24: Torque regulation without initial torque ramp. Speed (left) and angular positions (right). The synchronism is suddenly lost because the inner rotor inertia is much smaller than the outer one.



# Chapter 4

## Magnetic modelling

In this Chapter, several numerical models for the magnetic and electro-magnetic field computation are presented. All of them are especially tailored for the magnetic gear case and have been validated through the comparison with commercial Finite Element codes or through the comparison with experimental data retrieved in literature.

Sec. 4.1 shows the analytic modelling of magnetic gears based on the solution of the Laplace and Poisson equations, as introduced in Sec. 2.3. This fast simulation tool is the ideal method that can be used for the first approximated design of magnetic gears and it is particularly suited for stochastic optimizations.

In Sec. 4.2, a 2D Finite Element / Boundary Element code (FEM/BEM) is described and validated on a magnetic transmission test case. This efficient algorithm allows to simulate in details a general magneto-quasi static device with nonlinear magnetic materials, permanent magnets and multiple moving parts. This is the principal tool that can be adopted for the detailed simulation of a specific gear geometry.

Section 4.3 describes a method to accelerate fixed point iterations in nonlinear electromagnetic problems. The algorithm has been successfully tested on several static or quasi-static test cases, thus it has been implemented in the FEM/BEM algorithm of Sec. 4.2.

In Sec. 4.4 a dynamic hysteresis model capable to include eddy currents in laminated steels is presented and embedded into a FEM formulation. The hysteresis model is the one introduced in Sec. 4.3.7 to test the Anderson acceleration on the TEAM 32 case [90]. The post-processing and direct on-line application of the hysteresis model are compared on a magnetic gear test case.

Section 4.5 describes a nonlinear model for permanent magnets capable to simulate magnetization, demagnetization and recoil of rare-earth PMs. The Finite Element implementation is described as well as the material implementation. The proposed algorithm is validated through two experimental datasets retrieved in literature, and finally the in-situ simulation of a segmented-PMs magnetic gear rotor magnetization is carried out.

Secs. 4.6 and 4.7 focus on the losses mechanisms in magnetic gears: in the former Section an algorithm for the iron losses in highly rotational loci condition is discussed, while in the latter the models for eddy current loss estimation in PMs are reported.

In Sec. 4.8 2D and 3D FEM simulations of magnetic gears are compared since several authors in literature found mismatches between real prototypes and the classical 2D simulations adopted for electrical machines (e.g. [68]). The 3D Finite Element formulation is shown, including segmented permanent magnets. The PMs losses are also computed varying the number of segments.

Sec. 4.9 shows the losses trend varying the rotational speed and load percentage of a test case magnetic transmission.

The algorithms and results shown in this Chapter have been published in [84, 91, 92, 93].

### 4.1 Analytic modelling

This Section is organized as follows: in Secs. 4.1.1-4.1.3 the analytic approach for the field computation in low permeability regions (air and PMs) is described and details are provided regarding the implementation and the computational issues.

In Sec. 4.1.4 the field solution from Sec. 4.1.1 is extended to the high permeability domains (poles and yokes) through a simple finite difference scheme.

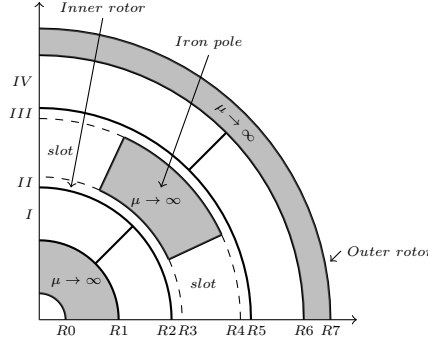


FIGURE 4.1: Magnetic gear structure and subdomains. According to [61], the regions are: Inner magnets  $\rightarrow I$ ; Inner airgap  $\rightarrow II$ ; Outer airgap  $\rightarrow III$ ; Outer magnets  $\rightarrow IV$ .

In Sec. 4.1.5 a simplified saturation model is discussed and formulated as optimization constraint.

Finally, in Sec. 4.1.6 the validation of the analytic simulation tool is carried out through the comparison with the commercial FEM code.

#### 4.1.1 Modelling in low permeability regions

The formulation adopted for low permeability regions is the one proposed in [61] which is exactly the dual of [60]. The eddy currents effect is neglected and the iron permeability is considered infinite in this Chapter. Adopting a 2D vector potential formulation, the magnetic field is  $\mathbf{B} = \nabla \times (0, 0, A_z)$  where  $A_z$  is the  $z$  component of the vector potential. The constitutive equation in the whole machine reads:

$$\mathbf{B} = \mu_0 \mu_r \mathbf{H} + \mu_0 \mathbf{M} \quad (4.1)$$

where  $\mathbf{M}$  is the magnetization (in magnetic media),  $\mu_0$  and  $\mu_r$  are the vacuum and relative permeability. Therefore, Ampere's law expressed in cylindrical coordinates can be expressed as:

$$-\nabla^2 A_z = \mu_0 \nabla \times \mathbf{M} \cdot \vec{e}_z = -\frac{\mu_0}{r} \frac{\partial M_r}{\partial \theta} \vec{e}_z \quad (4.2)$$

in the hypothesis of radially-magnetized permanent magnets. Considering that the magnets relative permeability is  $\mu_r \simeq 1$ , there is an analogy between this formulation and the one proposed in [60]:

$$\nabla^2 \Psi = \frac{1}{\mu_r} \nabla \cdot \mathbf{M} = \frac{1}{r \mu_r} \frac{\partial (r \cdot M_r)}{\partial r} \quad (4.3)$$

where  $\mathbf{H}$  is expressed through the scalar potential  $\Psi$  as  $\mathbf{H} = -\nabla \Psi$ . The Laplace equation in the air regions is:

$$\nabla^2 \xi = 0 \quad (4.4)$$

where  $\xi$  can be equal to  $A_z$  or  $\Psi$  depending on the adopted formulation. The solution of (4.2)-(4.4) is found by fixing the boundary conditions. At the inner and outer boundary the magnetic scalar and vector potentials are subjected to a Dirichlet and homogeneous Neumann boundary constraint respectively:

$$\begin{cases} \Psi^I(R1, \theta) = 0 \\ \Psi^{IV}(R6, \theta) = 0 \end{cases} \quad \begin{cases} \frac{\partial A_z^I(R1, \theta)}{\partial \theta} = 0 \\ \frac{\partial A_z^{IV}(R6, \theta)}{\partial \theta} = 0 \end{cases} \quad (4.5)$$

At the interface between the inner magnets and the inner air-gap, the normal component of the magnetic flux density  $B_r$  or the tangential magnetic field  $H_\theta$  are conserved and the potentials



are continuous:

$$\left\{ \begin{array}{l} \Psi^I(R2, \theta) = \Psi^{II}(R2, \theta) \\ \frac{\partial \Psi^{II}(R2, \theta)}{\partial r} = \frac{\partial \Psi^I(R2, \theta)}{\partial r} \end{array} \right\} \left\{ \begin{array}{l} A_z^I(R2, \theta) = A_z^{II}(R2, \theta) \\ \frac{\partial A_z^{II}(R2, \theta)}{\partial r} = \frac{\partial A_z^I(R2, \theta)}{\partial r} \end{array} \right\} \quad (4.6)$$

The conditions are at the surface between the inner air-gap and the slots  $S$  are the same of Eq. (4.6):

$$\left\{ \begin{array}{l} \Psi^S(R3, \theta) = \Psi^{II}(R3, \theta) \\ \frac{\partial \Psi^{II}(R3, \theta)}{\partial r} = \frac{\partial \Psi^S(R3, \theta)}{\partial r} \end{array} \right\} \left\{ \begin{array}{l} A_z^S(R3, \theta) = A_z^{II}(R3, \theta) \\ \frac{\partial A_z^{II}(R3, \theta)}{\partial r} = \frac{\partial A_z^S(R3, \theta)}{\partial r} \end{array} \right\} \quad (4.7)$$

while at the interfaces between iron poles and air gap the condition is a Dirichlet constraint for the  $\Psi$  formulation or an homogeneous Neumann for the  $A$  one. The flux lines are always normal to the iron regions with infinite permeability: this means that according to the  $\Psi$  formulation each ferromagnetic pole is equipotential with scalar potential  $\Psi_i$  associated to the  $i$ th pole, while in the  $A$  case the poles boundaries are subjected to homogeneous Neumann conditions. Eqs. (4.6) and (4.7) are also valid for the outer magnets and air-gap. The PDEs that have to be solved adopting the  $A$  formulation are:

$$\left\{ \begin{array}{l} \frac{\partial A_z}{\partial r^2} + \frac{1}{r} \frac{\partial A_z}{\partial r} + \frac{1}{r^2} \frac{\partial^2 A_z}{\partial \theta^2} = 0 \\ \frac{\partial A_z}{\partial r^2} + \frac{1}{r} \frac{\partial A_z}{\partial r} + \frac{1}{r^2} \frac{\partial^2 A_z}{\partial \theta^2} = \frac{\mu_0}{r} \frac{\partial(M_r)}{\partial \theta} \end{array} \right. \quad (4.8)$$

Using the separation of variables, the general solution in the air regions for both the  $A$  and  $\Psi$  formulation is:

$$\begin{aligned} \xi(r, \theta) = \sum_{n=1}^{\infty} & \left( (E_n r^n + F_n r^{-n}) \cos(n\theta) + (G_n r^n + \right. \\ & \left. + H_n \cdot r^{-n}) \sin(n\theta) \right) + E_0 \ln r + F_0 \end{aligned} \quad (4.9)$$

where  $n$  is the number of harmonics of the Fourier series and  $\xi$  can be  $A_z$  or  $\Psi$ . The summation in (4.9) is in fact computed with only  $K$  terms in the slot regions and  $N$  terms inside the air gaps. In the magnet regions, the equation involves permanent magnets magnetic field harmonics and reads for both the  $A$  and  $\Psi$  formulations:

$$\begin{aligned} \xi(r, \theta) = \sum_{n=1}^{\infty} & \left( A_n r^n + B_n r^{-n} + W_n(r) \cos(n\theta) \right) \cdot \\ & \cos(n\theta) + \left( C_n r^n + D_n r^{-n} + W_n(r) \sin(n\theta) \right) \sin(n\theta) \end{aligned} \quad (4.10)$$

where  $W_n$  is a function of the geometry and Fourier decomposition of the magnetic field produced by the magnets. The summation in (4.10) is in fact computed with  $N$  terms. As extensively explained in [61] and [60], additional equations have to be added to ensure the solenoidality of the magnetic flux density in the iron poles and in the air gap regions. Through the boundary conditions (4.5)-(4.7) all the unknown coefficients in (4.9) and (4.10) can be computed in all the gear domains. The  $A$  formulation has been implemented in this Chapter since the extension of the solution to the iron domains is easier than the dual one. In air domains the duality relation reads:

$$\mathbf{B} = \mu_0 \cdot \mathbf{H} \rightarrow \begin{pmatrix} 0 & 1 \\ -1 & 0 \end{pmatrix} \cdot \nabla A_z = -\mu_0 \cdot \nabla \Psi \quad (4.11)$$

### 4.1.2 Implementation and remarks

Being  $Q$  the number of slots, there are a total of  $e = 12N + 2KQ + 2Q + 1$  unknown Fourier coefficients. The Laplace operators can be discretized inside a matrix  $[A]_{e \times e}$  and the source terms can be discretized inside a vector  $[b]_{e \times 1}$ . The matrix setup and sparsity pattern is shown in (4.12), where  $I_j$  stands for the identity matrix of size  $j \times j$ ,  $P^j$  are blocks where non-zero

coefficients are computed through the procedure in [61] and  $R^j$  are the non-zero coefficients on the right end side. The  $[x]_{e \times 1}$  unknown Fourier coefficients can be found by solving the problem:

$$[A]_{e \times e} \cdot [x]_{e \times 1} = [b]_{e \times 1} \quad (4.13)$$

A problem that arises during the implementation of this approach is intrinsically related to exponential functions. When the number of poles of the outer rotor  $Po$  is high, the number of harmonics  $N$  has to be higher than  $Po$  in order to obtain a good representation through the Fourier series. All expressions have to be carefully written in order to minimize the numerical errors and considering reordering operations. As an example in the expression

$$\Delta = - \frac{\frac{n}{R1} \left(\frac{r}{R1}\right)^{n-1} - \frac{n}{R1} \left(\frac{r}{R1}\right)^{-n-1}}{\left(\frac{R2}{R1}\right)^n + \left(\frac{R2}{R1}\right)^{-n}} \quad (4.14)$$

that appears when building the term  $W_n$ , when  $r > R1$  and  $n$  is sufficiently high, the calculation can overflow;  $\Delta$  also suffers from cancellation errors that occur when the numerator tends to zero.

A further aspect is related to the solution of (4.13). When high ratio gears are analyzed, since the number of harmonics  $N$  is constrained by  $Po$ , the problem size grows with  $Po$  even if many of the  $n$  Fourier coefficients in each region will be zero. The harmonic content can be determined a-priori as combinations of  $Pi, Po, Q$  and the problem size can be reduced without loss of accuracy. Being  $e \times e$  the matrix size, once the  $e - m$  0-value harmonics are known, the system can be rewritten as:

$$\begin{array}{c} \overbrace{[A] [P]^t}^D \overbrace{[P] [x]}^y = [b] \\ \left[ \begin{array}{c|c} [D_{1,1}] & [D_{1,2}] \\ \hline [D_{2,1}] & [D_{2,2}] \end{array} \right] \left[ \begin{array}{c} [y_{1,1}] \\ \hline [0_{2,1}] \end{array} \right] = \left[ \begin{array}{c} [b_{1,1}] \\ \hline [b_{2,1}] \end{array} \right] \end{array} \quad (4.15)$$

where  $[P]$  is a permutation matrix that can be built once the unnecessary harmonics are known. In particular the effect of  $P$  is to shift all the  $m$  equations relative to non zero contributions to the upper part of  $D$ . The  $k - m$  null harmonics are shifted to the bottom part of  $D$ . Therefore the solution terms  $[y_{2,1}]$  will be zero and the system is reduced to:

$$[D_{1,1}][y_{1,1}] = [b_{1,1}] \quad (4.16)$$

The system size is reduced from the original size  $e \times e$  to  $m \times m$  where for typical problems  $m \approx \frac{e}{2}$ .

In order to find the non zero harmonics Eq. (3.7) has to be used. In the magnet regions the magnetization  $M_r$  is expressed as a square wave and the effect of both the rotors is visible. The harmonics due to the modulation effect of the iron pieces are also present. The expected harmonics in both the rotors are:

$$\begin{cases} Pi \cdot (2k + 1) \\ Po \cdot (2k + 1) \\ aPo \pm bPi \end{cases} \quad (4.17)$$

where  $k, a, b$  are 1, 2, 3.... Looking at the solution, the coefficients relative to the slots seem to decay quickly to zero and generally only the first 10 terms have to be considered. This aspect can be considered in the choice of the number of harmonics  $K$  that has to be adopted for the slot regions.

### 4.1.3 Problem conditioning

An important aspect that is worth to be considered is the matrix conditioning. Considering the general inverse problem  $Ax = b$ , the conditioning is an intrinsic matrix property that is linked to the sensitivity of the solution to a variation of the known term  $b$ . In particular if the problem is



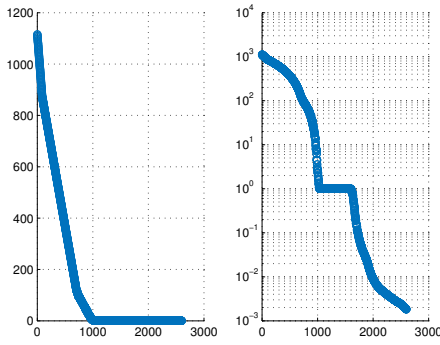


FIGURE 4.2: Singular values of the full matrix with  $Pi = 2$ ,  $Po = 7$ ,  $n = 200$ .

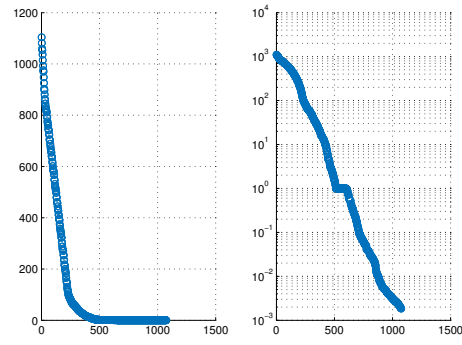


FIGURE 4.3: Singular values of the reduced matrix with  $Pi = 2$ ,  $Po = 7$ ,  $n = 200$ .

Parameters	Case	Cond. numb. $k$	Lost digits
$Pi = 2, Po = 7$	<i>Full</i> , $n = 200$	$6.1 \cdot 10^5$	5
$Pi = 2, Po = 7$	<i>Full</i> , $n = 500$	$3.89 \cdot 10^6$	6
$Pi = 2, Po = 7$	<i>Full</i> , $n = 700$	$7.61 \cdot 10^6$	6
$Pi = 2, Po = 7$	<i>Reduced</i> , $n = 200$	$5.98 \cdot 10^5$	5
$Pi = 2, Po = 7$	<i>Reduced</i> , $n = 500$	$3.85 \cdot 10^6$	6
$Pi = 2, Po = 7$	<i>Reduced</i> , $n = 700$	$7.57 \cdot 10^6$	6

TABLE 4.1: Effect of model reduction on the conditioning number.

bad conditioned or ill-conditioned a small variation of the term  $b$  will produce an huge variation of the solution  $x$ . Thus the solution of problem highly bad-conditioned can be challenging. The conditioning number is calculated as:

$$k(A) = \frac{\sigma_{max}}{\sigma_{min}} \quad (4.18)$$

where  $\sigma_{max}$  and  $\sigma_{min}$  are the maximum and minimum singular values of the matrix  $A$ . For backward stable methods such as the Matlab backslash operator based on QR factorizations the solution precision is:

$$\frac{\|x_v - x\|}{\|x\|} \leq k \cdot \epsilon_{machine} \quad (4.19)$$

where  $x_v$  is the computed solution and  $x$  the real one, while  $\epsilon_{machine}$  is the computer precision. Writing the conditioning number as  $k = 10^\tau$ , in each calculation  $\tau$  is the number of digits that is lost due to the precision of the numerical method.

As a test-case example, a magnetic gear with  $Pi = 2$  and  $Po = 7$  is considered. The singular values have been depicted changing for the case  $n = 200$  with and without reduction: in Fig. 4.2 the full matrix singular values is depicted while in Fig. 4.3, the reduced matrix is analyzed. The matrix reduction affects all the singular values while the conditioning number slightly decreases as visible in Tab. 4.1.

#### 4.1.4 Modelling in high permeability regions

For high permeability regions a finite difference approach has been adopted. The Laplace equation in cylindrical coordinates reads:

$$\frac{\partial^2 A_z}{\partial r^2} + \frac{1}{r} \frac{\partial A_z}{\partial r} + \frac{1}{r^2} \frac{\partial^2 A_z}{\partial \theta^2} = 0 \quad (4.20)$$

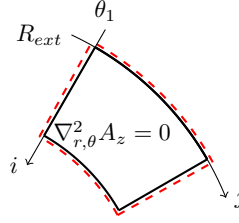


FIGURE 4.4: Vector potential boundary condition for iron regions.  $A_z$  is computed along the red line and applied on the black one as boundary condition.

which is solved using a finite difference method applied to a regular grid in cylindrical coordinates. Using the reference system of Fig. 4.4, the grid consists of the points:

$$r_i = R_{ext} - (i - \frac{1}{2})\Delta r \quad \theta_j = \theta_1 - (j - \frac{1}{2})\Delta\theta \quad (4.21)$$

In (4.20) the first and second derivatives are computed with respect to an arbitrary coordinate  $\xi$  as:

$$\frac{\partial U}{\partial \xi} = \frac{U_{i+1,j} - U_{i-1,j}}{2 \cdot \Delta \xi} \quad (4.22)$$

$$\begin{aligned} \frac{\partial^2 U}{\partial^2 \xi} &= \frac{1}{\Delta \xi} \left( \frac{U_{i+1,j} - U_{i,j}}{\Delta \xi} - \frac{U_{i,j} - U_{i-1,j}}{\Delta \xi} \right) \\ &= \frac{U_{i+1,j} + U_{i-1,j} - 2 \cdot U_{i,j}}{\Delta \xi^2} \end{aligned} \quad (4.23)$$

Once a regular grid is built in the iron regions, the previously calculated boundary potential is used as Dirichlet condition and the magnetic vector potential  $A_z$  can be found in each point by solving (4.20) using (4.22) and (4.23). When the potential inside the iron regions is known, the magnetic flux density components can be easily computed.

#### 4.1.5 Simplified iron saturation model

The magnetic material saturation level is a strict constraint when the weight of the magnetic gear has to be optimized. Since the analytic model considers iron regions with infinite permeability, the saturation effect is not taken into account directly. Therefore, the radial and tangential components of the magnetic flux densities are computed with a finite difference scheme and a simple limitation is added as follows:

$$|\mathbf{B}| = \begin{cases} |\mathbf{B}| & \text{if } |\mathbf{B}| < B_{sat} \\ B_{sat} & \text{if } |\mathbf{B}| \geq B_{sat} \end{cases} \quad (4.24)$$

where  $B_{sat}$  is the material saturation limit. When in a certain point  $h$  the magnetic flux density norm  $|\mathbf{B}|$  is higher or equal than  $B_{sat}$ , the cell area with barycentre  $h$  is assumed to be saturated; hence the percentage of ferromagnetic material above the saturation limit  $V_{sat}$  can be estimated. This parameter influences the gear performance: FEM simulations of nonlinear materials allow to compute the torque decay curve as function saturation percentage and once the working point of this curve has been chosen, the maximum saturation percentage  $V_{max}$  becomes an optimization constraint as follows:

$$V_{sat} = \frac{1}{V} \sum_{h=1}^{np} \left( V_h \text{ if } |\mathbf{B}| \geq B_{sat}; 0 \text{ otherwise} \right) \leq V_{\%max} \quad (4.25)$$

where  $V$  is the overall iron area,  $V_h$  is the area associated to the  $h^{th}$  cell,  $np$  is the global number of points in the iron domains.

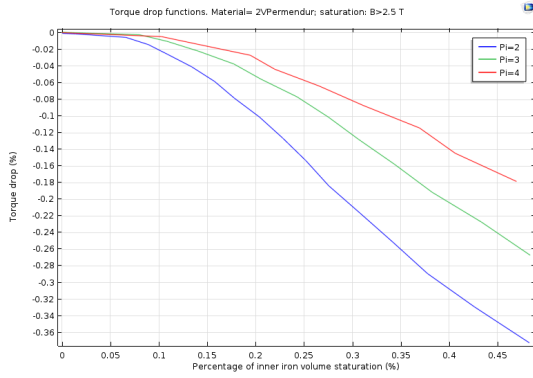


FIGURE 4.5: Torque drop, 2V-Supermendur.

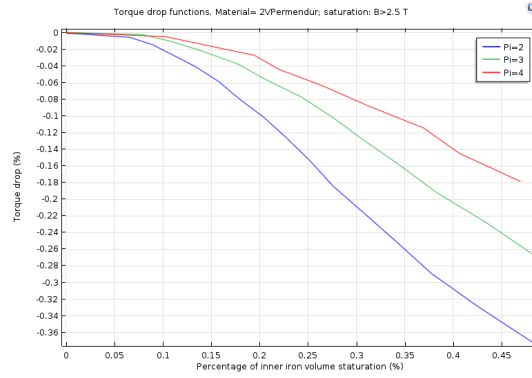


FIGURE 4.6: Torque drop, Silicon50PN800.

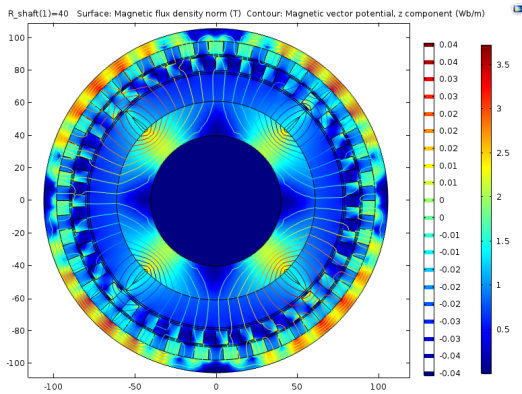


FIGURE 4.7: Low saturation case of the inner rotor yoke for the 2V-Supermendur material. The flux lines are completely closed inside the ferromagnetic material.

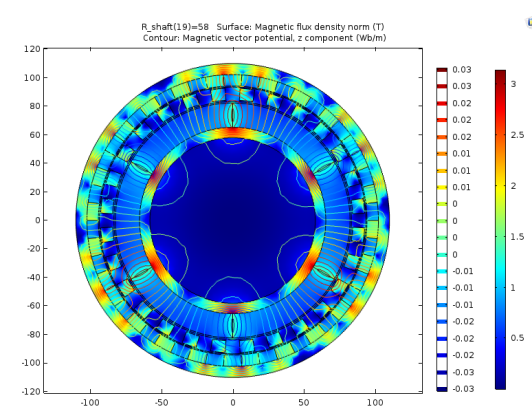


FIGURE 4.8: High saturation case of the inner rotor yoke for the 2V-Supermendur material. The flux lines are partially closed in air.

Two materials have been taken as test case and the torque drop functions have been calculated. The materials are 2V-Permendur and the non oriented steel Si50pm800. The drop functions have been reported in Figs. 4.5 and 4.6. The magnetic flux density norm and the magnetic vector potential contours have been reported in Fig. 4.8. The material is considered saturated when the differential permeability falls below  $\mu_{diff} = 30$ ; the saturation flux densities  $B_{sat}$  to substitute in (4.24) are therefore  $B = 2.5 T$  and  $B = 1.7 T$  respectively.

From the analysis of Figs. 4.5 and 4.6, the torque drop function depends on the material: 2V-Permendur has a lower decay slope which is visible also at low saturation percentages while the other material has a negligible torque decay when the saturation is lower than  $v_{sat} = 15\%$  and then the curves decays faster than the previous case. The inner number of poles  $Pi$  influences the decay function: the effect is lower increasing  $Pi$ .

In Fig. 4.9 a qualitative comparison between the flux loci computed through proposed simplified saturation model and the results given by the commercial finite element code is shown. The results match with a reasonable approximation.

#### 4.1.6 Model validation

Tab. 4.2 shows the comparison between the results obtained through the analytic procedure and the commercial finite element code Comsol Multiphysics [94]. The test case geometry is the one proposed in [61]. The stall torques, ripples and losses are in agreement. A qualitative comparison between the radial flux densities is reported in Fig. 4.10, where the colour-maps are in agreement.

Tab. 4.3 shows a comparison between the computational times of the proposed analytical tool and FEM results for two different pole pairs combinations: the analytical elements are the

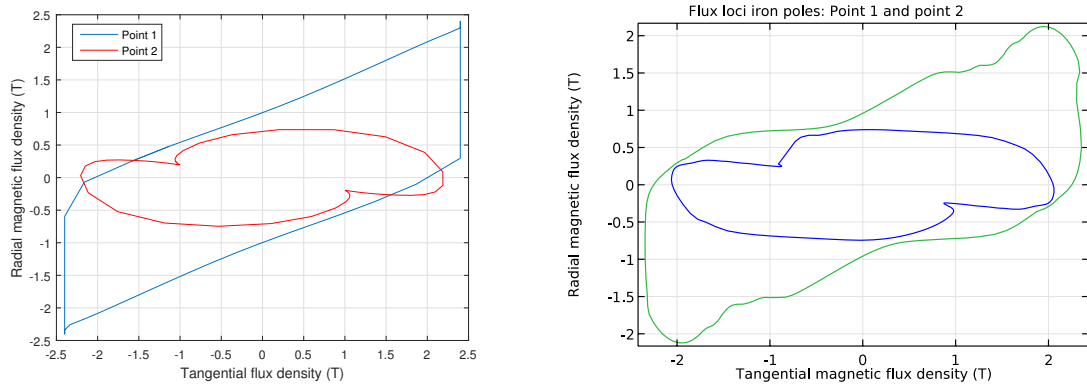


FIGURE 4.9: Comparison of radial and tangential flux density loci in two distinct nodes of the iron poles, computed with the simple model (4.24) through the analytical algorithm (left) or through the commercial FEM software (right).

Quantity	Analytic		FEM 2D	
	No segm.	Segm.	No segm.	Segm.
Inner stall torque (Nm)	70	70	65	65
Outer stall torque (Nm)	104	104	97.5	97.5
Inner ripple (Nm)	7.71	7.71	5.79	5.79
Outer ripple (Nm)	8.26	8.26	5.39	5.39
PM losses (W)	2761	84	2600	60
Iron loss GSE (W)	4.84	4.84	4.1	4.1
Efficiency max. load	0.7256	0.9912	0.7447	0.993

TABLE 4.2: Analytic model validation through 2d FEM. The geometry is taken from [62], with  $P_i = 2$  and  $P_o = 3$ . The rotational speed is  $\omega_{in} = 1500$  rpm. The iron loss model is the Generalized Steinmetz equation in Sec. 4.6.3, the PMs loss are computed according to Sec. 4.7.

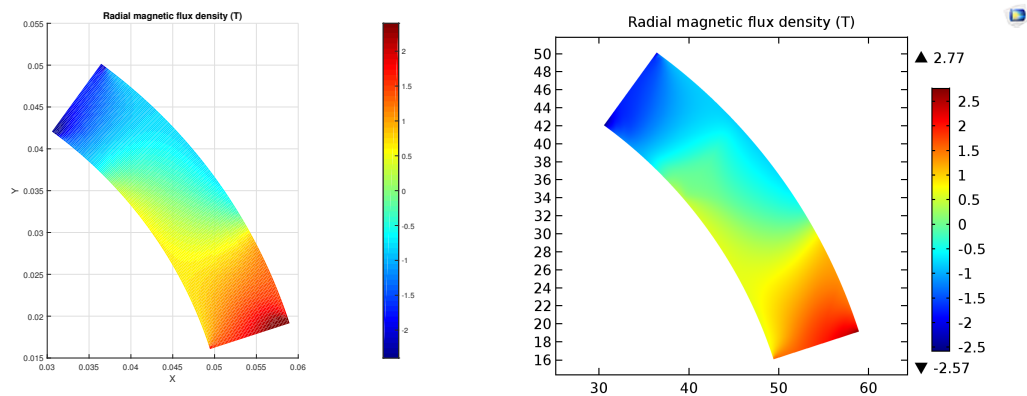


FIGURE 4.10: Example of comparison between the flux density radial component computed through the analytical algorithm (left) and the commercial Finite Element code (right).

Pi	Po	FEM DOF.	Analytic DOF.	FEM time	Analytic. time
2	17	82E3	52E3	525 s	147 s
3	25	96E3	66E3	669 s	164 s

TABLE 4.3: Time comparison between analytical (A) and commercial FEM relatively to  $12 \times 30 = 360$  simulations. The workstation adopted has two 6-core 12 thread processors (Intel Xeon E5645 @2.4 GHz) and 112 GB of RAM.

ones of the iron regions, while an equivalent discretization with FEM requires a higher number of elements since the air and permanent magnet domains have to be discretized. Tab. 4.3 shows the results for 12 simulations of different geometries, each one with an angular parametric sweep with 30 angles. FEM uses linear shape functions and linear materials and the triangulation time is taken into account in Tab. 4.3; both FEM and analytical procedure are parallelized on 12 cores. FEM results slower because of the re-meshing time and the stiffness matrix size. Tab. 4.2 shows the comparison between the proposed analytical tool and FEM results for two different geometries and the results are in accordance.

## 4.2 2D Finite Element / Boundary Element in Julia

Computer simulations of physical phenomena and devices play a key role in the modern product design process across all application areas, including the case of low frequency electromagnetics. Several commercial solutions provide reliable and flexible tools, typically based on the Finite Element Method, capable of solving the vast majority of problems of practical interest. However, this generality comes at the cost of either not being able to satisfactorily cover some niche applications or not being particularly optimized for some specific scenarios. Therefore it is sometimes convenient or necessary, particularly in an academic environment, to write either some parts or complete applications ex-novo. In such circumstances an initial decision has to be made concerning the implementation language, and at a more fundamental level the implementation approach. Common choices are:

1. C++, C and Fortran: best execution time, low level language, lengthy source codes, statically compiled
2. Matlab and Python: possibly slow, high level language, compact source codes, interpreted

Quite recently the Julia language, now at version 0.6, was born with the aim of providing, through an LLVM-based just-in-time (JIT) compiler, performances close to 1) (if written properly) with a high level syntax and compact source code similar to 2). The language, initially developed by computer scientists and mathematicians, alumni of MIT and Harvard, has over 1,800,000 downloads as of January 2018 and is together with C, C++, and Fortran among the only four high-level languages in which petaflop computational codes have been written.

In order to cope with the need for a specialized code for the design and optimization of magnetic gears which required some specific features not fully/optimally/robustly/conveniently provided by the commercial codes available to them, Julia was chosen because of its promising features. In this Section a 2D Finite Element Method-Boundary Element Method (FEM/BEM) code is described, with a special focus on its implementation in Julia. The main language features that have been used for the implementation are introduced in Sec. 4.2.1. Sec. 4.2.2 describes the formulation of the FEM/BEM algorithm adopted, with a special focus on the magnetic gear test case. In Sec. 4.2.4, the core parts of code are shown together with some remarks on the implementation. Finally, Sec. 4.2.6 reports the results for some magneto-static and magneto-quasi-static simulations, and the performances of the algorithm are compared to a commercial Finite Element software.

### 4.2.1 Julia features

Julia has a multitude of unique interesting features, partially deriving from other programming languages, the descriptions of which is beyond the scope of this thesis, and for a complete documentation the reader is referred to [95, 96]. Some characteristics of particular interest in the context of the developed FEM/BEM simulation code are:

- Method based language (see Appendix A.1);
- Simple interface with other languages (see Appendix A.2);
- Easy to parallelize (see Appendix A.3);
- Free and open source (MIT license);



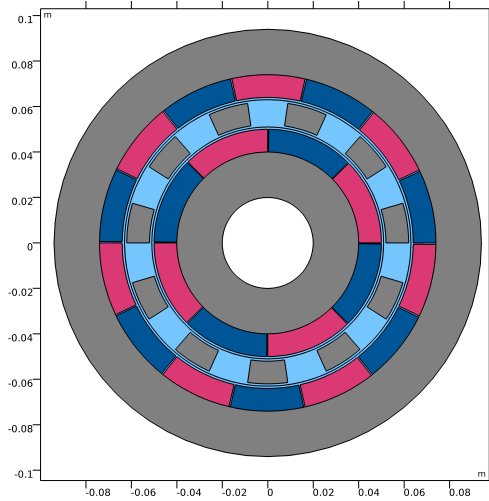


FIGURE 4.11: Magnetic gear test case geometry. Gray: iron, Red/Blue: permanent magnets, Cyan: air. In the physical device the outer iron region and magnets as well as the inner iron region and magnets rotate at different speeds while the field-shaping iron pole pieces, completely surrounded by air, are stationary.

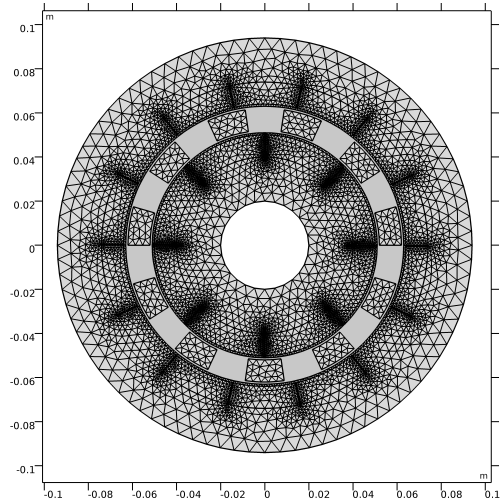


FIGURE 4.12: Typical mesh used by the FEM/BEM solver. The air-gaps and the air slots between the iron poles are not discretized since the boundary element method is adopted.

- Tools for memory and time profiling (see Appendix A.4);
- Greek letters can be used, thus the syntax can be closer to the mathematical notation.

In the following Sections some examples concerning the functionalities that have been used in the FEM/BEM implementation are shown.

#### 4.2.2 FEM/BEM algorithm for magnetic gears

Conventional strategies to deal with movement in FEM-based electrical machine simulations include re-meshing of the air-gap, lock-step movement, sliding interfaces or the use of Lagrange multipliers. All these approaches introduce limitations, computational bottlenecks or additional causes of simulation breakdown during long transients. The alternative approach followed in this Section is to adopt a hybrid FEM/BEM strategy. Obviously, also this choice is not devoid of inconveniences but it also offers interesting possibilities which were deemed to be the best option for this very specific application which refers to a magnetic gear, whose geometry and mesh are shown in Figs. 4.11 and 4.12, respectively. The air regions are not meshed since a BEM formulation is adopted in the air-gap and in the slots which separate the field-shaping iron pole pieces.

##### Finite element formulation

The main features of the Finite Element approach that has been implemented are:

- Linear shape functions;
- Mesh imported from external mesh generator;
- Nonlinear magnetization treated with a fixed point approach. The nonlinear problem will be extensively discussed in Sec. 4.3.

The 2D vector potential formulation in quasi-static case reads:

$$\sigma \frac{\partial A_z}{\partial t} - \nabla \cdot \nu \nabla A_z = J_z + \nabla_{2D} \times \mathbf{M}(A_z) \quad (4.26)$$

where  $A_z$  is the  $z$  component of the vector potential,  $\sigma$  is the electrical conductivity,  $\nu$  is the reluctivity,  $M(A_z)$  includes the nonlinear iron magnetization or the linear permanent magnet magnetization and  $J_z$  is the source current density. The vector potential Ampere's law (4.26) will be recalled several times in the thesis development, in the static or quasi-static, 2D or 3D, strong or weak forms, e.g. in Eqs. (4.48), (4.134), (4.135), (4.67), (4.77), (4.128), (7.1). For the sake of readability, the proper equation will be reported in all the sections where needed.

From the weak form of Eq. (4.26), the usual stiffness and mass matrices  $K$  and  $M$  are obtained with entries:

$$K_{i,j} = \int_{\Omega} \nu \nabla N_i \cdot \nabla N_j d\Omega \quad (4.27)$$

$$M_{i,j} = \int_{\Omega} \sigma N_i \cdot N_j d\Omega \quad (4.28)$$

where  $N_i$  indicates the  $i^{th}$  nodal shape function. A compact code listing for the FEM matrix assembly is available in Appendix A.5.

### Boundary element formulation

For the BEM part, since the method is only applied in the air-gap regions, the key points are the following:

- Linear shape functions
- Laplace fundamental solution

When the Boundary Element method is applied to the boundary of the BEM region, referred as  $\Gamma$ , denoting by  $\mathbf{n}$  the normal of  $\Gamma$  and  $\omega = \frac{-\log r}{2\pi}$  the fundamental solution of the Laplace equation, the general equation reads [97]:

$$c \cdot A_z(\xi, \eta) = - \int_{\Gamma} A_z \frac{\partial \omega}{\partial n} d\Gamma + \int_{\Gamma} \frac{\partial A_z}{\partial n} \omega d\Gamma \quad (4.29)$$

The coefficient  $c$  depends on the location of the point  $(\xi, \eta)$  and on the shape of the domain:  $c = 1$  if the point is inside the BEM domain,  $c = 0$  if the point is outside and  $c = \frac{\alpha}{2\pi}$  where  $\alpha$  is the angle formed by the edges of the BEM node if the point  $(\xi, \eta)$  is on the boundary of the BEM domain. Eq. (4.29) in matrix form is written as:

$$[G] \cdot \{A_z\} = [H] \cdot \left\{ \frac{\partial A_z}{\partial n} \right\} \quad (4.30)$$

All integrals are computed through Gauss-Legendre quadrature. The adopted parallel implementation for the BEM matrix assembly is available in Appendix A.6.

### FEM/BEM coupling

In the interface edges, the FEM/BEM coupling has to be performed. Since the FEM scheme is discretized through nodal shape functions, the coupling is trivial in the sense of nodal vector potential because the interface nodes shares the same  $A_z$ . The boundary fluxes instead have to be coupled: the FEM method uses edge-distributed boundary fluxes while BEM method uses nodal fluxes.

The FEM Neumann boundary condition of the  $i^{th}$  node in the weak form reads:

$$\begin{aligned} \int_{\Gamma} N_i \epsilon q^F d\Gamma &= \int_{\Gamma} \epsilon N_i^e (q_{i-1}^B N_{i-1}^e + q_i^B N_i^e) d\Gamma + \\ &+ \int_{\Gamma} \epsilon N_i^{e+1} (q_i^B N_i^{e+1} + q_{i+1}^B N_{i+1}^{e+1}) d\Gamma \end{aligned} \quad (4.31)$$

where  $\epsilon$  is the material property (considered constant along the edge),  $q^F$  is the FEM normal potential derivative,  $q_i^B$  is the BEM normal potential derivative associated to the  $i^{th}$  node,  $N_i$  is the nodal shape function and  $N_i^e$  is the  $N_i$  contribute from the  $e^{th}$  edge ( $N_i = \sum_e N_i^e$ ). Thus

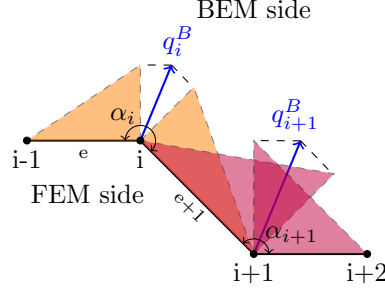


FIGURE 4.13: Interface edges between FEM and BEM regions. The nodal  $q^B$  in the BEM reference and the respective  $q^F$  are shown.

generally the potential derivatives in the FEM and BEM references are related through the matrix  $M$  in the expression  $q^F = [M]q^B$ , where the elements relative to the edge  $e + 1$  in case of linear shape functions are:

$$\begin{cases} M_{i,i}^{e+1} = \frac{1}{3}(L_e + L_{e+1}) \sin(\frac{\alpha_i}{2}) \\ M_{i,i+1}^{e+1} = \frac{1}{6}(L_e + L_{e+1}) \sin(\frac{\alpha_i}{2}) \\ M_{i+1,i}^{e+1} = \frac{1}{6}(L_e + L_{e+1}) \sin(\frac{\alpha_i}{2}) \end{cases} \quad (4.32)$$

The FEM/BEM linear system, for the magneto-static case, is:

$$\begin{bmatrix} [K_{FEM}] & [0] \\ [0] & [G] \end{bmatrix} \begin{bmatrix} [A_{FEM}] \\ [A_{int}] \\ [q_{BEM}] \end{bmatrix} = \begin{bmatrix} [g_{FE}] \\ 0 \\ 0 \end{bmatrix} \quad (4.33)$$

where  $K_{FEM}$  denotes the finite element stiffness matrix reordered to obtain the FEM/BEM interface node equations at the bottom,  $A_{FEM}$  and  $A_{int}$  denote the vector potential solution for the FEM nodes and for the BEM nodes respectively,  $G$  and  $H$  are the matrices from the BEM equation (4.30) and  $q_{BEM}$  are the nodal tractions  $q_{BEM} = \frac{\partial A_z}{\partial n}$ . The matrix  $M$  is the conversion matrix (4.32) from the BEM normal derivatives to the FEM Neumann conditions.

### Torque computation

Several techniques can be implemented for the torque calculation in electrical machines [98, 99]. Maxwell's stress tensor approach has been adopted in this thesis, therefore the magnetic flux density on a surface that encloses the rotor in the BEM domain has to be calculated. A circumference is taken to integrate the stress tensor, thus the magnetic flux density has to be evaluated in the query points, thus (4.29) has to be computed repeatedly with  $c = 1$ . This equation links the potential on a query point  $u_Q$  with two boundary integrals performed on the boundaries of the BEM domain.

Two different approaches can be adopted to calculate the flux density: the former uses (4.29) to evaluate  $A_z$  on the query points and then the  $x$  and  $y$  derivatives can be estimated through a finite difference scheme, the latter substitute the derivatives directly in (4.29). The second approach has been followed for the proposed algorithm. The distance between the query point and the BEM node is denoted by  $r = |\mathbf{r}| = \sqrt{r_x^2 + r_y^2}$ , while  $\mathbf{n}$  is the BEM normal vector.

$$B_x = -2 \int_{\Gamma} A_z \frac{r_y}{2\pi|r|^3} [\nabla r \cdot \mathbf{n}] d\Gamma + \int_{\Gamma} \frac{A_z}{2\pi|r|} \left[ \frac{(0,1)}{|r|} \cdot \mathbf{n} \right] d\Gamma - \int_{\Gamma} \frac{\partial A_z}{\partial n} \frac{r_y}{2\pi|r|^2} d\Gamma \quad (4.34)$$

A similar expression is obtained for  $B_y$ . The integrands involve different powers of the singular terms  $\frac{1}{r}$ , thus special care is required when  $r$  is close to zero because of the hypersingular terms. The integration could be performed numerically if the query points are in the center of the airgap with size  $\xi$ , thus the minimum distance is lower bounded by  $\frac{\xi}{2}$ .

As it will be extensively treated in Sec. 5.3, the forces are computed through the Maxwell stress tensor integration along a closed surface that includes the machine rotor:

$$[T] = \frac{1}{\mu_0} \begin{bmatrix} \frac{B_x^2 - B_y^2}{2} & B_x B_y \\ B_x B_y & \frac{B_y^2 - B_x^2}{2} \end{bmatrix} \quad (4.35)$$

The parallel implementation of the torque subroutine is reported in Appendix A.7.

### 4.2.3 Motion and time domain problem

The conventional strategies adopted to deal with the movement in electrical machine finite element simulations are the machine re-meshing, the locked step or the sliding interfaces. The new mesh is the less efficient since a new triangulation at each motion step has to be performed. The locked step approach requires the mesh to be uniform along the sliding circumference, while the last one is the most flexible since there are no special requirements on the triangulation but normally the formulation is more complicated because of the non conformal mesh. When an hybrid FEM/BEM is adopted, the motion can be implemented easily working on the BEM couplings. Since the BEM matrices depend on the node positions, the nodes on the rotors circumferences can be virtually shifted when the BEM matrices have to be computed, while the position of the real nodes does not change.

The time domain problem is addressed through a fixed time step integration:

- $\theta$ -method for DAEs;
- Modified Crank-Nicholson scheme [100].

The easiest approach to solve time domain problems is the  $\theta$  method. The general DAE problem is formulated as:

$$[M_1(\mathbf{x})] \cdot \mathbf{x} + [M_2] \frac{d\mathbf{x}}{dt} = \mathbf{s}(t) \quad (4.36)$$

where  $[M_1]$  is the nonlinear stiffness matrix,  $[M_2]$  is the mass matrix (considered constant),  $\mathbf{s}(t)$  is the source term. Applying the  $\theta$  method, the time derivative is expressed through finite differences as  $\frac{d\mathbf{x}}{dt} = \frac{\mathbf{x}^{n+1} - \mathbf{x}^n}{\Delta t}$  and (4.36) becomes:

$$\begin{aligned} & \left( \theta [M_1(\mathbf{x}^n)] + \frac{1}{\Delta t} [M_2] \right) \mathbf{x}^{n+1} = \\ & = \left( \frac{1}{\Delta t} [M_2] - (1 - \theta) [M_1(\mathbf{x}^n)] \right) \mathbf{x}^n + \theta \mathbf{s}^{n+1} + (1 - \theta) \mathbf{s}^n \end{aligned} \quad (4.37)$$

The parameter  $\theta$  allows to switch between different schemes: with  $\theta = 0$  the method is the explicit Euler approach,  $\theta = 1$  is the implicit Euler one and finally  $\theta = 0.5$  is the Crank-Nicolson (CN) algorithm. Normally the Crank-Nicolson approach is adopted since it is unconditionally stable and a second order scheme. As suggested in [100], depending on the system being modelled in some cases CN suffer from weakly damped oscillations due to the sudden jump of the boundary conditions at the first time step. From [100], the growth factor between consecutive time steps is:

$$g(\phi) = \frac{1 - 2\delta\gamma \sin^2(\frac{\phi}{2})}{1 + 2\delta\gamma \sin^2(\frac{\phi}{2})} \quad (4.38)$$

where  $\gamma = \frac{\Delta t}{\Delta x^2}$  is the ratio between the simulation time and squared spatial discretization respectively,  $\delta$  is the diffusion coefficient and  $\phi$  is a frequency dependent parameter. The relation  $0 \leq \phi \leq \pi$  holds and  $\phi \rightarrow 0$  means slowly varying components while  $\phi \rightarrow \pm\pi$  means highly oscillatory components of the solution. The growth factor  $g$  is always bounded since  $|g(\phi)| \leq 1$ , thus CN is said to be unconditionally stable.

When CN is applied for the solution of magneto quasi static problems, the diffusion coefficient is  $\delta = \frac{\nu}{\sigma}$ , where  $\nu$  is the reluctivity and  $\sigma$  is the conducibility. Fixing for example the parameters for an hypothetical electrical machine  $\Delta t = 5e - 4$  s and  $\Delta x = 1e - 3$  m,  $\sigma = 1e7$  S/m and

$\nu = 8e5 m/H$  (case of aluminium), the growth factor becomes:

$$g(\phi) \simeq \frac{1 - 40 \sin^2(\frac{\phi}{2})}{1 + 40 \sin^2(\frac{\phi}{2})} \quad (4.39)$$

In (4.39) the oscillatory components ( $\phi \rightarrow \pm\pi$ ) are propagated as weakly damped oscillations since  $g(\phi) \rightarrow -1$ .

The growth factor in the case of implicit Euler method reads:

$$g(\phi) = \frac{1}{1 + 4\delta\gamma \sin^2(\frac{\phi}{2})} \quad (4.40)$$

thus, as suggested in [100], one solution in this case is to adopt the implicit Euler method for the first two time steps and Crank-Nicolson for the subsequent steps.

When the mechanical transient has to be solved, an ordinary differential equation ODE is added to the system and the structure is the same of (4.36):

$$J \frac{d^2\theta}{dt^2} + b \frac{d\theta}{dt} = T_{em} - T_{load} \quad (4.41)$$

where  $\theta$  is the angular rotor position,  $J$  is the rotor inertia,  $b$  is the damping coefficient,  $T_{em}$  is the electromagnetic torque and  $T_{load}$  is the load torque. In order to solve the mechanical dynamic equation, (4.41) could be included in (4.36) or solved separately. In this Section the Verlet approaches have been adopted, thus (4.41) is discretized through central differences for the cases of linear or quadratic damping term. In the linear damping case,  $b$  is constant:

$$\begin{cases} \theta^{n+1} = \frac{2J\theta^n + (\frac{b}{2}\Delta t - J)\theta^{n-1} + \Delta t^2(T_{em} - T_{load})}{J + \frac{b}{2}\Delta t} \\ \theta^1 = \theta^0 + \Delta t\omega_0 + \frac{\Delta t^2}{2J}(-b\omega_0 + T_{em} - T_{load}) \end{cases} \quad (4.42)$$

while in the quadratic case,  $b = B|\omega|$ . If the nonlinear term is discretized through the mean term  $\theta^n|\theta^n| = \theta^{n+\frac{1}{2}}|\theta^{n-\frac{1}{2}}|$ , the updating equation reads:

$$\begin{cases} \theta^{n+1} = \frac{2J\theta^n - J\theta^{n-1} + b\theta^n|\theta^n - \theta^{n-1}| + \Delta t^2(T_{em} - T_{load})}{J + b|\theta^n - \theta^{n-1}|} \\ \theta^1 = \theta^0 + \Delta t\omega_0 + \frac{\Delta t^2}{2J}(-b\omega_0|\omega_0| + T_{em} - T_{load}) \end{cases} \quad (4.43)$$

#### 4.2.4 Julia implementation

##### Mesh import

The first step is the mesh import from a text file. This is rather easy once the file structure is known, therefore the parse instructions will not be reported. The key information that has to be imported are:

- Node coordinates;
- Triangle material domain;
- Connectivity matrix, with positively oriented triangles.

##### Useful packages

Some packages available online have been used to speed-up the implementation time of the code. 1D and 2D quadrature rules are required for numerical integration. In particular, line integrals have to be computed for the construction of the BEM matrices, while integrals on triangles have to be computed for the construction of the FEM matrices. The 1D case has been addressed with the fast and robust Julia package *FastGaussQuadrature.jl*, freely available on GitHub [101], which provides, among others, suitable Gauss-Legendre rules. On the other hand standard 2D quadrature rules on triangles have been implemented from scratch. The package *WriteVTK.jl*

[102] is useful for the export of VTK files, readable by *ParaView*, an open source tool for post processing operations.

*Dierckx.jl* [103] has been used for the interpolation of the nonlinear HB curve.

Finally, *Pardiso.jl* [104] has been used, in order to use the parallel system solver features combined with the MKL libraries.

#### 4.2.5 Acceleration methods for nonlinear problems

In literature, a variety of acceleration methods are available to try to speed-up the convergence rate of fixed point iteration. Among others, Anderson acceleration proved to have good performances in electronics component simulations, but it has been rarely applied to electro-magnetics. This acceleration has been tested on static and magneto-quasi static problems giving impressive speed-ups, thus the FEM/BEM algorithm here presented has been equipped with this acceleration technique. A separate Section (Sec. 4.3) has been dedicated to the method description and validation, which will not be described in the current one.

#### 4.2.6 Model validation

The nonlinear magnetic material used in the simulations is a silicon steel with non-oriented grains. Experimental data have been interpolated by means of the Langevin equation:

$$B(H) = k_1 \coth(k_2 \cdot H) - \frac{1}{k_2 \cdot H} + \mu_0 \cdot H \quad (4.44)$$

where  $B$  is the flux density,  $H$  is the magnetic field,  $k_1$  and  $k_2$  are the coefficients of the fit. For the given material,  $k_1 = 1.803$  and  $k_2 = 0.0027$ . The permanent magnets have a fixed remanence  $Br = 1.2$  T.

Figs. 4.14 and 4.15 show the  $z$  component of the magnetic vector potential and the magnetic flux density norm, respectively.

Fig. 4.16 shows the results of a magneto-static parametric sweep of the angular positions of inner and outer rotors. In particular, inner and outer torques are depicted and the respective Finite Element results are shown adopting linear and quadratic shape functions. It is worth noting that the FEM/BEM result is closer to the quadratic FEM case: this happens because the air-gap, the region where the mesh size impacts more on the torque, uses the BEM formulation, which is mathematically exact (the errors are due just to numerical integration).

Fig. 4.17 shows the comparison of the outer and inner rotor torques in dynamic operation, thus when the mechanical ordinary differential equations are solved. The wave forms are in full accordance, a small difference is noticeable at the beginning of the time domain simulation since the ramp-up of magnetizations and non-linearities is slower for the FEM/BEM case.

Fig. 4.18 shows the dynamic response of the magnetic gear when the initial rotors position is a non-equilibrium point. The positions show a damped oscillatory behaviour due to both electrical and mechanical damping, and the stationary position at the end of the transient is the zero torque equilibrium position.

Fig. 4.19 shows the speed-up obtained for the torque computation subroutine varying the number of parallel workers. While at low number of workers the speed-up is close to linear, increasing the number of processors the allocation time and inter-process communication impact becomes more relevant, thus the time speed-up saturates, as is to be expected. According to Amdahl's law, the parallel performance depends on both intrinsic features of the algorithm as well as the specific implementation details. The results shown Fig. 4.19 are in agreement with others available in literature for the same type of task.

In Tab. 4.4 the simulation time for the FEM/BEM algorithm and for the commercial finite element software are reported for a workstation with two 6-core 12 thread processors (Intel Xeon E5645 @2.4 GHz) and 112 GB of RAM. The number of degrees of freedom (DOFs) is different for the compared methods since in the FEM case the air-gap elements are considered, while in the FEM/BEM case the problem size is the one in (4.33). The *time/iterations* ratio is computed since in the dynamic case (time-domain) the FEM algorithm takes some small time steps at the beginning of the simulation in order to satisfy the same requirements on the relative tolerance

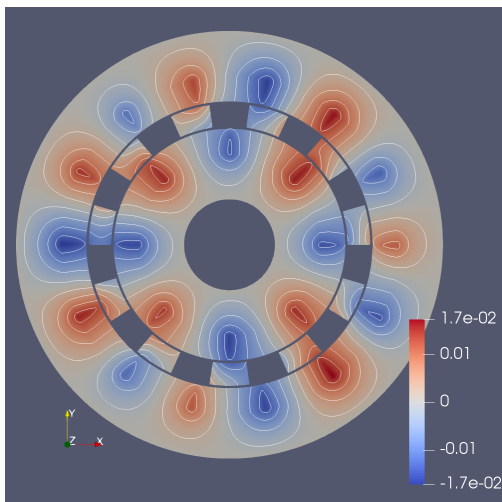


FIGURE 4.14: Magnetic gear test case:  $A_z$  plot obtained with ParaView.

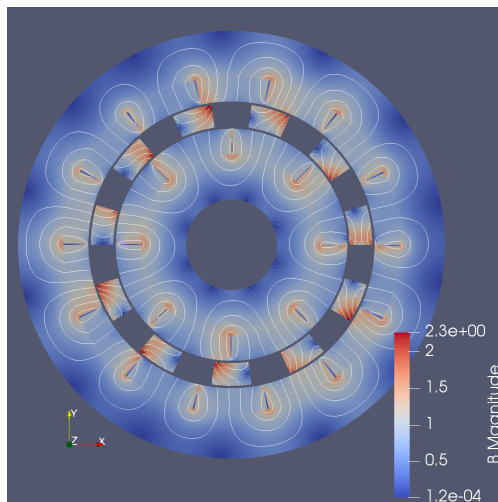


FIGURE 4.15: Magnetic gear test case: flux density norm plot obtained with ParaView.

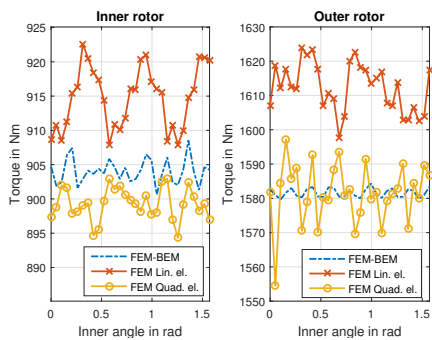


FIGURE 4.16: Torque comparison between FEM/BEM and commercial FEM with linear (Lin. el.) and quadratic (Quad. el.) shape functions. The problem is a magneto-static sweep of angular positions of inner and outer rotors.

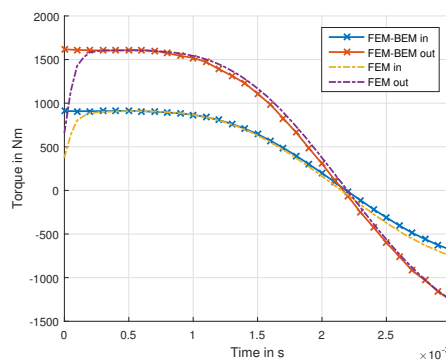


FIGURE 4.17: Torque comparison between FEM/BEM and commercial FEM with linear shape functions. The problem is magneto quasi static, the mechanical ordinary differential equations are included.

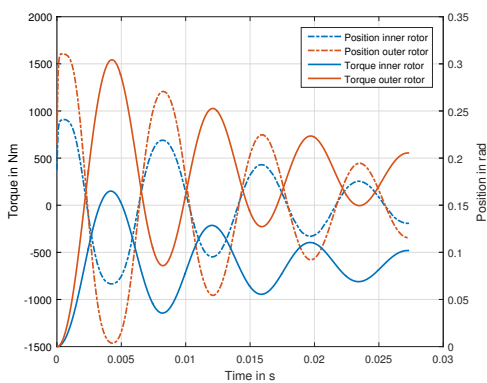


FIGURE 4.18: Torque and position computed by the FEM/BEM code during a free evolution from an initial non-equilibrium position.

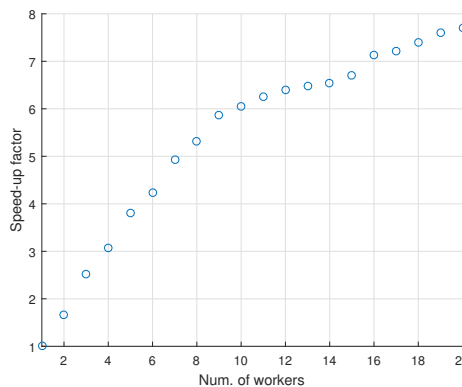


FIGURE 4.19: Speed-up of the parallel torque subroutine changing the number of workers.

Test case	Tool	DOFs	Time	Time/iterations
Position sweep	FEM/BEM	20567	39.64 s	1.32 s/iter
Position sweep	FEM	21287	70 s	2.33 s/iter
Time domain	FEM/BEM	20567	114.82 s	3.83 s/iter
Time domain	FEM	21287	387 s	8.41 s/iter

TABLE 4.4: Time comparison between the FEM/BEM algorithm and the commercial FEM, both with linear shape functions. The nonlinear convergence criteria is set to relative tolerance  $\Delta_A < 1e - 5$ . The workstation has two 6-core 12 thread processors (Intel Xeon E5645 @2.4 GHz) and 112 GB of RAM.

$\Delta_A$  of the FEM/BEM algorithm. Because of its features, the FEM/BEM algorithm is faster than the commercial FEM for this class of problems, while the accuracy regarding the torque computation is close to the higher order shape function FEM case.

### 4.3 Anderson acceleration for electromagnetic nonlinear problems

Numerical simulations are mandatory for general non-linear mathematical models and the common approach is to adopt algorithms of the Newton-Raphson (NR) family, which can provide convergence with a low number of iterations [105]. Normally, relaxation parameters are adopted to guarantee convergence, and their tuning can be either manual or self-adapted. A different approach that can be adopted to solve non-linear problems is the Fixed Point (FP) iteration. The FP approach is adopted, when possible, especially for its implementation simplicity and the lower requirements to achieve convergence in comparison to the NR scheme. On the contrary, it typically requires a high number of iterations to converge in comparison with the NR method, thus the choice is generally a trade-off dependent on the application. In electromagnetic problems, common non-linearities are due to ferromagnetic materials, which can exhibit hysteretic behaviour. For this special class of materials, NR methods cannot cope easily with the Preisach or Jiles-Atherton models, thus the FP iteration is still widely adopted in electromagnetics. In order to improve the convergence speed of FP methods, several acceleration techniques have been suggested in the past [106]. One of them, i.e. Anderson acceleration [107], has been widely applied to FP problems in electronic structure computations, but it is still not diffused in electromagnetic computations. In this Section Anderson acceleration is tested for the magneto-quasi-static case, and the performances of the resulting iterative scheme are compared to the standard FP implementation.

#### 4.3.1 Fixed point for the magnetostatic problem

In most electrical machines design problems saturation plays an important role, thus an important aspect to consider is the capability of the chosen formulation to model the BH curve non-linearity. In literature a common approach is the NR technique because of its super-linear convergence property. The well known NR iterative scheme allows to find the solution of a system of non-linear equations  $F(\mathbf{x}) = 0$  with an iterative scheme of the type  $\mathbf{x}_{k+1} = \mathbf{x}_k - [dF/d\mathbf{x}_k]^{-1}F(\mathbf{x}_k)$ , but for achieving convergence the terms  $[dF/d\mathbf{x}_k]^{-1}$  and  $d^2F/d\mathbf{x}_k^2$  have to be bounded and often in turn the BH curve and its first derivative have to be strictly monotonic. Practically the NR implementation is always supplemented by under-relaxation schemes, and this combination provides the most efficient tool for the solution of nonlinear equations, when it is convergent [108].

Another technique for the solution of systems of non-linear equations is the Picard-Banach fixed point (FP) iteration scheme, in which  $\mathbf{x}_{k+1} = G(\mathbf{x}_k)$ . This approach converges linearly for magneto-quasi-static problems, but choosing an optimal permeability and implementing suitable acceleration schemes the rate of convergence can be significantly improved. In order to guarantee convergence, the problem has to be formulated in such a way that  $G$  is a contraction, which can be exactly proven when the material function is Lipschitzian and uniformly monotone [108]. In particular, a function  $G$  is a contraction on a domain  $G : \Omega \rightarrow \Omega$  if  $\forall \mathbf{u}^* \in \Omega$  there exist a



coefficient  $0 \leq \alpha < 1$  for which [109]:

$$\|G(\mathbf{u}) - G(\mathbf{u}^*)\| \leq \alpha \|\mathbf{u} - \mathbf{u}^*\| \quad (4.45)$$

where  $\|\cdot\|$  is a suitable norm and  $\alpha$  the contraction coefficient. Because of the lower requirements on the differential reluctivity, FP can be adopted for example with hysteretic materials where NR cannot be.

In this Section the FP scheme has been adopted for its simplicity and to avoid the computation at each non-linear step of the Jacobian matrix. In order to understand if the iteration is a contraction, the approach in [108] is followed, leading to the same result of [109]. Maxwell's equations in the magnetostatic case read:

$$\begin{cases} \nabla \times \mathbf{H} = \mathbf{J} \\ \nabla \cdot \mathbf{B} = 0 \\ \mathbf{H} = f(\mathbf{B}) \end{cases} \quad (4.46)$$

where  $\mathbf{H}$  is the magnetic field,  $\mathbf{B}$  is the magnetic flux density and  $f$  stands for the non-linear BH relation. The ferromagnetic material law can be written as:

$$\mathbf{B} = \mu_0 \mu_{FP} \mathbf{H} + \mathbf{I} = \mu_0 (\mu_{FP} \mathbf{H} + \mathbf{M}) \quad (4.47)$$

where  $\mu_0$  is the vacuum permeability,  $\mu_{FP}$  is a reluctivity-like quantity that can be adjusted for convergence purposes and  $\mathbf{I}$  is the ferromagnetic non-linear polarization ( $\mathbf{M}$  is the dual non-linear magnetization). Substituting (4.47) into (4.46):

$$\nabla \times \mathbf{B} = \mu_0 \mu_{FP} \mathbf{J} + \mu_0 \nabla \times \mathbf{I} \quad (4.48)$$

In (4.48), the polarization  $\mathbf{I}$  is a function of the flux density  $\mathbf{B}$  through Ampere's law, but the material relation (4.47) still holds. Thus a fixed point problem has to be solved and adopting the  $\mathbf{B}$ -correction the iterative procedure is written as:

$$\mathbf{I}_{k+1} = \mathbf{B}_k - \mu_0 \mu_{FP} \mathbf{H}_k = G(\mathbf{B}(\mathbf{I}_k)) = \mathbf{F}(\mathbf{I}_k) \quad (4.49)$$

where the function  $\mathbf{F}$  is the fixed point function. The iterative procedure is set up as follows:

- a) an initial guess  $\mathbf{I}_0$  is fixed;
- b) Maxwell's equations in (4.46) are solved with  $\mathbf{B}_k = \mu_0 \mu_{FP} \mathbf{H}_k + \mathbf{I}_{k-1}$ ;
- c)  $\mathbf{I}_k = G(\mathbf{B}_k)$ ;
- d) repeat steps b) and c) till convergence.

According to [108], the relative permeability  $\mu_{FP}$  can be chosen in order to make the function  $G$  a contraction. Adopting the B-correction approach (4.49), in the case of isotropic media the choice  $\mu_{FP} < 2\mu_{rmin}$ , where  $\mu_{rmin}$  is the minimum permeability along the BH curve, ensures that the function  $G$  is a contraction. Since for a ferromagnetic material the minimum relative permeability is  $\mu_{rmin} \geq 1$ , the nonlinear medium can be replaced by a linear one with higher permeability in order to improve the convergence speed while the  $G$  function is still contractive. The optimal  $\mu_{FP}$  that results in the lowest  $\alpha$  in (4.45) is:

$$\mu_{FP}^{opt} = \left( \frac{\mu_{rmin}^{-1} + \mu_{rmax}^{-1}}{2} \right)^{-1} \quad (4.50)$$

Since the Picard-Banach iteration converges linearly, several techniques have been proposed to accelerate the convergence. In [109] a locally convergent fixed point scheme is suggested for the 2D case:

$$\mu_{FP} = \frac{2}{C\mu_0} \left( \left. \frac{\partial B_x}{\partial H_x} \right|^{k=0} + \left. \frac{\partial B_y}{\partial H_y} \right|^{k=0} \right) \quad (4.51)$$

where  $C > 1$  is a coefficient that should avoid convergence issues. (4.51) is evaluated at each iteration. A similar approach based on the optimal choice of  $\mu_{FP}$  has been studied in [110] and [111], but in these approaches the stiffness matrix has to be updated at each nonlinear iteration thus the complexity would be the same of NR with a linear or super-linear convergence still lower than quadratic.

[108] and [112] suggest to adopt a relaxation scheme  $\mathbf{B}_{k+1}^{new} = \mathbf{B}_k + \omega \Delta \mathbf{B}_{k+1}$  with  $\Delta \mathbf{B}_{k+1} = \mathbf{B}_{k+1} - \mathbf{B}_k$  to adjust the subsequent iterations.  $\mathbf{B}_{k+1}$  is the next iteration flux density computed through the fixed point iteration,  $\mathbf{B}_{k+1}^{new}$  is the flux density modified by the over-relaxation scheme and  $\omega$  is the relaxation parameter. The error at the  $k^{th}$  iteration referring to the fixed point solution  $\mathbf{B}^*$  is:

$$\|\mathbf{B}_{k+1} - \mathbf{B}^*\|_{1/\mu} \leq \frac{1}{1 - \alpha} \|\mathbf{I}_{k+1} - \mathbf{I}_k\|_{1/\mu} \quad (4.52)$$

thus the modified  $\mathbf{B}_{k+1}^{new}$  is sought such that  $\epsilon(\omega) = \|\mathbf{F}(\mathbf{I}_k) - \mathbf{I}_k\|_{\mu^{-1}}$  is the lowest possible. In [112] this dynamic over-relaxation scheme gives good results in terms of convergence of the non-linear problems.

Although the previous description of the FP technique was given for the static case for simplicity, similar results have been derived for the quasi-static case [109].

### 4.3.2 Anderson acceleration

The relaxation-based correction attempts to produce a better estimation of the fixed point based on the knowledge of the last two iterations. Following the same idea, one may expect that a more efficient FP scheme would be obtained considering all the previous iterations, i.e. through a Krylov space method. Anderson in [107] found an acceleration method based on the extrapolation from the previous  $k - 1$  residual vectors  $\mathbf{r}_k = G(\mathbf{x}_k) - \mathbf{x}_k$ , where the fixed point iteration is denoted by the expression  $\mathbf{x}_{k+1} = G(\mathbf{x}_k)$ .

Set  $\mathbf{x}^0$ ;  $m \geq 1$ ;

$\mathbf{x}_1 = G(\mathbf{x}_0)$ ;

For  $k = 1, 2, \dots$  convergence

$m_k = \min(m, k)$ ;

$R_k = (\mathbf{r}_{k-m_k}, \mathbf{r}_{k-m_k+1}, \dots, \mathbf{r}_k)$ ,

with  $\mathbf{r}_i = G(\mathbf{x}_i) - \mathbf{x}_i$ ;

Find  $\boldsymbol{\alpha}_k$ :  $\min_{\boldsymbol{\alpha}=(\alpha_0 \dots \alpha_{m_k})^T} \|R_k \boldsymbol{\alpha}\|_2 \dots$  such that  $\sum_{i=0}^{m_k} \alpha_i = 1$ ;

$$\mathbf{x}_{k+1} = \sum_{i=0}^{m_k} \alpha_{k,i} \left( (1 - \beta_k) \mathbf{x}_{k-m_k+i} + \beta_k G(\mathbf{x}_{k-m_k+i}) \right); \quad (4.53)$$

The parameter  $m$  is the maximum number of residuals used for the extrapolation and  $\beta_k$  is a relaxation parameter that is fixed to  $\beta_k = 1$  in this thesis. The residuals  $\mathbf{r}_i$  are calculated as magnetic flux density residuals  $\mathbf{r}_i = \mathbf{B}_{i+1} - \mathbf{B}_i$ , thus the algorithm in (4.53) is adopted to extrapolate the new step solution  $\mathbf{B}_{k+1}$ .

As shown in [113], this schemes tends to be the GMRES algorithm if all the previous residual vectors are used for the computation ( $m \rightarrow \infty$ ). In practice in order to limit the computational effort and to avoid ill conditioned matrices, the number of vectors taken for the projections is limited, and in this Section  $4 \leq m \leq 30$  is adopted.

The minimization problem in (4.53) is solved through QR updated factorizations which result in a good compromise between accuracy and conditioning. The function being minimized is rewritten as:

$$\min_{\boldsymbol{\gamma}} \left\| \underbrace{\begin{bmatrix} \mathbf{r}_{k-m_k+1} - \mathbf{r}_{k-m_k}, & \dots, & \mathbf{r}_k - \mathbf{r}_{k-1} \end{bmatrix}}_{T_k} \cdot \boldsymbol{\gamma} - \mathbf{r}_k \right\|_2 \quad (4.54)$$

where the matrix  $T_k$  is factorized through a QR-update procedure since consecutive iterations have the effect to overwrite the first column of the  $T$  matrix and to apply a circular shift.

The constrained least-squares problem in (4.53) can be recast in an unconstrained one whose solution can be easily determined making use of QR-update factorizations. Introducing the matrix  $T_k$  as in (4.54), the new solution becomes  $\gamma_k = (\gamma_{k0}, \dots, \gamma_{k m_k - 1})^T$  where  $\alpha_0 = \gamma_0$ ,  $\alpha_i = \gamma_i - \gamma_{i-1}$  with  $1 \leq i \leq m_k - 1$  and  $\alpha_{m_k} = 1 - \gamma_{m_k - 1}$ .

$$\begin{aligned}
& \text{Set } \mathbf{x}_0; m \geq 1; \\
& \mathbf{x}^1 = g(\mathbf{x}^0); \\
& \text{For } k = 1, 2 \dots \text{convergence} \\
& \quad m_k = \min(m, k); \\
& \quad \text{Find } \gamma_k : \min_{\gamma = (\gamma_0 \dots \gamma_{m_k - 1})^T} \|\mathbf{r}_k - T_k \gamma\|_2 \\
& \quad \mathbf{x}_{k+1} = G(\mathbf{x}_k) - \sum_{i=0}^{m_k - 1} \gamma_i^k \left( G(\mathbf{x}_{k - m_k + i - 1}) - G(\mathbf{x}_{k - m_k + i}) \right); \quad (4.55)
\end{aligned}$$

At each iteration, the new least-square problem can be solved simply updating the factors of the QR factorization  $T_k = Q_k R_k$ . The solution is determined solving the triangular linear system  $R_k \gamma = (Q_k)^T \mathbf{r}_k$ .

As previously noted, a proper choice of  $m_k$  is crucial to speed up the convergence of the algorithm. If  $m_k$  is chosen to be too small, too little information from the previous iterations is considered and therefore the acceleration may be negligible. On the contrary, if  $m_k$  is too large the problem may become ill-conditioned and this can result in a degraded convergence rate. Several techniques have been proposed to address the conditioning issue: [113] proposed to monitor the conditioning number  $\epsilon$  of the  $R_k$  matrix, deleting the older column data if  $\epsilon$  is greater than a certain threshold. [114] suggested to monitor the norm of the new solution, restarting the iterative procedure when the norm exceeds a threshold. [115] similarly to the GMRES algorithm, suggested to restart the iterations every  $m$  iterations.

For an extensive analysis of the Anderson acceleration convergence, the reader is referred to [116], where the r-linear convergence on non-linear problems is proven.

### 4.3.3 Test case validation: geometry

In order to evaluate the performances of the acceleration scheme, two different approaches are adopted to solve a magneto-quasi static test case. The first is a Finite Element/Boundary Element time-domain one, while the second is a Finite Element harmonic-balance one. Both algorithms are equipped with Anderson acceleration and the solution is validated through the comparison with a pure Finite Element commercial software. The test case geometry is shown in Figure 4.20.

In the first example, the coil is fed by a uniform sinusoidal current density. The frequency is chosen to be 50 Hz and the peak value is set to  $7 \times 10^7$  A m<sup>-2</sup> to strongly saturate the ferromagnetic core. Eddy currents are induced in the conductive domain which is linear, its conductivity is equal to  $3.774 \times 10^7$  S m<sup>-1</sup>. The ferromagnetic material is a non conductive domain. The nonlinear magnetic material is a silicon steel with non oriented grains, 35JN200. In order to help the Finite Element convergence, the BH curve is fitted through the Langevin equation:

$$B(H) = k_1 \coth(k_2 \cdot H) - \frac{1}{k_2 \cdot H} + \mu_0 \cdot H \quad (4.56)$$

where  $k_1$  and  $k_2$  are the coefficients of the fit. For the given material,  $k_1 = 1.803$  and  $k_2 = 0.0027$ .

In the second example, the excitation is the same as the one of the previous test case. The ferromagnetic material is non conductive and it is chosen to be linear with a constant permeability  $\mu_r = 1000$  H m<sup>-1</sup>. The conductive domain is a nonlinear material with a conductivity of  $0.7 \times 10^6$  S m<sup>-1</sup>, its BH curve is again the one of the 35JN200 steel.

### 4.3.4 FEM/BEM acceleration

The Finite Element / Boundary Element (FEM/BEM) approach is the one introduced in 4.2, the iron nonlinearity is enclosed into the magnetization at the right-end side of the equation as

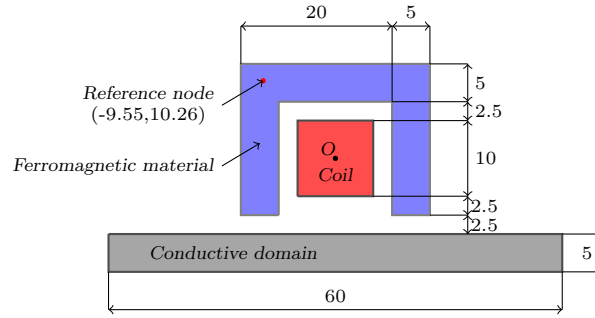


FIGURE 4.20: Test case (Dimension in mm)

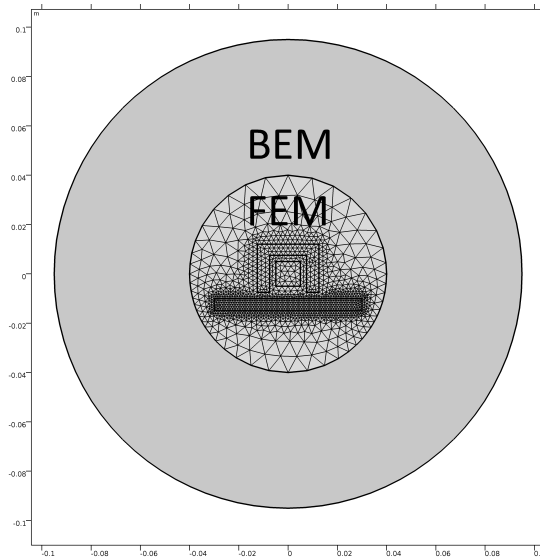


FIGURE 4.21: FEM/BEM domains subdivision and discretization.

in (4.48) and the fixed point method adopted is the one of Eq. (4.49). While the use of BEM part is not mandatory for this particular test case it was adopted to demonstrate the effect of Anderson acceleration on a nonlinear differential algebraic problem with general matrices (with sparse blocks and full blocks). The FEM/BEM problem discretization is shown in Fig. 4.21.

### 4.3.5 Harmonic Balance FEM acceleration

The Anderson acceleration is a general method that can be applied in arbitrary iterative schemes. In this Section, the Harmonic Balance (HB) formulation is adopted and accelerated through this method.

The Harmonic Balance method permits to determine an approximate steady-state solution of a nonlinear differential equation considering a truncated Fourier series expansion [117]. With this approach the steady-state solution of the problem is computed directly avoiding transient calculations and, therefore, this technique turns out to be computationally convenient especially for those systems which exhibit a slow dynamic. Here, the Harmonic Balance method coupled with a FEM discretization (HBFEM) is used to solve the eddy current PDE via a fixed point scheme.

The starting point is the use of the Galerkin method applied to the eddy current equation:

$$\nabla \times (\nu \nabla \times \mathbf{A}) + \sigma \frac{\partial \mathbf{A}}{\partial t} = \mathbf{J} \quad (4.57)$$

this permits to obtain the following nonlinear system of ordinary differential algebraic equations:

$$\mathbf{K}[\nu(\mathbf{x}(t))]\mathbf{x}(t) + \mathbf{M}(\sigma)\dot{\mathbf{x}}(t) = \mathbf{s}(t) \quad (4.58)$$

where  $\mathbf{K}[\nu(\mathbf{x}(t))]$  is the stiffness matrix,  $\mathbf{M}(\sigma)$  is the mass matrix,  $\mathbf{x}(t)$  is the unknown vector and  $\mathbf{s}(t)$  is the source which is assumed to be periodic with period  $T$ . The HB method is based on the ansatz that also the solution has to satisfy the condition  $\mathbf{x}(t) = \mathbf{x}(t + T)$ . The unknown vector is expressed with a truncated Fourier series representation:

$$\mathbf{x}(t) = \Re \left( \sum_{n=1}^N \mathbf{X}_n e^{jn\omega_0 t} \right) \quad (4.59)$$

where the terms  $\mathbf{X}_n$  can be computed as:

$$\mathbf{X}_n = \mathbf{F}_n(\mathbf{x}(t)) = \frac{1}{T} \int_T \mathbf{x}(t) e^{-jn\omega_0 t} dt \quad (4.60)$$

where  $\mathbf{F}_n$  stands for the Fourier operator. The solution of (4.58) is carried out adopting a fixed point scheme. In this case, the fixed point reluctivity  $\nu = \nu_{FP} + (\nu - \nu_{FP})$  is introduced in (4.57) to linearize the problem as:

$$\nabla \times (\nu_{FP} \nabla \times \mathbf{A}) + \sigma \frac{\partial \mathbf{A}}{\partial t} = \mathbf{J} + \nabla \times ((\nu_{FP} - \nu) \nabla \times \mathbf{A}) \quad (4.61)$$

The application of the Galerkin method to (4.61) gives rise to:

$$\mathbf{K}(\nu_{FP})\mathbf{x}(t) + \mathbf{M}(\sigma)\dot{\mathbf{x}}(t) = \mathbf{s}(t) + \mathbf{K}[\nu_{FP} - \nu(\mathbf{x}(t))]\mathbf{x}(t) \quad (4.62)$$

which can be recast in the iterative scheme:

$$\mathbf{K}(\nu_{FP})\mathbf{x}^{(k+1)} + \mathbf{M}(\sigma)\dot{\mathbf{x}}^{(k+1)} = \mathbf{s} + \mathbf{K}[\nu_{FP} - \nu(\mathbf{x}^{(k)})]\mathbf{x}^{(k)} \quad (4.63)$$

where the time dependence is not explicitly stated to simplify the notation. In this work, the value of  $\nu_{FP}$  is kept constant although [110] shows that adaptive approaches can be used to speed up the convergence of the iterative method. The only acceleration considered here is the one due to the Anderson scheme and therefore adaptivity will not be analyzed.

Finally, the Harmonic Balance method is applied to (4.63) equating the Fourier coefficients in the frequency domain:

$$[\mathbf{K}(\nu_{FP}) + jn\omega_0 \mathbf{M}(\sigma)] \mathbf{X}_n^{(k+1)} = \mathbf{F}_n[\mathbf{s} + \mathbf{K}(\nu_{FP} - \nu(\mathbf{x}^{(k)}))\mathbf{x}^{(k)}] \quad (4.64)$$

By using the fixed point approach decoupling has been performed allowing to solve each harmonic independently. For each iteration in (4.64),  $N$  complex linear systems have to be solved to determine the space dependent frequency domain solution.

### 4.3.6 Acceleration results

The two codes have been validated comparing the obtained solutions with the one computed with a FEM commercial software. Figure 4.22 shows the steady state solution in a reference mesh node of the ferromagnetic domain in Figure 4.20 for the two test cases analyzed. The comparison is shown for the reference node but the same applies to the whole mesh, demonstrating the correctness of the two implemented codes. The FEM/BEM simulation results of case 1 refers to times  $t \geq 50$  ms to guarantee that the steady state solution is achieved, the time step is fixed to  $\Delta t = 0.1$  ms and the convergence criterion is set on the residual norm that has to be lower than  $\epsilon = 1e - 6$ .

Fig. 4.23 shows a comparison of the behaviour of the residual  $r = |A^{k+1} - A^k|$  with and without acceleration for two different time instants. At the first iteration,  $r$  collapses to the norm of the potential  $r = |A^0|$  which is initialized as the previous iteration converged value. The fixed point residual decreases linearly while the accelerated residual is not monotonically decreasing.

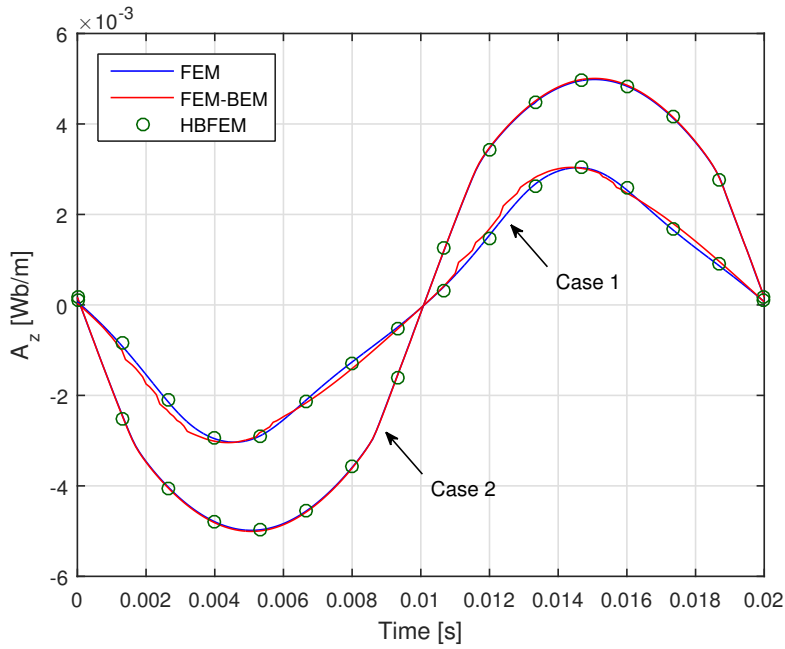


FIGURE 4.22: Comparison between the FEM/BEM, HBFEM and a commercial FEM code

Test case	Method	Iter.	Iter. AA	Reduction to
Case 1	FEM/BEM	23321	5113	22%
Case 1	HBFEM	409	75	18%
Case 2	FEM/BEM	38658	9914	26%
Case 2	HBFEM	1465	237	16%

TABLE 4.5: Comparison between the iterations required to achieve convergence.

The effect of the acceleration is especially visible at low fields (Fig. 4.22 left), when the fixed point permeability that guarantees the scheme contraction  $\mu_{FP} = 2\mu_{min}$  is far from the real one which is close to  $\mu = \mu_{max}$  below the BH knee. The comparison of the iterations number for the whole time domain simulation is reported in Fig. 4.24. The total number of iterations without acceleration is  $K_{FP} = 23321$ , while with Anderson accelerations the iterations are reduced to  $K_{FP+AA} = 5113$ , thus a 75% reduction in iterations which corresponds to a 75% reduction in time due to the negligible cost of the QR-updated factorisation. The HBFEM simulations have been carried out with a constant permeability  $\mu_{FP} = 2\mu_{min}$  to ensure the convergence of the iterative scheme. The number of harmonics considered for the approximation has been set to seven to guarantee an adequate accuracy for the solution. In this case, a suitable criterion to stop the iterative scheme is the one proposed in [111]. The solution is considered to be achieved when the maximum and the mean variations of the permeability in two consecutive iterations are below a suitable threshold, respectively equal to 1% and 0.1%. The acceleration due to the Anderson scheme is visible in the convergence diagram of the first test case shown in Figure 4.25. The natural implementation of the Anderson technique in the HBFEM code consists in the acceleration of the magnetic vector potential. This can be done only on the nodes of the nonlinear domain to reduce the size of the matrices that arise from the QR factorization. The optimal size of the basis used for Anderson scheme results  $m = 25$  and  $m = 20$  for the first and the second test case respectively. Table 4.5 summarizes the results obtained with the various techniques. The use of the Anderson scheme allows a very significant decrease of the iterations required to determine the solution in all cases.

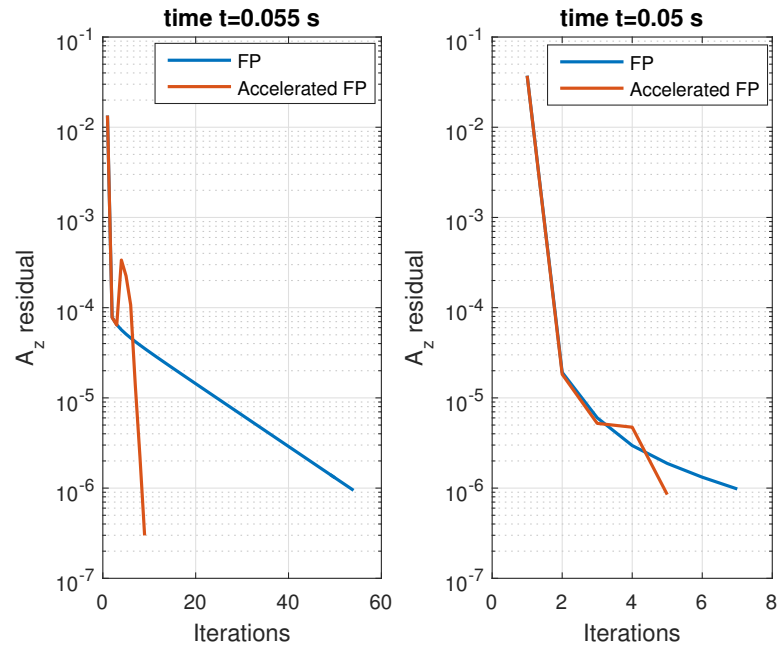


FIGURE 4.23: Convergence diagram FEM/BEM method of two different time steps. The basis size is set to  $m = 20$ .

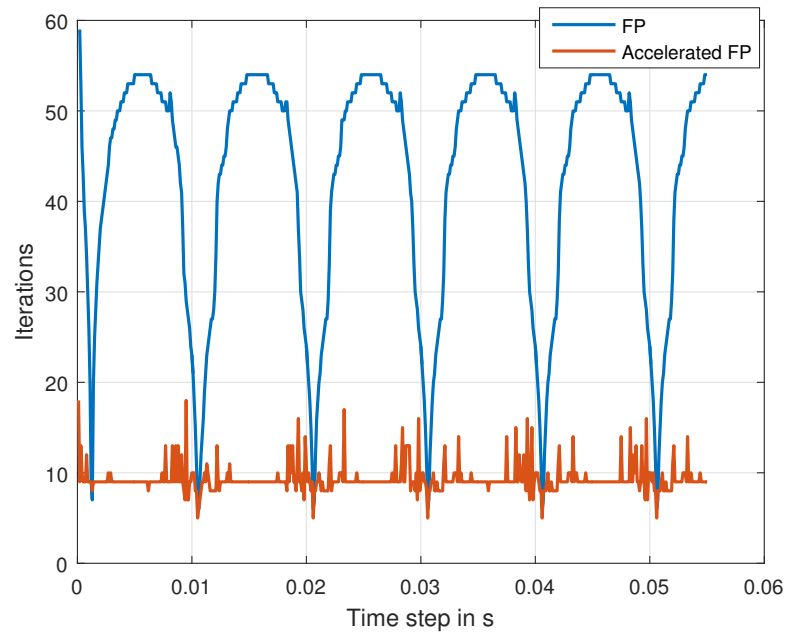


FIGURE 4.24: Iterations comparison with and without acceleration. Adopting the permeability  $\mu_{FP} = 2\mu_{min}$ , the fixed point maximum iterations are obtained at low fields.

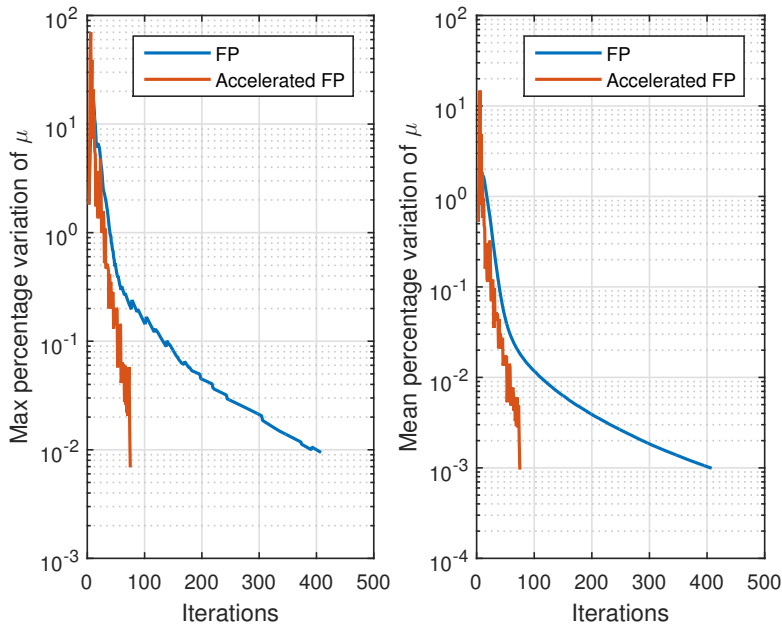


FIGURE 4.25: Convergence diagram of the HBFEM method for the first test case. The basis size is set to  $m = 25$ .

### 4.3.7 FEM/BEM case with hysteresis

The FEM/BEM approach introduced in Sec. 4.3.4 has been equipped with the simplified hysteresis model adopted in [118]. The magnetic field  $\mathbf{H}$  at each step is calculated as:

$$\mathbf{H}(\mathbf{B}, \dot{\mathbf{B}}, p_k) = (p_0 + p_1|\mathbf{B}|^{2p_2}) \cdot \mathbf{B} + p_3\dot{\mathbf{B}} + \frac{p_4\dot{\mathbf{B}}}{\sqrt{p_5^2 + |\dot{\mathbf{B}}|^2}} \quad (4.65)$$

where the dot indicates the time derivative. The parameters  $p_0 - p_5$  are the material constants that have been found through an identification procedure. Eq. (4.65) will also be adopted for the case of laminated sheets in magnetic gears in Sec. 4.4.

The benchmark geometry is the one of TEAM problem 32 [90], which is normally adopted to test vector hysteresis models. The hysteresis model accuracy depends on the fit of the material coefficients in (4.65) and is beyond the scope of the thesis. The relevant information concerns the performance of Anderson acceleration given a certain hysteresis model that normally requires the FP method to converge.

Fig. 4.26 shows the hysteresis cycle in the point  $C6$  for the case 2 defined in [90]. The model is therefore capable to catch nontrivial examples with minor loops as described in [118]. The iterations required for the hysteresis problem are reported in Tab. 4.6. If the number of iterations  $it$  is greater than 1000, the time step is considered as not converged. The restart approach is proven to be fundamental to avoid over-iterations steps, and the strategy that results in the best performance is to restart the acceleration every  $m$  steps, in accordance with [115].

## 4.4 Hysteresis in soft magnetic materials

The magnetic field components interactions play a crucial role in magnetic gear behavior. As discussed in Sec. 2.3, a variety of approaches in literature discuss both analytic and numerical models for magnetic field computation in the gears. To achieve a higher accuracy, the detailed magnetic gear design should be finite element-based. In particular, iron poles require an accurate model to assess losses and torque. However, the problem results numerically challenging because



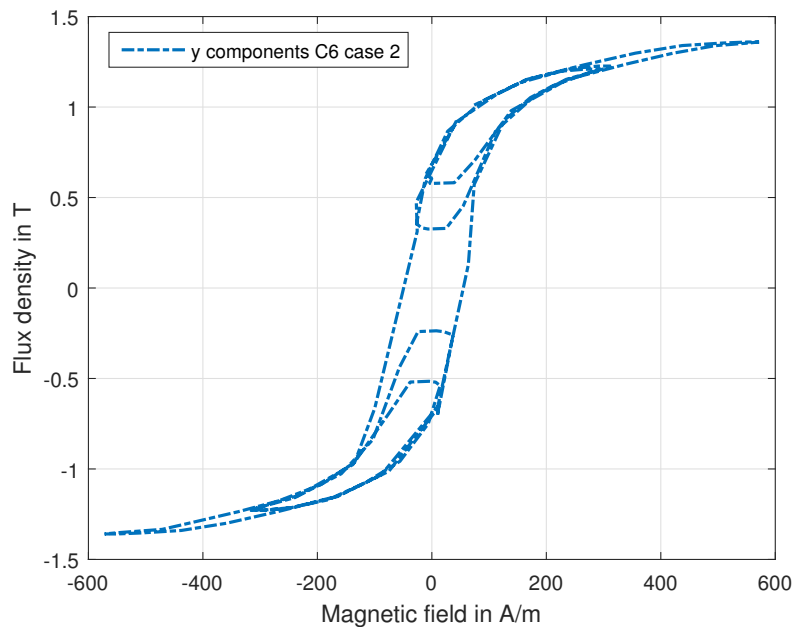


FIGURE 4.26: TEAM 32 case 2: hysteresis loop in point C6. The plot shows the By-Hy loop.

Method	Base	Restart	Iter.	Not conv. ( $it > 1000$ )	Reduction to
FP	No	No	17838	61	
FP+AA	$m = 30$	No	4968	13	28%
FP+AA	$m = 30$	50	4631	0	26%
FP+AA	$m = 30$	30	2716	0	15%

TABLE 4.6: Comparison between Anderson accelerations (AA) with different settings. The test case is the TEAM 32, case 2, and the convergence criterion is tolerance  $\tau < 1e - 5$ .

of the rotational nature of the magnetic flux density and the nonlinear hysteretic behavior in the ferromagnetic poles.

Li et al. in [119] discuss the role of hysteresis on the torque waveforms of a permanent magnet machine, while in [120] the intrinsic dependence between eddy currents and hysteresis is highlighted: hysteresis should be included for accurate machine modelling.

This Section deals with the hysteresis effect on a coaxial magnetic gear using the homogenized model already introduced in 4.3.7 for the Anderson acceleration test case. A simple post processing implementation based on the non-hysteretic FEM results (referred as open loop) is discussed and compared to a direct implementation (referred as closed loop implementation).

#### 4.4.1 FEM implementation

To overcome convergence problems of the simulation due to magnetic material models, a differential reluctivity tensor can be applied to solve the finite element formulation of the magnetic vector potential [118].

Using the 2D  $\mathbf{A}$  formulation, the magnetic flux density  $\mathbf{B}$  is defined as  $\mathbf{B} = \nabla \times \mathbf{A}$  and the magnetic vector potential  $\mathbf{A} = (0, 0, A_z)$  is discretized through linear piece-wise functions:

$$A_z(x, y, t) = \sum_{j=1}^{Ne} \alpha_j(t) \beta_j(x, y) \quad (4.66)$$

where  $Ne$  is the number of nodes,  $\alpha_j(t)$  is the nodal value of the vector potential  $z$  component,  $\beta_j(x, y)$  is the shape function. The vector associated to the shape function is  $\boldsymbol{\omega}_j = (0, 0, \beta_j)$  since in the 2D formulation only the  $z$  component of the magnetic vector potential is not zero.

Assuming negligible eddy currents in the permanent magnets, the weighted residual approach is applied on Ampere's law, leading to the weak formulation:

$$\int_{\Omega} \mathbf{H} \cdot \nabla \times \boldsymbol{\omega}_i d\Omega + \oint_{\partial\tau} \mathbf{H} \times \boldsymbol{\omega}_i d\tau = \int_{\Omega_s} \mathbf{J}_s \cdot \boldsymbol{\omega}_i d\Omega_s \quad (4.67)$$

where  $\mathbf{J}_s$  is the source current in a subspace  $\Omega_s$  of the entire domain  $\Omega$ . The closed integral on the boundary is equal to zero due to homogeneous Neumann or Dirichlet boundary conditions. To solve (4.67) in the time domain, a time-stepping technique is applied: this is due to the time dependencies of the hysteretic materials. If  $A(t_n)$  is a given state of the magnetic problem the state at the next time instant  $t_{n+1} = t_n + \Delta t$  is calculated using iterative Newton-Raphson (NR) method. For each NR iteration  $A^k = A^{k-1} + \Delta A^k$  the increment  $\Delta A^k$  must be calculated. Therefore Eq. (4.67) is linearized around  $A^{k-1}$ . This linearization is obtained deriving the equation with respect to  $\alpha_j$ , which can be achieved through the differential reluctivity:

$$\frac{d\mathbf{H}}{d\alpha_j} = \frac{d\mathbf{H}}{d\mathbf{B}} \cdot \nabla \times \boldsymbol{\omega}_j = \nu_d \nabla \times \boldsymbol{\omega}_j \quad (4.68)$$

Substituting (4.68) in (4.67), Ampere's law becomes:

$$\begin{aligned} & \sum_{j=1}^{Ne} \Delta \alpha_j^k \int_{\Omega} (\nu_d \cdot \nabla \times \boldsymbol{\omega}_j) \cdot (\nabla \times \boldsymbol{\omega}_i) d\Omega = \\ & = \int_{\Omega_s} \mathbf{J}(t_{n+1}) \cdot \boldsymbol{\omega}_i d\Omega - \int_{\Omega_s} \mathbf{H}^{k-1} \cdot \nabla \boldsymbol{\omega}_i d\Omega \end{aligned} \quad (4.69)$$

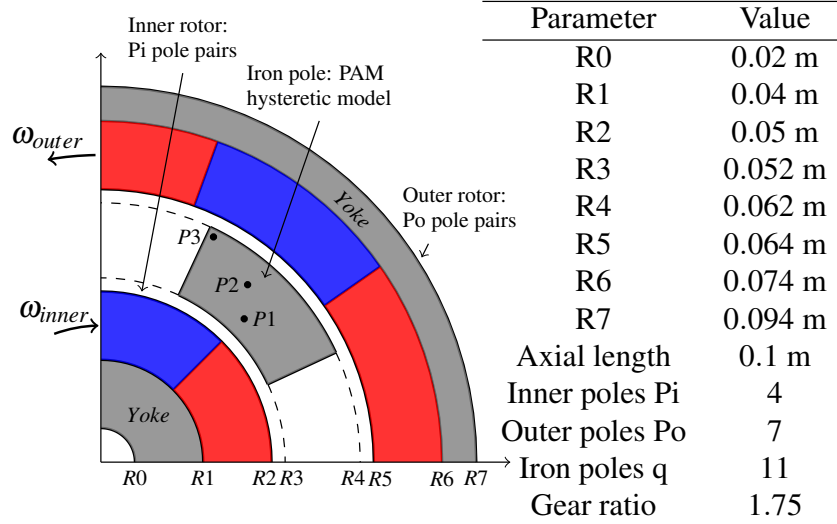
In the discrete time-stepping scheme the differential reluctivity can be expressed as  $\nu_d = \frac{\Delta \mathbf{H}}{\Delta \mathbf{B}} = \frac{\Delta \mathbf{H} \cdot \Delta \mathbf{B}}{\Delta \mathbf{B} \cdot \Delta \mathbf{H}}$  with  $\Delta \mathbf{H} = \mathbf{H}^{k+1}(t_{n+1}) - \mathbf{H}(t_n)$  and  $\Delta \mathbf{B} = \mathbf{B}^{k+1}(t_{n+1}) - \mathbf{B}(t_n)$ .

In all elements where hysteresis is considered, the homogenized parametric algebraic model (PAM) described in [121] is adopted to include eddy currents and hysteresis:

$$\mathbf{H}(\mathbf{B}, \dot{\mathbf{B}}, p_k) = (p_0 + p_1 |\mathbf{B}|^{2p_2}) \cdot \mathbf{B} + p_3 \dot{\mathbf{B}} + \frac{p_4 \dot{\mathbf{B}}}{\sqrt{p_5^2 + |\dot{\mathbf{B}}|^2}} \quad (4.70)$$

$p_0$	$p_1$	$p_2$	$p_3$	$p_4$	$p_5$	$B_s$
95.9	0.29	11.4	0.041	28.6	8.03	1.67 T

TABLE 4.7: List of parameters for the PAM model retrieved by [121].

FIGURE 4.27: Magnetic gear test geometry and query points  $P1$ ,  $P2$ ,  $P3$ .

$\dot{\mathbf{B}}$  is the time derivative of the magnetic flux density and the parameters  $p_0 - p_5$  are material constants that have been found through the identification procedure in [121]. In particular, the parameters  $p_0$ ,  $p_1$  and  $p_2$  are related to the anhysteretic magnetization curve,  $p_3$  is related to eddy currents in the laminated sheets,  $p_4$  and  $p_5$  are linked to the hysteresis phenomena. Since the term  $B^{2 \cdot p_2}$  is not asymptotic, Eq. (4.70) has been applied below the saturation flux density  $|B| = B_s$ , while above saturation the  $BH$  curve is assumed to be linear with a slope equal to the vacuum permeability  $\mu_0$ .  $B_s$  is computed as:

$$B_s = \sqrt[2p_2]{\frac{\frac{1}{\mu_0} - p_0}{p_1 \cdot (2p_2 + 1)}} \quad (4.71)$$

Since the waveforms in the magnetic gear are sinusoidal in first approximation, the set of parameters chosen from [121] is the one reported in Tab. 4.7.

Eq. (4.69) is computed elementwise for the hysteretic regions providing  $H_{elem}^k = f(B_{elem}^k(t_{n+1}), B_{elem}(t_n))$  which is subsequently substituted in the differential reluctivity expression. In the proposed strategy, (4.69) is directly implemented in the FEM model, constituting a closed loop integration of the PAM material model in the FEM algorithm. The open loop implementation consists of the simple implementation of (4.70) as post processing, while the nonlinear  $BH$  curve adopted for the FEM simulation is the one extracted by the anhysteretic part in (4.70).

#### 4.4.2 Magnetic gear test case

Fig. 4.27 shows the test case geometry (1/4th of the entire model) and dimensions. The iron poles are modelled using the hysteresis model, while for the yoke area the classical nonlinear  $BH$  curve is adopted. The rotational speed of the inner rotor is set to  $v_{in} = 955$  rpm and to  $v_{in} = 3180$  rpm, thus the outer rotor speed is  $v_{out} = 545.7$  rpm and  $v_{out} = 1817$  rpm respectively. The magnets use a linear model with magnetic remanence  $Br = 1.2$  T on both inner and outer rotors and unitary relative permeability. As test case geometry, a magnetic transmission gear with low fractional gear ratio and a high number of inner pole pairs ( $Pi = 4$ )

is adopted, hence the lowest order of harmonics of the cogging torque on the inner and outer rotor are  $h_1 = 154$  and  $h_2 = 286$  respectively according to [85]. These harmonics are due to the combined interaction between permanent magnets magneto-motive force and reluctances due to iron poles. In this Section, the open and closed loop application of Eq. (4.70) are compared: the resulting loss magnitude's order is validated through the dynamic version of the typical loss separation method applied for the steel M330-35HS with density  $\delta = 7650 \text{ kg/m}^3$ :

$$P_{St} = k_{hyst} f B^\alpha + k_{eddy} \left( \frac{dB}{dt} \right)^2 + k_{exc} \left( \frac{dB}{dt} \right)^{1.5} \quad (4.72)$$

where  $f$  is the frequency and the material parameters calculated through the fitting are:  $k_{hyst} = 0.0194 \text{ Wm}^{-3} \text{T}^{-\alpha} \text{s}$ ,  $k_{eddy} = 6.78 \cdot 10^{-5} \text{ Wm}^{-3} \text{T}^{-2} \text{s}^2$ ,  $k_{exc} = 8.77 \cdot 10^{-6} \text{ Wm}^{-3} \text{T}^{-1.5} \text{s}^{1.5}$ ,  $\alpha = 2$ . Eq. (4.72), referred as Bertotti's equation, is only used to compare the results of the PAM model with the most diffused semi-empirical method for loss calculation, but could lead to wrong estimations when applied to rotational loci or with frequencies  $f > 400 \text{ Hz}$  according to [122]. The validity of (4.70) has been extensively discussed in [121].

### 4.4.3 Model results

Fig. 4.28 shows the  $x$  and  $y$  components of the magnetic flux density in the points  $P1$ ,  $P2$  and  $P3$  depicted in Fig. 4.27. Since the differences between the waveforms with hysteresis and without hysteresis are hardly distinguishable, two different zooms have been depicted in Figs. 4.29 and 4.30. In particular Fig. 4.30 shows the multiple inflection points of  $B_y$  computed in  $P1$ ; multiple minor loops are therefore expected in the  $B_y H_y$  plane when the the flux density is maximum.

Fig. 4.31 shows the rotational flux loci computed at the points  $P1$ ,  $P2$ ,  $P3$  again in both cases with and without hysteresis.

Fig. 4.32 shows the  $B_x$  versus  $H_y$  waveform at  $P1$ . Similar results are obtained for  $P2$  and  $P3$ . Thus in this Section only the results relative to  $P1$  has been reported.

Fig. 4.33 shows the results for the  $y$  component of  $P1$ .

Fig. 4.34 shows the torques developed on inner and outer rotors and on the iron poles when the gear load angle is maximum.

### 4.4.4 Discussion and remarks

As depicted in Fig. 4.28, the field waveforms are composed of the fundamental harmonic with some additional higher order harmonics, due to the interaction between inner and outer magneto motive forces.

The implementation of the PAM model rather than its anhysteretic part during the FEM calculation affects only slightly the magnetic flux density (Fig. 4.29). This small difference justifies the application of hysteresis models as post processing (or in open loop), in an effort to combine the accuracy of the hysteresis models with the efficiency of the nonlinear FEM [123].

The flux loci in Fig. 4.31 are strongly rotational in all the nodes of the iron poles and the influence of the closed loop implementation is clearly visible.

The analysis of Figs. 4.32 and 4.33 is the key point in this Section that allows us to compare the open loop and closed loop implementation of the hysteresis models. In the case without hysteresis the component wise  $BH$  characteristics enclose an area in the first quadrant that is opposite to the one on the third quadrant: this is due to the fact that the nonlinear  $BH$  curve is applied at the absolute values of  $\mathbf{B}$  and  $\mathbf{H}$ , thus when looking at the  $x$  components the  $y$  components effects are implicitly included. In the cases with hysteresis the difference between open and closed loop has a remarkable impact on the  $BH$  loops: in particular with the closed chain the loop area is bigger than the other case. Some minor loops are also visible, as expected from Fig. 4.29 and 4.30 where  $B_x$  and  $B_y$  have an inflection point: minor loops have been observed in both implementations.

The same consideration of Fig. 4.32 applies with the exception of the minor loops that appear at high flux densities again due to the inflection points visible in Fig. 4.28.

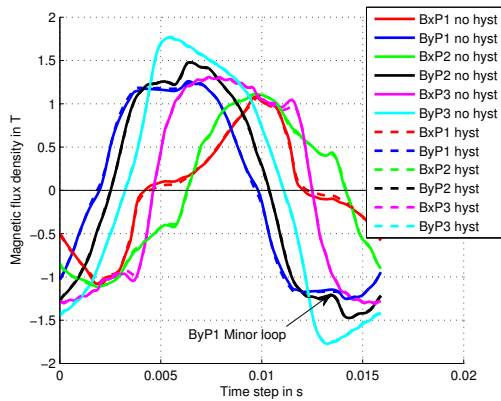


FIGURE 4.28: Magnetic flux density waveforms evaluated in the points  $P1$ ,  $P2$  and  $P3$  of Fig. 4.27. The results for both nonlinear  $BH$  curve without and with hysteresis are reported at inner rotational speed  $v_i n = 955$  rpm.

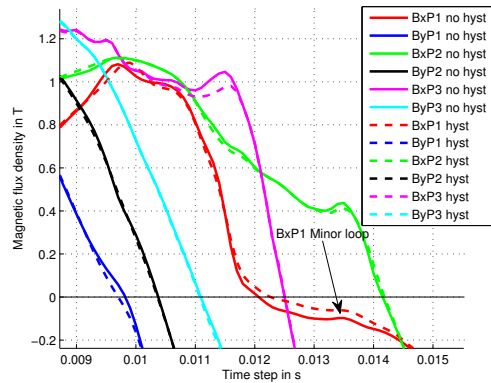


FIGURE 4.29: Zoom of Fig. 4.28. The difference between the magnetic flux density waveforms is only due to the closed loop implementation of the PAM model. A small inflection point on the  $B_x$  component on the point  $P1$  is depicted.

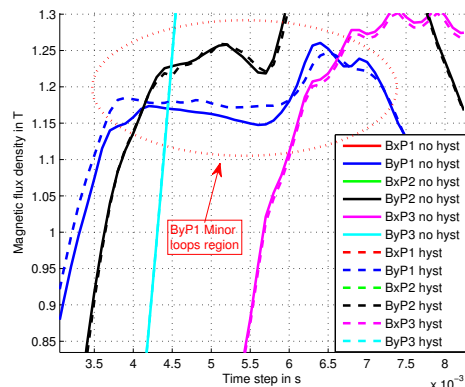


FIGURE 4.30: Zoom of Fig. 4.28. Multiple inflection points are shown in the  $B_y$  waveform of the point  $P1$ .

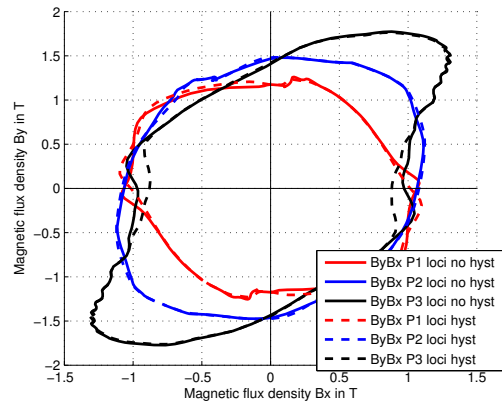


FIGURE 4.31: Magnetic flux density loci at points  $P1$ ,  $P2$ ,  $P3$  with and without hysteresis. The rotational behavior of the flux density in the iron poles is clearly visible.

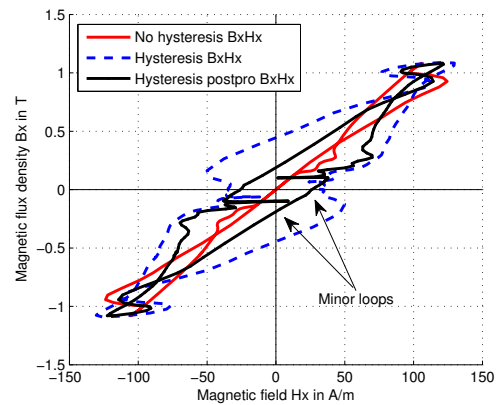


FIGURE 4.32:  $B_x$  versus  $H_x$  in point  $P1$  calculated without hysteresis and with the PAM model applied in closed loop and in open loop as post processing. Minor loops are highlighted in the low flux density region.

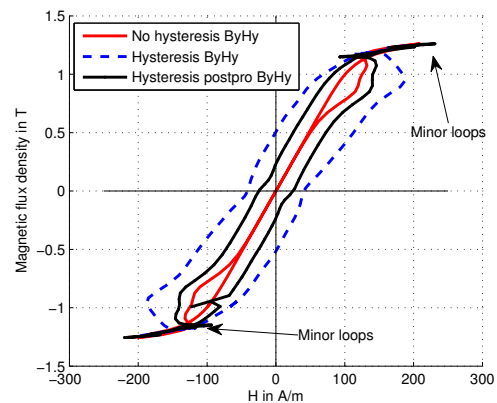


FIGURE 4.33:  $B_y$  versus  $H_y$  in  $P1$  calculated without hysteresis and with the PAM model applied in closed loop and in open loop as post processing. Minor loops are highlighted in the high flux density region.

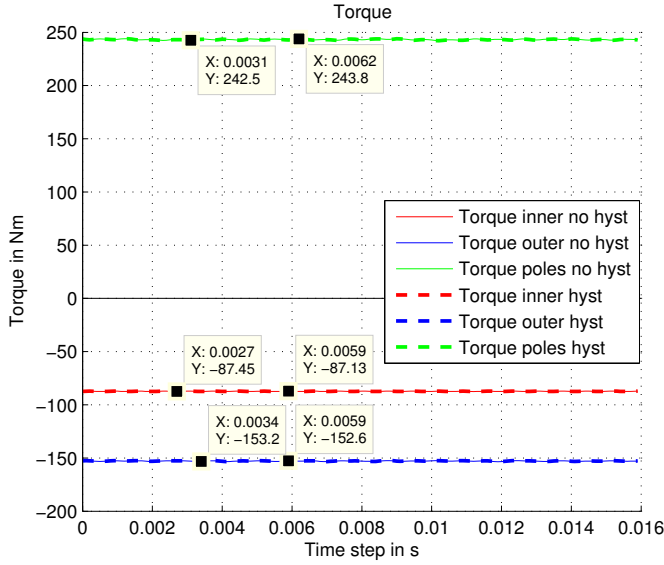


FIGURE 4.34: Computed torques on the inner, outer and iron poles rotor when the magnetic gear is at his maximum load capability. The torque ripple is lower than 0.5% because of the high number of pole pairs. The difference due to the hysteresis model is negligible on the torque waveforms in this case. The torque ripple harmonics are in accordance with the predictions in [85].

According to Fig. 4.34, the torque ripple is lower than  $\Delta R = 0.5\%$  for all the rotors because of the high number of pole pairs of the test case geometry. The shift due to the different model adopted is of the order of  $\Delta T = 0.07\%$ . The shift is directly linked to the power losses obtained in the iron poles when using the closed loop hysteresis implementation. In order to estimate the power loss, the areas of the  $BH$  loops have to be calculated:

$$P_{loss} = P_x + P_y = f \oint H_x dB_x + f \oint H_y dB_y \quad (4.73)$$

In order to improve the integral calculation, the  $H$  components are interpolated through piecewise cubic Hermite polynomial functions and then the integration is performed. This procedure allows us to estimate area of arbitrary loops accurately when the number of data points is reduced or crowded in certain regions of the  $BH$  space. The minor loop calculation is automatically included.

In Tab. 4.8 the results relative to two different gear speeds are reported. Eq. (4.73) is used using the magnetic field  $\mathbf{H}$  calculated from FEM in the first column of Tab. 4.8 or through (4.70) using the magnetic flux density  $\mathbf{B}$  from FEM in the second column. In the case of open loop,  $P_{loss}$  is zero since both the integrals are zero. When adopting the closed loop hysteresis, the post processing calculation of  $\mathbf{H}$  is performed through the same law adopted in the finite element implementation, thus the calculation will yield the same results: as expected in the open loop case direct integration gives approximatively zero (\*) and in the closed loop hysteresis model direct integration and post processing calculation are in agreement ( $\wedge$  and  $\wedge\wedge$ ). The most interesting comparison is the one between the losses computed through the open loop and closed loop application of the PAM equation (\*\* and  $\wedge$ ). In Tab. 4.8 the losses computed through closed loop are respectively 60% and 50% higher than the ones computed with open loop approximation. This implies that applying the PAM equation as post processing calculation could lead to very misleading results, even if the magnetic flux density  $\mathbf{B}$  variation due to the closed loop implementation is limited.

The losses computed through (4.72) and (4.73) are in agreement, thus the procedure based on the PAM model provides physically meaningful results and the material coefficients  $p_0 - p_5$  are reliable. In the high speed case, the losses computed through Bertotti's equation are 20% lower than the closed loop implementation while in the low speed case the discrepancy is less

W	$\int H dB$	$\int H_p dB$	$P_{hyst}$	$P_{eddy}$	$P_{exc}$	$P_{St}$
No hyst	-0.01*	3.12**	3.33	1.66	0.16	5.15
Hyst	4.91 <sup>^</sup>	4.95 <sup>^^</sup>	3.31	1.65	0.16	5.12
No hyst	-0.03*	24.29**	11.1	18.41	0.99	30.5
Hyst	36.2 <sup>^</sup>	36.3 <sup>^^</sup>	11.01	18.1	0.98	30.1

TABLE 4.8: Comparison between closed and open loop loss calculation.  $H_p$  stands for the post processing magnetic field while  $H$  is the one adopted in the finite element model. *No hyst* means that only the anysterecic part of the material model is implemented in FEM, while *Hyst* means that the FEM material model is the one in (4.70) with both hysteretic and anhysteretic parts.

noticeable. The mismatch occurs since the loss separation method is a simple procedure normally introduced in the linear material case [122]. Several modifications to the standard equation have been introduced in order to adapt the loss model to the more general cases such as waveforms with minor loops, DC biases and non linearities as shown in [124, 125]. In the magnetic gear case, where the  $\mathbf{B}$  loci are rotational and minor loops are present, (4.72) provide a poor estimate of losses. The theoretical rigorous approach for loss computation is the one in (4.73), where  $\mathbf{B}$  and  $\mathbf{H}$  take into account hysteresis, eddy currents and material non linearities. Assuming that the material coefficients  $p_0 - p_5$  are exactly fitted for the case under investigation, (4.73) should provide a better loss estimation than (4.72).

The discussion presented in this Section is based on the magnetic gear test case but the results can be extended to the general case: in fact the  $BH$  curves only affect the material coefficients  $p_0 - p_5$  while all the other comparisons between the open and closed loop implementations still hold.

## 4.5 Hysteresis and modelling of hard magnetic materials

Soft non-linear BH characteristic are normally implemented in FEM (e.g. Sec. 4.2), where linearly or quadratically converging schemes, such as the fixed point and Newton-Raphson methods, deal with the non-linearity iteratively. Several models [126, 127, 128] capable of taking into account permanent demagnetization phenomena have been proposed in literature, where classical hysteresis models are normally adapted for hard magnetic materials. In permanent magnets (PM) machines (except flux switching machines) the hard magnetic material are not subject to full hysteresis cycles, therefore a material class based on the measurement and interpolation would be preferable to a complex and approximated hysteresis model. Moreover, the initial condition imposed for the PM is a uniform magnetic flux density equal to the remanence, or dually a uniform coercive field. This condition would be the actual one if the magnetic field in all the points of the PM exceeds the magnetizing field above which the BH curves collapse to a single curve. For NdFeB hard materials this implies that the magnetic flux density has to reach high values (e.g. up to 3 T), leading to expensive capacitor banks. A trade-off could be to design a smaller capacitor bank, but the magnetization level at the end of the pulse is not uniform. Eddy currents are also to be considered in the magnetization procedure: the rapid field variation could even lead to reversed magnetization near the PM surface areas [93].

Several PM non-linear models have been proposed in literature, mainly to model the demagnetization in electrical machines. In [129] a dynamic PM model is adopted: the algorithm has the capability to switch between the second quadrant nonlinear BH curve and the linear recoil lines, but this model can only be adopted starting from premagnetized magnets.

In [130] magnets are magnetized in situ through simulations based on polynomial fitting of the demagnetization curves, but the procedure is limited to the case of isotropic magnets that obey such quadratic fit. [131] and [132] focus on isotropic ferrite magnets, through the knowledge of the remanence vs magnetizing field curve and permeability vs magnetic field, respectively. These models do not cover the case of recoil, anisotropic PMs or permanent demagnetization due to overload currents.

In [133] several demagnetization models are compared ranging from linear to the full hysteretic approaches. The well known full hysteresis models such as the Preisach [134, 135] one or

the Zirka one [136] are accurate but these algorithms can suffer from convergence issues and the tuning for hard magnetic materials can be non trivial [133].

In this Section a non-linear model capable of representing the PM during magnetization, demagnetization and recoil is presented. The model is based on pure PM non-linear curves interpolation while the recoils are considered as linear.

The proposed procedure can be adopted to assess, with a certain degree of approximation, the non-uniform fields in permanent magnets when little knowledge of the PMs is available, i.e. the virgin curve and some demagnetization curves.

The implementation of the model as an external material class within the framework of an existing finite element code (Comsol Multiphysics [94]) is described in Sec. 4.5.2 and the code is tested on the magnetization of a magnetic gear outer rotor with  $Po = 36$  poles which is equivalent to the rotor of a classical PM machine.

### 4.5.1 Nonlinear formulation

#### Finite element formulation

Permanent magnets are normally represented through a linear equation between the magnetic flux density  $\mathbf{B}$  and the magnetic field  $\mathbf{H}$ :

$$\mathbf{B} = \mu_0 \cdot \mathbf{H} + \mathbf{P} = \mu_0 \cdot (\mathbf{H} + \mathbf{M}) \quad (4.74)$$

where  $\mu_0$  is the vacuum permeability,  $\mathbf{P}$  is the polarization and  $\mathbf{M}$  is the magnetization. When adopting a formulation based on the magnetic vector potential  $\mathbf{A}$ ,  $\mathbf{B}$  is the output of the simulation and the material model is used to find the magnetic field  $\mathbf{H}$ :

$$\mathbf{H} = \mathbf{B} \cdot \nu_0 - \mathbf{M} \quad (4.75)$$

with  $\nu_0 = 1/\mu_0$ . Maxwell's equations in 3D adopting the AV formulation with the nonlinear magnetization term reads:

$$\begin{cases} \sigma \frac{\partial \mathbf{A}}{\partial t} + \nabla \times \nu \nabla \times \mathbf{A} + \sigma \nabla V = \mathbf{J} + \nabla \times \mathbf{M}(\mathbf{A}) \\ \nabla \cdot \sigma \left( \frac{\partial \mathbf{A}}{\partial t} + \nabla V \right) = 0 \end{cases} \quad (4.76)$$

where  $\mathbf{J}$  is the source current density,  $V$  is the scalar potential,  $\sigma$  is the conductivity and  $\nu$  is the reluctivity.

The PM scheme adopted in this Section can be applied for general 3D geometries. Since the test cases that have been chosen for validation are axisymmetric and 2D, the finite element formulation that will be shown is the two dimensional one, but the material class is implemented for the 3D case. In the 2D case (4.76) reads:

$$\sigma \frac{\partial A_z}{\partial t} - \nabla \cdot \nu \nabla A_z = J_z + \nabla_{2D} \times \mathbf{M}(A_z) \quad (4.77)$$

where  $J_z$  is the  $z$  component of the source current and  $\nabla_{2D} \times \mathbf{M}(A_z) = \partial_y M_x(A_z) - \partial_x M_y(A_z)$  is the 2D curl which can be expressed as a gradient. The finite element weak form of (4.77), without the boundary terms related to Dirichlet and Neumann conditions, reads:

$$\begin{aligned} & \int_{\Omega} \sigma \frac{\partial A_z}{\partial t} \omega d\Omega - \int_{\Omega} (\nabla \omega)^T \cdot \nu \cdot \nabla A_z d\Omega - \int_{\Omega} J_z \cdot \omega d\Omega = \\ & = \int_{\Omega_{PM}} \nabla_{2D} \times \mathbf{M}(A_z) \cdot \omega d\Omega = \\ & = \int_{\Omega_{PM}} \mathbf{M}(A_z) \cdot \nabla_{2D} \times \omega d\Omega - \int_{\Gamma_{PM}} (0, 0, \omega) \times \mathbf{M}(A_z) \cdot \mathbf{n} d\gamma \end{aligned} \quad (4.78)$$

where  $\omega$  is the shape function  $\Gamma_{PM}$  is the PM boundary,  $\Omega$  is the 2D domain and  $\Omega_{PM}$  is the PM domain only. The inclusion of the PM non-linearities can be obtained in two different ways, referred as Method 1 and Method 2 in the following Sections.



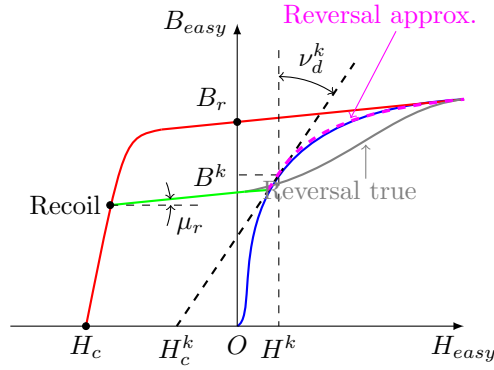


FIGURE 4.35: Easy axis BH characteristic of a permanent magnet: the blue curve is the virgin curve, the red curve is the non-linear demagnetization line, the green curve is the recoil line, the gray and magenta curves represent the true reversal curve and the approximated one, respectively. The differential reluctivity  $\nu_d^k$  and the linear magnetization field  $H_c^k$  relative to the working point  $(H^k, B^k)$  are shown.

### Method 1

According to this method, a linearization of the magnetization term  $\mathbf{M}(A_z)$  is adopted, leading to [137, 138]:

$$\begin{aligned} \mathbf{M}(\mathbf{A} + \Delta\mathbf{A}) &= \mathbf{M}(\mathbf{A}) + \frac{\partial(\nu_0\mathbf{B} - \mathbf{H})}{\partial\mathbf{B}} \frac{\partial\mathbf{B}}{\partial\mathbf{A}} \Delta\mathbf{A} = \\ &= \mathbf{M}(\mathbf{A}) + \left(\mathbf{1}\nu_0 - \overline{\overline{\nu}}_d\right) \cdot \nabla \times \Delta\mathbf{A} \end{aligned} \quad (4.79)$$

where  $\overline{\overline{\nu}}_d$  is the differential reluctivity tensor that has to be updated at each nonlinear step.

### Method 2

In this method the PM non-linearity is included in the reluctivity tensor and therefore the material law has to be linearised [139]. If the linearization of the problem is performed in each material point  $(\mathbf{H}^k, \mathbf{B}^k)$ , the equation using  $\mathbf{B}$  rather than  $\Delta\mathbf{B}$  is [140]:

$$\begin{cases} \mathbf{H}(\mathbf{B}) = \mathbf{H}_c^k + \overline{\overline{\nu}}_d^k \mathbf{B} \\ \mathbf{H}_c^k = H_c^k \cdot \frac{\mathbf{B}^k}{|\mathbf{B}^k|} \\ \nu_{d(i,j)}^k = \frac{\Delta H_i^k}{\Delta B_j^k} \quad i, j = 1 \dots 3 \end{cases} \quad (4.80)$$

The index  $k$  refers to the  $k^{\text{th}}$  nonlinear step. The application of (4.80) for the PM case is shown in Fig. 4.35. Substituting (4.80) in Ampere's law, the first Eq. in (4.76) becomes:

$$\sigma \frac{\partial \mathbf{A}^{(k+1)}}{\partial t} + \nabla \times \overline{\overline{\nu}}_d^k \nabla \times \mathbf{A}^{(k+1)} = \mathbf{J} - \nabla \times \mathbf{H}_c^k \quad (4.81)$$

The differential reluctivity tensor  $\overline{\overline{\nu}}_d^k$  needs special care because its components should be monotone to achieve convergence. Since the data relative to the magnetization  $\mathbf{M}$  is normally the result of measurement fitting, the monotonicity has to be enforced [137].

### Time dependent problem

The Differential Algebraic Equation (DAE) system that results from the FEM discretization is:

$$\mathbf{R}^*(t) = [M] \frac{\partial \mathbf{A}(t)}{\partial t} + [K(\mathbf{A}(t))] \mathbf{A}(t) - \mathbf{g}(t) = 0 \quad (4.82)$$

where the mass matrix  $[M]$  is semi-positive definite and  $[K]$  depends on the solution  $\mathbf{A}$ ,  $\mathbf{R}^*$  is the theoretical residual at exact convergence. The stiffness matrix  $[K]$  and the source term  $\mathbf{g}$

change according to the method adopted for including the non-linearities. The linearisation of the residual through the Jacobian  $[J]$  gives the iterative Newton-Raphson scheme:

$$\mathbf{A}(t+1) = \mathbf{A}(t) + \alpha[J]^{-1} \cdot \mathbf{R}(t) \quad (4.83)$$

In this section the formulation with the differential reluctivity is adopted (Method 2, Sec. 4.5.1), thus the material model is in the form  $\mathbf{H} = f(\mathbf{B})$  according to (4.75) and the matrices in (4.82) are computed as in [140]. The magnetization is denoted as  $\mathbf{M} = M \cdot \vec{\mathbf{e}}_{\mathbf{z}}$  where  $\vec{\mathbf{e}}_{\mathbf{z}}$  is the PM easy direction.

### PM measurements

From the measurements on the PM probe with different magnetic flux densities  $b_0, b_1 \dots b_n$  and different maximum magnetizing fields  $h_0, h_1 \dots h_n$ , the rectangular matrix  $M_{meas}$  can be built:

$$M_{meas} = \begin{bmatrix} M_{h_0, b_0} & M_{h_0, b_1} & \dots \\ \vdots & \ddots & \\ M_{h_k, b_0} & \dots & M_{h_k, b_n} \end{bmatrix} \quad (4.84)$$

Adopting a regular grid of measurements  $(h, b)$ , there is no need for 2D interpolation schemes based on Delaunay triangulation. If  $h^*$  and  $b^*$  are the nodal maximum magnetizing field during virgin magnetization and the magnetic flux density, the matrix  $M_{meas}$  can be easily reduced to the  $2 \times 2$  sub-matrix  $M_{point}$  for each node.

$$M_{point} = \begin{bmatrix} M_{h_i, b_j} & M_{h_i, b_{j+1}} \\ M_{h_{i+1}, b_j} & M_{h_{i+1}, b_{j+1}} \end{bmatrix} \quad (4.85)$$

Linear interpolation indices can be computed as follows:

$$k_h = \frac{h^* - h_i}{h_{i+1} - h_i} \quad k_b = \frac{b^* - b_j}{b_{j+1} - b_j} \quad (4.86)$$

and thus the nodal value of the magnetization  $M$  is found through the 2D linear interpolation. When recoil lines have to be implemented, a different approach has to be adopted. The usual relation for linear recoil lines in the hypothesis of constant magnetic susceptibility  $\chi$  is:

$$M_{rec} = \chi \cdot \Delta H + M_0 = \frac{\chi}{1 + \chi} \cdot (B - B_0)\nu_0 + M_0 \quad (4.87)$$

where  $M_0$  and  $B_0$  are the magnetization and magnetic flux density stored when the recoil starts. During recoil the vector  $M_{rec}(b_j, b_{j+1} \dots b_n) \forall b_j \geq B_0$  substitutes the values interpolated over the magnetizing field from (4.84).

For the numerical calculation of the reluctivity tensor, the quantities  $\Delta M$  and  $\Delta B$  are computed:

$$\Delta M = M_{h^*, b_{j+1}} - M_{h^*, b_j} \quad \Delta B = b_{j+1} - b_j \quad (4.88)$$

and the incremental reluctivity becomes:

$$\bar{\nu}_d = \begin{pmatrix} \nu_0 - \frac{\Delta M}{\Delta B} & 0 & 0 \\ 0 & \nu_0 & 0 \\ 0 & 0 & \nu_0 \end{pmatrix} \quad (4.89)$$

### PM algorithm

The material algorithm scheme is depicted in Fig. 4.36. The magnet easy axis is the vector  $\vec{\mathbf{e}}_{\mathbf{m}}$ , and along the hard axis the magnetic field is supposed to grow linearly as  $\mathbf{H}_{\perp} = \nu \cdot \mathbf{B}_{\perp}$ . According to Fig. 4.35, the blue path indicates the virgin magnetization, the red path indicates the PM demagnetization and the green path indicates the recoil line. The variable *ind* keeps

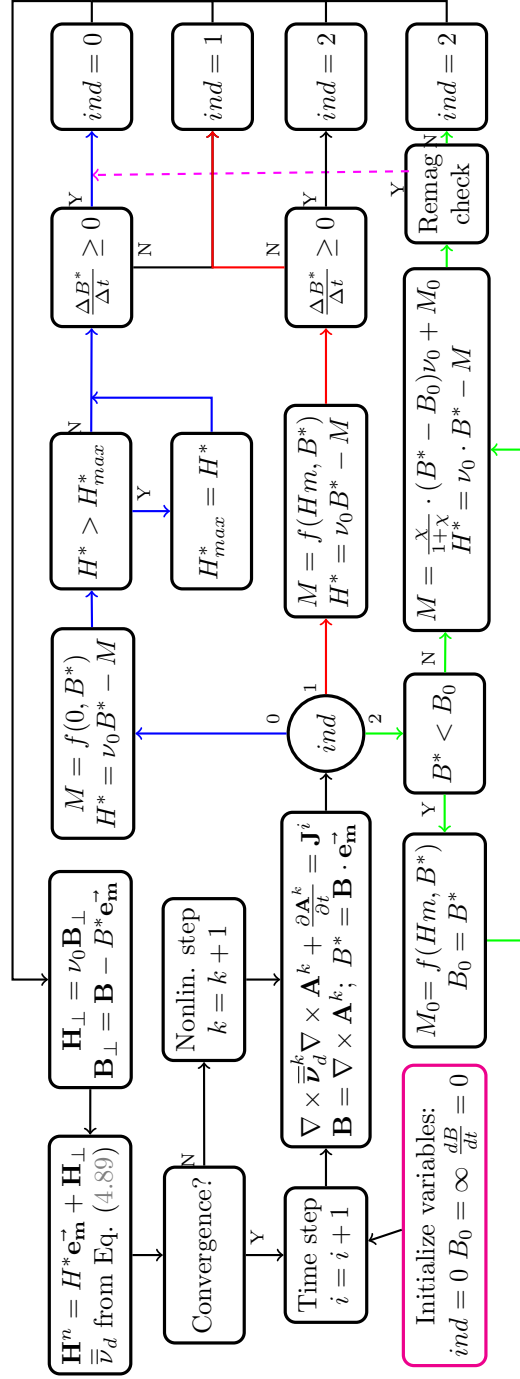


FIGURE 4.36: Block diagram of the algorithm. The blue path represents the virgin magnetization, the red path represents the demagnetization, the green path represent the recoil. The magnet easy axis is denoted by the vector  $\mathbf{e}_m^*$ . The magenta-dashed line represents the approximation adopted in this Section for re-magnetization, since the measurements of the whole PM minor loops are not available.

memory of the previous PM state:  $ind = 0$  is associated to the virgin state,  $ind = 1$  when the PM is demagnetized the first time and  $ind = 2$  when the magnet recoils. The variable  $ind$  switches its state when the time derivative of flux the density along the magnetization axis changes sign. The last state is the recoil one where the magnet normally remains trapped. However, in principle both further demagnetization or a re-magnetization are possible. In the former case a new working point will be reached on a parallel but lower recoil line, while in the latter case, typical of multi-step magnetization procedures (see test case 4.5.4) a different scenario occurs. The block *Remag. Check* accounts for this case and allows to switch from the recoil line (green line in Fig.4.35) to the re-magnetization curve, referred as *Reversal approx.* in Fig. 4.35. In this Section the measurements of the first reversal curves are assumed not be available, thus the re-magnetization curve is approximated with a linear recoil line until the intersection with the virgin curve (green curve Fig. 4.35) and with the virgin curve itself as the magnetic field further increases (dashed magenta curve in Fig. 4.35). This approximation is adopted only in the test cases where the PM magnetization is obtained through multiple steps, e.g. Sec. 4.5.4, while usually the PM works along the recoil line only. If minor-loop measurements are available they can be used within this material model instead of the proposed simplified approach, however when the main focus of the simulation are the minor loops, full hysteresis models should be preferred because of their higher accuracy.

When the time derivatives  $\frac{\Delta B^*}{\Delta t}$  have to be computed at the  $i^{th}$  time step, the last nonlinear step flux density  $\mathbf{B}$  and the last converged solution from the previous time step  $\mathbf{B}_{conv}$  are considered in order to avoid wrong detections due to the Newton-Raphson iterative scheme. The time derivative is therefore approximated as  $\frac{\Delta B^*}{\Delta t} = \frac{\mathbf{B} - \mathbf{B}_{conv}}{\Delta t} \cdot \mathbf{e}_m^* = \frac{B^* - B_{conv}^*}{\Delta t}$ , where  $\Delta t$  is the time step and the \* apex denotes the vector projections along the PM easy direction.

The model outputs are the new magnetic field  $\mathbf{H}^n$  and the differential reluctivity  $\bar{\nu}_d$ . After each nonlinear step  $k$  at time  $i$ , the convergence of the scheme is checked through a residual norm estimation; if the check fails the algorithm proceeds with the subsequent nonlinear iteration  $k+1$ , otherwise the time step counter is incremented.

It is worth noting that the proposed PM non-linear scheme can be adopted for arbitrary permanent magnets, once measurements of demagnetization curves are available and the PM saturation and anisotropy model are known.

## 4.5.2 Comsol implementation and results

In order to demonstrate the applicability of the proposed approach within the framework of existing FEM codes, the model depicted in Fig. 4.36 has been implemented in Comsol Multiphysics through an external material class written in C. This ensures a fast compiled function that does not create bottlenecks during the simulation. Several state variables have been introduced for the communication between the finite element solver and the external material class, as visible in Tab. 4.9). The state variables are domain variables computed and stored in each finite element belonging to a PM, while the parameters are global immutable variables. Concerning the solver

TABLE 4.9: List of state variables and parameters.

Variable	Symbol	Description
1	$\mathbf{B}_{conv}$	Flux density of previous time step
2	$\mathbf{B}$	Current iteration flux density
3	$\mathbf{H}$	Current iteration magnetic field
4	$\bar{\nu}_d$	Computed differential reluctivity
5	$H_{max}^*$	Max. magnetic field in magn. direction
6	$\Delta t$	Time step
7	$M_0$	Saved recoil magnetization
8	$B_0$	Saved recoil flux density
9	$\mathbf{H}^n$	New iteration mag. field
Param.	Symbol	Description
1	$\mathbf{e}_m^*$	PM Easy direction axis
2	$\chi$	Recoil slope of MH curve

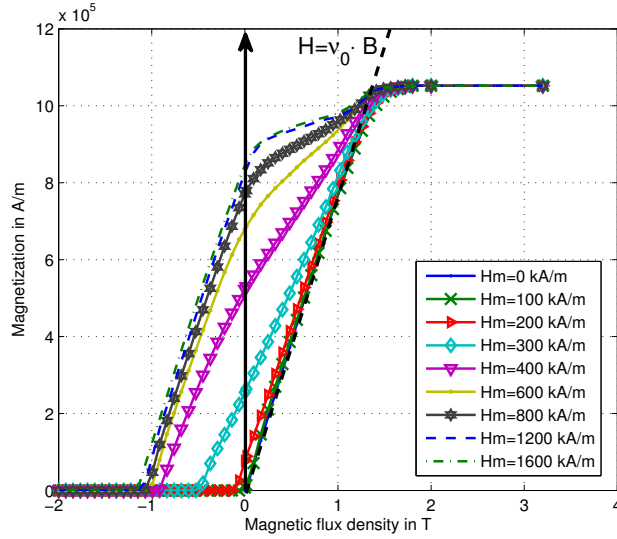


FIGURE 4.37: Magnetization against magnetic flux density for different magnetizing fields  $Hm$ . The data are retrieved from [141]: the soft magnetic behaviour is visible especially for high magnetizing field strength.

settings, in order to ensure stability, linear shape functions have been adopted and the tolerance on the norm of the residual has been fixed to  $toll = 1e - 5$ . The time dependent problem have been solved adopting the backward Euler formula with order five and self-adjusted time step.

Fig. 4.37 shows the magnetization curves as a function of the magnetic flux density for different magnetizing fields. The data has been fitted from [141] for a NdFeB magnet with grade N38, remanence  $Br = 1.25$  T, maximum energy  $BH = 310$  kJ/m<sup>3</sup>, resistivity  $\rho = 1.44$   $\mu\Omega m$ . The relative permeability during recoil is assumed to be constant and equal to  $\mu = 1.05 \cdot \mu_0$ .

### 4.5.3 Temperature dependence

Since the proposed material class is based on measurement interpolation, the temperature can be easily added as additional variable. In this case the measurement matrix  $M_{meas}$  is a 3D matrix:

$$M_{meas} = \begin{array}{c} \begin{array}{ccc} & & M_{h_0, b_0, T_1} \dots M_{h_0, b_n, T_1} \\ & M_{h_0, b_0, T_2} \dots M_{h_0, b_n, T_2} & b_n, T_1 \\ M_{h_0, b_0, T_3} \dots M_{h_0, b_n, T_3} & & b_n, T_2 \\ M_{h_k, b_0, T_3} \dots M_{h_k, b_n, T_3} & & b_n, T_3 \end{array} \end{array}$$

Adapting the scheme in Fig. 4.36, the recoil procedure can be triggered when permanent demagnetization has occurred because of the temperature. The dependence of the PM properties with the temperature can have an important role during the simulation of electrical machines, but the studies are assumed to be temperature independent because of the time scale of the current pulse.

### 4.5.4 Model validation

In this Chapter two experimental validations of the proposed method are reported: the former refers to a two-step magnetization of an electrical machine rotor through a fractional slot stator, while the latter refers to the magnetization of an axis-symmetric PM through a conventional winding. Both test cases show that the simulation results are in agreement with the experimental data.

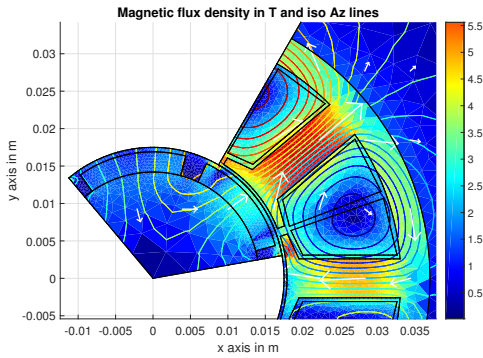


FIGURE 4.38: Radial magnetic flux density colormap and  $A_z$  contour at the current peak for the test case in [142]. The three parallel winding connection suggested in [142] has been chosen.

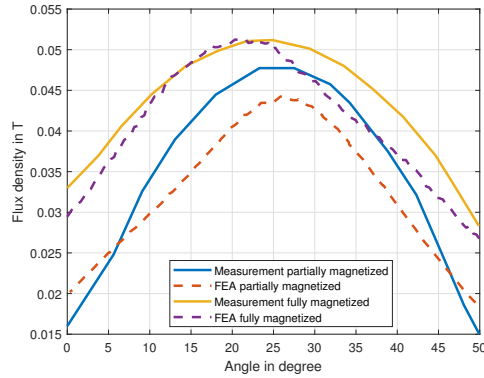


FIGURE 4.39: Comparison between the simulation results and the measurements in [142]. The partial magnetization is obtained through two consecutive pulses with amplitude  $|I_{max}| = 867$  A, the full one is obtained with  $|I_{max}| = 1334$  A.

### Two-step post assembly magnetization

[142] describes a two-step magnetization procedure of rare-earth PMs through a fractional slot stator and reports the post-assembly magnetization measurements after extracting the magnets from the machine. In order to model the procedure and ensuing measurements, the PM demagnetization curves, geometries and current values have been retrieved from [142]. In Fig. 4.38, the magnetic flux density at the first current peak with amplitude  $I_{max} = 1334$  A is shown: the ferromagnetic material of the stator is fully saturated and the magnets are not equally magnetized as expected, i.e. the one on the right has a much stronger magnetization. The flux density peak reaches the value  $B_p = 5.76$  T, which is normal in the soft iron parts during the pulse magnetization of rare-earth PMs. The nonlinear iron adopted is a standard one with initial relative permeability  $\mu_r = 1200$  and saturation  $B_s = 2.1$  T.

Fig. 4.39 shows the comparison between the measurements and the simulation of the magnetic flux density along the line reported in [142] after the second magnetization step and extraction from the machine at two different current peak values. The computed results match the measurements reasonably well, even if some discrepancies, in the order of 15% on average, can be observed. These are due to, among others, the limited knowledge on the ferromagnetic material of the stator, on the full PM hysteresis loop cycles and on the feeding current profile. Since the curves in [142] are only given for the virgin magnetization and for the demagnetization (first and second quadrants in the BH plane), the re-magnetization curve has been supposed to be the virgin curve (see 4.5.1). This latter approximation is mainly responsible for the mismatch of Fig. 4.39. It is worth noting that according to both measurements and simulations the flux density is asymmetric.

### Axisymmetric PM magnetizer

The geometry proposed in [141] is adopted here as an example of magnetization, demagnetization and recoil phenomena for a NdFeB permanent magnet. The results of the proposed material model have been compared with the measurements in [93] showing good agreement. Fig. 4.40 shows the geometry retrieved from [141]: the model is axis-symmetric and the coil consist of  $N = 440$  turns. Fig. 4.42 shows the comparison, already shown in [93], between the measurements and the simulation results for two points  $Q1$  and  $Q2$  close to the surface of the PM, on the edge and on the axis, respectively. The measurements and the simulations have been run changing the feeding voltage. The results match even if some discrepancies can be observed, especially in the centre of the permanent magnet. In this benchmark the causes for the discrepancies are the missing information of the demagnetization curves in the first quadrant and the missing information of the exact  $z$  coordinates of  $Q1$  and  $Q2$  which are not specified in [141]. Furthermore, in [141] a mismatch of 12% in the peak flux density was observed between measurements and FEM

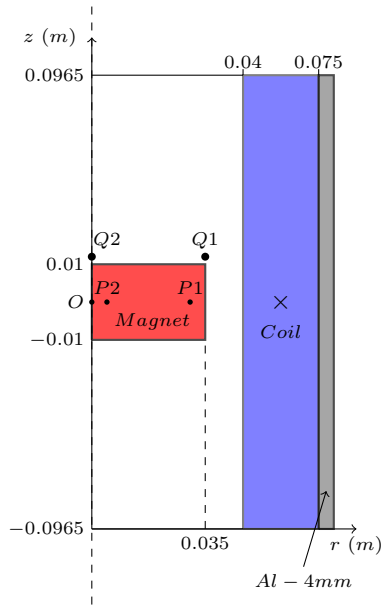


FIGURE 4.40: Pulse magnetizer test case taken from [141] and [93]. The model is axisymmetric and the coil is composed by  $N = 440$  turns.

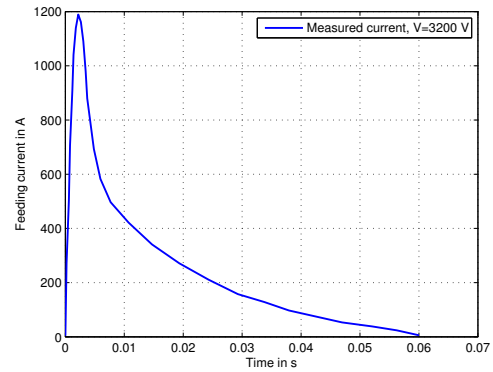


FIGURE 4.41: Magnetic flux density at the end of current pulse. Contour lines: iso  $A\phi$  lines in Wb/m. Color map: magnetic flux density in T. Arrow plot: magnetic flux density vector plot.

simulations and the source of the discrepancy was attributed to be the Hall sensor fluxmeter. An additional mismatch of 10% was found between the simulated and measured current values because of the accuracy of parameters in the lumped model. Because of these reasons, and since the flux density in the centre is more challenging to be computed because the eddy current effects and self-demagnetization are severe on the magnet axis, the simulation in Fig. 4.42 provides a qualitative validation which is fully acceptable.

In the benchmark of Figs. 4.43 and 4.44, which differs from the one presented in [93], an initial positive magnetization pulse is followed by two smaller negative pulses, as shown in Fig. 4.43. Since the second negative current peak is greater than the first, two distinct recoil lines are expected.

Fig. 4.44 shows the BH characteristics for the points  $P1$  and  $P2$  depicted in Fig. 4.40. The point  $P1$  is close to the magnetizing winding therefore the magnetic flux density reached during the magnetization is  $B_m = 2.7$  T while the maximum field reached in  $P2$  is  $B_m = 2.3$  T. This non-uniform distribution leads to different magnetization levels inside the PM domain and the

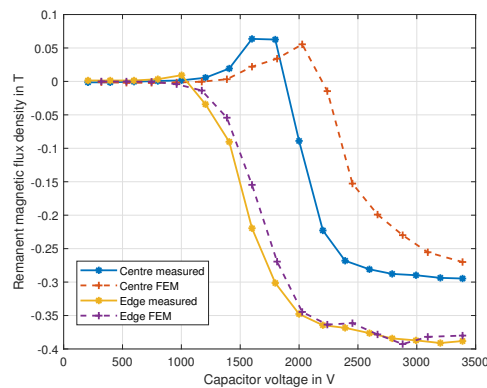


FIGURE 4.42: Comparison between the measured and simulated  $z$  components of the magnetic flux density at point  $Q2$  on the PM axis and at point  $Q1$  on the PM edge. For further details, the reader is referred to [93].

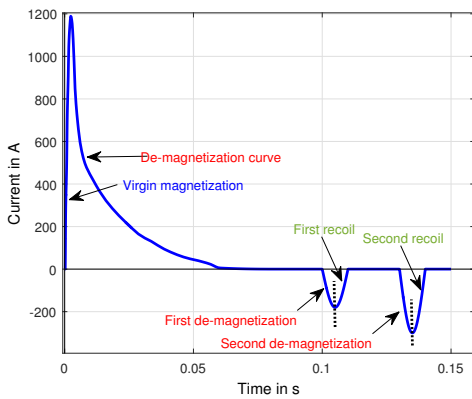


FIGURE 4.43: Current waveform adopted for testing the PM model: from  $t = 0$  to  $t = 0.1$  s the magnet is magnetized. After  $t = 0.1$  s two successive negative current pulses are applied to test the magnet with increasing amplitude. Labels color are in accordance with Fig. 4.36.

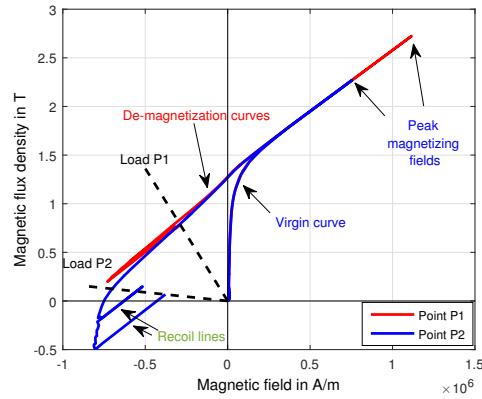


FIGURE 4.44: Simulated  $B_z H_z$  characteristics of two points of the geometry from [141]. The points load lines are also depicted. The effect of induced eddy currents is also visible: the point  $P2$  first recoil line exceed the load line because of the sudden change in the sinusoidal pulse, while the opposite happens for the point  $P1$ .

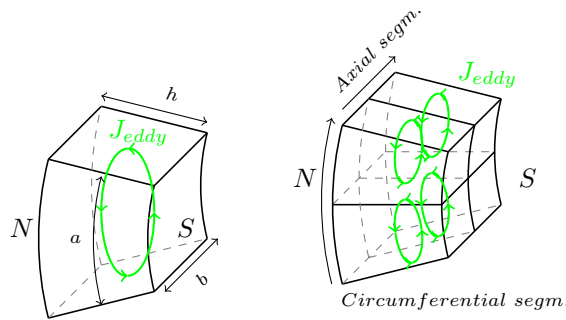


FIGURE 4.45: Example of magnet segmentation along axial and circumferential axis. Normally the magnet curvature is low therefore the equivalent linear magnet model is considered in this analysis based on the dimensions  $a, b$  and  $h$ .

regions near the magnet axis are subject to lower magnetization. This is clear in the second quadrant when the negative current pulses occur: the recoil lines of the point  $P1$  are almost coincident with the demagnetization line itself, but in the point  $P2$  the demagnetization due to the negative current pulses is more visible. The load lines at the end of the simulation are also depicted in Fig. 4.44: since the PM is wide, the central points tends to be demagnetized by the outer regions.

#### 4.5.5 Magnetic gear test case

This example refers to a device, a magnetic gear, characterized by a fairly complex geometry. In such devices the easiest way to reduce the losses consists in magnet segmentation similarly to the approach of laminating ferromagnetic parts. Fig. 4.45 shows the example of a solid magnet and of a segmented one. The segmentations are circumferential and axial since the cuts have to be tangential to the magnetic flux density.

Considering the geometry depicted in Fig. 4.45 where  $b > a$ , from Maxwell's laws:

$$\int_l \mathbf{E} \cdot \mathbf{t} dl = -\frac{\partial}{\partial t} \int_S \mathbf{B} \cdot \mathbf{u}_n dS \quad (4.90)$$



where  $\mathbf{E}$  is the induced electric field and  $\mathbf{B}$  is the magnetic flux density. Adopting the hypothesis of constant  $\mathbf{B}$  on the magnet surface, the electric field integral becomes [143]:

$$U = \int_l \mathbf{E} \cdot \mathbf{t} dl = -\frac{\partial B}{\partial t} \cdot a \cdot b \quad (4.91)$$

The resistance considering the hypothesis of negligible skin depth effect and assuming an even current distribution can be calculated as:

$$R = \rho \frac{\text{length}}{\text{Section}} = \rho \cdot \left( \frac{a}{\frac{bh}{2}} + \frac{b}{\frac{ah}{2}} \right) = \frac{\rho}{h} \cdot \left( \frac{2a}{b} + \frac{2b}{a} \right) \quad (4.92)$$

The power loss can be calculated as:

$$P = \frac{U^2}{R} = \left( \frac{\partial B}{\partial t} \right)^2 \frac{a^2 b^2 h}{\rho \left( \frac{2a}{b} + \frac{2b}{a} \right)} = \left( \frac{\partial B}{\partial t} \right)^2 \frac{a^3 b^3 h}{2\rho \cdot (a^2 + b^2)} \quad (4.93)$$

From (4.93) the power losses are linearly proportional to the magnets thickness  $h$ . This means that magnet segmentations normal to the magnetic flux density do not affect the losses. Since the commercial magnet shapes have limited geometrical ratios, the magnet can be cut along the circumferential direction without increasing the losses.

The result obtained in (4.93) is a simple relation that considers the current flowing into a rectangular loop with size  $\frac{1}{2}$  of the magnet edges. If different current paths are considered the power loss changes; the key factors are the dependencies between the power loss and the geometrical parameters, which remain unaltered.

In the case of axial segmentation the power loss is:

$$\begin{aligned} P_{axial} &= n_{axial} \cdot \left( \frac{\partial B}{\partial t} \right)^2 \cdot \frac{a^3 b^3 h}{2\rho \cdot n_{axial}^3 \cdot \left( a^2 + \frac{b^2}{n_{axial}^2} \right)} \\ &= \left( \frac{\partial B}{\partial t} \right)^2 \cdot \frac{a^3 b^3 h}{2\rho \cdot (n_{axial}^2 \cdot a^2 + b^2)} \end{aligned} \quad (4.94)$$

where  $n_{axial}$  is the number of axial segments. From (4.94) the axial segmentation produces negligible effects if the magnets have a rather elongated shape, while when  $n_{axial}^2 \cdot a^2 \simeq b^2$  the axial segmentation effects are more visible.

A similar formula can be found in case of circumferential segmentation:

$$\begin{aligned} P_{circ} &= n_{circ} \cdot \left( \frac{\partial B}{\partial t} \right)^2 \cdot \frac{a^3 b^3 h}{2\rho \cdot n_{circ}^3 \cdot \left( b^2 + \frac{a^2}{n_{circ}^2} \right)} \\ &= \left( \frac{\partial B}{\partial t} \right)^2 \cdot \frac{a^3 b^3 h}{2\rho \cdot (n_{circ}^2 \cdot b^2 + a^2)} \end{aligned} \quad (4.95)$$

where  $n_{circ}$  is the number of circumferential segments. From (4.95) the advantage given by this kind of segmentation is clearly visible:  $n_{circ}^2 \cdot b^2 > a$  according to the previous hypothesis and therefore the power losses are proportional to  $\frac{1}{n_{circ}^2}$  when  $n_{circ}^2 \cdot b^2 \gg a$ . The effectiveness of (4.95) is proven in Sec. 4.8, where the equation is used to fit the PMs losses in 3D finite element simulations.

Considering 2D simulations the circumferential and radial segmentation can be taken into account but the axial segmentation requires a further modification. Since the power loss is related to  $\rho$ , an artificial magnet resistivity  $\rho'$  can be used in order to consider the axial segmentation:

$$\rho' = \rho \cdot \frac{n_{axial}^2 \cdot a^2 + b^2}{a^2 + b^2} \quad (4.96)$$

The limitations of the magnets segmentation are discussed in [144]: above a certain number of segments the eddy currents increase and therefore an optimal magnet segmentation size exists.

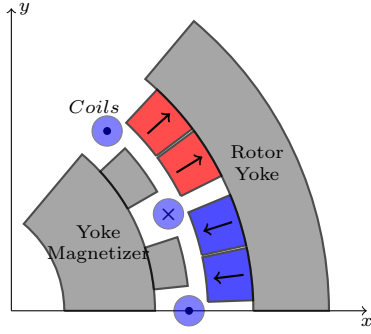


FIGURE 4.46: Test case geometry of magnetic gear external rotor with segmented magnets with back yoke. The coils are constituted by  $N = 10$  turns and the magnetizing current has the same shape of the one in Fig. 4.43 between  $t = 0$  and  $t = 0.1$  s but the peak is scaled to  $I_{peak} = 3$  kA.

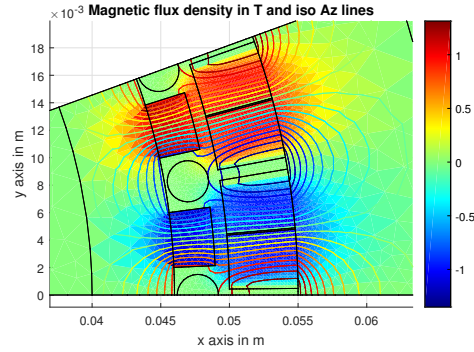


FIGURE 4.47: Radial magnetic flux density colormap and  $A_z$  isolines after the rotor magnetization.

The main drawback related to segmentation is the mechanical assembly that is complicated due to the small size of the magnets and the repelling forces acting between the segments. In this case the benefit of the PMs a-posteriori magnetization is clear.

The test case geometry of a rotor magnetizer for high segmented poles is shown in Fig. 4.46: only two segments are displayed but the number of segments can be arbitrary. A magnetizing yoke made with the steel 35JN200 with saturation  $B_s = 1.73$  T is adopted in order to limit the feeding current.

Fig. 4.47 shows the magnetic flux density plot and the flux lines when the current pulse is completed: the distribution is symmetric and the edges are subject to low flux density.

Fig. 4.48 shows the magnetic flux density at the current peak. Since the iron is saturated the flux lines are distributed differently than Fig. 4.47; the higher magnetization is obtained close to the magnetizer teeth, where the magnetic flux density is higher.

Fig. 4.49 shows the magnetization in the permanent magnets: the current with this magnetizer geometry is not sufficient to achieve a good level of magnetization especially in the regions near to the outer edges. The design of the magnetizer can be optimized in order to maximize the field obtained in the PM domains and minimizing the energy stored in the capacitor bank; the variables of the search space are geometrical dimensions, materials and currents (capacitor voltages).

#### 4.5.6 Demagnetization in magnetic gears

The intrinsic coercive force  $H_{ci}$  is a key parameter in order to evaluate limit working conditions of the permanent magnets.  $H_{ci}$  decays linearly with the temperature according to:

$$H_{ci}|^T = H_{ci}|^{T_0} \cdot (1 + \beta\Delta T) \quad (4.97)$$

where  $\beta$  is the material temperature dependence parameter that can be considered to be constant if the temperature ranges between  $0 - 100^\circ\text{C}$ . The magnetic flux density expression is:

$$B = \mu_0 \cdot \mu_r \cdot H + B_r \cdot (1 + \alpha\Delta T) \quad (4.98)$$

where  $B_r$  is the residual magnetic flux density,  $\alpha$  is a temperature decay parameter,  $\mu_0$  and  $\mu_r$  represent the vacuum and permanent magnet permeability. Considering the permanent magnets curves approximated as depicted in Fig. 4.50, the limit magnetic flux density  $B_{lim}$  is:

$$B_{lim} = \mu_0 \cdot \mu_r \cdot H_{ci} \cdot (1 + \beta\Delta T) + B_r \cdot (1 + \alpha\Delta T) \quad (4.99)$$

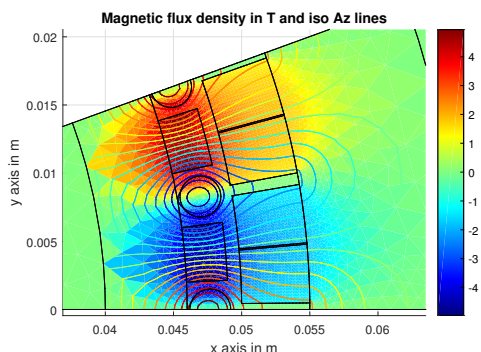


FIGURE 4.48: Radial magnetix flux density colormap and  $A_z$  isolines at the current peak ( $t = 2.3$  ms). The distribution is substantially different from the one in Fig. 4.47 because the iron is highly saturated.

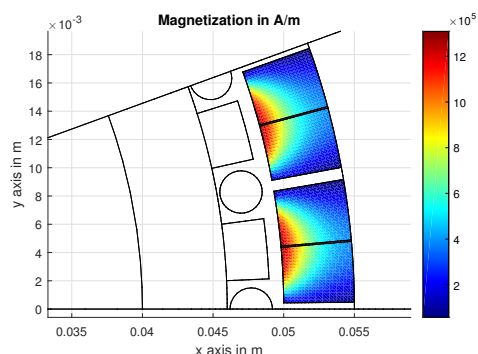


FIGURE 4.49: Elemental radial magnetization in A/m at the end of the current pulse. The regions closer to the magnetizer yoke are subjected to an higher filed while the far regions are weakly magnetized. In order to improve the magnet usage with the same magnetizer geometry, the current peak have to be higher.

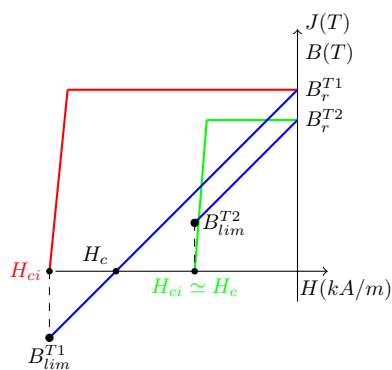


FIGURE 4.50: Permanent magnet approximated BH curves and polarization vs magnetic field curves for two different temperatures ( $T1 < T2$ ).

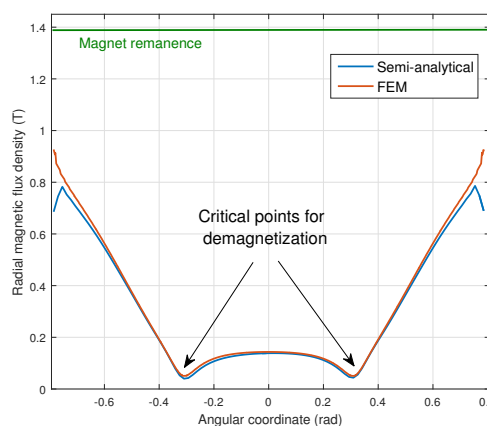


FIGURE 4.51: FEM validation of the radial magnetic flux density computed through the analytic approach for the geometry analyzed in [61]. The plot refers to an arc lying on the surface of the magnet with the lowest magnetic flux density (worst case for demagnetization).

and the maximum working temperature may be computed as:

$$T_{max} = T_0 + \frac{B_{lim} - \mu_0 \cdot \mu_r \cdot H_{ci} - Br}{\beta \cdot \mu_0 \cdot \mu_r \cdot H_{ci} + \alpha \cdot Br} \quad (4.100)$$

where  $T_0$  is the reference temperature according to the magnets datasheets. On the side of caution,  $a$  will be considered nil since  $a$  and  $b$  are both negative and  $|\alpha| < |\beta|$ . The maximum temperature then becomes:

$$T_{max} = T_0 + \frac{B_{lim} - \mu_0 \cdot \mu_r \cdot H_{ci} - Br}{\beta \cdot \mu_0 \cdot \mu_r \cdot H_{ci}} \quad (4.101)$$

In order to apply (4.101),  $B_{lim}$  has to be computed: this value is calculated from the Fourier coefficients of the magnetic vector potential  $A_z$  in the permanent magnet regions. In particular the radial magnetic flux density coincides with the magnet local working point in terms of BH curve.

Therefore, as result of magneto-static simulations  $B_{lim}$  is computed as function of the rotors positions and applying Eq. (4.101) the maximum temperature working point  $T_{max}$  can now be calculated. In order to understand if the machine cooling is sufficient, a thermal model has to be built in order to estimate the temperature  $T_{sim}$  reached in all the permanent magnet regions. If  $T_{sim} > T_{max}$ , the demagnetization constraint is not satisfied and either a permanent magnet with an higher grade need to be used or a forced cooling through the machine has to be impressed.

Fig. 4.51 shows the  $B_{lim}$  plots on the magnet-air gap interface of the most stressed magnet in the worst alignment condition between the inner and outer rotors and the iron poles. The worst alignment is the one of Fig. 5.10 on the left. In this case  $B_{lim}$  results 0.05 T and using Eq. 4.101 the maximum temperature  $T_{max}$  to avoid the permanent demagnetization can be computed. Since its calculation has been performed in the worst alignment condition,  $T_{max}$  is the limit temperature for all the inner magnets to avoid demagnetization.

High energy rare-earth magnets are nowadays applied in many applications ranging from electro-mechanical devices to sensors [141]. The virgin material magnetization requires the application of magnetic fields up to several kA/m. To achieve sufficient fields in the magnetizing coils currents in range of several hundred kA are produced by pulse magnetizers [145]. The magnetization process is the key point for obtaining high performance magnets: non-uniform patterns could lead to failures in the worst cases. It is therefore crucial to dispose of numerical tools [146] and measuring devices [147] capable of correctly assessing the physical properties of the permanent magnet subjected to a magnetization process. Some authors have adopted the classical Preisach [148] or Jiles-Atherton [149] hysteresis model to predict the behaviour of hard magnetic materials: these approaches generally works for fully (pre-)magnetized samples, while the inter-dependency of the virgin magnetization process and the demagnetization is still challenging. In this Section, a FEM-based simulation scheme that rely on interpolations of virgin-field dependent demagnetization curves is proposed. This scheme is suitable for evaluating the local magnetic flux density in all the points of the permanent magnet once the geometry and the current pulses are known.

## 4.6 Losses in ferromagnetic materials

The advantage of the magnetic gear is the absence of mechanical contacts; this means that the losses are limited only to the bearings losses, viscous losses due to the air friction and iron losses. In order to assess the torque transfer in steady state conditions and dynamic operation, it is extremely important to model all the loss contribution in magnetic transmissions. The aspect of magnetic losses evaluation is particularly difficult because the magnetic flux density locus has a rotational shape in all of the iron regions. For the magnetic gear special case, previous papers assessed power loss by measurements only [150, 151, 152] and in [153] only the losses due to eddy currents are taken into account.

This Section provides some models that can be adopted for the loss calculation in magnetic gears. In Sec. 4.6.1 the loss theoretical formulation is derived from Maxwell's equations.

Since the iron cores in magnetic gears are laminated, in order to apply (4.107) correctly the sheet conductivity  $\sigma$  and the power loss expression should be modified as shown in Sec. 4.6.2.

Sec. 4.6.3 shows instead one of the classical empirically-based approach normally adopted for the electrical machines case, where the flux loci exhibit traces less rotational than the magnetic gear case.

In Sec. 4.6.4 an approach still based on the loss separation method is adopted, but its formulation is tailored for general rotational loci.

### 4.6.1 Theoretical formulation

Losses in ferromagnetic materials such as nickel, iron and alloys can be derived using Maxwell's equations and Poynting's theorem.

$$\begin{cases} \nabla \times \mathbf{E}(t) = -\frac{\partial \mathbf{B}(t)}{\partial t} \\ \nabla \times \mathbf{H}(t) = \mathbf{J}(t) \end{cases} \quad (4.102)$$

The energy that flows inside a volume can be calculated according to the Poynting's theorem:

$$U = \frac{1}{2} \int_V (\mathbf{E} \cdot \mathbf{D} + \mathbf{B} \cdot \mathbf{H}) dV \quad (4.103)$$

$$\frac{\partial U}{\partial t} = - \int_{\partial V} (\mathbf{E} \times \mathbf{H}) dS - \int_V \mathbf{E} \cdot \mathbf{J} dV = - \int_V \nabla \cdot (\mathbf{E} \times \mathbf{H}) dV \quad (4.104)$$

where  $U$  is the energy and the term  $\mathbf{E} \cdot \mathbf{J}$  can be neglected if there are no charges inside the material (hypothesis of perfect conductor). Using the vector identity:

$$\nabla \cdot (\mathbf{A} \times \mathbf{B}) = (\nabla \times \mathbf{A}) \cdot \mathbf{B} - \mathbf{A} \cdot (\nabla \times \mathbf{B}) \quad (4.105)$$

the energy per unit time which flows inside the material can be rewritten as:

$$- \int_V \nabla \cdot (\mathbf{E} \times \mathbf{H}) dV = \int_V \left( \mathbf{H}(t) \frac{\partial \mathbf{B}(t)}{\partial t} + \mathbf{E}(t) \cdot \mathbf{J}(t) \right) dV \quad (4.106)$$

Considering a magnetic flux density variation  $\frac{d\mathbf{B}(t)}{dt}$  and if the material properties are isotropic, the vectorial relation becomes a scalar one:

$$\frac{\partial U}{\partial t} = \int_V \left( H \frac{dB}{dt} + \rho J^2 \right) dV \quad (4.107)$$

However the behaviour of the iron materials is hysteretic as shown in Secs. 4.4 and 4.5 and when rotational fields are applied the magnetic flux density lags the magnetic field. The hysteresis phenomena is related to rotation and movement of magnetic domains and depends on the material properties. Because of the complexity of hysteresis model, the common practice is to use empirical formulas for the losses estimation in electrical machines.

### 4.6.2 Lamination effect

Another challenge that has to be faced to estimate the iron losses is the iron lamination. In order to reduce the eddy current losses, many insulated sheets are stacked together and the result is a reduced section where the currents are induced. The lamination modelling is a challenging task in FEA analysis since the reproduction of all the iron sheets geometry would produce an huge mesh. Some formulations have been proposed in order to overcome these aspects and the simplest idea is to introduce an anisotropic conductivity and permeability as suggested in [33].

$$[\sigma] = \begin{bmatrix} \sigma_x & & \\ & \sigma_y & \\ & & \sigma_z \end{bmatrix} = \begin{bmatrix} F\sigma & & \\ & \sigma' & \\ & & F\sigma \end{bmatrix} \quad (4.108)$$

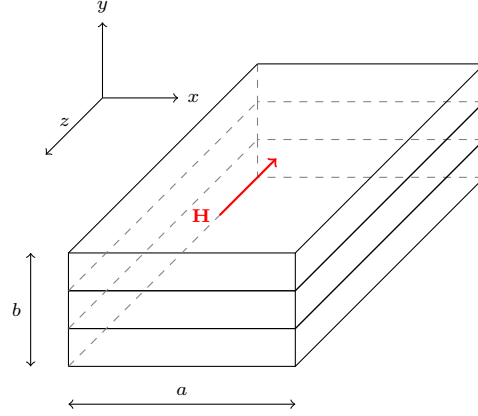


FIGURE 4.52: Example of laminated iron.

$$[\mu] = \begin{bmatrix} \mu_x & & \\ & \mu_y & \\ & & \mu_z \end{bmatrix} = \begin{bmatrix} (1-F)\mu_0 + F\mu_{Fe} & & \\ & \frac{\mu_{Fe}}{F + \frac{(1-F)\mu_{Fe}}{\mu_0}} & \\ & & (1-F)\mu_0 + F\mu_{Fe} \end{bmatrix} \quad (4.109)$$

In (4.108) and (4.109) the lamination direction is along the  $y$  axis according to Fig. 4.52;  $F$  is the stacking factor. From (4.102) developing the curls:

$$\frac{\partial H_z}{\partial y} = \sigma_x E_x \quad \frac{\partial H_z}{\partial x} = -\sigma_y E_y \quad (4.110)$$

Considering the eddy currents to have only  $x$  component,  $H_z$  is uniform along  $x$ . In a single iron sheet the boundary condition is:

$$H_z(y)|_{y=\pm d/2} = H_0 \quad (4.111)$$

Substituting the Maxwell equations the 1D differential equation is obtained:

$$\frac{\partial^2 H_z}{\partial y^2} = j\omega\mu_z\sigma H_z \quad (4.112)$$

Solving the equation and applying the Poynting's theorem the specific power loss becomes:

$$p = \frac{H_0^2 \xi}{\sigma d^2} \cdot \frac{\sinh \xi - \sin \xi}{\cosh \xi - \cos \xi} \quad (4.113)$$

where

$$\xi = \frac{d}{\sqrt{\frac{2}{\omega\mu_z\sigma}}} \quad (4.114)$$

In [33] under the low-frequency approximation the equivalent conductivity is:

$$\sigma' = \frac{1}{F} \left(\frac{d}{a}\right)^2 \cdot \sigma \quad (4.115)$$

Equation (4.115) can be applied when solving simple cases such as transformer cores or eddy current problems in cylindrical coordinates when the induced current is of the type  $\mathbf{J} = [0, J_\phi, 0]$ . When studying electrical machines the problem is more complicated and equation (4.115) cannot be applied, thus in this case the common approach is to use a-posteriori procedures where the losses effect on the simulations are neglected. This is for example the case of Secs. 4.6.3 and 4.6.4.

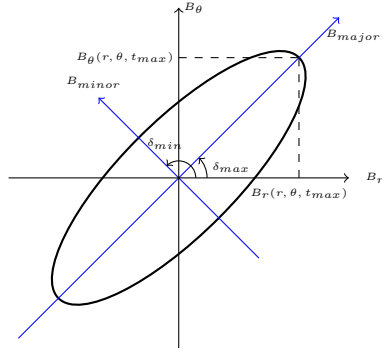
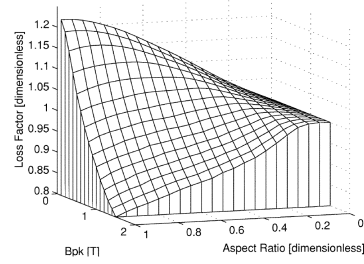


FIGURE 4.53: Elliptic flux loci: major and minor axis.

FIGURE 4.54: Knockman  $\gamma$  parameter.

### 4.6.3 Generalized Steinmetz's equation model

Generally, Steinmetz empirical formulas are adopted in order to compute the losses associated to ferromagnetic components. The most common equation is:

$$P_{iron} = K \cdot f^\alpha \cdot B^\beta \quad (4.116)$$

where  $B = \mu \cdot H$  is the magnetic flux density,  $f$  the frequency and  $K$  is a material constant. This approach is valid in the hypothesis of sinusoidally varying magnetic field with frequency  $f$ . In the case of magnetic gears the hypothesis of sinusoidal single frequency waveforms is not valid: according to Sec. 4.1, the harmonic responsible of the torque transmission is not the only one that appears. This is especially true inside the iron poles, where the flux loci exhibit a rotational behaviour (see Figs. 4.9 and 4.31). In order to avoid the frequency and equivalent frequency based models, the Generalized Steinmetz equation (GSE) has been chosen for the inner and outer iron yokes [154]:

$$P = \frac{1}{T} \int_0^T k \left| \frac{dB}{dt} \right|^\alpha \cdot |B(t)|^{\beta-\alpha} dt \quad (4.117)$$

where  $\alpha$  and  $\beta$  are experimental coefficients and:

$$k = \frac{K}{2\pi^{(\alpha-1)} \cdot \int_0^{2\pi} |\cos \theta|^\alpha \cdot |\sin \theta|^{\beta-\alpha} d\theta} \quad (4.118)$$

where  $K$  is the coefficient of the classical Steinmetz approach. The magnetic flux densities are known inside the iron regions, therefore using several magneto-static simulations the derivative term  $\left| \frac{dB}{dt} \right|$  can be computed using the central difference approach:

$$\left| \frac{dB}{dt} \right|_t = \frac{B_{t+1} - B_{t-1}}{2 \cdot \Delta t} \quad (4.119)$$

In the iron poles the losses are calculated according to an approach based on an experimental coefficient  $\gamma$  [155]:

$$\gamma = \frac{P(a, B_{major})}{P_0(B_{major}) + P_{90}(aB_{major})} \quad (4.120)$$

where  $a$  is the ratio between  $B_{minor}$  and  $B_{major}$ ,  $P$  is the power loss produced by an elliptical field,  $P_0$  are the losses produced by an alternating magnetic field parallel to the rolling direction and  $P_{90}$  are the losses produced by an alternating magnetic field perpendicular to the rolling direction. The magnetic flux densities are known in cylindrical coordinates, therefore for each point of the grid the major and minor flux densities have to be calculated. Considering the flux

Material	$k$	$\alpha$	$\beta$	$k - range$	$\alpha - range$	$\beta - range$
NO10	0.0017	1.425	1.759	0.0013 – 0.0022	1.396 – 1.454	1.724 – 1.794
NO20	0.001527	1.506	1.797	0.00126 – 0.0018	1.485 – 1.528	1.772 – 1.822
NO20-1200	0.00077	1.583	1.908	0.00063 – 0.00091	1.56 – 1.606	1.883 – 1.934
Hiperco 50 0.15	0.0012	1.506	1.836	0.0006 – 0.0018	1.439 – 1.573	1.747 – 1.924

TABLE 4.10: Steinmetz coefficients examples.

loci to be elliptical:

$$\begin{cases} B_{major}(r, \theta) = \max_t \sqrt{(B_r(r, \theta, t))^2 + B_\theta(r, \theta, t)^2} \\ B_{minor}(r, \theta) = \min_t \sqrt{(B_r(r, \theta, t))^2 + B_\theta(r, \theta, t)^2} \\ \delta_{max}(r, \theta) = \arctan_2 \frac{B_\theta(r, \theta, t_{max})}{B_r(r, \theta, t_{max})} \\ \delta_{min}(r, \theta) = \arctan_2 \frac{B_\theta(r, \theta, t_{min})}{B_r(r, \theta, t_{min})} \end{cases} \quad (4.121)$$

The term  $|\frac{dB}{dt}|$  can be computed along minor and major axis using (4.119). According to (4.117) and (4.120), the iron poles losses are computed as:

$$P = \gamma \cdot (P_0(B_{major}) + P_{90}(B_{minor})) \quad (4.122)$$

As example, some Steinmetz empirical coefficients have been found fitting the losses data for three non oriented electrical steels (data retrived from [156]) and also for an high saturation material. The fitting expression is the conventional Steinmetz equation (4.116). The fit results are depicted in Tab. 4.10. These coefficients are the basis to apply the MSE approach.

#### 4.6.4 2D Rotational loss model

In this section a more precise loss model tailored for rotational loci is adopted.

The formulation of a comprehensive two-dimensional magnetic hysteresis model of magnetic sheets by which the loss might be calculated under arbitrary polarization loci (alternating, circular, elliptical, etc.) and time behavior has been accomplished to little extent so far. However, a rational approach to the 2D magnetic losses and their frequency dependence can be pursued in non-oriented steel (NO) sheets following the method proposed in [157] and [158]. This method is based on the concept of loss separation, by which the total loss  $W$  is expressed as:

$$W = W_{hyst} + W_{exc} + W_{class}, \quad (4.123)$$

the sum of the hysteresis, excess, and classical components, and the connection with their unidirectional (scalar) counterpart by an equivalent ellipsoid. Following this approach, the hysteresis loss for a given elliptical flux locus is expressed as:

$$W_{hyst}(J_p, a) \simeq W_{hyst}^{(ALT)}(J_p) + W_{hyst}^{(ALT)}(aJ_p)(R_{hyst}(J_p) - 1) \quad (4.124)$$

where  $R_{hyst} = W_{hyst}^{(ROT)}/W_{hyst}^{(ALT)}$  is the experimental ratio between the hysteresis losses obtained under circular and alternating polarization,  $J_p$ , expressed as  $J_p = B_p - \mu_0 H_p$ , is the peak polarization measured along the major axis of the ellipse, and  $a$  is the ratio between minor to major axis lengths. If  $a = 0$  only alternating loss are present while  $a = 1$  means purely rotating loss. Fig. 4.55 shows the experimental behavior of  $W_{hyst}^{(ROT)}$ ,  $W_{hyst}^{(ALT)}$  and the ensuing ratio  $R_{hyst}(J_p)$  versus  $J_p/J_s$  for a non-oriented Fe-(3.2 wt%)Si sheet, thickness  $d = 0.356$  mm, electrical conductivity  $\sigma = 2.04$  MS/m, density  $\delta = 7650$  kg/m<sup>3</sup>, and saturation polarization  $J_s = 2.01$  T. The experimental data are retrieved from [159]. It is worth noting that, as demonstrated in [160], the ratio  $R_{hyst}(J_p)$  can be assumed as generally valid for any ferromagnetic material at different sheet thicknesses and lamination types.



The excess loss is expressed as:

$$W_{\text{exc}}(J_p, a, f) \simeq g(a) \frac{\sqrt{f}}{\sqrt{f_0}} \cdot \left\{ W_{\text{exc}}^{(ALT)}(J_p, f_0) + W_{\text{exc}}^{(ALT)}(aJ_p, f_0) \left[ \frac{R_{\text{exc}}(J_p)}{g(1)} - 1 \right] \right\} \quad (4.125)$$

where  $W_{\text{exc}}^{(ALT)}(J_p, f_0)$  is the excess loss obtained under alternating conditions at peak polarization  $J_p$  and at the reference frequency  $f_0 = 50$  Hz,  $R_{\text{exc}}(J_p)$  is the experimental ratio, at a given frequency, between the excess losses obtained under circular and alternating polarization and the function:

$$g(a) = \frac{\sqrt{2\pi}}{8.76} \int_0^{2\pi} (\sin^2(\varphi) + a^2 \cos^2(\varphi))^{3/4} d\varphi \quad (4.126)$$

The function  $g(a)$  calculated for circular polarization ( $a = 1$ ) is  $g(1) = 1.8$ . Fig. 4.56 shows, for the same material, the experimental behavior of  $W_{\text{exc}}^{(ROT)}$ ,  $W_{\text{exc}}^{(ALT)}$  and their ratio  $R_{\text{exc}}(J_p)$  versus  $J_p/J_s$  [159]. It is worth noting that the ratio  $R_{\text{exc}}(J_p)$  is to a good extent independent of the frequency.

The classical loss, under negligible skin effect, at frequency  $f$  is obtained as:

$$W_{\text{class}} = \frac{\sigma d^2}{12} \int_0^{1/f} \left[ \left( \frac{dB_x}{dt} \right)^2 + \left( \frac{dB_y}{dt} \right)^2 \right] dt \quad (4.127)$$

where  $B_x(t)$  and  $B_y(t)$  are the induction components along  $x$  and  $y$  axis respectively.

The proposed equations are used to evaluate the losses in the iron poles. As the loci of magnetic flux density are not always elliptical due to harmonic distortion and geometrical effects, a simulated ellipse equivalent to the actual one is generated for every point in the pole keeping as fixed the peak of the polarization and the area of the locus. On this equivalent locus the parameter  $a$  is computed. An example of this simulated ellipse is reported in Fig. 4.57.

## 4.7 Losses in PMs

Usually the losses inside the magnets are neglected when studying electrical machines. In the case of magnetic gears this is no more true as pointed out in Sec. 4.8, where 3D simulations were conducted to evaluate the eddy current losses in PMs. In fact there are spatial magnetomotive forces that are synchronous with both the rotors (and these MMFs are useful for the torque transmission) and others that are asynchronous and only contribute to losses. Considering sintered NdFeB magnets, the resistivity is around  $150 \mu\Omega m$  while the iron resistivity is approximately  $\frac{1}{3}$  of this value. In this thesis the PMs are supposed to exhibit only eddy current losses, thus the hysteresis loss contribute in minor loops is neglected according to the study in [161].

Since different formulations have been proposed for the gear modelling in Sec. 4.1, Sec. 4.2 and Sec. 4.8, different approaches are adopted for the eddy current loss estimation in PMs.

If the analytic approach of Sec. 4.1 is adopted, the PMs eddy currents have to be found through different approaches. The analytic solver in PM domains solves:

$$\nabla_{r\theta}^2 A_z = \frac{\mu_0}{r} \cdot \frac{\partial M_r}{\partial \theta} \quad (4.128)$$

and from post processing calculations  $A_z$  can be computed in a grid of points. The eddy current is therefore:

$$J_{\text{eddy}} = -\sigma \cdot \frac{\partial A}{\partial t} + c'(t, V) \quad (4.129)$$

where  $\sigma$  is the material conductivity. As already discussed the analytical solver does not take into account the eddy current as well as the magnetic material real behaviour. In the hypothesis of low eddy currents, in the (4.129) the term  $J_{\text{magnets}} + J_{\text{eddy}} \simeq J_{\text{magnets}}$ . Calculating the term  $\sigma \cdot \frac{\partial A_z}{\partial t}$ , the eddy currents will be calculated in the hypothesis of negligible contribute on the

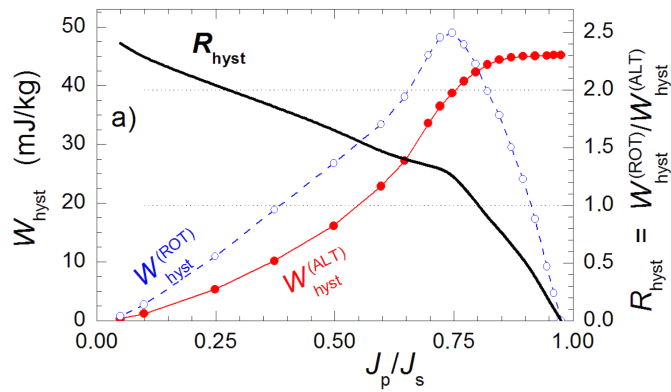


FIGURE 4.55: Alternating and rotational hysteresis loss components and their ratio  $R_{\text{hyst}}$  as a function of the reduced polarization  $J_p/J_s$  for the the NO 0.356 mm thick Fe-Si sheet (experimental data retrieved from [159]).

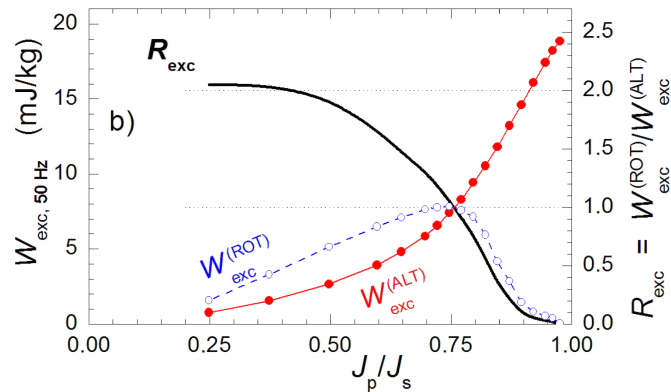


FIGURE 4.56: Behavior of the excess alternating and rotational losses versus  $J_p/J_s$  at 50 Hz and their ratio from [159].

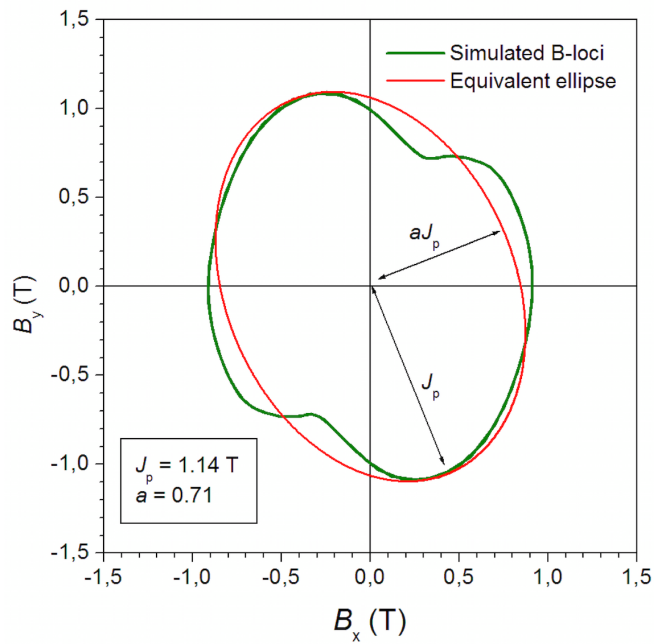


FIGURE 4.57:  $B$ -locus at a given point within the iron pole: computed cycle and equivalent ellipsoidal one.

magnetic fields. This hypothesis have to be verified in an efficient magnetic gear, otherwise the magnet heating would be excessive and the performance quite poor. Therefore simply storing the  $A_z$  values in regular grids of points at each time instant the losses can be computed as:

$$P_{magnets} = \frac{1}{T} \int_t \int_V \rho \cdot J_{eddy}^2 dV dt = \frac{1}{T} \int_t \int_V \frac{1}{\rho} \cdot \left( \frac{Az_{t+1} - Az_{t-1}}{2 \cdot \Delta t} + c(t, V) \right)^2 dV dt \quad (4.130)$$

using the expression of the central finite differences.  $\rho$  is the magnet bulk resistivity. The coefficient  $c(t, V)$  is the term that fix the eddy current surface integral on the cross sections to be null:

$$c(t, V) = - \int_S J_{eddy} dS \quad (4.131)$$

Indeed considering the magnets cross section, the global current that flows through the section has to be null because the magnets are insulated from the machine iron. The constant  $c$  depends on the time instant and can be easily computed as post-processing operation.

In Sec. 4.8 an equivalence between the 3D and 2D eddy current modelling will be introduced through empirical coefficients based on the assumptions in (4.94) and (4.95). Adopting the 3D formulation (4.135), the PMs losses  $P_{PM}^{3D}$  in segmented case can be computed as:

$$P_{PM}^{3D} = \sum_i \int_{V_{PM^i}} \frac{1}{\sigma} \left( \frac{\partial \mathbf{A}}{\partial t} \right)^2 dV \quad (4.132)$$

in accordance with the symbolism in (4.135) and where  $V_{PM^i}$  is the volume of the  $i^{th}$  segment of PMs.

If instead the 2D formulation (4.134) is adopted, the PMs losses are computed through:

$$P_{PM}^{2D} = \int_{\Omega_{PM}} \frac{\sigma_{PM}}{k} \left( \frac{\partial A_z}{\partial t} + \sigma \frac{V_{PM}}{L} \right)^2 d\Omega \quad (4.133)$$

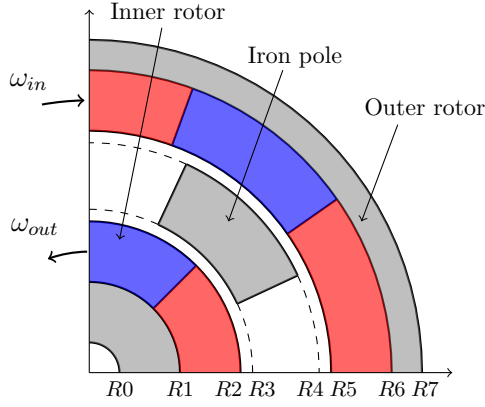
where  $\Omega_{PM}$  is the PM cross section and  $k$  is a reduction coefficient that consider the PMs segmentation with an equivalent electrical property in the same spirit of (4.96) in Sec. 4.5.5. An example of the coefficient  $k$  for a test case geometry can be found in Tab. 4.12.

## 4.8 2D vs. 3D simulations

In magnetic transmissions, the presence of the flux modulator constituted by the iron poles gives rise to a wide air gap and a consequent high reluctance path for the magnetic flux of the permanent magnets. According to this consideration, it is hard to estimate if a 2D model of the machine can provide accurate results as typically happens for classical electric rotating machines [162]. For this reason, a preliminary analysis has been carried out in order to compare the results in terms of magnetic flux distribution for a 3D and a 2D finite element model for the test case in Fig. 4.58.

The equations that have to be solved within the gear domain, are the quasi-static Maxwell equations. In this Section, the magnetic field, flux density and current density will be referred as  $\mathbf{H}$ ,  $\mathbf{B}$  and  $\mathbf{J}$ .

High permeability domains are modelled neglecting the eddy currents effects but considering the iron non-linearities  $\mathbf{H} = \nu(|\mathbf{B}|) \cdot \mathbf{B}$ . The material law adopted for the permanent magnets (PMs) is the linear equation  $\mathbf{B} = \mu \cdot \mathbf{H} + \mathbf{B}_r$ , where  $\mu$  is the magnet permeability and  $\mathbf{B}_r$  is the residual flux density. The current density term  $\mathbf{J}$  in the studied case is only constituted by eddy currents since there are no source terms due to windings. In the 2D case, the problem geometry allows the eddy currents to close at infinity, the current density integral over the cross section  $V$  of each magnet is not zero: this net current is present in the induction machine case since all the rotor bars are short-circuited, but in the PMs case the net current flowing through the cross section has to be nil. In order to impose the eddy currents  $\mathbf{J}_e = J_e \mathbf{e}_z$  to be solenoidal in each permanent magnet, an additional equation  $\int_V \mathbf{J}_e dV = 0$  is adopted for each PM. The  $\mathbf{A}$



Parameter	Value
$R0$	0.02 m
$R1$	0.04 m
$R2$	0.05 m
$R3$	0.052 m
$R4$	0.062 m
$R5$	0.064 m
$R6$	0.074 m
$R7$	0.09 m
Axial length $L$	0.1 m
Inner pole pairs $P_i$	2
Outer pole pairs $P_o$	11
Iron poles $q$	13
Gear ratio $ G  =  -P_o/P_i $	5.5

FIGURE 4.58: Magnetic gear structure and list of parameters adopted.

formulation in the  $i^{th}$  PM, with  $\mathbf{A} = (0, 0, A_z)$  is:

$$\begin{cases} \nabla \times (\nu \nabla \times \mathbf{A}) = -\sigma \frac{\partial \mathbf{A}}{\partial t} - \sigma \frac{V_{PM}^i}{L} \mathbf{e}_z + \nabla \times (\nu \mathbf{B}_r) \\ \int_V \mathbf{J}_e dV = \int_V \left( -\sigma \frac{\partial \mathbf{A}}{\partial t} - \sigma \frac{V_{PM}^i}{L} \mathbf{e}_z \right) dV = 0 \end{cases} \quad (4.134)$$

where  $\sigma$  is the magnet conductivity,  $L$  is the machine length,  $-\sigma \frac{V_{PM}^i}{L} \mathbf{e}_z$  is the additional current density term and  $V_{PM}^i$  is the equivalent voltage drop across the  $i^{th}$  PM that ensures the solenoidal property. In this work the magnets are considered to be made of *NdFeB* with conductivity  $\sigma = 0.65$  MS/m. Such a low value is a fictitious conductivity that takes into account the segmentation effects in 2D simulations, and it is consistent with the considerations in Tab. 4.12. The 3D formulation adopted is standard, based on the magnetic vector potential  $\mathbf{A}$  and the scalar electric potential  $V$  on the conductive permanent magnet regions:

$$\begin{cases} \nabla \times \nu \nabla \times \mathbf{A} + \sigma \frac{\partial \mathbf{A}}{\partial t} = \mathbf{J} + \nabla \times \mathbf{M} - \sigma \nabla V \\ \nabla \cdot \left( \frac{\partial \mathbf{A}}{\partial t} + \nabla V \right) = \nabla \cdot \mathbf{J}' = 0 \\ \mathbf{J}'_s \cdot \mathbf{n} = 0 \text{ (segmentation planes)} \\ V = 0 \text{ (PM segments gauge)} \\ \nabla \cdot \frac{1}{\mu(\Psi)} \nabla \Psi = 0 \text{ (current free regions)} \\ \nabla \times \mathbf{A} \cdot \mathbf{n} = -\mu \nabla \Psi \cdot \mathbf{n} \text{ (interfaces)} \\ \nu \nabla \times \mathbf{A} \times \mathbf{n} = -\nabla \Psi \times \mathbf{n} \text{ (interfaces)} \end{cases} \quad (4.135)$$

The resulting magnetic flux density norm and the induced eddy currents of the 3D model are shown in Fig. 4.59. These results are compared with the ones provided by the 2D model of the magnetic gear in correspondence of different sections of the machine and for its three main parts.

In Fig. 4.59 cross-sections of a 3D model of the magnetic gear, without segmentations, is shown. The plot shows the flux density norm and the white arrows represent the induced eddy currents.

Fig. 4.61-4.62 show comparisons of the flux density along lines taken inside the inner rotor, outer rotor and non-linear iron poles, respectively. In each plot three curves are displayed, one for the 2D case and the others for the 3D case where the query points lie on two slices located at  $z = L/2$  (half machine) and  $z = 9L/10$  (close to the machine edge). Some unphysical peaks are visible in Fig. 4.62, these are due to the rather coarse 3D model mesh which had to be used in order to limit the computational requirements. The comparison shows anyway a good match between 2D and 3D simulations, especially as far as the main quantities are concerned. In

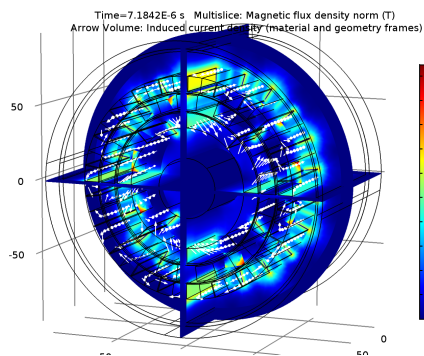


FIGURE 4.59: Magnetic flux density norm and eddy current arrow plot. The model does not include segmentations.

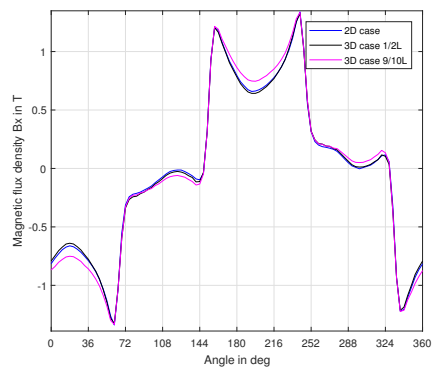


FIGURE 4.60: Comparison of  $B_x(r = 86.3 \text{ mm}, \text{angle} = 0 - 360^\circ)$  between 2D and 3D simulations (outer rotor).

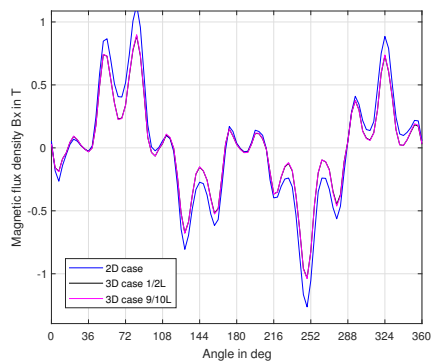


FIGURE 4.61: Comparison of  $B_x(r = 36.4 \text{ mm}, \text{angle} = 0 - 360^\circ)$  between 2D and 3D simulations (inner rotor).

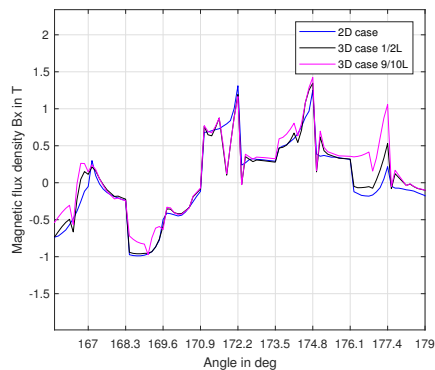


FIGURE 4.62: Comparison of  $B_x(r = 52.5 \text{ mm}, \text{angle} = 167 - 180^\circ)$  between 2D and 3D simulations (iron poles).

Slice	Norm ratio $\frac{ \Delta B }{ B }$
$z = L/2$	13.6%
$z = 9L/10$	18.3%

TABLE 4.11: Flux density norm comparison referring to the 2D simulation.

Model	Inner segm.	Outer segm.	$\sigma_{PMin}$	$\sigma_{PMout}$	$P_{PMin}$ (W)	$P_{PMout}$ (W)
3D	No	No	$\sigma$	$\sigma$	230	560
3D	2C.	2C.	$\sigma$	$\sigma$	220	160
3D	2A	2A	$\sigma$	$\sigma$	209	490
3D	2A+2C	2A+2C	$\sigma$	$\sigma$	205	155
3D	2A+3C	2A+3C	$\sigma$	$\sigma$	190	77
3D	2A+14C	2A+3C	$\sigma$	$\sigma$	87.5	77
2D	No	No	$\sigma/1.2$	$\sigma/1.52$	252	620
2D	2C	2C	$\sigma/1.6$	$\sigma/5.5$	221	165
2D	2A	2A	$\sigma/1.8$	$\sigma/1.9$	205	488
2D	2A+2C	2A+2C	$\sigma/1.95$	$\sigma/6$	206	155
2D	2A+3C	2A+3C	$\sigma/2.28$	$\sigma/11.7$	187	78
2D	2A+14C	2A+3C	$\sigma/4.5$	$\sigma/11.7$	87	78

TABLE 4.12: Comparison of the PMs losses at  $\omega_{in} = 5000$  rpm with no segmentation and with circumferential (C) or axial (A) segmentation.

Table 4.11 the norm of the difference vector  $|\Delta B| = \frac{\|\mathbf{B}_{3D} - \mathbf{B}_{2D}\|}{B_{3D}}$  where  $\mathbf{B}$  is a vector containing the flux density norm in all query points, is reported. This is higher if the slice is close to the machine edge rather than the machine center, since some flux lines close in the air, but the 2D approximation is still satisfactory. Based on these considerations, the loss estimation is based on the flux density computed from 2D simulations.

From the comparison of 2D and 3D simulations, an interesting aspect is the evaluation of the eddy currents, an intrinsic 3D phenomena, and the PM losses, according to Sec. 4.7. In Tab. 4.12 the PM Joule losses  $P_{PM}^{3D}$  are computed through 3D finite element simulations with inner speed  $\omega_{in} = 5000$  rpm with and without segmentations with the usual volume integration equation (4.132).

The physical effects of the segmentation with two axial segment and two circumferential segments are shown in Fig. 4.63 and Fig. 4.64 for outer permanent magnets and inner permanent magnets respectively. These figures show that the segmentation is much more effective for the outer PMs while the losses are lowered by a smaller factor for the inner PMs. In the case of the outer rotor, shown in Fig. 4.63, the eddy current is evenly distributed in the segments. Conversely, Fig. 4.64 shows that, in the inner permanent magnets, the eddy currents distribution locally concentrates in correspondence of the stationary pole pieces. In this case, the loss reduction is less effective as the adopted segmentation of the inner magnets gives rise to segments wider than the concentration regions.

By collecting the results reported in Table 4.12, it is possible to obtain the behavior of the PMs losses as a function of the number of circumferential segmentations shown in Fig. 4.64. For convenience, the analyzed points are interpolated through a fitting function in order to better point out the losses trend. Fig. 4.65 indicates that, despite the circumferential segmentation allows to strongly decrease the PMs losses, it starts to be less effective after a certain number of segments.

On the base of the discussed results, the overall loss evaluation for the gear test-case in this Section is carried out by considering 2 axial segmentations and 14 circular segmentations for the inner magnets, 2 axial segmentations and 3 circular segmentations for the outer magnets. This kind of segmentation gives rise to comparable segments surface for inner and outer PMs. In the 2D model this means to consider an equivalent conductivity of the inner rotor PMs  $\sigma_{PMin} = \sigma/k_{in} = \sigma/4.5$  and an equivalent conductivity of the outer rotor PMs

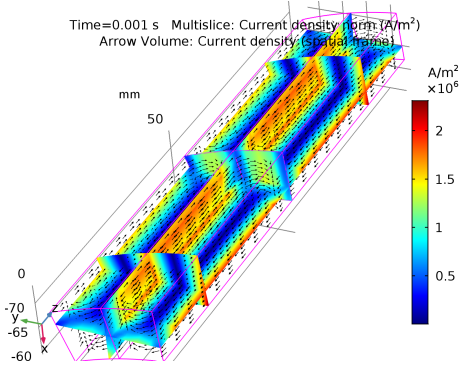


FIGURE 4.63: Effect of outer permanent magnet segmentation on eddy currents: current density norm (multislice colormap) and current vectors (black arrows). The figure refers to the 3D simulation with 2 axial segments and 2 circumferential segments.

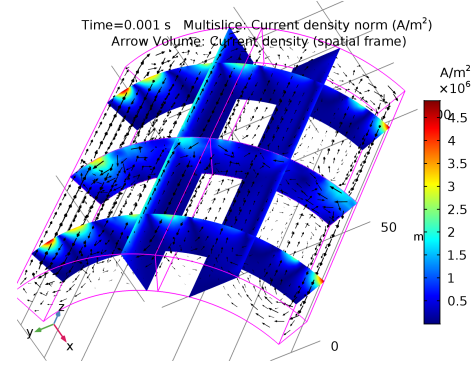


FIGURE 4.64: Effect of inner permanent magnet segmentation on eddy currents: current density norm (multislice colormap) and current vectors (black arrows). The figure refers to the 3D simulation with 2 axial segments and 2 circumferential segments.

$\sigma_{PMout} = \sigma/k_{out} = \sigma/11.7$ . Hence, the latter is the value of PMs conductivity adopted for the loss computation.

By collecting the results reported in Table 4.12, it is possible to obtain the behavior of the PMs losses as a function of the number of circumferential segmentations shown in Fig. 4.64. For convenience, the analyzed points are interpolated through a fitting function in order to better point out the losses trend; the fitting equation will be presented in Sec. 4.5.5. Fig. 4.65 indicates that, despite the circumferential segmentation allows to strongly decrease the PMs losses, it starts to be less effective after a certain number of segments.

## 4.9 Losses vs. speed

In this Section the losses for the magnetic gear test case in Fig. 4.58 are computed for different operational speeds in the range  $\omega_{in} = 0 - 5000$  rpm. Soft material losses have been estimated through the approach in Sec. 4.6.4, while the PMs losses are evaluated through (4.133).

Similarly to the electric rotating machines, the power loss depends on the rotational speed and also on the load angle  $\theta_L$  (i.e. the phase shift between the first harmonic of the rotating magnetic fields generated by the inner and the outer rotor, respectively):

$$\theta_L = \theta_{in} - \theta_{out} \cdot \left( -\frac{P_o}{P_i} \right) = \theta_{in} - \theta_{out} \cdot G \quad (4.136)$$

In this Section, the results relative to the maximum torque capability are shown. A great part of the iron loss has to be attributed to iron poles as they are subject to high flux densities that, as shown in the previous section, show rotational behavior. The iron yokes are interested by the superposition of fields with periodicity  $P_i$  and  $P_o$ , hence rotational loci are also expected even if the area enclosed by the loop is smaller than the one of the iron poles and a DC bias is present. The loci frequency in the gear components, at  $\omega_{in} = 5000$  rpm,  $\omega_{poles} = 0$  rpm,  $\omega_{out} = -909.09$  rpm, reads:

$$\begin{cases} f_{poles} = \frac{\omega_{in}}{60} P_i \\ f_{in \ yoke} = \frac{\omega_{in}}{60} q \\ f_{out \ yoke} = \frac{\omega_{in}}{60} \frac{P_i \cdot q}{P_o} \end{cases} \longrightarrow \begin{cases} f_{poles} = 167 \text{ Hz} \\ f_{in \ yoke} = 1083 \text{ Hz} \\ f_{out \ yoke} = 197 \text{ Hz} \end{cases} \quad (4.137)$$

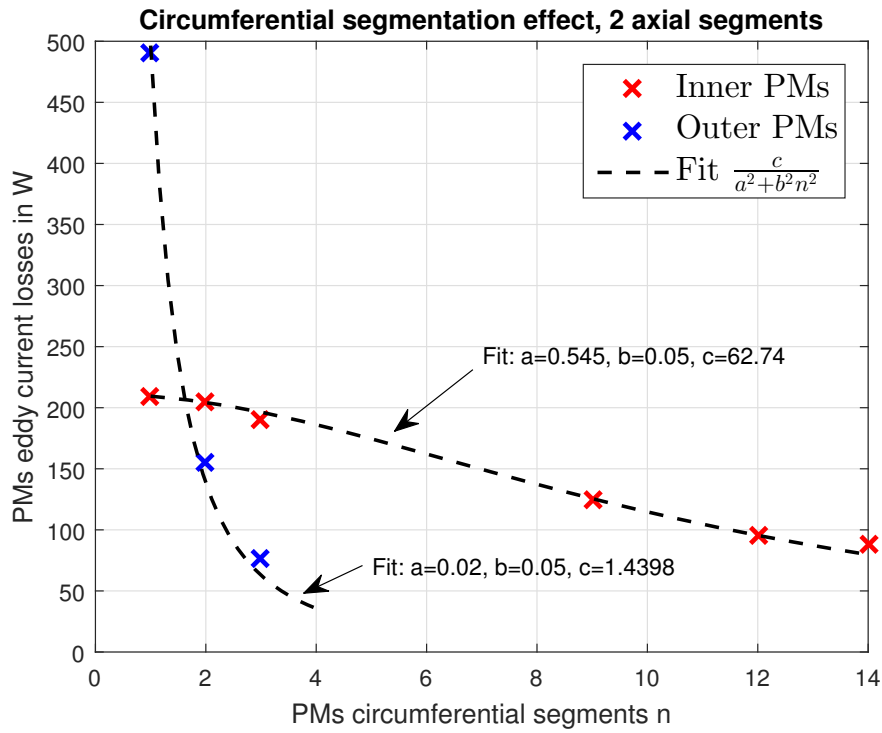


FIGURE 4.65: PMs losses trend, comparison with constant number of axial segments and variable number of circumferential segments. The fit is made according to the expression in (4.96). According to Fig. 4.45, the parameters  $a$  and  $b$  are in agreement with the PMs size as predicted in Sec. 4.5.5.

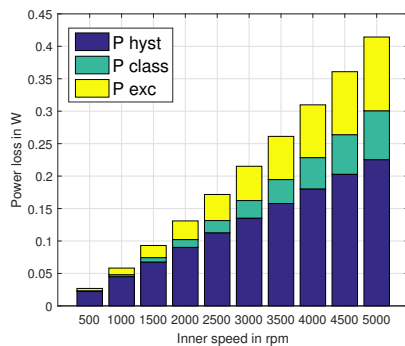


FIGURE 4.66: Inner iron yoke loss components. The losses are computed varying the rotors speed at the maximum torque capability.

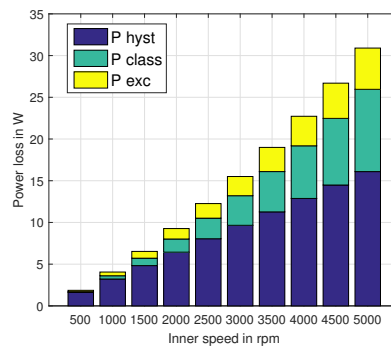


FIGURE 4.67: Outer iron yoke loss components. The losses are computed varying the rotors speed at the maximum torque capability.



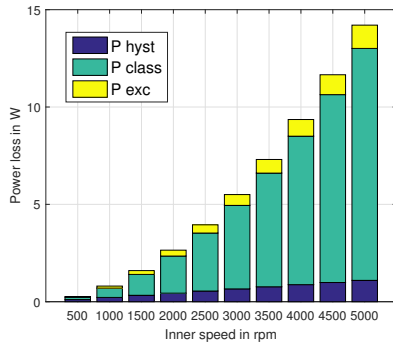


FIGURE 4.68: Iron poles loss components. The losses are computed varying the rotors speed at the maximum torque capability.

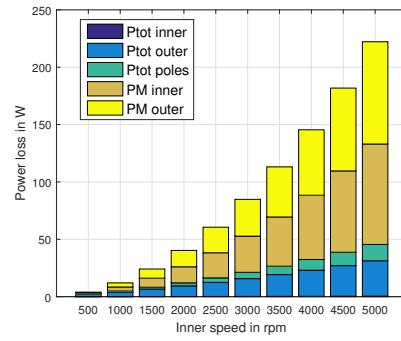


FIGURE 4.69: Total inner yoke, outer yoke, iron poles power losses  $P_{tot\ inner}$ ,  $P_{tot\ outer}$ ,  $P_{tot\ poles}$  and permanent magnets power losses varying the rotational speed. The inner yoke losses are negligible for the efficiency calculation.

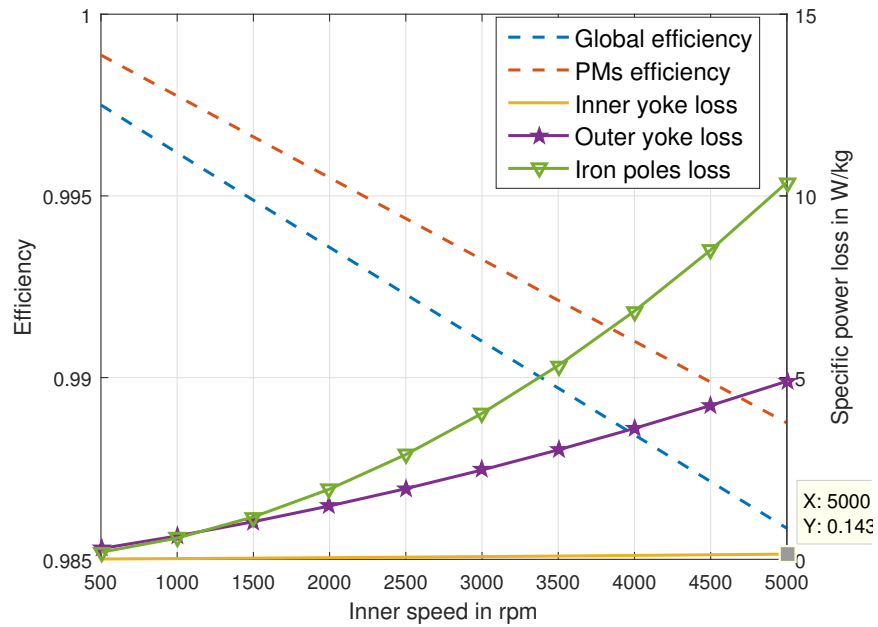


FIGURE 4.70: Global efficiency, permanent magnets efficiency and specific iron loss plots varying the rotational speed. The efficiency decay is practically linear in this speed range and above  $\omega_{in} = 1000$  rpm the highest specific losses are in the iron poles.

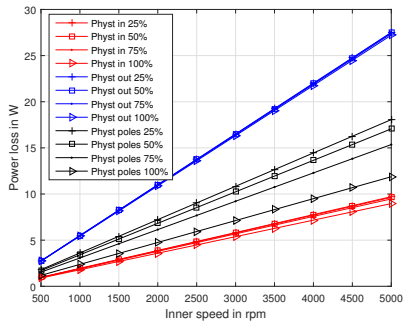


FIGURE 4.71: Hysteresis losses varying rotational velocities and load angle.

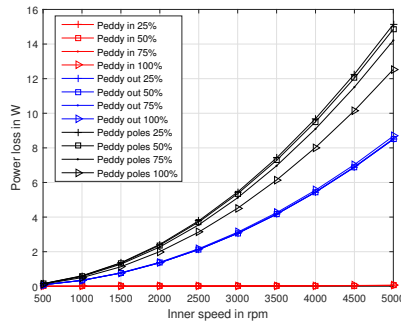


FIGURE 4.72: Eddy current losses varying rotational velocities and load angle.

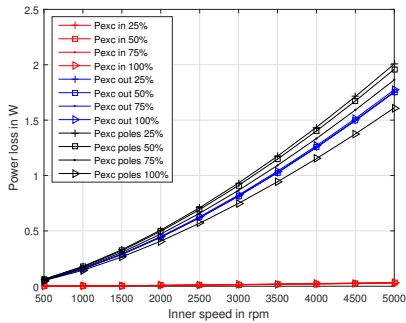


FIGURE 4.73: Excess losses varying rotational velocities and load angle.

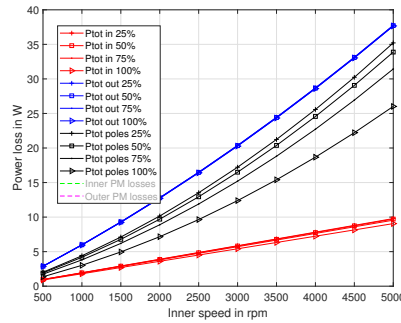


FIGURE 4.74: Global losses varying rotational velocities and load angle.

Fig. 4.66 shows the losses components in the inner yoke versus the inner rotational speed. The classical Steinmetz frequency dependency applies to the plot: the hysteresis loss grows linearly with the rotational speed, the classical component quadratically and the excess component as  $\omega_{in}^{1.5}$ . The hysteresis loss is the predominant term with lamination thickness  $\delta = 0.356$  mm.

Fig. 4.67 shows the losses components in the outer yoke and the same considerations of Fig. 4.66 applies. The absolute loss value differs by 2 orders of magnitude in comparison to the previous case: this happens because of the bigger iron volume and because the inner rotor magnetic field has a strong influence on the outer loci while, on the contrary, a great part of the flux lines of the outer rotor magnets close on the iron poles without affecting the inner yoke.

Fig. 4.68 shows the losses in the iron poles: the eddy current loss is the predominant one, while the hysteresis and excess relative contributes are lower than in the inner and outer yokes cases. This is due to the change in the loss mechanism: because of the reduced volume, the flux density in the iron poles is higher than the yokes. At these  $J_P$  values, according to Fig. 4.55 and Fig. 4.56 due to the rotational component of flux density the loss contributions drop and this explains the smaller contributions of excess and hysteresis loss. For further details on the loss mechanism in hysteretic materials, the reader is referred to [163].

As a final evaluation, Fig. 4.69 shows the total losses on inner and outer yokes, iron poles and permanent magnets. The inner yoke losses are negligible while the PMs losses are not, since their value is higher than the one of the iron losses in ferromagnetic part.

Finally, Fig. 4.70 shows the global efficiency plot, the PMs efficiency contribution and the specific power losses in the iron domains. The highest specific loss is obtained in the iron poles. This high specific loss has to be expected in any case as the iron poles are the elements subject to the highest magnetic induction at the highest harmonic content.

The iron losses are function of the load angle since the magnetic flux density map changes when the transmitted torque varies. 4 torque levels are set for the magnetic gear of Fig. 4.58 and the iron losses in the soft materials are depicted in Figs. 4.71,4.72,4.73, 4.74. The major

changes are visible in the iron poles, where hysteresis, eddy current and excess losses tend to decrease increasing the torque.



# Chapter 5

## Mechanical and thermal modelling

Magnetic gears, as all the electro-mechanical devices, are multi-physic devices. Often to simplify the problem, the physics interactions are neglected or not strongly coupled.

In this thesis, the coupled multi-physic problem is not solved, but rather the coupling between electro-magnetic, mechanical and thermal physics is uni-directional, meaning that strains, displacements and temperatures are supposed to have a negligible effect on the electro-magnetic simulation. In the previous Chapters, the coupling between temperature and electro-magnetic simulations has already been introduced, in particular in Secs. 4.5.3 and 4.5.6. In this Chapter the mechanical and thermal problems are stated for the magnetic transmission.

In Sec. 5.1 the mechanical limit speed due to internal stresses is analyzed, for both cases with and without retaining sleeve. Moreover, the speed limit due to penetration depth is analyzed, especially for the cases with solid cores. Finally, the relations between rotation speed and resonance frequencies is introduced.

In Sec. 5.2 the case of three moving rotors is analyzed, and the power split due to the magnetic gear is studied.

Sec. 5.3 shows how to apply the Maxwell's stress tensor for the computation of the forces acting on the pole pieces.

In Sec. 5.4, a simplified mechanical model for the displacements analysis of the iron poles is introduced for the cases with and without rods.

In Sec. 5.5 an equivalent lumped thermal model is adopted to study the temperature distribution inside the magnetic gear.

The models and results in this Chapter have been published in [71].

### 5.1 Rotational speed limit for magnetic gears

From the mechanical point of view, the first parameter that is worth to be discussed is the rotational speed. The rotational velocity is strictly linked to the losses calculation and once the geometry is defined, the speed limit is obtained considering efficiency, structural constraints and thermal aspects.

High-speed electrical machines have been studied for several years, and are still an hot topic [164]. Magnetic gears, because of their intrinsic modulation effect that causes many spatial harmonics, could not reach such high values of rotational speed mainly because of excessive losses and demagnetization issues. Nevertheless, in [150] a magnetic gear prototype was built with an efficiency  $\eta = 92\%$  with an inner speed  $rpm_{in} = 19$  krpm. At these high speeds, the mechanical limitations due to the rotor structure must be checked in order to avoid failures.

Sec. 5.1.1 introduces the mechanical rotor speed limitations due to internal stresses, while in Sec. 5.1.3 the speed-related skin effect is described. Finally, in Sec. 5.1.4 the vibrations role on the speed limit is discussed.

### 5.1.1 Rotor speed limit without retaining sleeve

In the easiest configuration for SPM machines, the permanent magnets are glued to the iron laminates through adhesive layers. In this case, the glue has to withstand the radial and tangential forces developed on the permanent magnets. These forces are due to both mechanical accelerations (centrifugal, Euler force) and magnetic interactions. In this Section, a simplified analysis will be carried out considering that the PMs are only subjected to radial forces and considering that the temperature is not affecting the bonded joints. Thus, the only loading conditions that are considered for the adhesive layer are tension and compression, while shear, cleavage and peel are neglected.

Fig. 5.1 shows the cases of inner and outer rotors. If the magnet is considered to have thickness  $t_{PM}$ , angular pitch  $\theta_{PM}$  and density  $\rho_{PM}$ , the PM mass is  $m_{PM} = \frac{(R+t_{PM})^2 - R^2}{2} \theta_{PM} L \rho_{PM} = \frac{t_{PM}^2 + 2Rt_{PM}}{2} L \theta_{PM} \rho_{PM}$ , where  $R$  is defined according to Fig. 5.1 and  $L$  is the machine axial length. Considering the case of inner rotor in steady state (no Euler force contribution) with a magnetic force  $F_M$ , the global adhesive tensile stress  $\sigma$  is:

$$\begin{aligned} \sigma &= \frac{\sum F}{LR\theta_{PM}} = \frac{m_{PM}\omega_{in}^2 R + F_M}{R\theta_{PM}L} = \frac{\frac{t_{PM}^2 + 2Rt_{PM}}{2} L \theta_{PM} R \omega_{in}^2 \rho_{PM} + F_M}{LR\theta_{PM}} = \\ &= \frac{t_{PM}^2 + 2Rt_{PM}}{2} \omega_{in}^2 \rho_{PM} + \frac{F_M}{LR\theta_{PM}} \end{aligned} \quad (5.1)$$

From (5.1), if  $\sigma_T^{lim}$  is minimum value between the limit tensile stress of the adhesive and the PM limit tensile strength  $\sigma_T^{lim} = \min(\sigma_{ad.-T}^{lim}, \sigma_{PM-T}^{lim})$ , the speed  $\omega_{in}$  has to satisfy:

$$\omega_{in} \leq \sqrt{\left(\sigma_T^{lim} - \frac{F_M}{LR\theta_{PM}}\right) \frac{2}{(t_{PM}^2 + 2Rt_{PM})\rho_{PM}}} \quad (5.2)$$

For example, considering  $\sigma_T^{lim} = \sigma_{ad.-T}^{lim} = 10$  MPa,  $F_M = 1000$  N,  $L = 0.1$  m,  $R = 0.04$  m,  $t_{PM} = 0.007$  m,  $\theta_{PM} = \pi/2$  and  $\rho_{PM} = 7500$  kg/m<sup>3</sup>, the inner rotor speed has to be  $\omega_{in} < 28$  krpm according to (5.2). The value of  $\sigma_{ad.-T}$  is in accordance with the measurements in [165].

For the outer rotor case, the approach of (5.1) is adopted, but this time the centrifugal force results in a compressive stress, thus the PM compressive stress limit defines the speed limit. At zero speed the adhesive has to withstand the magnetic force:  $\sigma_{ad.}^{lim} > \frac{F_M}{LR\theta_{PM}}$ . Once this is verified, the limit compressive stress is the minimum between PM and adhesive ones  $\sigma_C^{lim} = \min(\sigma_{ad.-C}^{lim}, \sigma_{PM-C}^{lim})$ . The outer speed limit has to satisfy:

$$\omega_{out} \leq \sqrt{\left(\sigma_C^{lim} - \frac{F_M}{LR\theta_{PM}}\right) \frac{2}{(-t_{PM}^2 + 2Rt_{PM})\rho_{PM}}} \quad (5.3)$$

The approach shown in this Section allows to obtain a simplified estimation of the mechanical speed at which the adhesive or the PMs fails. The parameters required for the estimation are the adhesive tensile and compressive strength of both adhesive and permanent magnets.

### 5.1.2 Rotor speed limit with retaining sleeve

Before showing the stresses calculation in magnetic gear rotors, the basic equations of radial and tangential stresses are reported for the cases of homogeneous hollow and bulky cylinder according to the plain strain hypothesis (see. [166] for an extensive survey on the rotor stresses).

Considering an hollow cylinder with inner radius  $r_i$  outer radius  $r_o$ , density  $\rho$  and Poisson ratio  $\nu$ , the radial and tangential stresses  $\sigma_r$  and  $\sigma_\theta$  in a cylindrical reference system are:

$$\sigma_r = \frac{3 + \nu}{8} \cdot \rho \cdot \omega^2 \cdot \left( r_o^2 + r_i^2 - \frac{r_o^2 r_i^2}{r^2} - r^2 \right) \quad (5.4)$$

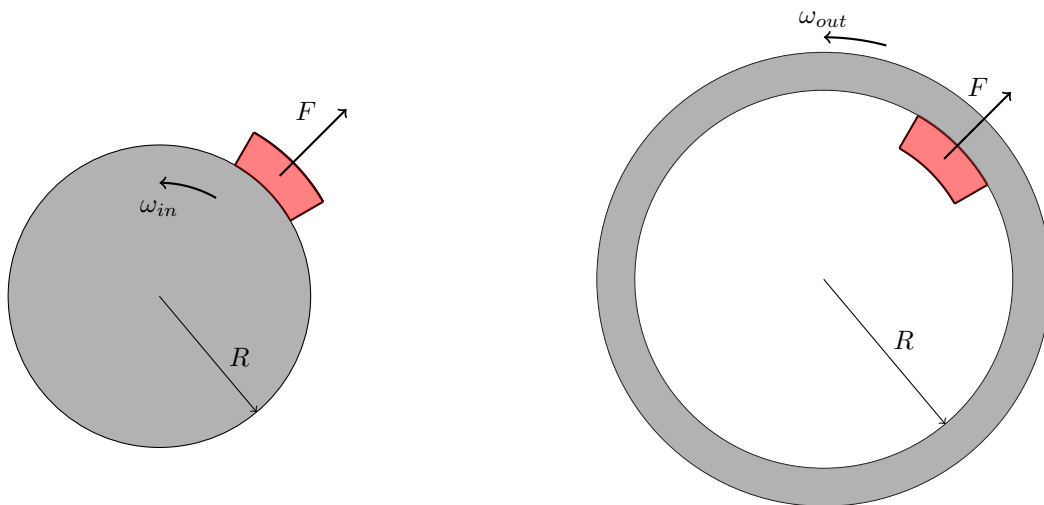


FIGURE 5.1: Inner and outer rotors of an SPM magnetic gear and centrifugal force  $F$ .

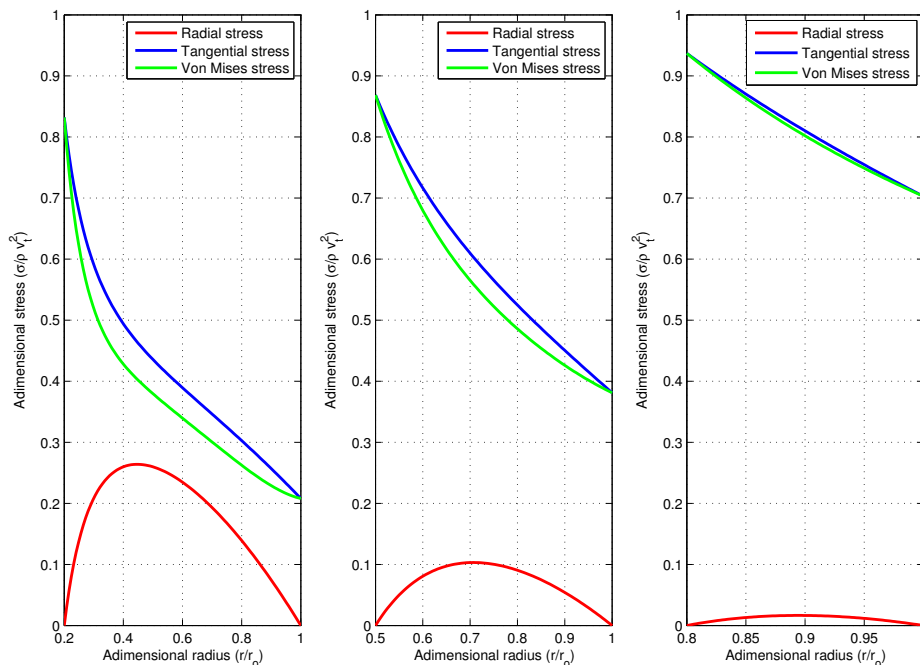


FIGURE 5.2: Hollow rotor dimensionless stresses with  $r_i/r_o = 0.2$ ,  $r_i/r_o = 0.5$  and  $r_i/r_o = 0.8$ .

$$\sigma_\theta = \frac{3+\nu}{8} \cdot \rho \cdot \omega^2 \cdot \left( r_o^2 + r_i^2 + \frac{r_o^2 r_i^2}{r^2} - \frac{1+3\nu}{3+\nu} \cdot r^2 \right) \quad (5.5)$$

The maximum stress calculated through Von Mises  $\sigma_{VM}$  criterion occurs at the inner radius  $r_i$ :

$$\sigma_{VM} = \sqrt{\sigma_r^2 + \sigma_\theta^2 - \sigma_r \sigma_\theta} \quad (5.6)$$

$$\sigma_{VM}^{max} = (3+\nu) \frac{\rho v_o^2}{4} + (1-\nu) \frac{\rho v_o^2}{4} \left( \frac{r_i}{r_o} \right) \simeq \rho v_o^2 \quad (5.7)$$

In Fig. 5.2,  $\sigma_r$ ,  $\sigma_\theta$  and  $\sigma_{VM}$  are shown for three different ratios between inner and outer radius. The tangential stress is the dominant one, and the maximum occurs at the inner radius.

Considering instead the case of a bulky cylinder with radius  $r_o$ , Eq. (5.4) and (5.5) become:

$$\sigma_r = \frac{3+\nu}{8} \cdot \rho \cdot \omega^2 \cdot \left( r_o^2 - r^2 \right) \quad (5.8)$$

$$\sigma_\theta = \frac{3+\nu}{8} \cdot \rho \cdot \omega^2 \cdot \left( r_o^2 - \frac{1+3\nu}{3+\nu} \cdot r^2 \right) \quad (5.9)$$

The maximum stress occurs at the cylinder central point:

$$\sigma_{VM}^{max} = (3+\nu) \frac{\rho v_o^2}{8} \quad (5.10)$$

Since the ratio between the hollow case maximum stress when  $\lim(r_i) \rightarrow 0$  and the full cylinder stress is 0.5, the bulky cylinder allows a rotational speed  $\sqrt{2}$  times higher than the hollow one keeping the same outer radius.

High speed rotors are generally equipped with glass or carbon fibers enclosures. These non magnetic materials have the role to ensure the structural integrity at high speeds.

In a rotor constituted by  $k$  elements (e.g. shaft, PMs annulus, glass fiber annulus), adopting the hypothesis of non-orthotropic materials, inside the  $i^{th}$  domain the stresses  $\sigma$  and displacements  $u$  obey to:

$$\begin{cases} \sigma_{ri} = \frac{E'}{1-\nu'} A_i - \frac{E'}{1+\nu'} \frac{B_i}{r^2} - \frac{3+\nu'}{8} \rho r^2 \omega^2 \\ \sigma_{\theta i} = \frac{E'}{1-\nu'} A_i + \frac{E'}{1+\nu'} \frac{B_i}{r^2} - \frac{1+3\nu'}{8} \rho r^2 \omega^2 \\ u_i = A_i \cdot r \frac{B_i}{r} - (1-\nu'^2) \frac{\rho r^3 \omega^2}{8E'} \end{cases} \quad (5.11)$$

where  $\omega$  is the rotational speed,  $E'$  and  $\nu'$ , for the case of plane strain, are related to the material Young modulus  $E$  and the Poisson ratio  $\nu$  as:  $E' = \frac{E}{1-\nu^2}$  and  $\nu' = \frac{\nu}{1-\nu}$ . The coefficients  $A_i$  and  $B_i$  can be found using the boundary conditions:

$$\begin{cases} \sigma_{ri}(R_{i-1}^i) - \sigma_{r(i-1)}(R_{i-1}^i) = 0 \\ u_{ri}(R_{i-1}^i) - u_{r(i-1)}(R_{i-1}^i) = \delta(R_{i-1}^i) \rightarrow i = 2 : k \\ \sigma_{rk}(R_{ext}) = 0 \end{cases} \quad (5.12)$$

where  $R_{i-1}^i$  stands for the interface radius between the domains  $i-1$  and  $i$  and  $\delta(R_{i-1}^i)$  is the interference parameter at the  $R_{i-1}^i$  domains interface. Combining (5.12) and (5.11), the radial and tangential stresses are computed in all the rotor regions, and the expressions can be rewritten in the compact form:

$$\begin{cases} \sigma_r = \Upsilon_r \omega + \Psi_r \delta \\ \sigma_\theta = \Upsilon_\theta \omega + \Psi_\theta \delta \\ \sigma_{VM} = \sqrt{\sigma_r^2 + \sigma_\theta^2 - \sigma_r \sigma_\theta} \end{cases} \quad (5.13)$$

where the functions  $\Upsilon$  and  $\Psi$  depend on the geometry and on the material parameters. The mechanical constraints impose that the limit stress  $\sigma_U > \tau \sigma_{VM}^{max}$  with  $\tau$  safety factor, and



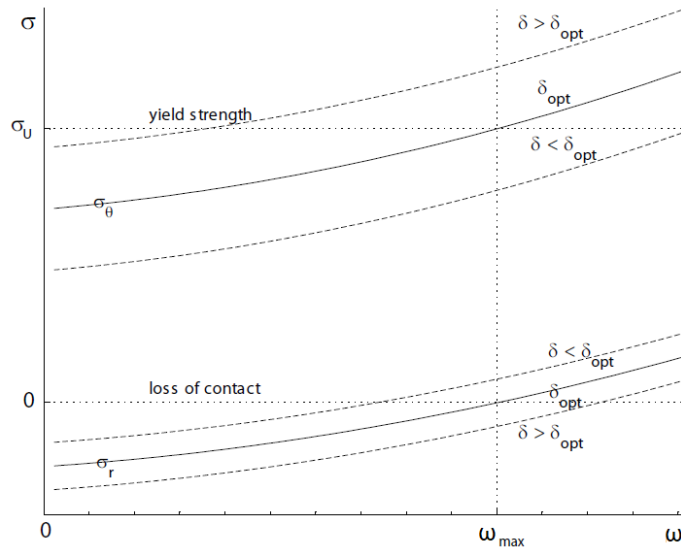


FIGURE 5.3: Structural limits and influence of the interference parameter  $\delta$  on the maximum speed [166].

the contact pressure between magnets and yoke must be negative (otherwise contact is not maintained). Thus, the interference  $\delta$  affects the maximum speed in (5.13) as shown in Fig. 5.3.

### 5.1.3 Skin depth

Another speed limit is the one due to the skin effect. When time-varying magnetic fields are involved, the penetration depth  $\delta$  can be calculated as:

$$\delta = \sqrt{\frac{\rho}{\pi \cdot \mu \cdot f}} \quad (5.14)$$

The magnetic fundamental magnetic field for both rotors has an electrical frequency equal to:

$$f = \frac{rpm_{in} \cdot Pi}{60} = \frac{rpm_{out} \cdot Po}{60} \quad (5.15)$$

where  $rpm_{in}$  and  $rpm_{out}$  are the inner and outer rotor rotational speeds.

The maximum rotational speed in order to guarantee that the penetration depth  $\delta$  is at least larger than the smallest dimension of the magnetic conductors  $\xi$  is:

$$rpm_{in} < \frac{60 \cdot \rho}{Pi \cdot \pi \cdot \mu \cdot \xi^2} \quad (5.16)$$

Therefore using steels with high resistivity and low magnetic permeabilities the speed limit can be increased. The magnetic relative permeability  $\mu$  decreases when the iron starts to saturate; this means that (5.16) is non-linear. In Fig. 5.4 the speed limit is depicted as function of the magnetic conductor dimension and of the flux density. From Fig. 5.4, while (5.16) is normally fulfilled in the case of standard laminations, in the case of solid magnetic cores Eq. (5.16) can limit the gear operation speed. This is the case of [46], where the inner speed was set to  $rpm_{in} = 30$  rpm.

### 5.1.4 Vibrations modes

The low vibration operation and the capability to suppress the input rotor shaft vibration are, among others, some of the main reason which drains attention on the magnetic transmissions

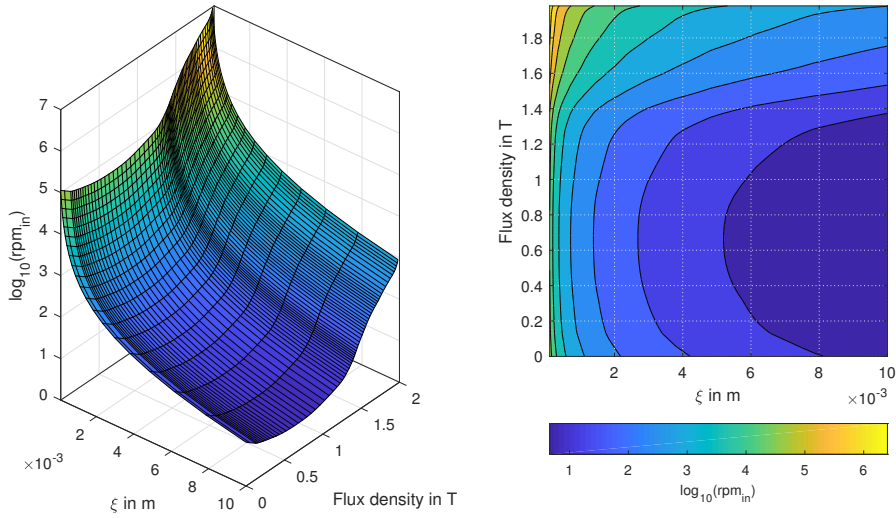


FIGURE 5.4: Speed limit changing the flux density  $B$  and the magnetic conductor size. The material in this analysis is the electrical steel NGO35PN250, and the number of inner pole pairs is  $Pi = 2$ .

(see Chapter 2). Indeed, the low torsional stiffness and the non-contact motion transmission play a fundamental role in terms of vibrations. Still, the electromagnetic interactions between the rotors and the cogging torque produce vibrations, that have to be evaluated to avoid resonances and to assess the noise level of the magnetic transmission.

[167] suggested a general equation to find the shaft resonance frequencies of an electrical machine rotor:

$$\omega_n|^{res} = \alpha_n \sqrt{\frac{EI}{\mu}} \quad (5.17)$$

where  $E$  and  $I$  are the rotor Young modulus and inertia,  $\mu$  is the rotor mass and  $\alpha_n$  are boundary-dependent coefficients. Eq. (5.17) can be applied with the coefficients retrieved from [167] for a simple identification of the resonance frequencies and rotors critical speeds, but FEM simulations are requested for precise calculations.

Once the structure resonance frequencies are found, the mechanical constraint that must be satisfied is:

$$\left| \frac{\omega_{in} - \omega_{n-in}|^{res}}{\omega_{n-in}|^{res}} \right| \geq \tau \quad (5.18)$$

where  $\tau$  defines a safety tolerance margin. An equation identical to (5.18) can be adopted for the outer rotor.

For the special case of magnetic gears, [168] and [169] focused on the vibration problem of coaxial gearboxes, but literature still largely lacks of models for the iron poles rotor natural frequencies evaluation.

## 5.2 Variable speed

Considering  $T_m$  the maximum torque developed in the iron poles rotor and adopting the same notation of Sec. 3.5, the torque expressions are the following:

$$\begin{cases} T_{in} = T_m \cdot \frac{Pi}{q} \cdot \sin(\theta_e) \\ T_{out} = T_m \cdot \frac{P_e}{q} \cdot \sin(\theta_e) \\ T_{poles} = -T_m \cdot \sin(\theta_e) \end{cases} \quad (5.19)$$

where

$$\theta_e = P_i \cdot \theta_{in} + P_o \cdot \theta_{out} - q \cdot \theta_s \quad (5.20)$$

In stationary conditions the angle  $\theta$  for each rotor can be expressed as  $\theta_0 + \omega \cdot t$ . Therefore the  $\theta_e$  expression becomes:

$$\theta_e = P_i \cdot \theta_{in0} + P_i \cdot \omega_{in} \cdot t + P_o \cdot \theta_{out0} + P_o \cdot \omega_{out} \cdot t - q \cdot \theta_{poles0} - q \cdot \omega_{poles} \cdot t \quad (5.21)$$

The space harmonic rotational velocity expression found in Sec. 3.17 was:

$$\omega_{in} = -\frac{P_o}{P_i} \cdot \omega_{out} + \frac{q}{P_i} \cdot \omega_{poles} \quad (5.22)$$

and substituting (5.22) in (5.21), the angle  $\theta_e$  becomes:

$$\theta_e = P_i \cdot \theta_{in0} + P_o \cdot \theta_{out0} - q \cdot \theta_{poles0} \quad (5.23)$$

The angle  $\theta_e$  is therefore stationary when the three rotors are in stationary conditions (constant speed). Considering that the load torque is constant changing the rotational speed, if the iron poles are suddenly rotated reaching a regime velocity, the load angle will be subjected to a transient but the final condition will be again a steady state as in (5.23).

The power balance is given by the product between torques and rotational speeds:

$$\begin{cases} W_i = T_m \cdot \frac{P_i}{q} \cdot \left( -\frac{P_o}{P_i} \cdot \omega_{out} + \frac{q}{P_i} \cdot \omega_{poles} \right) \cdot \sin \theta_e \\ W_o = T_m \cdot \frac{P_o}{q} \cdot \omega_{out} \cdot \sin \theta_e \\ W_{poles} = -T_m \cdot \omega_{poles} \cdot \sin \theta_e \end{cases} = \quad (5.24)$$

$$= \begin{cases} W_i = T_m \cdot \left( -\frac{P_o}{q} \omega_{out} + \omega_{poles} \right) \cdot \sin \theta_e \\ W_o = T_m \cdot \frac{P_o}{q} \cdot \omega_{out} \cdot \sin \theta_e \\ W_{poles} = -T_m \cdot \omega_{poles} \cdot \sin \theta_e \end{cases}$$

where  $W_i$ ,  $W_o$  and  $W_{poles}$  are the inner, outer and poles rotor powers respectively. Writing the gear ratio  $G$  including the poles rotor motion, the equation reads:

$$G(> 1) = \frac{\omega_{in}}{\omega_{out}} = -\frac{P_o}{P_i} + \frac{q}{P_i} \cdot \frac{\omega_{poles}}{\omega_{out}} = -G_n + \frac{q}{P_i} \cdot \frac{\omega_{poles}}{\omega_{out}} \quad (5.25)$$

the gear ratio relative variation  $\Delta$  due to the rotation of the iron poles can be expressed as:

$$\Delta = \frac{\frac{q \cdot \omega_{poles}}{P_i \cdot \omega_{out}}}{\frac{P_o}{P_i}} = \frac{q}{P_o} \cdot \frac{\omega_{poles}}{\omega_{out}} \quad (5.26)$$

If the gear ratio  $G$  is high (5 and higher), the ratio  $\frac{q}{P_o}$  is approximatively equal to 1, therefore the in order to guarantee a variation  $\Delta$  the ratio  $\frac{\omega_s}{\omega_{out}} = \Delta$ . The power that must be provided in order to guarantee  $\Delta$  is:

$$W_{poles} = -T_m \cdot \frac{P_o}{q} \cdot \Delta \cdot \omega_{out} \cdot \sin \theta_e \quad (5.27)$$

while the power on the low speed rotor (considered as the other input):

$$W_o = T_m \cdot \frac{P_o}{q} \cdot \omega_{out} \cdot \sin \theta_e \quad (5.28)$$

The control power that is injected in order to change the gear ratio is  $\Delta$  times the output power. This means that the torque required to move the iron poles is high and this surely affects the design of the electrical machines connected to the iron poles.

Another solution could be to use the outer rotor as control rotor. In this case the input is again the inner rotor and the output is the iron poles rotor. In this case the gear ratio is:

$$G(> 1) = \frac{\omega_{poles}}{\omega_{in}} = \frac{Pi}{q} + \frac{Po}{q} \cdot \frac{\omega_{out}}{\omega_{in}} \quad (5.29)$$

and the gear ratio variation becomes:

$$\Delta = \frac{\frac{Po \cdot \omega_{out}}{q \cdot \omega_{in}}}{\frac{Pi}{q}} = \frac{Po}{Pi} \cdot \frac{\omega_{out}}{\omega_{in}} \quad (5.30)$$

In this case the ratio  $\frac{\omega_{out}}{\omega_{in}} = \Delta \cdot \frac{Pi}{Po}$ . The power that must be injected when the gear ratio is modified is:

$$W_o = T_m \cdot \frac{Po}{q} \cdot \frac{Pi}{Po} \cdot \Delta \cdot \omega_{in} \quad (5.31)$$

while the input power is:

$$W_i = T_m \cdot \frac{Pi}{q} \cdot \omega_{in} \quad (5.32)$$

and therefore the ratio between the control power and the input power is  $\Delta$ .

### 5.3 Magnetic forces on iron poles

The flux modulator in a magnetic gear is a key component that has to be designed in order to withstand the cyclic forces on each iron pole. As reported in [170], the forces are generally higher in the cases of low gear ratios.

The Maxwell stress tensor is an important method to compute forces and torques. The local force acting on the domain with volume  $V$  in Fig. 5.5 can be computed according to the Lorentz force:

$$f = \mathbf{J} \times \mathbf{B} \quad (5.33)$$

and the total force is given by volume integration:

$$F = \int_V \mathbf{J} \times \mathbf{B} dV \quad (5.34)$$

This expression can be easily implemented in finite element codes where there are active coils with currents flowing through them. When this relation has to be applied to magnetically active regions the current formulation is not practical. Using the Ampere's law the following relation holds:

$$\mathbf{J} = \frac{1}{\mu_0} \nabla \times \mathbf{B} \quad (5.35)$$

where  $\mathbf{J}$  includes real currents and permanent magnets equivalent currents. The force reads:

$$F = \frac{1}{\mu_0} \int_V (\nabla \times \mathbf{B}) \times \mathbf{B} dV \quad (5.36)$$

and developing the curl operator, the force becomes:

$$F = \frac{1}{\mu_0} \int_V \left( B_z \cdot \frac{\partial B_x}{\partial z} - B_z \cdot \frac{\partial B_z}{\partial x} - B_y \cdot \frac{\partial B_y}{\partial x} + B_y \cdot \frac{\partial B_x}{\partial y} \right) dV \quad (5.37)$$

Considering the following vector:

$$\mathbf{R}_x = \frac{1}{\mu_0} \cdot \left( \mathbf{x} \cdot \frac{B_z^2 - B_y^2 - B_z^2}{2} + \mathbf{y} \cdot B_x \cdot B_y + \mathbf{z} \cdot B_z \cdot B_x \right) \quad (5.38)$$

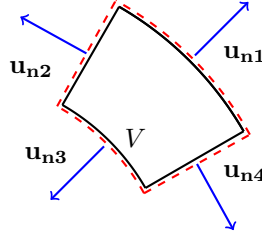


FIGURE 5.5: Iron pole: the Maxwell stress tensor is integrated on the surface with is the extrusion of the red border in the  $z$  direction.

and its divergence results:

$$\begin{aligned}\nabla \cdot R_x &= B_x \left( \frac{\partial B_x}{\partial x} + \frac{\partial B_y}{\partial y} + \frac{\partial B_z}{\partial z} \right) - B_y \frac{\partial B_y}{\partial x} - B_z \frac{\partial B_y}{\partial x} + B_y \frac{\partial B_x}{\partial y} + B_z \frac{\partial B_x}{\partial z} \\ &= -B_y \frac{\partial B_y}{\partial x} - B_z \frac{\partial B_y}{\partial x} + B_y \frac{\partial B_x}{\partial y} + B_z \frac{\partial B_x}{\partial z}\end{aligned}\quad (5.39)$$

The force along the  $\mathbf{x}$  direction can be expressed as:

$$F_x = \frac{1}{\mu_0} \cdot \int_V \nabla \cdot \mathbf{R}_x dV = \frac{1}{\mu_0} \cdot \int_S \mathbf{R}_x \cdot \mathbf{n} \cdot dS \quad (5.40)$$

where  $\mathbf{n}$  is the normal of the integration path shown in Fig. 5.5. The global force is computed as:

$$\mathbf{F}_{xyz} = \frac{1}{\mu_0} \cdot \int_S \mathbf{R} \cdot \mathbf{n} \cdot dS \quad (5.41)$$

where  $R$  is the Maxwell stress tensor:

$$R_{xyz} = \begin{pmatrix} \frac{B_x^2 - B_y^2 - B_z^2}{2} & B_x \cdot B_y & B_x \cdot B_z \\ B_y \cdot B_x & \frac{B_y^2 - B_x^2 - B_z^2}{2} & B_y \cdot B_z \\ B_x \cdot B_z & B_z \cdot B_y & \frac{B_z^2 - B_x^2 - B_y^2}{2} \end{pmatrix} \quad (5.42)$$

In a similar way the Maxwell stress tensor is derived for a cylindrical coordinate system:

$$R_{r\theta z} = \begin{pmatrix} \frac{B_r^2 - B_\theta^2 - B_z^2}{2} & B_r \cdot B_\theta & B_r \cdot B_z \\ B_r \cdot B_z & \frac{B_\theta^2 - B_r^2 - B_z^2}{2} & B_r \cdot B_\theta \\ B_\theta \cdot B_z & B_r \cdot B_\theta & \frac{B_z^2 - B_r^2 - B_\theta^2}{2} \end{pmatrix} \quad (5.43)$$

and the force expression is:

$$\mathbf{F}_{r\theta z} = \frac{1}{\mu_0} \cdot \int_S \mathbf{R}_{r\theta z} \cdot \mathbf{n} \cdot dS \quad (5.44)$$

The global radial force is given only by the contributes calculated on the segments 1 and 3:

$$F_r = \int_{\theta_1}^{\theta_2} \frac{B_r^2}{2\mu_0} \cdot L \cdot r \cdot d\theta - \int_{\theta_1}^{\theta_2} \frac{B_r^2}{2\mu_0} \cdot L \cdot r_2 \cdot d\theta \quad (5.45)$$

and the tangential force (positive anticlockwise) is:

$$F_\theta = \int_{r_1}^{r_2} \frac{B_{\theta 1}^2}{2\mu_0} \cdot L \cdot dr - \int_{r_1}^{r_2} \frac{B_{\theta 2}^2}{2\mu_0} \cdot L \cdot dr \quad (5.46)$$

The cylindrical forces are useful to compute the displacements of the iron poles. If the  $xy$  components are required considering the barycentre coordinates the following equation can be

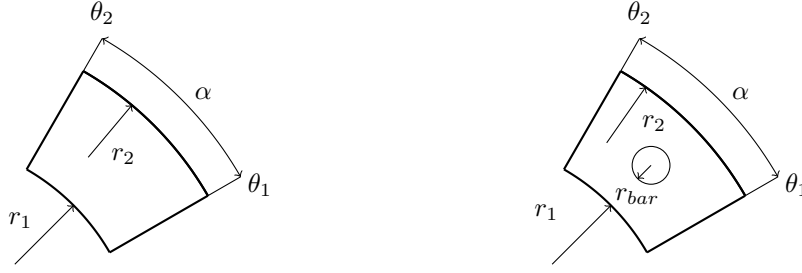


FIGURE 5.6: Iron pole geometry without and with structural rod.

adopted:

$$\begin{cases} F_x = F_r \cdot \cos \theta_{barycentre} - F_\theta \cdot \sin \theta_{barycentre} \\ F_y = F_r \cdot \sin \theta_{barycentre} + F_\theta \cdot \cos \theta_{barycentre} \end{cases} \quad (5.47)$$

## 5.4 Mechanical deformations

In order to calculate the mechanical deformations of the ferromagnetic poles, the mechanical structure and its stiffness need to be known. Two different cases are considered in this thesis. In the former the pole pieces are considered to withstand the electro-magnetic forces alone without additional structures. This is the case for example of solid pole pieces. In the latter case, circular rods are inserted inside the pole pieces, thus the pole stiffness is supposed to be only due to the bars. Different cases can be easily solved once the equivalent bending moments are evaluated.

### 5.4.1 Solid poles case

In this case the poles withstand the forces without additional rods, thus the inertias that have to be considered are the ones of the iron pole itself. This is the case of [46], where solid poles were adopted. This would also be the case of iron poles made by soft magnetic composites (SMC): because of the recent developments on high-strength composites [171], a solution for the flux modulator realization could adopt SMCs, as shown in [152].

The area of the iron pole is computed as:

$$A = \int_{\theta_1}^{\theta_2} \int_{r_1}^{r_2} r \cdot dr \cdot d\theta = \alpha \cdot \frac{r_2^2 - r_1^2}{2} \quad (5.48)$$

The barycentric radius can be computed as the  $x$  static moment when  $\theta_1 = -\theta_2$ . The relation is:

$$x_b = \frac{\int_A r^2 \cos \theta d\theta dr}{A} = \frac{4}{3 \cdot \alpha} \frac{r_2^3 - r_1^3}{r_2^2 - r_1^2} \sin \frac{\alpha}{2} \quad (5.49)$$

The second order moments can be computed as:

$$I_\theta = \int_{r_1}^{r_2} \int_{\theta_1}^{\theta_2} r^3 \cdot \sin^2 \theta d\theta dr = \left( \frac{1}{2} \alpha - \frac{\sin(2 \cdot \alpha)}{4} \right) \left( \frac{r_2^4 - r_1^4}{4} \right) \quad (5.50)$$

$$I_r = \int_{r_1}^{r_2} \int_{\theta_1}^{\theta_2} r^3 \cdot \cos^2 \theta d\theta dr = \left( \frac{1}{2} \alpha + \frac{\sin(2 \cdot \alpha)}{4} \right) \left( \frac{r_2^4 - r_1^4}{4} \right) - \frac{\alpha}{2} (r_2^2 - r_1^2) \cdot x_b \quad (5.51)$$

### 5.4.2 Stiffness rods case

The additional rods are supposed to be in the center of the iron poles as depicted in Fig. 5.6. An additional hypothesis is to consider that the ferromagnetic laminates do not contribute to the mechanical stiffness of the assembly. Hence, the inertias calculated along the radial and

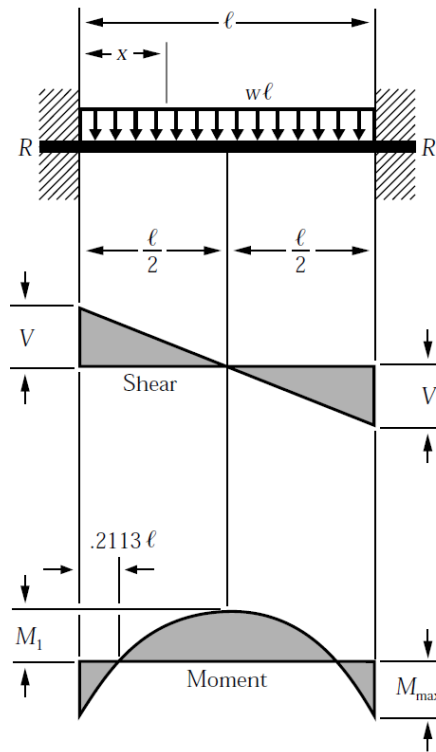


FIGURE 5.7: Iron pole considered as a beam fixed at both the extremities.

tangential directions  $I_r$  and  $I_\theta$  are equal to:

$$I_\theta = I_r = \frac{\pi r_{bar}^4}{4} \quad (5.52)$$

where  $r_{bar}$  is the radius of the bar.

### 5.4.3 Displacements and stresses

Considering the magnetic forces as distributed loads acting on a beam fixed at both extremities (see Fig. 5.7), the maximum displacement  $\Delta_{max}$  occurs in the middle of the beam:

$$\Delta_{max} = \frac{w \cdot L^4}{384 \cdot E \cdot I} \quad (5.53)$$

where  $E$  is the equivalent Young modulus of the structure in the  $z$  direction and  $I$  is the moment of inertia. This approach is generally followed with isotropic materials: the hypothesis is still valid with iron poles made with moulding compound materials (SMC), but because of the anisotropy this approach is theoretically incorrect when dealing with glued laminated sheets. This approach can still be applied using an equivalent Young modulus  $E$  along the axial direction that has to be evaluated experimentally. The maximum bending moment occurs at the extremities of the beam and can be expressed as  $M = \frac{w \cdot L^2}{12}$ . The global force can be calculated using the Maxwell stress tensor integration. In the hypothesis of radial and tangential forces applied on the barycentre projection in the  $z$  direction, the distributed forces are  $F_r = w_r \cdot L$  and  $F_\theta = w_\theta \cdot L$ . The global displacements are evaluated as:

$$\Delta_r = \frac{F_r \cdot L^3}{384 \cdot E \cdot I_r}, \quad \Delta_\theta = \frac{F_\theta \cdot L^3}{384 \cdot E \cdot I_\theta} \quad (5.54)$$

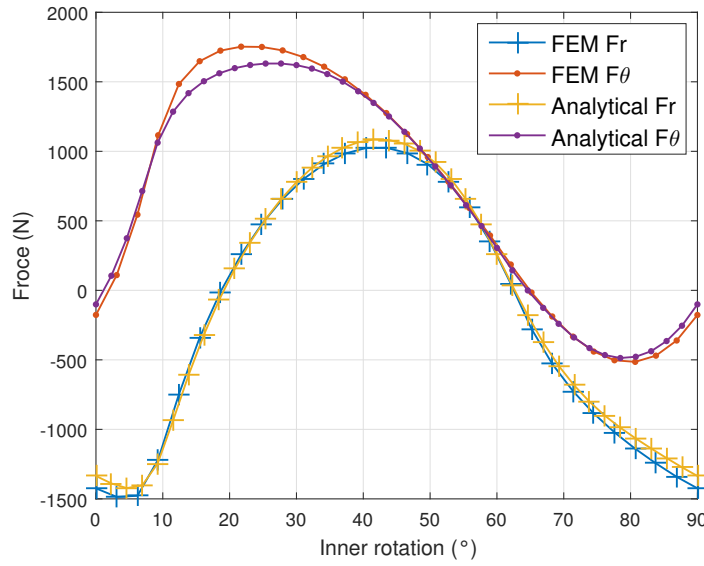


FIGURE 5.8: Validation of the analytic force model through linear FEM for the geometry in [61] varying the inner and outer rotor angles  $\theta_{in}$  and  $\theta_{out} = -\theta_{in} \cdot \frac{P_i}{P_o}$ . The initial position is set in order to obtain the maximum transmission torque, the radial force is positive if pointing towards the inner rotor.

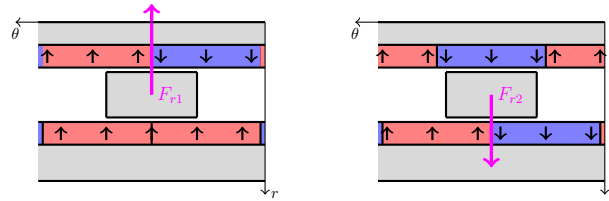


FIGURE 5.9: Linearized magnetic gear: maximum radial forces  $F_{r1}$  and  $F_{r2}$  for an high ratio magnetic gear ( $q \simeq P_o$ ). These alignments correspond to the positions  $\theta_{in} = 0$  and  $\theta_{in} = 45^\circ$  in Fig. 5.8: even if the hypothesis of high gear ratio is not verified, the radial force peaks match.

This procedure is valid in the hypothesis of long beams. If the machine is axially long ( $L \gg D$ ), the iron poles are typically immersed in plastic materials in order to obtain a stronger mechanical design (see Chapter 7): in this case the displacements have to be computed through more sophisticated FEM-based analysis for higher accuracy.

Fig. 5.8 shows the comparison between the analytically and FEM-computed forces acting on an iron pole for the geometry studied in [61] with gear ratio  $|G| = 1.5$ ; since the machine is axially short, the maximum radial displacement is  $\Delta_r \simeq 1\% \cdot \text{gapsize}$  far below the limit (here fixed to  $\Delta_{r-max} = 0.4 \cdot \text{gapsize}$  considering the Young modulus equal to  $E_{axial} = 100 \text{ GPa}$ ).

Fig. 5.9 and 5.10 show the positions of maximum and minimum radial and tangential forces in high ratio magnetic gears ( $|G| \geq 2.5$ ,  $q \simeq P_o$ ): the  $x$  axis represents the inner rotor angle  $\theta_{in}$ , the outer rotor angle is  $\theta_{out} = G \cdot \theta_{in}$  where  $G$  is the gear ratio. The plots are not in full accordance with Fig. 5.8 because the hypothesis of long machine are not fulfilled. The displacements relative to these positions can be evaluated easily, giving an immediate feedback about the design feasibility.

From the forces and the geometric parameters, the local stresses can be evaluated in the hypothesis of bulky iron poles (otherwise if laminates are considered, the cases of plain stresses or strain have to be discussed).

The stresses associated to the radial and tangential bending moments are calculated as:

$$\sigma_{zz}(Mr) = \frac{M_r}{W_r} = \frac{M_r}{I_r} \cdot d \quad (5.55)$$



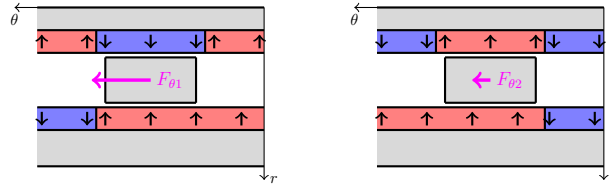


FIGURE 5.10: Linearized magnetic gear: maximum and minimum tangential forces for an high ratio magnetic gear ( $q \simeq P\theta$ ). These alignments correspond to the positions  $\theta_{in} = 27^\circ$  and  $\theta_{in} = 63^\circ$  in Fig. 5.8: the mismatch due to the low gear ratio is especially visible in  $F\theta2$ .

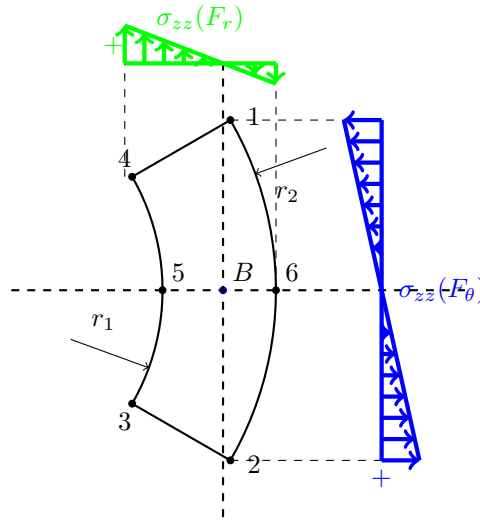


FIGURE 5.11: Iron pole stresses  $\sigma_{zz}$  due to the bending moments of the forces  $F_r$  and  $F_\theta$ .

$$\sigma_{zz}(M\theta) = \frac{M_\theta}{W_\theta} = \frac{M_\theta}{I_\theta} \cdot d \quad (5.56)$$

where  $d$  is the distance from the neutral axis,  $W$  is the bending flexibility and  $I$  is the inertia moment. An example of the stresses  $\sigma_{zz}$  due to the radial and tangential forces on a bulky iron pole are shown in Fig. 5.11. The barycentre location is also depicted and the stresses due to the bending moment vary linearly with the distance from the barycentre.

The stress equation that has to be verified in each point is for example according to the Von Mises criterion:

$$\sigma_{VM} = \sqrt{(\sigma_1 - \sigma_2)^2 + (\sigma_2 - \sigma_3)^2 + (\sigma_1 - \sigma_3)^2} \leq \sigma_{limit} \quad (5.57)$$

where  $\sigma_1$ ,  $\sigma_2$  and  $\sigma_3$  are the principal stresses computed in each point of the structure and  $\sigma_{limit}$  is the material limit stress. According to the previous hypothesis of axially-long machine and neglecting the shear stresses, (5.57) can be approximated to  $\sum \sigma_{zz} \leq \sigma_{limit}$ .

Fatigue analysis can also be performed, but these are beyond the scope of the thesis.

## 5.5 Thermal model

The thermal model is useful in order to understand if the temperatures exceed the limit values: these are generally the Curie temperatures, temperatures at which the PMs exhibit permanent demagnetization and other limits related to the structure. The general heat equation written in differential form is:

$$c_p \cdot \rho \cdot \frac{\partial T}{\partial t} = Q + \nabla \cdot \lambda \nabla T \quad (5.58)$$

where  $c_p$ ,  $\rho$ ,  $Q$  and  $\lambda$  are heat capacity, material density, local heat source and thermal conductivity respectively. A general analytic approach is based on equivalent thermal networks in analogy to the electrical networks: all the components are modelled through the thermal resistances and the thermal capacitances, while the power losses are modelled as current generators. Unfortunately the analytical model of rotating electrical machines is a challenging problem because the Navier Stokes equations are involved and secondary flows rise because of the rotational components of the air flows.

Several complicated thermal equivalent networks have been studied in literature; these networks try to fit the real behaviour using high number of components. In this case a simple network have been chosen, knowing that when the model complexity increases the finite element method provides more reliable results than the analytic model (that also requires a non-negligible effort for the components discretization).

The analytic network does not aim to fit exactly the real behaviour but only to give an idea of the temperatures order of magnitude.

### 5.5.1 Air flow distribution

In the general case, an air flux will be forced to flow through the machine airgaps; this air flow can be produced for example by a fan connected to the high speed rotor or by an external fan. The machine geometry can have different sections where the air is free to flow: if the inner rotor is hollow one channel is the inner hollow cylinder, the other paths are given by the inner and outer airpags and the external rotor-box airgap. In order to increase the iron poles stiffness, the inter-pole space can be filled with mechanically performant materials (see Fig. 5.12); in this case the inner and outer gaps are split and two independent channels are formed. The air flow therefore has to be split between the channels and the axial speed in each one depends on the gear geometry and hydraulic losses, function of the rotational speeds. The first step is the computation the air repartition between the channels. In the hypothesis of axially-imposed air flux, the fluid flow in each channel can be supposed to be only due to the hydraulic conditions (pressure, velocity, hydraulic losses), while the change of fluid density can be neglected (thus the natural convection phenomenon are neglected). The classical fluid loss equation for pipe flows is given by:

$$\Delta p = \frac{\lambda(Re, \epsilon_r, d_H)}{d_H} \cdot L \cdot \rho \cdot v_{axial}^2 \quad (5.59)$$

where  $d_H$  is the hydraulic diameter,  $Re$  is the Reynolds number and  $\epsilon_r$  is the relative roughness,  $L$  is the axial length,  $\rho$  the gas density and  $v_{axial}$  is the air speed in the axial direction. A well-known relation for the friction factor  $\lambda$  has been introduced by Colebrook [172]:

$$\frac{1}{\sqrt{\lambda}} = -2 \cdot \log_{10} \left( \frac{\epsilon_r}{3.7d_H} + \frac{2.523}{Re\sqrt{\lambda}} \right) \quad (5.60)$$

Supposing that the Reynolds number due to axial and tangential velocities is higher than the laminar to turbulent transition, the  $\lambda$  factor can be calculated in several ways as reported in [173], e.g. with the approximation:

$$\lambda = \frac{0.25}{\log_{10}^2 \left( \frac{\epsilon_r}{3.7} + \frac{5.4}{Re^{0.9}} \right)} \quad (5.61)$$

The axial Reynolds number is calculated as:

$$Re = \frac{\rho \cdot v_{axial} \cdot d_H}{\mu} \quad (5.62)$$

where  $\mu$  is the fluid dynamic viscosity. In order to keep into account the air swirl motion, an additional coefficient have been introduced in [174]:

$$k_{corrective} = \left( 1 + \left( \frac{7}{8} \right) \cdot \left( \frac{\omega \cdot r}{2 \cdot v_{axial}} \right)^2 \right)^{0.38} \quad (5.63)$$

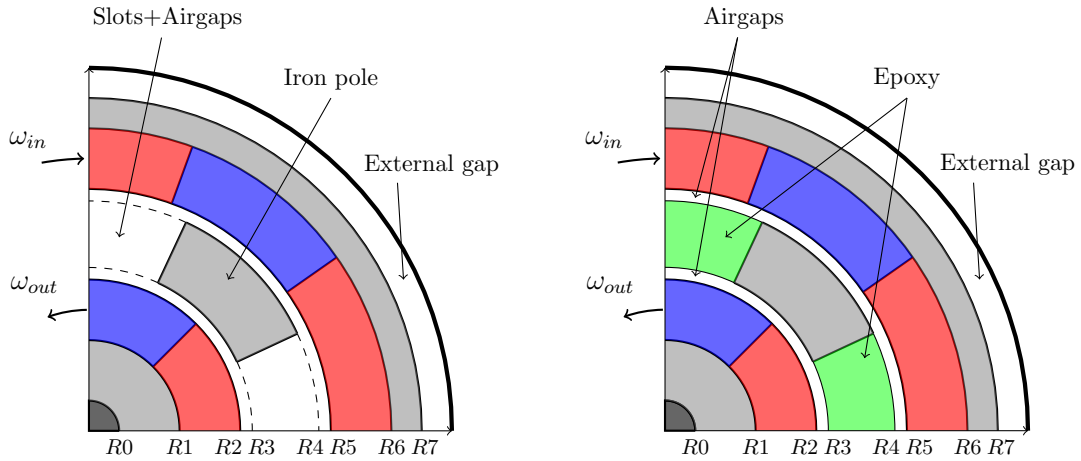


FIGURE 5.12: Air flow cross sections with 2 channels (left) or 3 channels (right).

where  $\omega \cdot r$  is the tangential rotor speed. This equation has been introduced for the case of air flow passing through an annular gap with the inner cylinder kept into rotation. Additional shock losses have been estimated in [174] when the axial Reynolds number range between (2300-12000) as:

$$k_{shock} = 0.043 \cdot \left( \frac{\omega r}{v_{axial}} \right)^2 \quad (5.64)$$

therefore the overall loss factor becomes:

$$\lambda_{rot} = \frac{0.25}{\log_{10} \left( \frac{\epsilon_r}{3.7} + \frac{5.4}{Re^{0.9}} \right)} \cdot \left( \left( 1 + \left( \frac{7}{8} \right) \cdot \left( \frac{\omega r}{2 \cdot v_{axial}} \right)^2 \right)^{0.38} + 0.043 \cdot \left( \frac{\omega r}{v_{axial}} \right)^2 \right) \quad (5.65)$$

The loss factor is a function of  $\epsilon_r, r, v_{axial}$ . Considering a magnetic gear with a bulky inner rotor, there can be 2 or 3 airgaps where the air can circulate depending on the structure (see Fig. 5.12). The solution with 2 airgaps is obtained if the iron poles are completely surrounded by air (slots are not filled), thus the two gear airgaps are connected and the external airgap is the one between the external box and the outer rotor. The second solution is obtained when the slots are filled with reinforcing fibers. In this case the outer air will be divided between 3 paths and the speed in each one have to be calculated fixing the same pressure drop along the three channels. Combining (5.59) and (5.65), the nonlinear equation to be solved reads:

$$\frac{\lambda_{rot1}(v_1)}{d_{H1}} L \rho v_1^2 = \frac{\lambda_{rot2}(v_2)}{d_{H1}} L \rho v_2^2 = \Delta p^{ext} \quad (5.66)$$

where  $\lambda_{rot1}$  and  $\lambda_{rot2}$  are the friction loss coefficients, while  $\Delta p^{ext}$  is the externally imposed pressure (for example, due to a fan).

The expressions that have been reported are based on empirical coefficients found for simple cases. The solutions  $v_1$  and  $v_2$  of (5.66) can give inaccurate results for the real complex cases. For finer calculations, the use of other numerical methods (e.g. finite elements or finite volumes) is recommended since several coupled effects are involved and the swirl flow with Taylor vortices is still challenging.

### 5.5.2 Thermal resistance

Once the axial velocities in each channel have been computed from Sec. 5.5.1, the equivalent thermal resistances and capacitances can be calculated to complete the thermal analysis. The thermal resistance concept derives from the Fourier's law:

$$q = -\lambda \cdot \nabla T \quad (5.67)$$

where  $\lambda$  is the thermal conductivity and  $T$  is the temperature variable. When  $\lambda$  is constant and the heat propagating direction is known, the 1D Fourier's expression reads:

$$q_x = -\lambda \cdot S \cdot \frac{\Delta T}{\Delta x} = -\lambda \cdot S \cdot \frac{T_1 - T_2}{d} = \frac{T_1 - T_2}{R_{th}} \quad (5.68)$$

where  $R_{th} = \frac{d}{\lambda \cdot S}$  is the thermal resistance,  $d$  is the thickness in the propagating direction,  $S$  is the area crossed by the heat flux and  $T_1$  and  $T_2$  are the temperatures at the extremities. The thermal resistance of cylindrical objects is found as:

$$R_{th} = \int_{R1}^{R2} \frac{dr}{\lambda \cdot r \cdot \alpha \cdot L} = \frac{1}{\lambda \cdot L \cdot \alpha} \cdot \log \left( \frac{R_2}{R_1} \right) \quad (5.69)$$

where  $\alpha$  is the angular length of the arc ( $\alpha = 2\pi$  if the object is an annulus). The iron yokes, magnets, iron poles and shaft thermal resistances are calculated according to (5.69).

The most difficult contribution to be estimated is the convective heat exchange of a rotating object. The thermal resistance between a solid surface and a fluid is:

$$R_{th} = \frac{1}{\alpha \cdot S} \quad (5.70)$$

where  $\alpha$  is the heat transfer coefficient and  $S$  is the area subjected to convection. The heat transfer coefficient normally requires precise numerical approaches in order to be correctly estimated (see [175] for an example of simulation setup) and because of the problem complexity the solution proposed in this Section is considered as a rough estimation of the real one.

Adopting the approaches already available for electrical machines [176],[177], dimensionless numbers are introduced to describe the heat exchange. The Nusselt number represents the ratio between convective and conductive heat transfer:

$$\alpha = \frac{\lambda_{air} \cdot Nu}{d_h} \quad (5.71)$$

where  $d_h = \delta \cdot \sqrt{\frac{8}{3}}$ .  $Nu = 2$  corresponds to laminar flow, while with higher speeds or uneven surfaces the parameter tends to grow.

In order to assess the heat exchange between moving objects, another dimensionless parameter has to be introduced. The Taylor's number is the ratio between centrifugal forces due to the rotation and the viscous forces and the calculation gives:

$$Ta = \frac{\rho_{air}^2 \cdot \omega^2 \cdot r_g \cdot \delta^3}{\mu^2} \quad (5.72)$$

where, in accordance to the previous notation,  $\rho_{air}$  is the air density,  $\omega$  is the rotor speed,  $r_g$  is the middle radius,  $\delta$  is the airgap length and  $\mu$  is the air dynamic viscosity. Increasing the Taylor's number above a certain threshold, the Couette flow evolves and axisymmetric toroidal vortex emerges, turning the flow to Taylor's flow. In order to keep into account the Taylor-Couette flow, a modified parameter  $Ta_1$  is evaluated [176]:

$$Ta_1 = Ta \cdot \frac{1697 \cdot \left( 0.0056 + 0.0571 \cdot \left( \frac{2 \cdot r_g - 2.304 \cdot \delta}{2 \cdot r_g - \delta} \right)^2 \right) \cdot \left( 1 - \frac{\delta}{2 \cdot r_g} \right)}{\pi^4 \left( \frac{2 \cdot r_g - 2.304 \delta}{2 \cdot r_g - \delta} \right)} \quad (5.73)$$

The Nusselt number is:

$$\begin{cases} Nu = 2 & Ta_1 < 1700 \\ Nu = 0.128 \cdot Ta_1^{0.367} & 1700 < Ta_1 < 10^4 \\ Nu = 0.409 \cdot Ta_1^{0.241} & 10^4 < Ta_1 < 10^7 \end{cases} \quad (5.74)$$

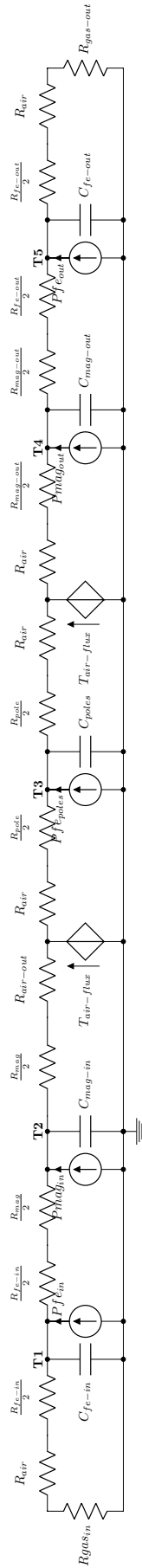


FIGURE 5.13: Thermal network implemented. All the components are depicted as electrical components.

When the rotational speed is high  $Ta_1 > 10^7$  the Nusselt number becomes:

$$Nu = 0.0214 \cdot \left( \left( \frac{\rho \cdot v_r \cdot d_h}{\mu} \right)^{0.8} - 100 \right) \cdot Pr^{0.4} \cdot \left( 1 + \left( \frac{d_h}{L} \right)^{0.66} \right) \quad (5.75)$$

$$v_r = \sqrt{\left( \frac{\omega R}{2} \right)^2 + v_{axial}^2} \quad (5.76)$$

Substituting all the parameters in (5.71), the  $\alpha$  parameter is known and the air thermal resistance can be modelled.

After the calculation of the air equivalent thermal resistance, the air temperature has to be computed in order to solve the model. Considering that the inlet air flux is split in inner air, poles air and outer air three different temperatures will be considered respectively. The temperature raise is:

$$\Delta T = \frac{Q}{c_{air} \cdot \rho_{air} \cdot v_{axial} \cdot S} \quad (5.77)$$

where  $Q$  is the heat flux,  $c_{air}$  is the air specific heat,  $\rho_{air}$  is the air density,  $v_{axial}$  is the air axial speed and  $S$  is the cross section. Since the temperature generator depends on the heat flux, the cooling air flux can be modelled as a thermal resistance. The expressions for the thermal resistances  $R_{gas-in}$  and  $R_{gas-out}$  are therefore:

$$R_{gas} = \frac{\Delta T}{Q} = \frac{1}{c_{air} \cdot \rho_{air} \cdot v_{axial} \cdot S} \quad (5.78)$$

In the poles zone, two temperature generators have to be used, but in the hypothesis of perfect air mixing (reasonable considering the turbulent flow with open slots) the two impressed temperatures will be the same. This temperature value depends on the global heat flux adsorbed by the air flow, thus two driven temperature generators have been used. In particular, the temperature  $T_{air-flux}$  is:

$$T_{air-flux} = \frac{Q1 + Q2}{c_{air} \cdot \rho_{air} \cdot v_{axial} \cdot S} \quad (5.79)$$

where  $Q1$  and  $Q2$  are the heat fluxes flowing through the driven generators. The two terms can be easily modelled through the thermal resistance matrix as off-diagonal terms.

### 5.5.3 Capacitance

The knowledge of the thermal resistances allows to find the temperature distribution in stationary conditions. The time domain temperature can also be computed if the equivalent thermal capacity is assessed. The general expression is:

$$C_{th} = \int_V \rho \cdot c_{sp} \cdot dV \quad (5.80)$$

where  $\rho$  is the material density and  $c_{sp}$  is the specific heat.

### 5.5.4 Matrix notation

The general Tableau for the thermal network solution is:

$$\begin{aligned} & \begin{bmatrix} [A]_{n-1 \times l} & [0]_{n-1 \times l} & [0]_{n-1 \times n-1} \\ [0]_{l \times l} & [-1]_{l \times l} & [A]_{l \times n-1}^t \\ [R_{th}]_{n-1 \times l}^t & [G_{th}]_{n-1 \times l}^t & [0]_{n-1 \times n-1}^t \end{bmatrix} \cdot \begin{bmatrix} [q]_l \\ [\Delta T]_l \\ [T]_{n-1} \end{bmatrix} + \\ & + \begin{bmatrix} [0]_{n-1 \times l} & [0]_{n-1 \times l} & [0]_{n-1 \times n-1} \\ [0]_{l \times l} & [0]_{l \times l} & [0]_{l \times n-1}^t \\ [0]_{n-1 \times l}^t & [C_{th}]_{n-1 \times l}^t & [0]_{n-1 \times n-1}^t \end{bmatrix} \cdot \frac{d}{dt} \begin{bmatrix} [q]_l \\ [\Delta T]_l \\ [T]_{n-1} \end{bmatrix} = [0]_{2l+n-1,1} \end{aligned} \quad (5.81)$$

Parameter	Symbol	Value	Unit
Fe conductivity	$\lambda_{Fe}$	25	$\frac{W}{mK}$
PM conductivity	$\lambda_{PM}$	9	$\frac{W}{mK}$
Air conductivity	$\lambda_{air}$	0.024	$\frac{W}{mK}$
Shaft conductivity	$\lambda_s$	40	$\frac{W}{mK}$
Air density	$\rho_{air}$	1.3	$\frac{kg}{m^3}$
Air dyn. viscosity	$\nu_{air}$	$1.95e - 5$	Pas
Prandtl air	$Pr$	0.75	-

TABLE 5.1: Parameters adopted for the thermal modelling of the magnetic gear.

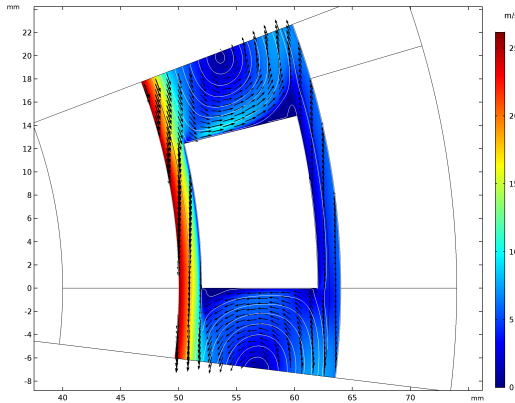
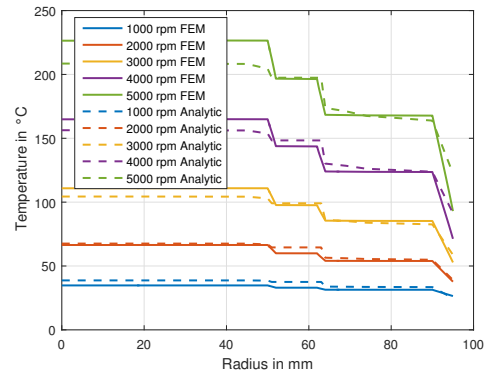
FIGURE 5.14: Fluid dynamic simulation of the magnetic gear with empty slots. The FEM simulations, for simplicity, are 2D. The turbulence model adopted is the RANS algebraic  $\gamma$ Plus of Comsol Multiphysics [94].

FIGURE 5.15: Parametric temperature variation with the radial dimension for the case without slots computed with Comsol and with the analytic procedure proposed in this Section.

where  $q$  and  $\Delta T$  are the heat fluxes and temperature drop on each branch,  $T_j$  is the  $j^{th}$  nodal temperature,  $A$  is the incidence matrix,  $R_{th}$  is the thermal resistance matrix,  $G_{th}$  is the thermal conductance matrix. The proposed thermal network is the one depicted in Fig. 5.13. The solution of (5.81) allows to compute the temperature in each gear domain. These temperatures normally have to be compliant to the PMs requirements or the maximum temperatures that the insulation material can withstand. The constraints are formulated as:

$$T_{domain} \leq T_{max-domain} \quad (5.82)$$

### 5.5.5 Thermal model validation

As extensively highlighted in this Chapter, the thermal model validation requires complicated analysis that involve the coupling between fluid dynamics and thermal physics. In order to simplify the computation, a 2D machine model is adopted for the case of magnetic gear with open slots, while a 2D axisymmetric model can be adopted in the case of filled slots. The Taylor vortex cannot be seen in a simple 2D simulation (vortex are intrinsic 3D phenomena), but the 2D axisymmetric case can model the swirl flow and these vortex.

For the analytic model validation, the magnetic gear of Fig. 4.58 is considered. The slots are considered empty, thus the air is free to circulate between airgaps and slots, while the axial flux is fixed to  $v_{axial} = 1.5$  m/s in the casing gap and considered as negligible in the gear airgaps (no imposed axial flux). The thermal parameters are summarized in Tab. 5.1.

Fig. 5.14 shows the FEM velocity map in the airgaps and slots and the streamline plot. The counter-rotating effect produces  $q$  vortex in the  $q$  slots that increase the ventilation losses in the trasmission. In Fig. 5.15 the comparison between the FEM-computed and analytically-computed temperatures is reported for different values of the inner rotational speed (the outer is set to the correspondent steady state value). The results match with a reasonable approximation.





## Chapter 6

# Optimized gear design

In order to obtain a competitive device, the magnetic gear has to be optimized. Depending on the application requirements, the objectives can be different e.g. overall weight, dimensions, torque density, torque ripple, magnet quantity, efficiency. The optimization variables are all the geometrical dimensions, the number of inner or outer poles and the materials used to build the magnetic gear.

The problem to be solved is heavily constrained. The constraints can be divided in two categories: the explicit ones depend directly on variables or functions of variables and their evaluation does not require any simulation results while the implicit ones involve the objectives or other quantities computed through the simulation results. While the former can be checked directly before evaluating the objective function, the latter can be verified only after the objective function has been calculated and thus computational resources have been spent. In the case of real constrained problems, such as the present one, the probability of unfeasible population members is generally high due to both implicit and explicit constraints. The detection of constraint violations at the beginning of the parallel function evaluation reduces memory and processor usage significantly. Depending on the adopted parallel structure, the population size can be chosen to be bigger than the number of computational cores relying on the fact that in each iteration some individuals will be unfeasible.

Depending on the model accuracy, several constraints can be included.

The key is therefore to find an algorithm that allows to find  $n$ -dimensional Pareto's fronts for  $k$ -dimensional problems.

Optimization problems can be solved generally adopting different strategies:

- deterministic algorithms;
- stochastic algorithms;
- genetic algorithms.

Deterministic methods start the research from a seed point and then the consecutive points are chosen according to some gradient expressions; an example could be the steepest descent method and the conjugate gradient method. Stochastic methods are based on evolutionary schemes: they do not involve the derivatives calculation but they follow the "survival of the fittest" rule. Common examples are the particle swarm optimization PSO and differential evolution DE.

In this Chapter, a Differential Evolution algorithm has been chosen for the magnetic gear optimization.

In Sec. 6.1, the complexity definition of a general optimization problem is stated.

Sec. 6.2 reports the DE implementation and discusses how to implement the constraints.

In Sec. 6.3 the optimization problem is formulated with the identification of constraints and objective functions.

Sec. 6.4 reports the optimization results for a single-stage magnetic gear, while in 6.5 a multi-stage gear is optimized and discussed.

Finally, in Sec. 6.6 mechanical and optimized-magnetic solutions are compared.

The results shown in this Chapter have also been published in [71, 91, 178, 179, 180].

<i>Problem type</i>	<i>Verifiable in P time</i>	<i>Solvable in P time</i>	<i>Complexity</i>
<i>P</i>	<i>Yes</i>	<i>Yes</i>	<i>+</i>
<i>NP</i>	<i>Yes</i>	<i>Yes – No*</i>	<i>++</i>
<i>NP – complete</i>	<i>Yes</i>	<i>Unknown</i>	<i>+++</i>
<i>NP – Hard</i>	<i>Yes – No**</i>	<i>Unknown***</i>	<i>++++</i>

TABLE 6.1: Summary of optimization complexity. (\*): NP problem which is also P is solvable in P time; (\*\*) NP-Hard problem which is also NP-Complete is verifiable in P time; (\*\*\*) NP-Complete problem might be solvable in P time, the rest NP-Hard are not solvable in P time.

## 6.1 Complexity definition

According to [181], if one word is used to differentiate between easy and hard problems, convexity is probably the "watershed". A set  $X \subset \mathfrak{R}^n$  is said to be convex if all the segments are inside  $X$ :

$$\forall(x, y, \alpha) \in X \times X \times [0, 1], (1 - \alpha)x + \alpha y \in X$$

The same property can be defined for a function  $f : X \rightarrow \mathfrak{R}$ :

$$\forall(x, y, \alpha) \in X \times X \times [0, 1], f((1 - \alpha)x + \alpha y) \leq f((1 - \alpha)x) + \alpha f(y)$$

which means that all the chords are above the function  $f$ . In convex problems if  $x$  is a local minimum of  $f$  then  $x$  is also a global minimum of  $f$ : the optimization of such problems can be performed using fast gradient-based approaches. When dealing with engineering problems most of the times the objective functions and-or constraints are nonconvex and therefore the problems are hard. Since convexity is not topological invariant under change of variables [181] a diffused technique is the transformation of the problem to an equivalent convex one. This method is problem-dependent and cannot be applied to arbitrary object functions.

Randomized heuristic algorithms are robust problem-independent search strategies. This is an important advantage if the objective function is not known or when there is no knowledge to build a problem-dependent algorithm. The algorithm efficiency is evaluated on the time required to find the optimal solution: the method is efficient if the solution time is bounded above by a polynomial function of the problem size.

A classification of the optimization problems have been adopted in the computer combinatorial fields. If a decision problem is in the **P** class, there is an algorithm capable of solving it in polynomial time. If the problem belongs to **NP-Hard** class, then it is not expected that an algorithm can find a solution in polynomial time unless **P=NP** (that still have to be proven, but the equivalence is considered unlikely) [182]. A brief summary of the optimization complexity is depicted in Tab. 6.1.

The magnetic gear optimization is in general NP-Hard with non-convex constraints and objective functions. Because of these reasons, the stochastic approaches are generally adopted for the electrical machine case, and in this thesis a Differential Evolution strategy is implemented for the gear optimization.

## 6.2 Differential Evolution strategy

Evolution strategies and genetic algorithms try to imitate the natural evolutionary behavior. These method are "zeroth order" and hence function derivative calculations are not involved. This feature is particularly useful when the optimization is non-convex and the variables are integer, discontinuous and discrete. Evolutionary strategies can also be easily run in parallel; the main drawback is the high number of evaluations of the objective function and the parameters tuning which is non trivial.

### 6.2.1 Mutation and crossover

Mutation and crossover are the essential components of the Differential Evolution method [183]. Starting from an initial random population, mutation is applied as follows:

$$y_i^{t+1} = x_{a1}^t + F \cdot (x_{a2}^t - x_{a3}^t) \quad (6.1)$$

where  $x_{a1}^t, x_{a2}^t, x_{a3}^t$  are the variable vectors of 3 randomly chosen population members  $a1, a2, a3$  taken at generation  $t$ ; the result  $y_i^{t+1}$  is the  $i$ th of  $m$  elements. The crossover operator allows to combine a previous element  $x_i^t$  with a mutated element  $y_i^{t+1}$  through a random procedure:

$$u_{i,j}^{t+1} = \begin{cases} y_{i,j}^{t+1} & \text{if } \text{frand}_{i,j} \leq CR \\ x_{i,j}^t & \text{otherwise} \end{cases} \quad (6.2)$$

where  $t + 1$  indicates next generation and the elements  $u^{t+1}$  are the result of mutation and crossover operation.

One of the main problems in evolution strategies is the choice of the control parameters: in the case of DE mutation and crossover have to be set in order to prevent premature convergence or stagnation and to ensure an acceptable convergence ratio towards the global optimum. Since in DE the perturbation is based on differences between population elements, when the population loses diversity the perturbation vanishes and therefore the algorithm stagnates. In order to avoid premature convergence it is important to calculate the population diversity e.g. by measuring the variance.

According to [184] if  $x = (x_1, x_2 \dots x_m)$  is the current population,  $y = (y_1, y_2 \dots y_m)$  is the intermediate population after applying mutation and  $u = (u_1, u_2 \dots u_m)$  is the population obtained crossing  $x$  and  $y$ , the expected values  $E()$  are:

$$E(\text{Var}(y)) = \left(2F^2 + \frac{m-1}{m}\right) \text{Var}(x) \quad (6.3)$$

$$E(\text{Var}(u)) = \left(2F^2CR - \frac{2CR}{m} + \frac{CR^2}{m} + 1\right) \text{Var}(x) \quad (6.4)$$

where  $CR$  is the crossover probability,  $m$  is the population size,  $F$  is the mutation coefficient and  $\text{Var}$  is the variance  $\text{Var}(x) = E[(x - \bar{x})^2]$ . If  $2F^2CR - \frac{2CR}{m} + \frac{CR^2}{m} < 0$  the population variance tends to decrease after mutation and crossover otherwise the variance tends to increase; this relation has been implemented in order to guarantee an increase the variance.

According to [185], in order to improve the population distribution, NSGA-II concepts have been implemented: in each step the current individuals and the ones stored inside an archive are ranked in fronts and the elements on the same fronts are ordered according to their crowding distance.

### 6.2.2 Constraints handling

Since multiple constraints handling procedures have been introduced in the algorithm, the benchmark problems *CF6* and *CF7* [186] have been used in order to test the performances. The benchmark variable space has the same dimension of the magnetic gear case and the objectives are non-convex subjected to non-convex constraints. The maximum number of iterations in the CEC contest was fixed to  $n_{max} = 300k$ .

Three different algorithms have been tested and the results are shown in Fig. (6.1)-(6.6) and in Table 6.2. *DE-direct* is a simple DE algorithm with the NSGA-II concepts of multiple front ranking and crowding distance. *DE-direct+reseed* is similar to the *DE-direct* but additionally a population reseed scheme has been implemented: when the algorithm stagnates, the population is restarted keeping the previous Pareto front in an archive. *DE-indirect+reseed* scheme handles the constraints in an indirect way and reseeding is applied as in the previous algorithm.

Fig. 6.1, 6.2 and 6.3 show the results for *CF6*. The first part of the Pareto front is well approximated by all the algorithms; the constraints limit the second and third portion of the front. Clearly the simple direct implementation is really inefficient when constraints are present.

Problem	Algorithm	% unfeasible	IGD		
			Mean	Min	Max
CF-06	DE-direct	13.69	0.1266 ± 0.047	0.0406	0.1984
CF-06	DE-direct-reseed	16.8	0.0599 ± 0.029	0.0283	0.1182
CF-06	DE-indirect-reseed	27.42	0.0234 ± 0.0027	0.0186	0.0299
CF-07	DE-direct	12.11	0.3255 ± 0.1266	0.161	0.6982
CF-07	DE-direct-reseed	16.35	0.0881 ± 0.0335	0.0435	0.1583
CF-07	DE-indirect-reseed	29.81	0.0597 ± 0.0135	0.044	0.0858

TABLE 6.2: Direct and indirect optimization comparison on CEC-09 benchmarks [186]. Maximum iterations  $n = 300$ ,  $k = 300$ ,  $F = 0.5$ ,  $CR = 0.55$ ,  $Pop. size = 100$ . In the "reseed" versions population reseeding is applied when the algorithm stagnates.

Adding the reseeding scheme the performance improves but the standard deviation of the results is high. The indirect scheme guarantees better results with a far better standard deviation.

Fig. 6.4, 6.5 and 6.6 show the results relatively to the *CF7* benchmark. In this case the constraints are much more severe and the first approach can find only few points of the true front. The reseeding scheme gives a much better performance but the optimization results are affected by a high standard deviation. Again, the indirect procedure allows to find a better Pareto front approximation with lower standard deviations.

### NSGA-II directly constrained

The algorithm that has been implemented for magnetic gears is a non-dominated sorting genetic algorithm (NSGA-II) where the Pareto's front is split in multi-rank parts and crowding distances are calculated in order to obtain non-clustered solutions.

The variables on which the solver acts can be classified in geometrical and non-geometrical variables. The geometrical parameters are all the geometrical parameters of the gear in Fig. 4.58, while the non geometrical parameters are rotational speeds and materials generally.

The flag index represents the geometry feasibility: if its value is zero the geometry does not violate any constraint, otherwise at each failure a respective flag value is associated. When  $flag \neq 0$  the individual violates at least one constraint and the algorithm decides how to proceed. In case of number of failures during one iteration below a given number, the solver proceeds with the subsequent iterations. The new calculation can produce a new feasible or unfeasible individual starting from the previous. The flag can be included inside the domination calculation as follows:

- If both the points satisfies the constraints, the domination is computed according to the fitness;
- if one point is feasible while the other is unfeasible the feasible is considered as dominant;
- if both the points violate the constraints, the dominant is the one with the best fitness.

which is similar to an unfeasible elimination scheme. This criterion is easy to be implemented but the performance will be poor since the unfeasible areas are completely unexplored.

When the constraints are expressed as inequality constraints a different approach may be adopted given by the unfeasible solution sorting based on the degree of unfeasibility. In each step the bad points are ranked based on the RMS sum of distances from the constraints. For example given a set of inequality constraints  $\epsilon_i^j < c_i$  where  $i$  stands for the constraint number and  $j$  is the population individual identifier, the degree of unfeasibility of the individual  $j$  is  $\gamma^j = \sqrt{\sum_i \psi_i^j}$ , where:

$$\psi_i^j = \begin{cases} 0 & \text{if } \epsilon_i^j < c_i \\ (\epsilon_i^j - c_i)^2 & \text{otherwise} \end{cases} \quad (6.5)$$

In this implementation apart from the heuristic mutation  $F$ , crossover  $CR$  and population size  $Np$ , additional parameters have to be fixed such as the number of "bad points" in each iteration and the number of converted ones because of low rank index.

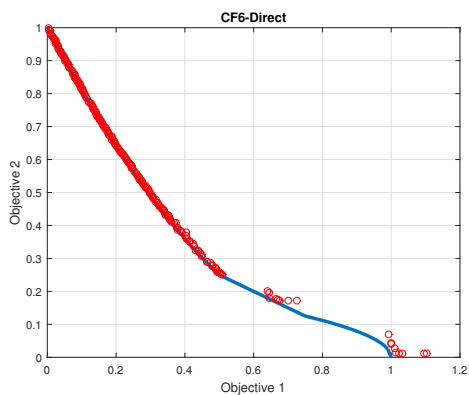


FIGURE 6.1: Direct implementation: minimum *IGD* Pareto front of the CF6 function [186].

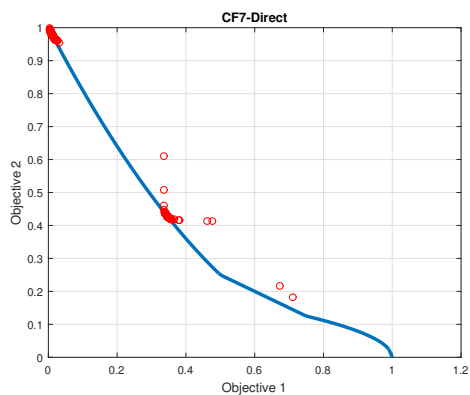


FIGURE 6.4: Direct implementation: minimum *IGD* Pareto front of the CF7 function [186].

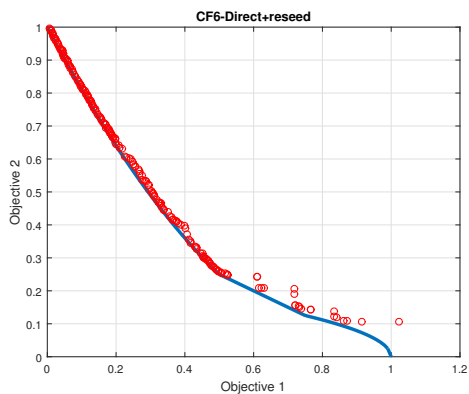


FIGURE 6.2: Direct implementation with reseeding scheme: minimum *IGD* Pareto front of the CF6 function [186].

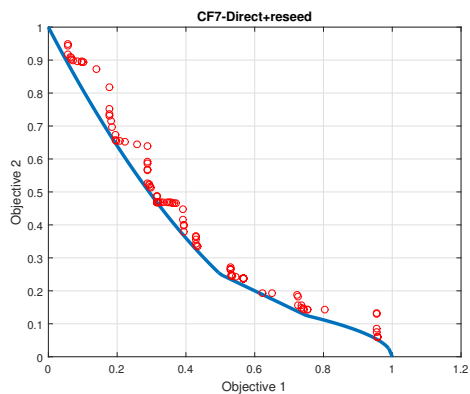


FIGURE 6.5: Direct implementation with reseeding scheme: minimum *IGD* Pareto front of the CF7 function [186].

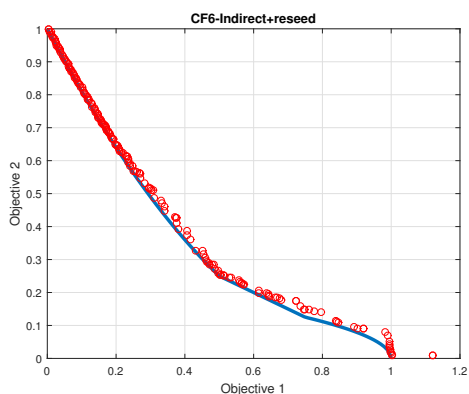


FIGURE 6.3: Indirect implementation with reseeding scheme: minimum *IGD* Pareto front of the CF6 function [186].

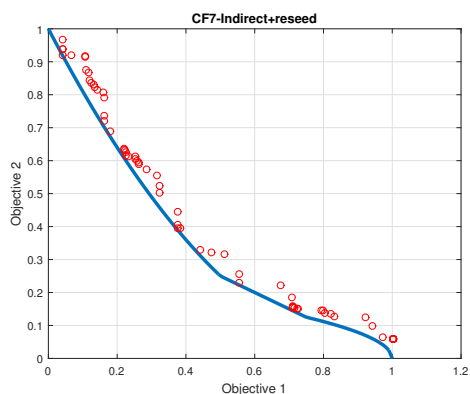


FIGURE 6.6: Indirect implementation with reseeding: minimum *IGD* Pareto front of the CF7 function [186].

### NSGA-II indirectly constrained

Another way to deal with constraints is the indirect implementation: in this case an additional object that represent the constraints violation is built. In this manner the population naturally drift through feasible regions, allowing in each iteration also unfeasible points that can be chosen for mutation and crossover.

In this implementation the control of the unfeasible points in each iteration is lost: if the constraints are too restrictive, the final solution could have a low populated feasible front and this is the main drawback of this implementation.

## 6.3 Optimization problem statement

Depending on the optimization targets (e.g. space limitation, weight limitation etc.), several objectives can be chosen. In this Section, three variables are chosen:

- Efficiency  $\eta$  to be maximized, computed with the approximated GSE approach in Sec. 4.6.3 for soft materials and with the approach in Sec. 4.7 for hard materials.
- Specific torque  $K_t$  to be maximized, computed according to (6.6);
- Number of inner pole pairs  $P_i$ , to be minimized.

The algorithm is designed to find global minima hence the efficiency and specific torque are considered as negative in order to keep the same calculation procedure independently of the objective functions.

The specific torque  $K_t$  is computed only considering the permanent magnets and magnetic iron weights  $\sum w_{mag}$  and  $\sum w_{iron}$ , neglecting the weight of the shafts and other mechanical components (such as gear housing, bearings, etc.):

$$K_t = \frac{\max(|T_{out}|)}{\sum w_{mag} + \sum w_{iron}} \quad (6.6)$$

The number of pole pairs  $P_i$  is both an optimization variable and an objective function: gears with low number of pole pairs are preferred since they are easier to assembly and they require bigger magnets if compared to gears with equal size and gear ratio, with higher number of inner poles  $P_i$ .

The optimization constraints are summarized in Table 6.3.

The variables that are chosen for the optimization are all the geometrical dimensions of Fig. 4.1, the number of inner and outer pole pairs and the hard and soft magnetic materials. Basic relations from electrical machines theory are applied to define the search space boundaries: the magnetic flux density value in the yokes are set and from the magnets magneto-motive force the yokes dimensions are derived.

## 6.4 Example of single gear optimization

The Pareto set for a problem with 10 variables is shown in Fig. 6.7. The constraints limitations on the variable range have been analysed and depicted. The constraints are frequently in conflict: from Fig. 6.7 an example could be torque density against saturation level. The best trade-off depends on the objective functions and is the goal of the optimization algorithm. In this Section the results relative to one single-stage and one multi-stage gear are presented.

The multi-objective optimization results of a single stage magnetic gear with gear ratio  $|G| \simeq 8.5$  are reported in Figs. 6.8, 6.9, 6.10 and 6.11. The materials have been set as follows: the iron adopted is *2V-Permendur*, a high saturating ferromagnetic material, while the magnets are *NdFeB* with grade REN50H. The inner speed is fixed to  $v_{in} = 1400 \text{ rpm}$ , the inner and outer magnet circumferential segmentation consist of 12 and 3 segments respectively, the axial length is  $L = 0.1 \text{ m}$ . Fig. 6.8 shows the optimal points location in the objective space: the red dots

Constraint	From	Constraint Expression
Magnetic	Eq. (4.101)	$T_{max} > T_{sim}$
Magnetic	Sec. 3.4	$\Delta Torque\% \leq \Delta Torque\%_{max} = 15\%$
Numerical	Eq. (4.18)	$k(A) < 1e8$
Saturation	Eq. (4.25)	$V_{sat} \leq V\%_{max} = 15\%$
Saturation	Eq. (5.16)	$rpm_{in} \leq rpm_{in}^{limit}$
Mechanical	Eqs.(5.2), (5.3)	$\omega_{in} \leq k_{in}, \omega_{out} \leq k_{out}$
Mechanical	Eq. (5.13)	$\sigma_U \leq k\sigma_{VM}^{max}$
Mechanical	Eq. (5.54)	$\Delta_r \leq \Delta_r-max; \Delta_\theta \leq \Delta_\theta-max$
Mechanical	Eq. (5.57)	$\sigma_{VM} \leq \sigma_{limit} = 50 \text{ MPa}$
Mechanical	Eq. (5.18)	$ \frac{\omega_{in} - \omega_{n-in}^{r.e.s}}{\omega_{n-in}^{r.e.s}}  \geq 0.04$
Thermal	Eq. (5.82)	$T \leq T_{max}$
Efficiency	Sec. 4.6	$ \eta  \geq \eta_{min} = 0.85$
Specific torque	Eq. (6.6)	$ K_t  \geq K_{t-min} = 10 \frac{Nm}{kg}$

TABLE 6.3: List of implemented constraints for the magnetic gear optimization.

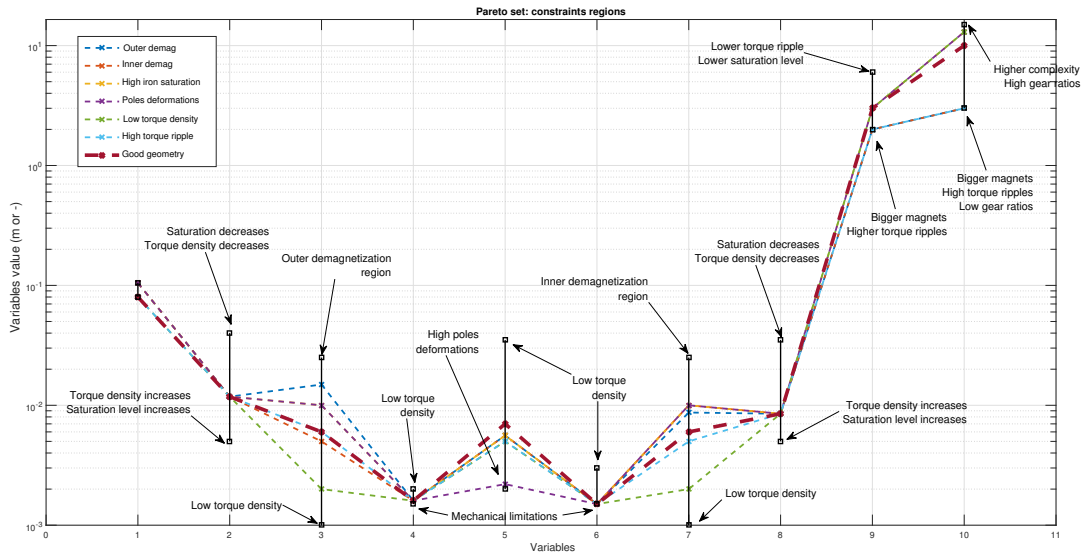


FIGURE 6.7: Constraints visualization on the Pareto set. Variables: 1) Outer radius, 2) Inner iron thickness, 3) Inner magnets thickness, 4) Inner airgap thickness, 5) Iron poles thickness, 6) Outer gap thickness, 7) Outer magnets thickness, 8) Outer iron thickness, 9) Number of inner pole pairs, 10) Number of outer pole pairs. The black vertical lines define the variables range. 7 examples of Pareto set are displayed: for 6 solutions the constraints were not satisfied therefore only one combination is feasible.

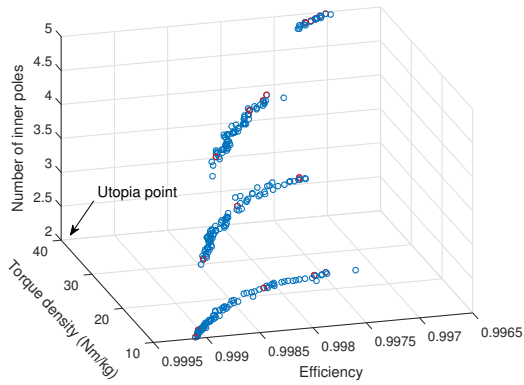


FIGURE 6.8: Pareto front of a single stage magnetic gear. The optimization objectives are: specific torque ( $Nm/kg$ ), efficiency and number of inner pole pairs. Red dots represent the optimal population while the blue dots represent the archive individuals found in previous iterations.

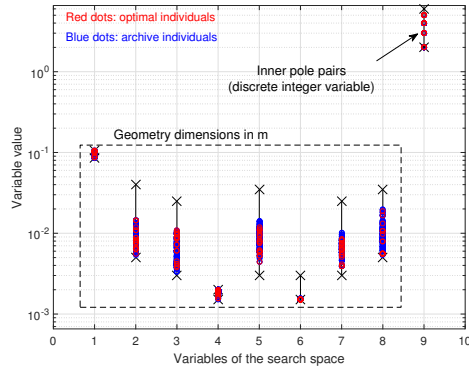


FIGURE 6.9: Set of variables of the single stage magnetic gear: 1) Outer radius, 2) Inner iron thickness, 3) Inner magnets thickness, 4) Inner air-gap thickness, 5) Iron poles thickness, 6) Outer gap thickness, 7) Outer magnets thickness, 8) Outer iron thickness, 9) Number of inner pole pairs. The vertical black lines represent the variables possible range. The gear ratio is fixed to be  $|G| \simeq 8.5$ .

Pi	Po	ratio	L(m)	D(m)	Mag. segm.	$rpm_{in}$	Mass(kg)	Tool	mat.	Nm/kg	$T_o(Nm)$	$\eta$
5	42	8.4	0.1	0.2	12x2, 3x2	1400	12	An.	Hiperco50	39.47	473.6	0.997
								FEM lin.	lossless	37.92	455	0.997
								FEM	Hiperco50	37.08	445	0.996

TABLE 6.4: Optimal magnetic gears: analytic (An.) validation through a FEM code.

represent the population in the last iteration while the blue dots are the elements stored in the archive (see [185] for further details). The specific torque and efficiency increase with the number of inner pole pairs: since higher pole pairs implies smaller magnets for the same geometry, the best trade-off design of the outer magnets is also defined by the technological limitations. Fig. 6.9 shows the optimal Pareto set: the outer gap (variable 6) has a great influence on the torque since all the optimal solutions are crowded near the lower variable boundary. In Fig. 6.10 the constraint violation of all the optimization test geometries is shown. Fixing the number of inner pole pairs the specific torque is limited by the saturation constraint (see saturation region in Fig. 6.10) while increasing the number of pole pairs the saturation volume tends to decrease pushing further the specific torque ratio. Fig. 6.11 shows an example of optimal geometry taken from the Pareto front: since one objective function is the specific torque, the optimal machines tend to fill completely the available volume (maximum outer radius) and to be hollow.

Tab. 6.4 reports the results comparison obtained for the optimal geometry in Fig. 6.11: the analytic torque and efficiency are compared with the ones computed through the commercial finite element code. For the analytic case, PMs losses are computed through the simplified approach (4.130), while soft magnetic material losses are computed through the GSE model (4.117). According to the low losses obtained in [150], the high efficiency values obtained in Tab. 6.4 are due to the PMs segmentation.

## 6.5 Multi-stage gears

When high ratio mechanical gearboxes are designed, a common practice is to adopt a multi-shaft structure. The same concept can be applied to magnetic gears: in this case the machine becomes a three stage device with an inner, outer and middle shaft, where one magnetic gear is placed inside another hollow magnetic gear resulting in a multi-stage coaxial gear. In [187] different connections between magnetic gears are analyzed and optimized; the cascade-connection seems to be the most promising in terms of efficiency and torque density. The approach used in [61] imposes a homogeneous Neumann condition on the inner and outer boundaries while the



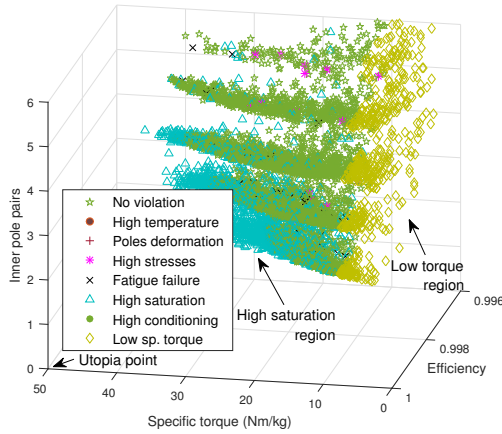


FIGURE 6.10: Constraint violation during the single stage optimization. The flag list cover thermal, mechanical, magnetic constraint violation. The most severe are high volume saturation and low torque density.

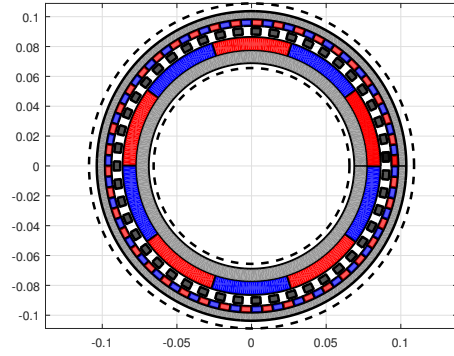


FIGURE 6.11: Example of optimal geometry taken from the Pareto front in Fig. 6.8. Optimizing the specific torque in  $Nm/kg$ , the optimal solutions tends to be hollow: hosting a second magnetic gear inside the previous optimal gear the topology becomes a multi-stage magnetic gear.

solution in the airgaps is known up to a constant  $A_0$  that is normally fixed to zero. Adopting the hypothesis of infinite permeability, the inner and outer magnetic gears can be studied separately adopting the same gauge  $A_0 = 0$ . The middle iron forms a closure path for the flux lines and the magnetic fields inside the low permeability regions of the multi-stage gear are exactly the same in the two separated gears. Therefore, considering the magnetic vector potential  $A_z$  along the two sides of the middle iron and given the relative displacement  $\delta$  between the inner and outer gears, the magnetic vector potential inside the middle iron can be computed.

The minimum simulation angle of inner and outer gears referred to the middle rotor of the multi-stage gear are respectively  $\Delta_{out} = \frac{2\pi}{P_{out} \cdot q_{out}}$  and  $\Delta_{in} = \frac{2\pi}{P_{in} \cdot q_{in}}$ , where the index *out* means outer gear and *in* identifies the inner gear. Since the effect of inner and outer gear generally have different periodicities, a global rotation of the middle rotor  $\xi$  equal to  $2\pi$  have been considered.

Considering two equal magnetic gears with ratio  $z$  and torque per unit mass  $k$ , one solution that allows to obtain a reduction ratio  $k^2$  is the cascade connection. The output shaft torque is  $c$ , the medium shaft torque is  $\frac{c}{z}$  and the input torque is  $\frac{c}{z^2}$ . The overall torque density ( $Nm/kg$ ) is:

$$K_{tot} = \frac{c}{kg_2 + kg_1} = \frac{c}{\frac{c}{k} + \frac{c}{k \cdot z}} = k \cdot \frac{z}{z + 1} \quad (6.7)$$

when the ratio of the single stage  $z$  is high, the overall torque to weight ratio can be approximated to the single stage specific torque  $k$ .

Combining two different gears with reduction ratios  $z_1, z_2$  and torque per unit mass  $k_1, k_2$  the relation becomes:

$$K_{tot} = \frac{c}{kg_1 + kg_2} = \frac{c}{\frac{c}{k_2} + \frac{c}{k_1 \cdot z_2}} = \frac{z_2 \cdot k_1 \cdot k_2}{k_2 + z_2 \cdot k_1} \quad (6.8)$$

The contour plot of (6.8) has been reported in Fig. 6.14. The Torque per unit weight  $k_1$  and  $k_2$  are variables in the range (10 – 50)  $Nm/kg$  while the ratio of the second gear  $z_2$  varies in the range (2 – 40). From the results analysis the torque per unit weight of the combined gear is always lower the maximum torque per unit weight of both the stadiums. Rearranging (6.8) as  $K_{tot} = \frac{xy}{x+y}$ ,  $K_{tot} < x$ ,  $K_{tot} < y \forall x, y > 0$ . It is worth to notice that when the transmission ratio of the second gear is sufficiently high the influence of the first stadium torque to weight ratio is low on the overall torque to weight, regardless the first stadium transmission ratio. In order to obtain an high overall torque per unit weight both the second stage ratio and the product  $z_2 \cdot k_1$  have to be the high.

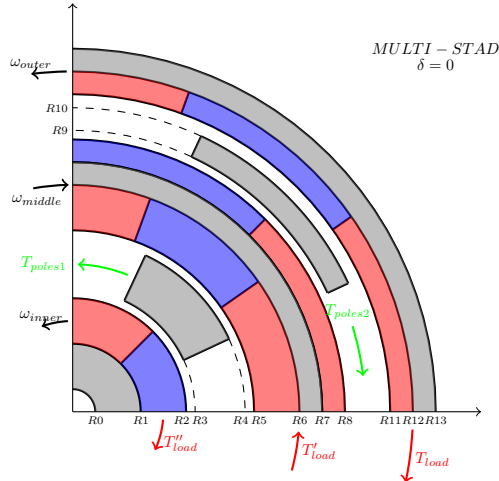


FIGURE 6.12: Multi-stage magnetic gear, relative displacement angle  $\delta = 0^\circ$ .

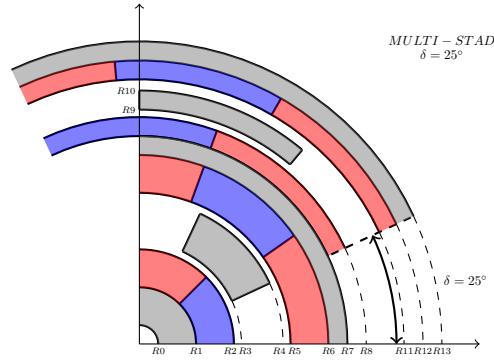


FIGURE 6.13: Multi-stage magnetic gear, relative displacement angle  $\delta = 25^\circ$ .

stad.	Pi	Po	ratio	L(m)	D(m)	Mag. segm.	$rpm_{in}$	Mass(kg)	Tool	mat.	Nm/kg	$T_o(Nm)$	$\eta$
Slow	2	11	5.5			$30 \times 2, 8 \times 2$	1111	19.52	An.	NO20	15.29	298.5	0.995
Fast	2	9	4.5	0.1	0.2	$30 \times 2, 8 \times 2$	5000		FEM lin.	lossless	14.75	288	0.997
									FEM	NO20	13.93	272	0.996

TABLE 6.5: Optimal magnetic gears: analytic (An.) validation through a FEM code.

When the input shaft speed is high, the geometry may be affected by the peripheral rotor speed or the efficiency of a single stadium gear can be low. If two gears are combined these problems can be avoided.

For a given multi-stage transmission, the inner and outer gear will be referred with the indexes *in* and *out* respectively and the geometrical parameters are in accordance with the ones adopted in Figs. 6.12 and 6.13. The outer machine radius has been fixed to  $R_{13} = 0.1 m$  as well as the axial length  $L = 0.1 m$ . The variables are therefore all the 13 geometrical variables (see Figs. 6.12 and 6.13). The target gear has a gear ratio  $|G| = 25$ , an inner speed  $v_{inner} = 5000 rpm$  and the inner number of pole pairs for both inner and outer magnetic gear are fixed to  $P_{i_{in}} = P_{i_{out}} = 2$ . The number of outer gear outer pole pairs  $P_{o_{out}}$  has been chosen as variable ranging in the discrete set  $\{9, 11, 13, 15\}$  in order to avoid integer gear ratios. The inner gear ratio is therefore found satisfying the requirement on the overall gear ratio  $|G|$ . The last optimization variable is the relative displacement angle  $\delta$  described in Figs. 6.12 and 6.13. The ferromagnetic material is fixed to *NO20* and the magnets have a fixed grade *REN 50H*.

Figs. 6.15, 6.16, 6.17 show the Pareto front, set of variables, flag violation history during the iterations with the same conventions adopted in Figs. 6.8-6.11. The optimization variables are the specific torque and efficiency of the global machine. As can be seen in Fig. 6.15, the front is divided in two parts: the solutions with an outer gear ratio  $|G_{out}| = 4.5$  provide a lower specific torque but an higher efficiency, while the opposite happens when  $|G_{out}| = 5.5$ . Another interesting fact also visible from Fig. 6.16 is that the optimal multi-stage solutions seem to be composed by equal gear ratio units since the optimal variable  $P_{o_{out}}$  lies exactly in the middle of the given range. Therefore, given a target gear ratio  $|G_n|$  that has to be obtained through two connected stages, each single stage should have a gear ratio close to  $\sqrt{|G_n|}$  if the constraints are satisfied rather than having two units with very different gear ratios. Fig. 6.17 shows the flag violations plot: high saturation and low specific torque are the most severe constraints in accordance with the objective functions choice. Finally, Fig. 6.18 shows an optimal geometry point chosen from those in Fig. 6.15.

Tab. 6.5 shows the results regarding a multi-stadium gear compared to the 2D FEM analysis results, where the transmissions are disposed in line (not one inside the other): the torque values on the outer rotor  $T_o$  computed through the analytic model are slightly over-estimated in comparison to the FEM procedure while the efficiencies computed with both methods matches since the loss estimations are based on the same approach of Sec. 4.6.3.

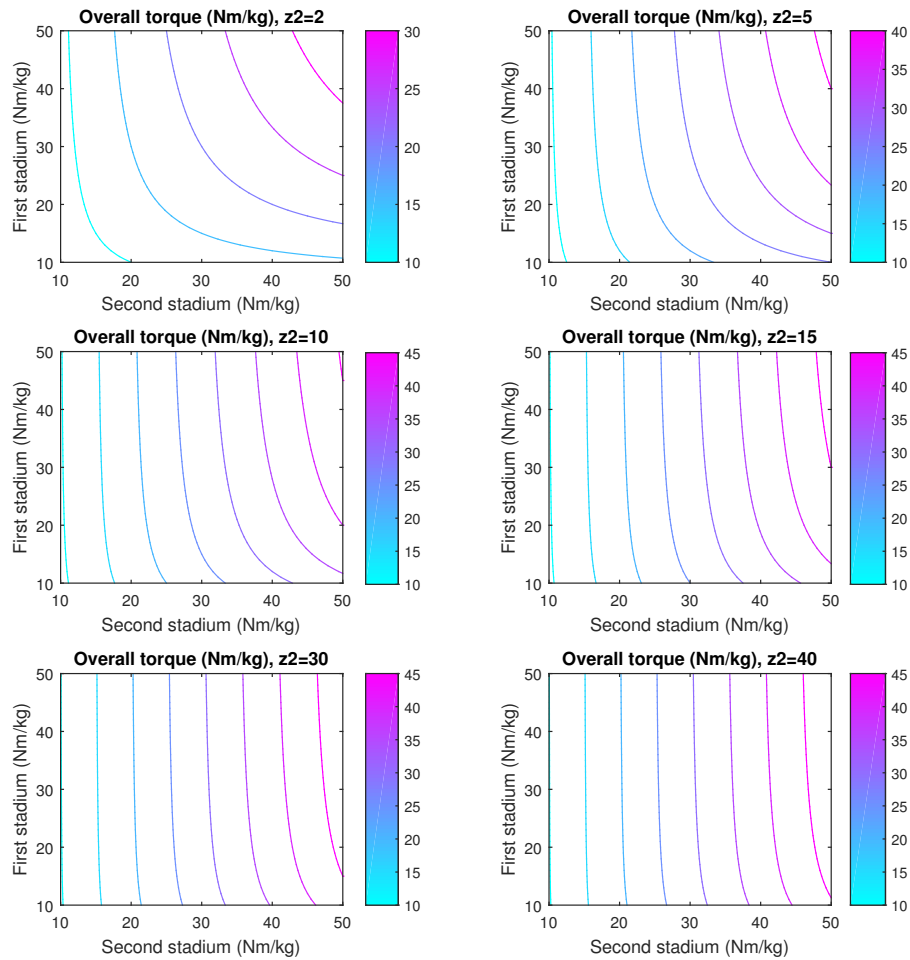


FIGURE 6.14: Analytic contour of (6.8). For a fixed target torque  $c$ , higher gear ratios on the second stage lead to a lower effect of the first stage specific torque.

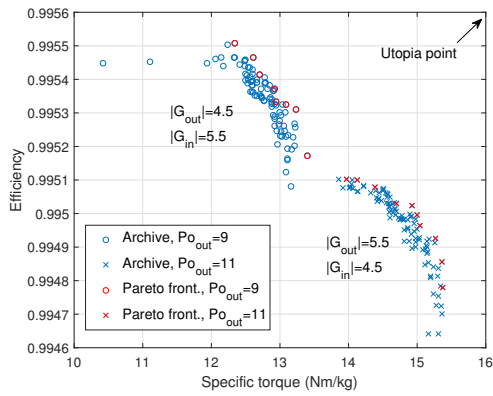


FIGURE 6.15: Multi-stage Pareto front. The optimization variables are the Specific Torque and Efficiency. Red marks represent the optimal population from the last iteration while the blue marks represents the individuals stored into the archive found in previous iterations.

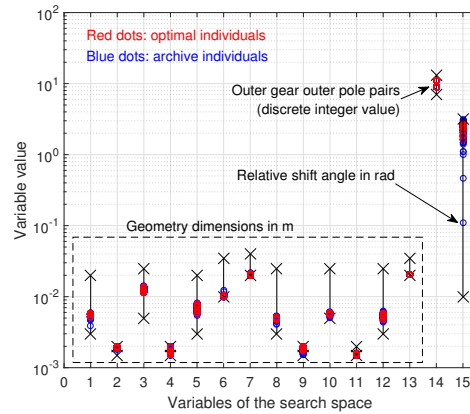


FIGURE 6.16: Multi-stage variable set. 1) Outer gear inner magnets thickness, 2) Outer gear inner airgap thickness, 3) Outer gear iron poles thickness, 4) Outer gear outer gap thickness, 5) Outer gear outer magnets thickness, 6) Outer gear outer iron thickness, 7) Inner gear inner iron thickness, 8) Inner gear inner magnets thickness, 9) Inner gear inner airgap thickness, 10) Inner gear iron poles thickness, 11) Inner gear outer gap thickness, 12) Inner gear outer magnets thickness, 13) Middle iron thickness, 14) Outer gear outer pole pairs, 15) Relative angle shift. The vertical black lines represent the variables range.

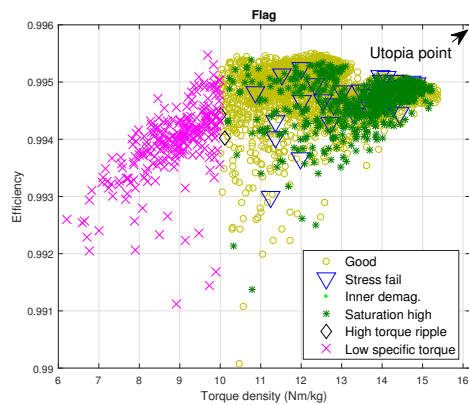


FIGURE 6.17: Multi-stage constraint violation plot. During the optimization, the most severe constraints were inner demagnetization, high inner temperature, high saturation, high torque ripple, low torque density.

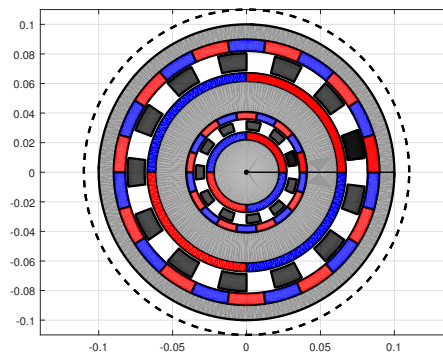


FIGURE 6.18: Example of multi-stage optimal geometry chosen from the Pareto front Fig. 6.15. The relative angle shift between inner and outer gears is set to zero in this picture.

ID	ratio	Pi	Po	L(m)	D (m)	Weight (kg)	(Nm/kg)	$T_o$ An. (Nm)	$T_o$ FEM (Nm)	$\eta$ An.
1M	8.4	5	42	0.1	0.4	43.46	50.1	2177	2080.5	0.9963
2M	8.5	4	34	0.1	0.4	36.38	45.89	1667	1506	0.996
3M	8.33	3	25	0.1	0.4	27.64	35.82	990.1	889.3	0.996
4M	8.5	2	17	0.1	0.4	26.934	15.61	420.4	392.1	0.995
5M	27.5	2	55	0.1	0.4	55.05	22.67	1248	1109	0.9922

TABLE 6.6: Examples of optimal magnetic gears: the input speed is fixed to  $v_{in} = 1400$  rpm, while the magnets segmentation pattern is fixed to  $15 \times 2$  for the inner PMs and  $4 \times 2$  for the outer PMs. The ID column is an identifier, and M stands for magnetic. The weights does not include housing, shaft and bearings.

ID	code	ratio	L	D	$rpm_{in}$	weight (kg)	Torqued.(Nm/kg)	$T_o$ (Nm)	Eff.
1H	mec502C	8.38	0.2	0.2	1400	16	$225/16 = 14.06$	225	0.96
2H	mec502C	25.85	0.18	0.18	1400	16	$320/16 = 20$	320	0.96
3H	mec702C	8.82	0.2	0.2	1400	32	$410/32 = 12.81$	410	0.96
4H	mec702C	29.23	0.2	0.2	1400	32	$675/32 = 21.09$	675	0.96
5H	mec852C	8.33	0.26	0.38	1400	80	$800/80 = 10$	800	0.96
6H	mec852C	25.88	0.26	0.38	1400	80	$1600/80 = 20$	1600	0.96
7H	mec1200	8.15	0.3	0.412	1400	120	$2100/120 = 17.5$	2100	0.96
8H	mec1200	27.78	0.3	0.412	1400	120	$2900/120 = 24.16$	2900	0.96
9H	mec1102	8.15	0.3	0.45	1400	165	$3400/165 = 20.6$	3400	0.96
10H	mec1102	27.78	0.3	0.45	1400	165	$4500/165 = 27.27$	4500	0.96
11H	mec853C	70.05	0.32	0.22	1400	71	$1800/71 = 25.35$	1800	0.94

TABLE 6.7: Mechanical gears data, retrieved from [188]. The ID column is an identifier, and H stands for hydraulic mechanical gearbox.

## 6.6 Comparison between magnetic and mechanical gears

Tab. 6.6 reports some examples of optimal points taken from 3D Pareto fronts for different gear ratios. The optimizations are similar to the one in Sec. 6.4, with 3 objectives and single-station transmissions. The outer gear size axial length  $L$  and diameter  $D$  are fixed, while the constraints have been fixed as in Tab. 6.3. From 6.6, it is clear that higher pole pairs give higher torque densities keeping constant axial length and outer gear diameter: this is due to the lower fluxes in the yokes that allows to further reduce the yokes size. In turn, higher pole pairs lead to smaller PMs and iron poles, thus mechanical and manufacturing limits become more important.

In order to compare the torque densities with the ones of equivalent mechanical transmissions, Tab. 6.7 reports the details of the conventional gears retrieved from [188], where the weight includes the lubrication oil. If from one side the torque density can quickly compared between Tabs. 6.7 and 6.6, a detailed comparison require to set some common parameters between the gearboxes. For example, if the target outer diameter  $D$  is set to  $D = 0.4$  m and the gear ratio  $k$  is set to  $8 \leq k \leq 8.5$ , 1M could be compared to 7H. The outer torque is appreciatively the same, while the weight is lower for the magnetic gearbox case. According to Sec. 1.2, the prototypes so far reached a maximum torque density of  $K_{mass} \approx 20 Nm/kg$ , value which is comparable to the ones found in Tab. 6.6 (but shafts, housing and bearings weight have not been estimated). The efficiency is higher for the magnetic transmission case. Another interesting comparison could be between 5M and 8H, where outer diameters and gear ratios are appreciatively equal. The mechanical outer torque is 2.6 times higher since the axial length is 3 times higher. Since both magnetic gear torque and weight grow linearly with the machine length, the torque density remains constant changing the machine length (in the hypothesis of non-violated constraints due to the increased length in Tab. 6.3). The torque density is approximatively the same for the mechanical and magnetic transmissions. This is mainly due to the high saturation values reached with low number of pole pairs. In Figs. 6.19 and 6.20 the constraint violation and the geometry that results in the highest torque density for the optimization of the 5M-type gear are shown. The most severe constraints is the high saturation one, in Fig. 6.20 the yokes give the highest contribute on the gear mass.

The mechanical gear 11H in Tab. 6.7 is made by three mechanical stages and such a high gear ratio is difficult to be obtained with a single magnetic gear stage. In order to compare this solution with a combination of two magnetic gears as explained in Sec. 6.5, three solution are adopted, as reported in Tab. 6.8. All the magnetic gears have the same fixed maximum diameter  $D = 0.2$  m, similar to the mechanical one 11H. The cascade connection is therefore made placing the second stage consecutively to the first gear stage, while in Sec. 6.5 the high

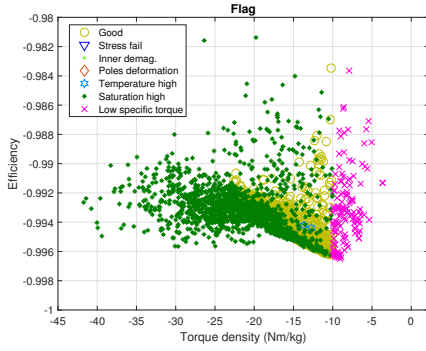


FIGURE 6.19: Constraint violation plot for the optimization of the case 5M in Tab. 6.6 (axis are reversed referring to the previous cases). The most severe constraints were low specific torque, high saturation and high poles deformation.

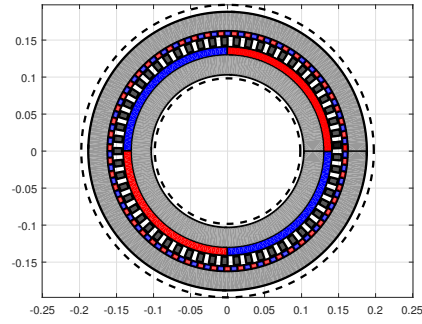


FIGURE 6.20: Example of optimal geometry for the case 5M in Tab. 6.6. The point taken on the Pareto front is the one that maximize the torque density.

<i>opt</i>	Pi	Po	ratio	L (m)	D (m)	segm.	$rpm_{in}$	Weight (kg)	Nm/kg	$T_o$ Nm	$\eta$
First	5	42	8.4	0.037	0.2	12x2, 3x2	1400	4.52	39.53	178.26	0.997
Second	5	42	8.4	0.312	0.2	12x2, 3x2	1400/8.5	38.33	39.53	1515.2	0.995
Coupled	-	-	70.56	0.349	0.2	-	1400	42.85	35.36	1515.2	0.992
First	6	16	2.667	0.0068	0.2	10x2, 3x2	1400	1.38	39.83	55.1	0.997
Second	2	55	27.5	0.28	0.2	15x2, 8x2	1400/2.67	50.49	23.03	1515	0.996
Coupled	-	-	73.43	0.28	0.2	-	1400	51.87	29.21	1515	0.993
First	2	55	27.5	0.069	0.2	15x2, 8x2	1400	24.86	22.85	568	0.992
Second	6	16	2.667	0.187	0.2	10x2, 3x2	1400/27.5	38	39.83	1515	0.997
Coupled	-	-	73.43	0.256	0.2	-	1400	62.86	24.1	1515	0.989

TABLE 6.8: Combinations of optimal magnetic gears to trying to obtain the total gear ratio  $k_{tot} = 70.05$  of the gear 11H in Tab. 6.7. The weight estimations does not include housing, bearings and shaft.

speed stage was directly embedded in the low speed stage. The first case in Tab. 6.8 adopts two equal gears with gear ratio  $k_1 = k_2 = 8.5$ ; in accordance to the conclusions in Sec. 6.5, this solution results in the maximum torque density.

In the second and third case, two gears with  $k_1 = 2.67$   $k_2 = 27.5$  and  $k_1 = 27.5$   $k_2 = 2.67$  are connected respectively. These solutions results in a torque density that is still comparable to the one obtained from the mechanical solution 11H (again the weight of shafts, housing and bearings is not included), but lower than the equal stage case. The efficiencies are for all the cases higher than the mechanical ones.

# Chapter 7

## Damping effects in magnetic gears

As already introduced in Sec. 2.4.5 and simulated in Sec. 3.5, the asynchronous operation offers an intrinsic advantage since mechanical frictions are no more required in the transmission chain. On the other hand, special care has to be taken if the synchronism is lost, since the rotors speed can become excessive [189, 37]. A common constructive practice is to fill the slots between the iron poles with epoxy resins or glass fibers and normally stainless-steel rods are adopted for enhancing the structure's stiffness. In this Section the iron poles rotor has a fixed position and the rods are connected together when the synchronism is lost through an external switch. Thus, in analogy with damping windings of synchronous machines, a damping effect is introduced to limit the rotor rotational speed. The switch could be commanded also to damp the oscillations due to rapid dynamics that normally arise because of mechanical load or speed variations. The effect is the same obtained in [37] without adding damper windings.

This Chapter is organized as follows: Sec. 7.1 describes the test case geometry and the model adopted for the equivalent network.

In Sec. 7.2 the 2D (FEM/BEM) technique adopted in Sec. 4.2 is equipped with the circuit equations needed for the rods-cage modelling.

In Sec. 7.3, the circuital 2D FEM/BEM is validated through the comparison with Comsol Multiphysics [94] for both static and quasi-static cases.

In Sec. 7.4, the rods-cage damping effect is shown for the test case geometry and the computational time is compared to the commercial FEM one.

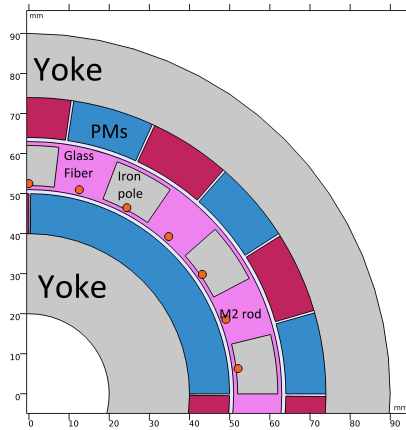
### 7.1 Magnetic gear geometry

The crucial component in magnetic gears is the flux modulator. Large forces are developed on the iron poles (Sec. 5.3), thus glass fibres, epoxy resins and stainless rods are normally adopted to enhance the iron pole stiffness (Sec. 5.4.2). A possible solution is shown in Fig. 7.1, where a magnetic gear with  $P_i = 2$  inner pole pairs,  $P_o = 11$  outer pole pairs and  $q = 13$  pole pieces is equipped with  $2q$  stainless rods, and the assembly of rods and iron poles is encapsulated with glass fibres. The rods are practically solid conductors with a conductivity in the order of  $\sigma \simeq 1 \text{ MS/m}$ . Normally the induced eddy currents have a negligible effect, but if the bars are short circuited through conductive rings, a closed cage is built and the current is free to circulate. The lumped equivalent circuit is depicted in Fig. 7.2, where the model of the outer rings is constituted just by a resistive network (since the end-ring self and mutual inductances calculation would require a 3D FEM calculation).

### 7.2 Problem formulation

The usual 2D vector potential formulation adopted in this thesis reads:

$$\sigma \frac{V_{PM}}{L} + \sigma \frac{\partial A_z}{\partial t} - \nabla \cdot \nu \nabla A_z = J_z + \nabla_{2D} \times \mathbf{M}(A_z) \quad (7.1)$$



Parameter	Symbol	Value
Inner radius	$R_{in}$	0.02 m
Inner yoke	$y_{in}$	0.02 m
PMs thickness	$t_{PM}$	0.01 m
Airgaps size	$t_{gap}$	0.002 m
Poles thickness	$t_{pole}$	0.01 m
Outer yoke	$y_{out}$	0.014 m
Rods radius	$r_{rods}$	0.001 m
Axial length	$L$	0.1 m

FIGURE 7.1: Test case geometry with M2 stainless steel rods (orange color) positioned close to the inner airgap. In this Section, the flux modulator is fixed, while inner and outer rotors can rotate.

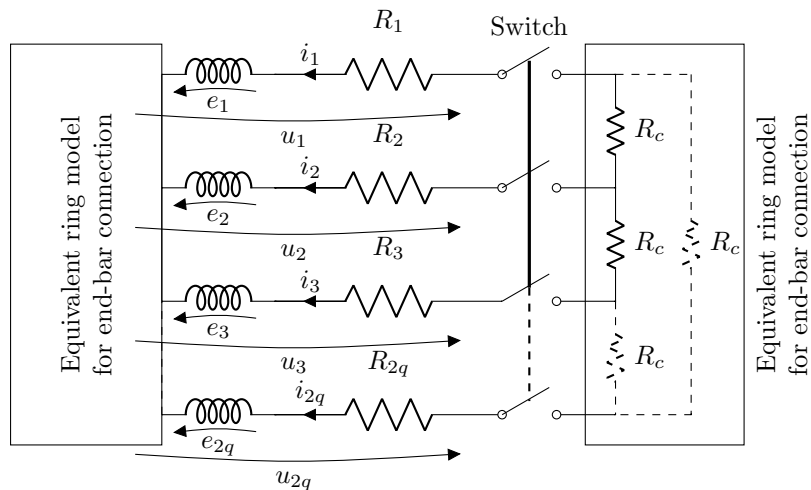


FIGURE 7.2: Circuit scheme of the magnetic gear with bars: the ring model is considered as a purely resistive network in this case, while inductances are used symbolically in the picture but are actually modelled by FEM.



where, in accordance to the previous notations,  $A_z$  is the  $z$  component of the vector potential,  $\sigma$  is the electrical conductivity,  $V_{PM}$  is the voltage between the permanent magnets (PMs) end faces,  $L$  is the machine length,  $\nu$  is the reluctivity,  $M(A_z)$  includes the nonlinear iron magnetization or the linear PMs magnetization and  $J_z$  is the source current density. In the case of non-magnetic solid conductors or single turn windings, (7.1) reads [190]:

$$\begin{cases} \sigma_i \frac{\partial A_z}{\partial t} - \nabla \cdot \nu \nabla A_z - \frac{\sigma_i}{S_i} \int_{\Omega_i} \frac{\partial A}{\partial t} d\Omega = \frac{i_i}{S_i} \\ \frac{L}{S_i} \int_{\Omega_i} \frac{\partial A}{\partial t} d\Omega + \frac{i_i}{\sigma_i S_i} = e_i + R_i \cdot i_i = u_i \end{cases} \quad (7.2)$$

where  $\sigma_i$ ,  $S_i$ ,  $\Omega_i$  are the  $i^{th}$  bar conductivity, cross section and computational domain,  $i_i$ ,  $u_i$ ,  $E_i$  and  $R_i$  are the  $i^{th}$  bar net current, voltage, electromotive force and resistance respectively (see Fig. 7.2).

Following the same steps in Sec. 4.2, Eqs. (7.1), (7.2) and the BEM equations are coupled with two mechanical ordinary differential equations (ODE) as shown in Sec. 4.2.3:

$$J \frac{d^2 \theta}{dt^2} + \left( b + k_{fan} \cdot \frac{d\theta}{dt} \right) \cdot \frac{d\theta}{dt} = T_{em}(\theta) + T_{mecc} \quad (7.3)$$

where  $J$  is the rotor inertia,  $b$  and  $k_{fan}$  are the linear and cubic damping factors due to bearings and air friction respectively,  $\theta$  is the rotor angular position,  $T_{em}$  is the electro-magnetic torque developed on the rotor and  $T_{mecc}$  is the external mechanical torque applied. When the switch closes, their resistance value in the circuit equations changes accordingly. In Eq. (7.1), considering the case of insulated and segmented PMs,  $V_{PM} = \frac{L}{S_i} \int_{\Omega_i} \frac{\partial A}{\partial t} d\Omega$  and  $\sigma$  is taken as a fictitious value  $\sigma' = \sigma_{PM}/k$  to consider the segmentation effect. In particular this reduction factor is  $k = 10$  for the outer PMs and  $k = 4.5$  for the inner ones in accordance to the results found in Sec. 4.8.

Since the time domain simulation is computationally expensive, the  $\theta$ -method scheme adopted in Sec. 4.2.3 is equipped with a simple adaptive feature: the time step  $\Delta t$  is doubled if the number of nonlinear iterations is below a fixed threshold (and vice versa).

## 7.3 Model validation

In Fig. 7.3, the model is validated with a constant speed quasi-static problem where the initial solution is the null vector: at  $t = 0$  s the magnetic field starts to diffuse and the torque grows till the steady state value. Adopting the same discretization, the FEM/BEM results are closer to the quadratic order FEM case because of the BEM higher accuracy. The same simulation is run in Fig. 7.4, with short-circuited rods and  $R_c = 1 \mu\Omega$  in Fig. 7.2. In order to obtain the same solution accuracy, the FEM degrees of freedom in the airgap have been increased by a factor 2. The bar current is reported in Fig. 7.5: the initial peak is due to the sudden magnetization step at  $t = 0$  s. The electromagnetic torques on the inner and outer rotors required to keep the stationary-speed regime are higher in Fig. 7.2 than Fig. 7.3, because of the damping effect due to the rods cage.

## 7.4 Damping effect

The magnetic gear studied in this Chapter has the parameters in Tab. 7.1. The rotors inertias are lower than the real values for this test case in order to reduce the mechanical time constants and consequently the computational time required, but the steady state results are not affected. The power source connected to the inner shaft is supposed to deliver a constant torque  $T_{mecc}$  below the maximum power point and a constant power above the same point. When the synchronism is lost, in the hypothesis of no action from the source controller (because of slow operation or fault in detection systems), Eq. (7.3) for the inner rotor can be written as:

$$J_{in} \frac{d\omega_{in}}{dt} + (k_q + k_e) \cdot \omega_{in}^2 + b_{in} \omega_{in} = T_{mecc} = \frac{P_{max}}{\omega_{in}} \quad (7.4)$$

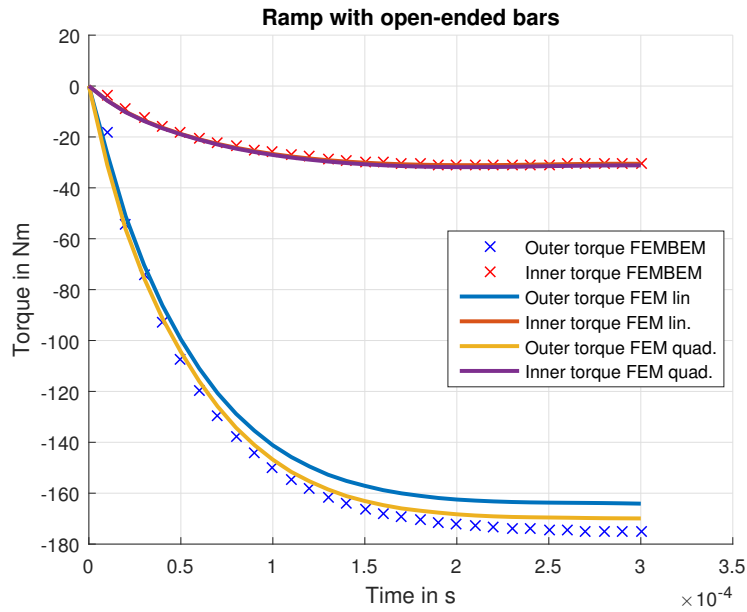


FIGURE 7.3: Validation of the proposed algorithm with open-ended bars through the comparison with the commercial FEM Comsol. Inner and outer speeds are fixed according to the gear ratio  $\omega_{in} = 5000$  rpm  $\omega_{out} = -909$  rpm.

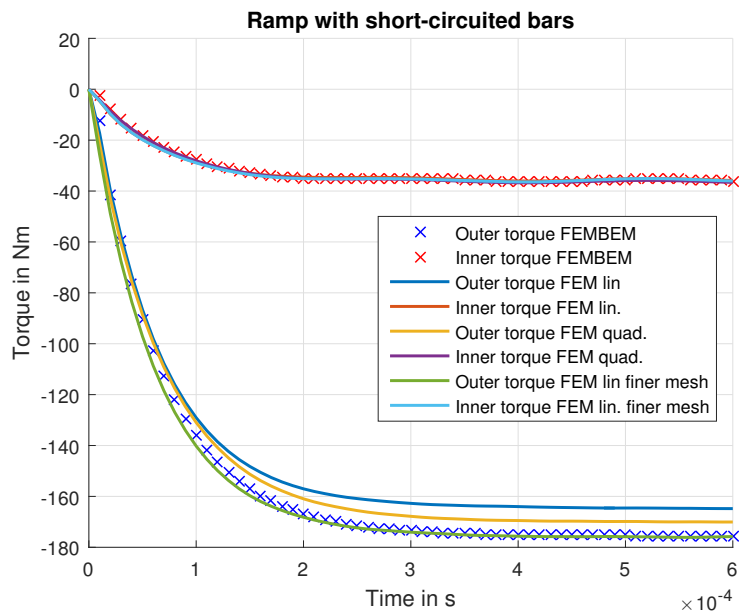


FIGURE 7.4: Same simulation of Fig. 7.3 with short-circuited bars.

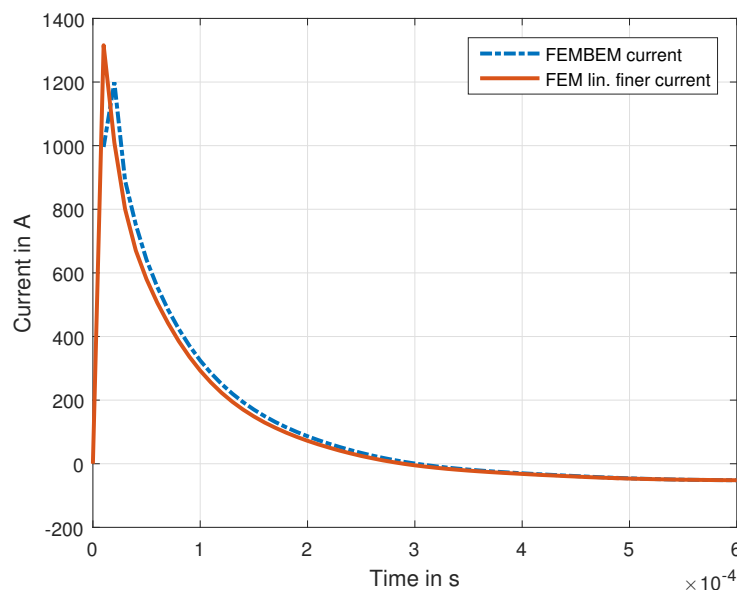


FIGURE 7.5: Current comparison for one bar for the simulation in Fig. 7.4.

where  $k_q$  is the quadratic damping term that includes the air friction coefficient  $k_{fan}$  and the eddy current loss in yokes and iron poles,  $k_e$  is the electrical damping coefficient that includes eddy current losses in PMs and also the losses associated to the rods currents. Thus, the transmission electromagnetic loss due to iron sheets and PMs previously embedded in the term  $T_{em}$  of (7.3) have been incorporated into  $k_q$  and  $k_e$  respectively.

In order to show the rods-cage damping effect, two identical simulations have been used, one with open switch and the other with closed switch. The magnetic gear is in a zero-torque equilibrium as initial condition and a step torque  $T_{mecc} = 30$  Nm is applied at  $t = 0$ , causing the asynchronous operation of the magnetic transmission.

Fig. 7.6 shows the steady state solutions varying  $k_q$  and  $k_e$  and the dynamic response of the nonlinear ODE (7.4). Magnetic gears with high mechanical and electromagnetic efficiency have small  $k_q$  coefficients and the reduction effect due to the electrical damping  $k_e$  is more visible. For the study case under investigation, the simulation time is in the range  $[0 - 0.05]$  s, according to Fig. 7.6.

Fig. 7.7 shows the comparison between the inner and outer rotor torques for the cases with open and closed switch. When the rods are not connected, the torque components are sinusoidal and the inner torque has a small negative DC bias due to the PMs eddy current loss. In the closed-circuit case, the negative DC bias is bigger because of the additional damping contribute due to the rods. This DC bias allows to reduce the stationary speed, as visible in Fig. 7.8. The inner rotor tip speed is reduced from  $\omega_{in} = 23.3$  krpm to  $\omega_{in} = 13.7$  krpm, with a reduction factor  $k = 1.71$ . Therefore, the rods-cage damping effect can prevent mechanical failures in the fast transients during the asynchronous operation. The bar current peak in steady state is  $I^p = 150$  A and the closed-switch operation is limited by the rods over-temperature limit  $\Delta T$ . According to the geometry and the material parameters, the limit operation time with closed switch has been estimated as  $\Delta t = 1.9$  s in adiabatic conditions according to  $c\rho V_b \Delta T = P_b \Delta t$ , where  $c = 500$  J/kgK,  $\rho = 7800$  kg/m<sup>3</sup>,  $V_b = 314$  mm<sup>3</sup> and  $P_b \approx 500$  W are specific weight, heat capacity, volume and power loss of each bar ( $\Delta T = 800$  K).

In Tab. 7.2 the FEM/BEM code time is compared with the commercial software Comsol. The discretization in Comsol is based on linear shape functions and the time domain problem is solved through a backward difference method (BDF) with fixed time step  $\Delta t = 1e - 4$  s. The simulations are run on a workstation with two 6-core 12 thread processors (Intel Xeon E5645 @2.4 GHz) and 112 GB of RAM. For both cases,  $DOF \approx 40k$  holds. The case study 2 is a gear initially operating in steady state with open switch. At  $t = 0.18$  s, the outer rotor is suddenly

Quantity	Symbol	Value	Unit
Inner pole pairs	$P_i$	2	-
Outer pole pairs	$P_o$	11	-
Modulator poles	$q$	13	-
Inner rotor inertia	$J_{in}$	$1E-4$	$kgm^2$
Outer rotor inertia	$J_{out}$	0.17	$kgm^2$
Inner rotor damping	$b_{in}$	$1E-3$	$Nm \cdot s/rad$
Outer rotor damping	$b_{out}$	1.7	$Nm \cdot s/rad$
Air friction + iron loss	$k_q$	$1E-6$	$Nms^2/rad^2$
Nominal inner speed	$\omega_{in}$	5000	$rpm$
Failure speed	$\omega_{in}^{max}$	15	$krpm$
Nominal torque	$T_{mecc-n}$	30	$Nm$
Max source power	$P_{max}$	18	$kW$
Rings resistance	$R_C$	1	$\mu\Omega$
Rod conductivity	$\sigma_r$	1.45	$MS/m$
PMs remanence	$B_r$	1.2	$T$

TABLE 7.1: Electro-mechanical parameters: the rotor inertias are lower than the real ones ( $\approx 1/10$ ) to limit the computational time.

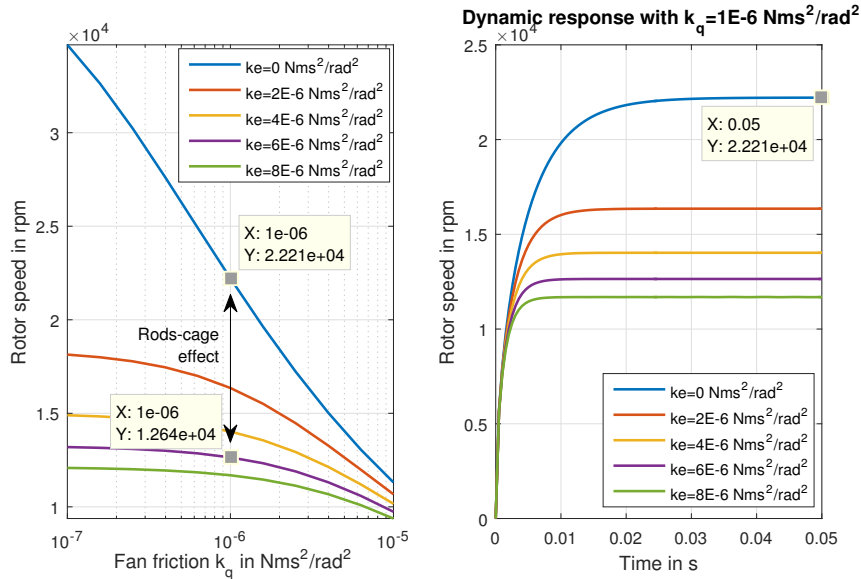


FIGURE 7.6: Steady state solution of Eq. (7.4) varying  $k_q$  and  $k_e$  (left). Dynamic response of Eq. (7.4) with  $k_q = 1e-6 Nms^2/rad^2$  according to Tab 7.1 (right).

Switch state	Tool	Method	Convergence	Time
Open	Comsol	BDF	Tol. factor $\tau < 0.1$	15148 s
Open	FEM/BEM	$\theta$ -method	Rel.Tol. $\gamma < 10^{-4}$	7057 s
Closed	FEM/BEM	$\theta$ -method	Rel.Tol. $\gamma < 10^{-4}$	8072 s

TABLE 7.2: Computational time for FEM/BEM and commercial code. Both methods adopts linear shape functions.

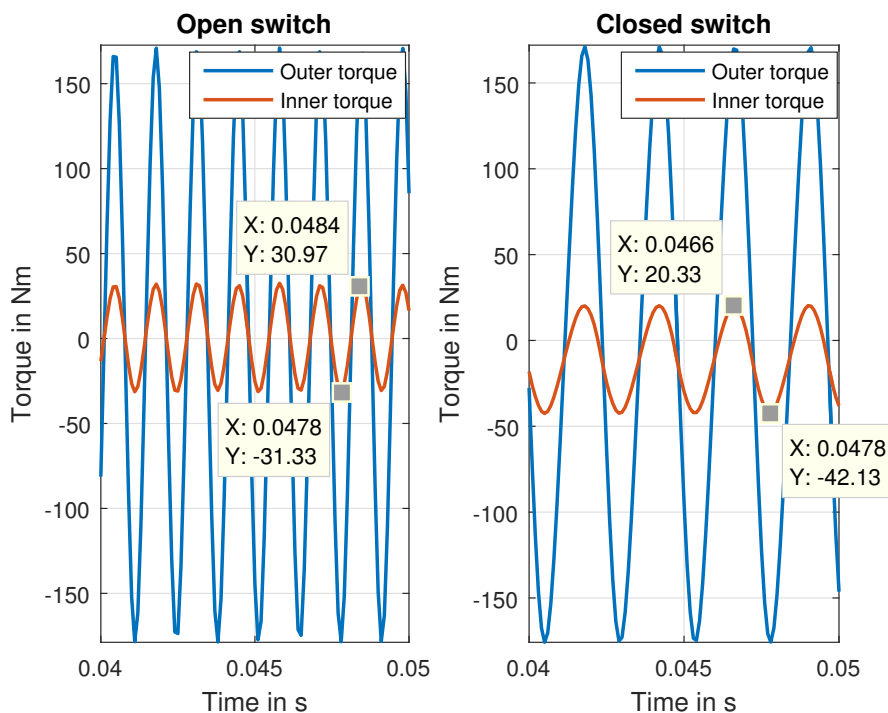


FIGURE 7.7: Comparison between the electromagnetic torques of inner and outer rotor in steady state for the cases with open and closed switch. The PM eddy current loss and rods-induced currents generate a constant resistive torque. The steady state rods current density is  $J \approx 50 \text{ A/m}^2$ .

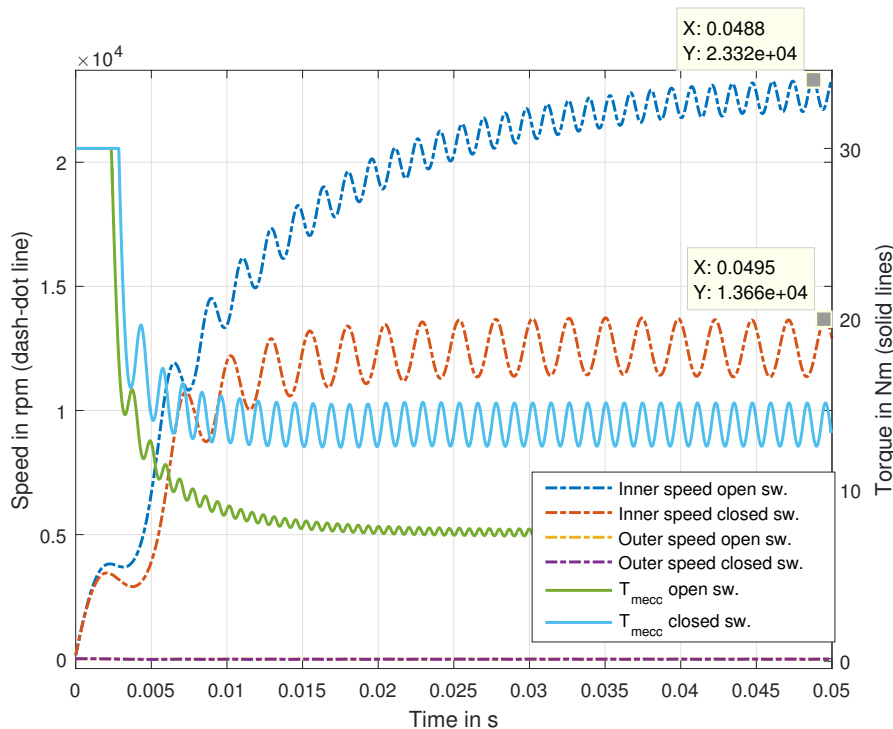


FIGURE 7.8: Inner rotor speed and external torque for open and close switch cases. The rods-cage decreased the tip speed by a factor  $k = 1.71$ . Since the source is power-limited, the torque  $T_{mecc}$  is higher in the case with lower speed.

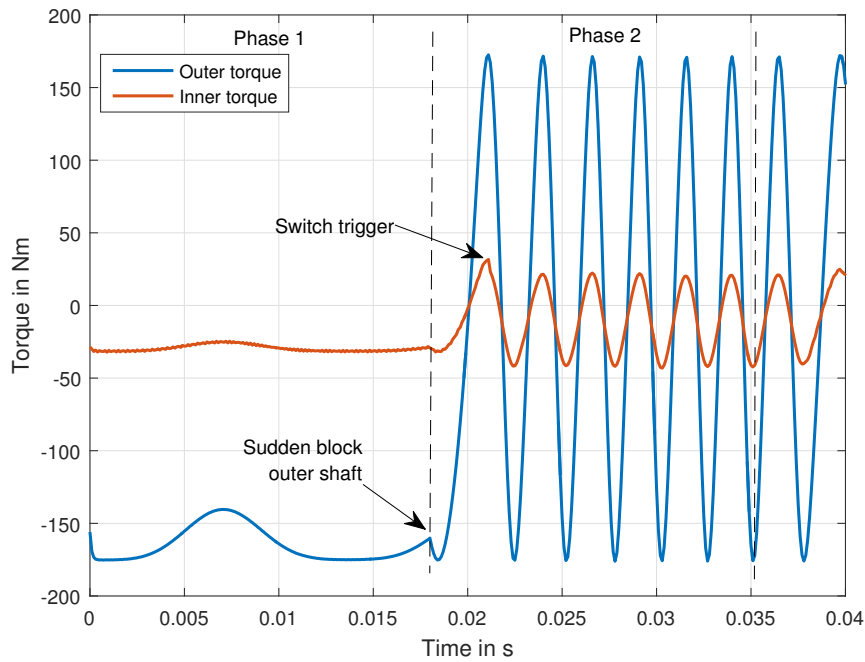


FIGURE 7.9: Inner and outer torques (study case 2). In phase 1 the gear operates in steady state and at  $t = 0.18$  the outer rotor is suddenly blocked. The rods switch is triggered when the inner rotor speed is  $\omega_{in} > 10$  krpm.

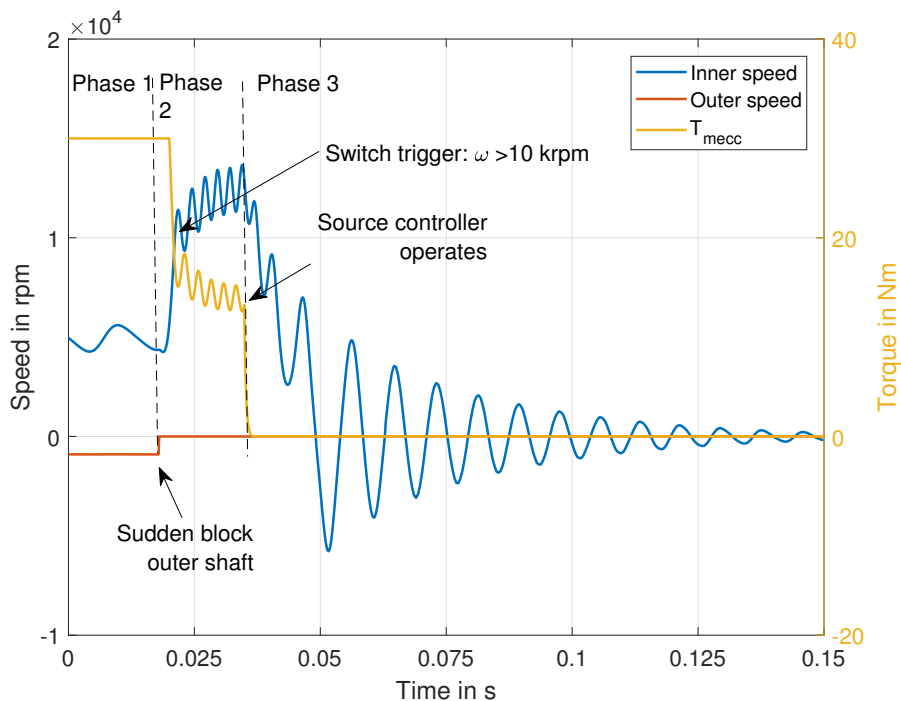


FIGURE 7.10: Inner, outer rotors speed and external torque (study case 2). Phase 1 is the steady state operation, phase 2 is the accelerating fast inner transient and phase 3 is the damped transient till stop. The maximum inner speed in phase 2 is the same obtained in Fig. 7.8 with closed switch.

blocked and the operation becomes asynchronous. Considering that the source controller takes  $\Delta t = 15$  ms to detect the fault and nullify the source power, the inner rotor starts to accelerate and the switch closes when the rotor speed  $\omega_{in} > 10$  krpm. Figs. 7.9 and 7.10 show the torques and speed for this test case. The rods damping is fundamental to reduce the rotor speed in phase 2 of Fig. 7.10.

The switch could also be commanded in order to reduce the oscillatory performance when sudden load variations occur. In this case, the switch should be replaced with electronic transistors in order to change the circuit impedance smoothly from the closed circuit state (damping phase) to the open circuit one (undamped phase). This solution is proposed to avoid the oscillatory behavior due to the quick transition between the damped and undamped phases. A further advantage of the electronic switches is the possibility to control the current that flows in each bar through thermistors and vibration detectors. With a proper control, the bars can be automatically short-circuited when speed oscillations occur, and the thermistors can limit the asynchronous operation when the rods temperature become excessive. This solution is clearly more expensive than the mechanical switch, but it could help to increase the low torsional rigidity in dynamic conditions.





## Chapter 8

# Conclusions and future work

In this thesis, a complete modelling and optimization approach for magnetic transmissions is presented. The approach consists of an initial magnetic gear design tool based on a fast and simplified magnetic analysis, which is coupled with mechanical and thermal constraints and embedded into a Differential Evolution scheme. This efficient optimization tool allows to identify the optimal Pareto set and front once the objective functions are chosen. The detailed analysis of designs on the Pareto front can be conducted through the proposed Finite Element / Boundary Element method, that allows to include non linearities, motion, eddy currents, circuit equations and mechanical equations which are neglected or highly simplified in the analytic model. A special effort has been devoted to increasing the efficiency of the numerical FEM/BEM technique: a powerful acceleration method (Anderson acceleration) has been implemented and successfully tested on different classes of electro-magnetic problems and implemented, providing iteration reductions up to 75%.

Models for hysteresis simulation in laminated sheets cases and for the non-linear BH simulation of permanent magnets are also proposed and validated in the case of in-situ magnetization of a segmented-PMs rotor.

All the proposed algorithms have been compared to commercial Finite Element codes or to experimental data retrieved from literature.

For the future work activity, the most important step is the validation of the algorithms through the comparison with measurements on a magnetic gear prototype. As already explained in the Abstract, this activity was originally planned, but because of external factors the prototype has not been built, although several companies declared their interest and preliminary discussions and technical meetings were held.

Furthermore, an investigation that would be important concerns the analysis of demagnetization due to bad alignment of the rotors and to permanent magnets over-temperature. The algorithm introduced for the analysis of magnetization, demagnetization and recoil developed in this thesis can be adopted for this purpose.

Finally, the 2D FEM/BEM algorithm developed in this work can be extended to the 3D case, since magnetic gears two-dimensional simulations are known to over-estimate the stall torque because of possible non negligible fringing and end effects.



# Appendix A

## Julia code

The code examples reported in this appendix aim at guiding the reader interested in the Julia programming language in understanding some of the basic operations normally required for numerical modelling. The code snippets are extracted from the developed software.

### A.1 Methods

The Julia language is based on multiple dispatch, thus methods and functions are polymorphic and each operation selects dynamically the best implementation among the ones available based on the arguments being processed. Let us consider for example the sum operation: typing `+` on the command window the available methods are shown:

```
+ has 181 methods:
+(A::AbstractArray, B::AbstractArray)
+(A::Number, B::AbstractArray)
+(A::AbstractArray, B::Number)
+(A::Bidiagonal, B::Bidiagonal)
+(A::BitArray, B::BitArray)
+(x::Bool, y::Bool)
+(x::Bool, y::T)
+(y::AbstractFloat, x::Bool)
+(x::Char, y::Integer)
+ ...
```

The sum of two `AbstractArrays` is different from the one of two `Bools` and so on. Each operation is optimized based on the type of the arguments, and this is one of the peculiarities on which Julia bases its speed while allowing a very high level syntax.

### A.2 Call external code

In Julia calling external high-quality, mature libraries for numerical computing already written in C and Fortran does not require the use of wrappers. For example the following code shows a direct call to the `DQRINC` Fortran subroutine included in the `QRUPDATE` dynamic link library [191].

```
function dqrinc!(Q,R::Matrix{Float64},x::Vector{Float64})
    # matrix in input must have the dimension of Q1 and R1!!
    #input parameters
    m::Int64=size(Q,1);
    n::Int64=size(Q,2)-1;
    k=n;
    ldq::Int64=max(m,k);
    ldr::Int64=n+1;
    w=zeros(Float64,k);
    j=n+1;
    ccall(("DQRINC", "QRUPDATE.dll"), Void, (Ptr{Int64},Ptr{Int64},...,&n,&k,Q,&ldq,R,&ldr,&j,x,w)
end
```

The subroutine in the external library is called with just one line of code, where the pointers to the memory locations or the objects are set.

### A.3 Parallelism

In Julia code parallelization can be achieved with limited effort, with mechanisms similar to those provided by OpenMP or MPI.

The following code shows a toy code with OpenMP-like parallelization, similar to the "parfor" syntax provided by Matlab :

```
function parallel_test()
    @time for i=1:5
        sleep(1);
    end
    @time @sync @parallel for j=1:5
        sleep(1);
    end
    nothing
end

#The output calling parallel_test are:
addprocs(5);
parallel_test();
5.0086 seconds (25 allocations: 960 bytes)
1.0054 seconds (768 allocations: 46.313 KiB)
#parallelism works!
```

MPI-like parallelization is shown in the following code, where the computation of the function *field\_shared\_chunk* is segmented in multiple chunks and the function *myrange* assigns tasks to the different workers:

```
@everywhere function myrange(q::SharedArray)
    idx = indexpids(q)
    if idx == 0 #master worker
        return 1:0, 1:0
    end
    nchunks = length(procs(q))
    splits = [round{Int, s} for s in linspace(0, size(q,1),nchunks+1)]
    out::UnitRange{Int64}=splits[idx]+1:splits[idx+1];
    return out
end

@sync begin
    for p in procs(cBx)
        #processor has the identifier p!
        @async remotecall_wait(field_shared_chunk!, data..., myrange(cBx))
    end
end
```

The different mechanisms to call parallel tasks provide maximum flexibility, since the code can be effectively optimized based on the hardware and on the requirements.

## A.4 Memory profiling

Julia natively offers several tools to measure execution time and to track memory allocations. The macros *@timev*, *@elapsed*, *@profile* are available for this purposes. A toy example is shown below. Launching Julia in track-allocation mode, the file *emf.mem* contains the memory allocations of each single source code line:

```
#emf.mem memory alloc tracker
- function main()
-     temp=0.0;
80096 a=zeros(10000);
0 emf!(a,temp);
0     return nothing
- end
- function emf!(a,temp)
0     for i=1:size(a,1)
0         a[i]=i^2;
0         temp=temp+i;
-     end
0     return nothing
- end

@timev main()
#The results in the command window are:
0.000045 seconds (6 alloc: 78.359 KiB)
elapsed time (ns): 45340
bytes allocated: 80240
pool allocs: 5
malloc() calls: 1
```

The memory allocations are therefore easy to track for an immediate feedback on code bottlenecks.

## A.5 Finite element matrices assembly

This part is standard and the commented code is reported below. It is worth noting the compact syntax of the routine and the math-like expressions of the quantities.

```
@time for iel=1:nf #sweep on triangles, track assembly time and allocations!
    nd::Vector{Int64}=facs[:,iel]; #nd contains the nodes index of the iel triangle 3X1
    v=coords[:,nd];
```

```

∇λ,area,k0= trinorm(v); #∇λ is a matrix 2X3 with the gradient of Φ1,Φ2,Φ3
#of the vertex of the iel tri
if (area<=0) #check on area: if non positive oriented tri, break
    print("impossible negative area");
    break
end
#curl matrix: in 2d=gradient rotated
rotx[1:3,iel]=∇λ[2,1:3];
roty[1:3,iel]=-∇λ[1,1:3];
Weights::Vector{Float64}=area*w.gauss;
for igp=1:rules.npoints #sweep gauss points
    ip=ip+1;
    for i=1:3 #sweep tri nodes of current tri
        nd2[1]=nd[i];
        ∇wi::Vector{Float64}=view(∇λ,1:2,i);#grad Wi
        Wi::Float64=k0[i]+∇λ[1,i]*x[ip]+∇λ[2,i]*y[ip]; #Wi for mass matrix
        if (isempty(findin(pm_num_dom,domains[iel]))==false)
            #magnetization rhs calculation (only in PM domains)
            ip2=ip2+1;
            temp::Float64=(-Mpm[ip,2]*∇λ[1,i]+Mpm[ip,1]*∇λ[2,i]);
            temp2::Float64=getindex(Weights,igp);
            M.val[ip2]=temp.*temp2; #∫ Hc∇×WidΩ = ∫ Hcx*b - Hcy*a
            irow_M[ip2]=nd2[1]; #store magnetization index
        end #PM element case
        for j=1:3 #sweep tri nodes-> Wj
            nd2[2]=nd[j];
            ∇wj::Vector{Float64}=view(∇λ,1:2,j); #grad Wj
            Wj::Float64=k0[j]+∇λ[1,j]*x[ip]+∇λ[2,j]*y[ip];
            a1::Float64=getindex(f,ip);
            b1::Float64=getindex(Weights,igp);
            dot_prod::Float64=dot(∇wi,∇wj);
            vv::Float64=broadcast(*,a1,b1,dot_prod);#local stiffness element
            #local mass element
            a::Float64=getindex(f.mass,ip);
            mass::Float64=broadcast(*,a,Wi,Wj,b1); #mass=f.mass[ip]*Wi*Wj*Weights[igp];
            nnz=nnz+1;
            #store the values for stiffness and mass matrices
            irow[nnz]=nd2[1];
            icol[nnz]=nd2[2];
            vals[nnz]=vv;
            vals_mass[nnz]=mass;
            #update mur stiffness, useful if mur is changed dynamically
            if is_Fe[iel]==1
                ip3=ip3+1;
                store_mur_ind[1:2,ip3]=nd2;
                store_mur_ind[3,ip3]=iel;
                store_mur[1,ip3]=-vv; #negative cause the stiffness matrix is build with minus
                store_mur[2,ip3]=-b1*dot_prod;
            end #nonlinear iron element
        end #enddo on i
    end #enddo on j
end #enddo on gp
end #enddo on iel

```

## A.6 BEM matrices assembly

In this part, the 2D Boundary Element matrices are set up. This task is done in parallel (Sec. A.3), and the notation is the same of Eq. (4.30). The SharedArray class has been adopted in order to allow each process to access the proper matrix location. For the sake of clarity, only the key parts are shown while the standard BEM assembly is not reported.

```

#initialize BEM matrices, shared between workers
G=SharedArray{Float64}(length(nodes_border),length(nodes_border));
H=SharedArray{Float64}(length(nodes_border),length(nodes_border));
#parallel sweep on the BEM points, exit when all the tasks have been executed!
@sync @parallel for r in eachindex(nodes_border)
    point_rx=getindex(points_tot,r,1); #bem point1 x coord
    point_ry=getindex(points_tot,r,2); #bem point1 y coord
    #variables initialization:
    r_components_x1=Array{Float64}(dim); ... #several other declarations
    for k in eachindex(nodes_border) #inner sweep of nodes
        point_kx=getindex(points_tot,k,1)
        point_ky=getindex(points_tot,k,2)
        dist_x=-punto_rx+punto_kx
        dist_y=-punto_ry+punto_ky
        compute_stuff ... #several computation not reported here, including:
        #find nodes of the edges that shares node k; extract the values of interp function needed,
        #compute jacobians, compute gauss points coordinates, compute distances, compute potential
        #derivative along normal vectors, compute ai_bem contributes, compute bi_bem contributes
        G[r,k]=int; #write on the shared array!
    end
end

```

```

    H[r,k]=int2; #write on the shared array!
end
end
return G,H #return the BEM matrices
end

```

## A.7 Torque calculation

The torque developed on the inner and outer rotors is computed through (4.35) once the flux densities  $B_x$  and  $B_y$  are known (see(4.34)). The computation of the flux densities in the query points is parallelized (Sec. A.3, as well as the stress tensor integration along the query points. The parallelism is set in this routine through the MPI-like approach in Sec. A.3, for example  $B_x$  is computed as:

```

@sync begin
  for p in procs(Bx)
    #processor has the identifier p! #func myrange defined in Sec. parallelism
    @async remotecall_wait(field_shared_chunk!,data...,myrange(Bx));
  end
end

```

where the function *field\_shared\_chunk!* actually computes the magnetic flux density.

# Bibliography

- [1] Nicolas Walter Frank. *Analysis of the concentric planetary magnetic gear*. PhD thesis. Texas A&M University, 2011. URL: <http://hdl.handle.net/1969.1/ETD-TAMU-2011-05-9158>.
- [2] *Gear Failures: how to recognize them, what causes them, how to avoid them*. Tech. rep. URL: <https://www.xtek.com/wp-content/uploads/2018/05/xtek-gear-failures.pdf>.
- [3] J. Ribrant and L. M. Bertling. “Survey of Failures in Wind Power Systems With Focus on Swedish Wind Power Plants During 1997 ndash;2005”. In: *IEEE Transactions on Energy Conversion* 22.1 (Mar. 2007), pp. 167–173. ISSN: 0885-8969. DOI: 10.1109/TEC.2006.889614.
- [4] Shawn Sheng. *Gearbox typical failure modes, detection, and mitigation methods (Presentation)*. Tech. rep. National Renewable Energy Laboratory (NREL), Golden, CO., 2014. URL: <https://www.nrel.gov/docs/fy14osti/60982.pdf>.
- [5] B.-R Höhn and K Michaelis. “Influence of oil temperature on gear failures”. In: *Tribology International* 37.2 (2004). Austrib 2002, pp. 103 –109. ISSN: 0301-679X. DOI: [https://doi.org/10.1016/S0301-679X\(03\)00047-1](https://doi.org/10.1016/S0301-679X(03)00047-1). URL: <http://www.sciencedirect.com/science/article/pii/S0301679X03000471>.
- [6] Osman Asi. “Fatigue failure of a helical gear in a gearbox”. In: *Engineering Failure Analysis* 13.7 (2006), pp. 1116 –1125. ISSN: 1350-6307. DOI: <https://doi.org/10.1016/j.engfailanal.2005.07.020>. URL: <http://www.sciencedirect.com/science/article/pii/S1350630705001780>.
- [7] Samroeng Netpu and Panya Srichandr. “Failure of a helical gear in a power plant”. In: *Engineering Failure Analysis* 32 (2013), pp. 81 –90. ISSN: 1350-6307. DOI: <https://doi.org/10.1016/j.engfailanal.2013.03.002>. URL: <http://www.sciencedirect.com/science/article/pii/S1350630713001027>.
- [8] S.K. Bhaumik, M. Sujata, M. Suresh Kumar, M.A. Venkataswamy, and M.A. Parameswara. “Failure of an intermediate gearbox of a helicopter”. In: *Engineering Failure Analysis* 14.1 (2007), pp. 85 –100. ISSN: 1350-6307. DOI: <https://doi.org/10.1016/j.engfailanal.2005.12.006>. URL: <http://www.sciencedirect.com/science/article/pii/S1350630706000215>.
- [9] E. Gouda, S. Mezani, L. Baghli, and A. Rezzoug. “Comparative Study Between Mechanical and Magnetic Planetary Gears”. In: *IEEE Transactions on Magnetics* 47.2 (Feb. 2011), pp. 439–450. ISSN: 0018-9464. DOI: 10.1109/TMAG.2010.2090890.
- [10] Efren Diez-Jimenez, Rocio Sanchez-Montero, and Miriam Martinez-Muñoz. “Towards Miniaturization of Magnetic Gears: Torque Performance Assessment”. In: *Micromachines* 9.1 (2018). ISSN: 2072-666X. DOI: 10.3390/mi9010016. URL: <http://www.mdpi.com/2072-666X/9/1/16>.
- [11] Dana Painter. “A Comparative Study of the Performance Capabilities of Magnetic Gears”. In: (2016). University Honors Theses. DOI: 10.15760/honors.316.
- [12] M. C. Gardner, B. E. Jack, M. Johnson, and H. A. Toliyat. “Comparison of Surface Mounted Permanent Magnet Coaxial Radial Flux Magnetic Gears Independently Optimized for Volume, Cost, and Mass”. In: *IEEE Transactions on Industry Applications* 54.3 (May 2018), pp. 2237–2245. ISSN: 0093-9994. DOI: 10.1109/TIA.2018.2803039.
- [13] Justin Jon Scheidler. “A review of noise and vibration control technologies for rotorcraft transmissions”. In: *INTER-NOISE and NOISE-CON congress and conference proceedings*. Vol. 253. 5. Institute of Noise Control Engineering. 2016, pp. 2986–2997.

- [14] X. Zhang, X. Liu, and Z. Chen. “A Novel Dual-Flux-Modulator Coaxial Magnetic Gear for High Torque Capability”. In: *IEEE Transactions on Energy Conversion* 33.2 (June 2018), pp. 682–691. ISSN: 0885-8969. DOI: 10.1109/TEC.2017.2778285.
- [15] Ben McGilton, Richard Crozier, Alasdair McDonald, and Markus Mueller. “Review of magnetic gear technologies and their applications in marine energy”. In: *IET Renewable Power Generation* 12.2 (2017), pp. 174–181. DOI: 10.1049/iet-rpg.2017.0210.
- [16] *Magnomatics*. Tech. rep. Magnomatics Limited, <http://www.magnomatics.com>, accessed June 2016.
- [17] *Mag Soar*. Tech. rep. Mag Soar, <http://www.magsoar.com>, accessed Oct. 2017.
- [18] *Sintex*. Tech. rep. Mag Soar, <https://www.sintex.com/en/magnetic-technologies/magnetic-gear>, accessed Aug. 2018.
- [19] C.G. Armstrong. *Power-transmitting device*. US Patent 687,292. Nov. 1901.
- [20] H.T. Faus. *Magnet gearing*. US Patent 2,243,555. May 1941.
- [21] M.J.T. B. *Magnetic transmission*. US Patent 3,378,710. Apr. 1968.
- [22] K. Atallah and D. Howe. “A novel high-performance magnetic gear”. In: *IEEE Transactions on Magnetics* 37.4 (July 2001), pp. 2844–2846. DOI: 10.1109/20.951324.
- [23] O. S. Chiril, D. Stoia, M. Cernat, and K. Hamayer. “High-performance magnetic gears topologies”. In: *2010 12th International Conference on Optimization of Electrical and Electronic Equipment*. May 2010, pp. 1091–1096. DOI: 10.1109/OPTIM.2010.5510496.
- [24] Mu Chen, Kwok Tong Chau, Wenlong Li, and Chunhua Liu. “Development of Non-rare-earth Magnetic Gears for Electric Vehicles”. In: *Journal of Asian Electric Vehicles* 10.2 (2012), pp. 1607–1613. DOI: 10.4130/jaev.10.1607.
- [25] X. Li, K.-T. Chau, M. Cheng, and W. Hua. “Comparison of magnetic-g geared permanent-magnet machines”. In: *Progress In Electromagnetics Research* 133 (2013), pp. 177–198. DOI: 10.2528/PIER12080808.
- [26] Z. Q. Zhu and D. Evans. “Overview of recent advances in innovative electrical machines – With particular reference to magnetically geared switched flux machines”. In: *2014 17th International Conference on Electrical Machines and Systems (ICEMS)*. Oct. 2014, pp. 1–10. DOI: 10.1109/ICEMS.2014.7013921.
- [27] P. M. Tlali, R. J. Wang, and S. Gerber. “Magnetic gear technologies: A review”. In: *2014 International Conference on Electrical Machines (ICEM)*. Sept. 2014, pp. 544–550. DOI: 10.1109/ICELMACH.2014.6960233.
- [28] Daniel Fodorean. “State of the Art of Magnetic Gears, their Design, and Characteristics with Respect to EV Application”. In: *Modeling and Simulation for Electric Vehicle Applications*. Ed. by Mohamed Amine Fakhfakh. Rijeka: InTech, 2016. Chap. 04. DOI: 10.5772/64174.
- [29] Y. Wang, M. Filippini, N. Bianchi, and P. Alotto. “A Review on Magnetic Gears: Topologies, Computational Models and Design Aspects”. In: *2018 XIII International Conference on Electrical Machines (ICEM)*. Sept. 2018, pp. 527–533. DOI: 10.1109/ICELMACH.2018.8507204.
- [30] K. Ikuta, S. Makita, and S. Arimoto. “Non-contact magnetic gear for micro transmission mechanism”. In: *1991 Proceedings. IEEE Micro Electro Mechanical Systems*. Jan. 1991, pp. 125–130. DOI: 10.1109/MEMSYS.1991.114782.
- [31] S. Kikuchi and K. Tsurumoto. “Design and characteristics of a new magnetic worm gear using permanent magnet”. In: *IEEE Transactions on Magnetics* 29.6 (Nov. 1993), pp. 2923–2925. DOI: 10.1109/20.280916.
- [32] Y. D. Yao, D. R. Huang, C. C. Hsieh, D. Y. Chiang, S. J. Wang, and T. F. Ying. “The radial magnetic coupling studies of perpendicular magnetic gears”. In: *IEEE Transactions on Magnetics* 32.5 (Sept. 1996), pp. 5061–5063. DOI: 10.1109/20.539490.



- [33] J. Wang, K. Atallah, and W. Wang. “Analysis of a Magnetic Screw for High Force Density Linear Electromagnetic Actuators”. In: *IEEE Transactions on Magnetics* 47.10 (Oct. 2011), pp. 4477–4480. ISSN: 0018-9464. DOI: 10.1109/TMAG.2011.2157464.
- [34] C. C. Huang, M. C. Tsai, D. G. Dorrell, and B. J. Lin. “Development of a Magnetic Planetary Gearbox”. In: *IEEE Transactions on Magnetics* 44.3 (Mar. 2008), pp. 403–412. DOI: 10.1109/TMAG.2007.914665.
- [35] F. T. Jorgensen, T. O. Andersen, and P. O. Rasmussen. “The Cycloid Permanent Magnetic Gear”. In: *IEEE Transactions on Industry Applications* 44.6 (Nov. 2008), pp. 1659–1665. DOI: 10.1109/TIA.2008.2006295.
- [36] J. Rens, K. Atallah, S. D. Calverley, and D. Howe. “A Novel Magnetic Harmonic Gear”. In: *IEEE Transactions on Industry Applications* 46.1 (Jan. 2010), pp. 206–212. DOI: 10.1109/TIA.2009.2036507.
- [37] S. Pakdelian, N. W. Frank, and H. A. Toliyat. “Analysis and design of the trans-rotary magnetic gear”. In: *2012 IEEE Energy Conversion Congress and Exposition (ECCE)*. Sept. 2012, pp. 3340–3347. DOI: 10.1109/ECCE.2012.6342333.
- [38] P. O. Rasmussen, T. O. Andersen, F. T. Jorgensen, and O. Nielsen. “Development of a high-performance magnetic gear”. In: *IEEE Transactions on Industry Applications* 41.3 (May 2005), pp. 764–770. DOI: 10.1109/TIA.2005.847319.
- [39] K. Uppalapati and J. Bird. “A flux focusing ferrite magnetic gear”. In: *6th IET International Conference on Power Electronics, Machines and Drives (PEMD 2012)*. Mar. 2012, pp. 1–6. DOI: 10.1049/cp.2012.0303.
- [40] N. W. Frank, S. Pakdelian, and H. A. Toliyat. “Passive Suppression of Transient Oscillations in the Concentric Planetary Magnetic Gear”. In: *IEEE Transactions on Energy Conversion* 26.3 (Sept. 2011), pp. 933–939. DOI: 10.1109/TEC.2011.2143715.
- [41] Xinhua Liu, K. T. Chau, J. Z. Jiang, and Chuang Yu. “Design and analysis of interior-magnet outer-rotor concentric magnetic gears”. In: *Journal of Applied Physics* 105.7 (2009), 07F101. DOI: 10.1063/1.3058619.
- [42] L. Jian and K. T. Chau. “A Coaxial Magnetic Gear With Halbach Permanent-Magnet Arrays”. In: *IEEE Transactions on Energy Conversion* 25.2 (June 2010), pp. 319–328. DOI: 10.1109/TEC.2010.2046997.
- [43] T. Fujita, Y. Ando, K. Nagaya, M. Oka, T. Todaka, M. Enokizono, and K. Sugiura. “Surface Magnet Gears with a New Magnet Arrangement and Optimal Shape of Stationary Pole Pieces”. In: *Journal of Electromagnetic Analysis and Applications* 5.6 (2013), pp. 243–249. DOI: 10.4236/jemaa.2013.56039.
- [44] K. Aiso and K. Akatsu. “A novel reluctance magnetic gear for high speed motor”. In: *2016 IEEE Energy Conversion Congress and Exposition (ECCE)*. Sept. 2016, pp. 1–7. DOI: 10.1109/ECCE.2016.7854742.
- [45] A.S. Abdel-Khalik, S. Ahmed, and A. Massoud. “A bearingless coaxial magnetic gearbox”. In: *Alexandria Engineering Journal* 53.3 (2014), pp. 573–582. DOI: <https://doi.org/10.1016/j.aej.2014.06.002>.
- [46] Y. Liu, S. L. Ho, and W. N. Fu. “A Novel Magnetic Gear With Intersecting Axes”. In: *IEEE Transactions on Magnetics* 50.11 (Nov. 2014), pp. 1–4. DOI: 10.1109/TMAG.2014.2325608.
- [47] S. Mezani, K. Atallah, and D. Howe. “A high-performance axial-field magnetic gear”. In: *Journal of Applied Physics* 99.8 (2006), 08R303. DOI: 10.1063/1.2158966.
- [48] M. Tsai and L. Ku. “3D printing based design of axial flux magnetic gear for high torque density”. In: *2015 IEEE Magnetics Conference (INTERMAG)*. May 2015, pp. 1–1. DOI: 10.1109/INTMAG.2015.7156626.
- [49] X. Yin, P. Pfister, and Y. Fang. “A novel magnetic gear: Towards a higher torque density”. In: *2015 IEEE Magnetics Conference (INTERMAG)*. May 2015, pp. 1–1. DOI: 10.1109/INTMAG.2015.7157676.

- [50] S. Peng, W. N. Fu, and S. L. Ho. "A Novel Triple-Permanent-Magnet-Excited Hybrid-Flux Magnetic Gear and Its Design Method Using 3-D Finite Element Method". In: *IEEE Transactions on Magnetics* 50.11 (Nov. 2014), pp. 1–4. DOI: 10.1109/TMAG.2014.2327068.
- [51] K. Atallah, J. Wang, and D. Howe. "A high-performance linear magnetic gear". In: *Journal of Applied Physics* 97.10 (2005), 10N516. DOI: 10.1063/1.1853900.
- [52] W. Li, K. T. Chau, and J. Li. "Simulation of a Tubular Linear Magnetic Gear Using HTS Bulks for Field Modulation". In: *IEEE Transactions on Applied Superconductivity* 21.3 (June 2011), pp. 1167–1170. DOI: 10.1109/TASC.2010.2080255.
- [53] S. Kikuchi and K. Tsurumoto. "Trial construction of a new magnetic skew gear using permanent magnet". In: *IEEE Transactions on Magnetics* 30.6 (Nov. 1994), pp. 4767–4769. DOI: 10.1109/20.334216.
- [54] K. Atallah, S. D. Calverley, and D. Howe. "Design, analysis and realisation of a high-performance magnetic gear". In: *IEE Proceedings - Electric Power Applications* 151.2 (Mar. 2004), pp. 135–143. DOI: 10.1049/ip-epa:20040224.
- [55] M. Johnson, M. C. Gardner, and H. A. Toliyat. "Design and analysis of an axial flux magnetically geared generator". In: *2015 IEEE Energy Conversion Congress and Exposition (ECCE)*. Sept. 2015, pp. 6511–6518. DOI: 10.1109/ECCE.2015.7310572.
- [56] M. H. Nagrial, J. Rizk, and A. Hellany. "Design and Development of Magnetic Torque Couplers and Magnetic Gears". In: *2007 International Conference on Electrical Engineering*. Apr. 2007, pp. 1–5. DOI: 10.1109/ICEE.2007.4287283.
- [57] Y. Li, J. W. Xing, Y. P. Lu, and Z. J. Yin. "Torque Analysis of a Novel Non-Contact Permanent Variable Transmission". In: *IEEE Transactions on Magnetics* 47.10 (Oct. 2011), pp. 4465–4468. DOI: 10.1109/TMAG.2011.2157807.
- [58] D. Thyroff, S. Meier, and I. Hahn. "Modeling integrated magnetic gears using a magnetic equivalent circuit". In: *IECON 2015 - 41st Annual Conference of the IEEE Industrial Electronics Society*. Nov. 2015, pp. 002904–002908. DOI: 10.1109/IECON.2015.7392543.
- [59] M. Fukuoka, K. Nakamura, and O. Ichinokura. "Dynamic Analysis of Planetary-Type Magnetic Gear Based on Reluctance Network Analysis". In: *IEEE Transactions on Magnetics* 47.10 (Oct. 2011), pp. 2414–2417. DOI: 10.1109/TMAG.2011.2157100.
- [60] L. Jian and K.-T. Chau. "Analytical calculation of magnetic field distribution in coaxial magnetic gears". In: *Progress In Electromagnetics Research* 92 (2009), pp. 1–16.
- [61] T. Lubin, S. Mezani, and A. Rezzoug. "Analytical Computation of the Magnetic Field Distribution in a Magnetic Gear". In: *IEEE Transactions on Magnetics* 46.7 (July 2010), pp. 2611–2621. DOI: 10.1109/TMAG.2010.2044187.
- [62] T. Lubin, S. Mezani, and A. Rezzoug. "Development of a 2-D Analytical Model for the Electromagnetic Computation of Axial-Field Magnetic Gears". In: *IEEE Transactions on Magnetics* 49.11 (Nov. 2013), pp. 5507–5521. DOI: 10.1109/TMAG.2013.2267746.
- [63] E P Furlani. "Analytical analysis of magnetically coupled multipole cylinders". In: *Journal of Physics D: Applied Physics* 33.1 (2000), p. 28. URL: <http://stacks.iop.org/0022-3727/33/i=1/a=305>.
- [64] F. T. Jorgensen, T. O. Andersen, and P. O. Rasmussen. "Two dimensional model of a permanent magnet spur gear". In: *Fourtieth IAS Annual Meeting. Conference Record of the 2005 Industry Applications Conference*. Vol. 1. Oct. 2005, pp. 261–265. DOI: 10.1109/IAS.2005.1518319.
- [65] W. Wu, H. C. Lovatt, and J. B. Dunlop. "Analysis And Design Optimization Of Magnetic Couplings Using 3D Finite Element Modelling". In: *Magnetics Conference, 1997. Digests of INTERMAG '97., 1997 IEEE International*. Apr. 1997, BC–BC. DOI: 10.1109/INTMAG.1997.597440.

- [66] Yi-Chang Wu and Bo-Syuan Jian. “Magnetic field analysis of a coaxial magnetic gear mechanism by two-dimensional equivalent magnetic circuit network method and finite-element method”. In: *Applied Mathematical Modelling* 39.19 (2015), pp. 5746–5758. DOI: <https://doi.org/10.1016/j.apm.2014.11.058>.
- [67] K. T. Chau, Dong Zhang, J. Z. Jiang, and Linni Jian. “Transient analysis of coaxial magnetic gears using finite element comodeling”. In: *Journal of Applied Physics* 103.7 (2008), 07F101. DOI: [10.1063/1.2831491](https://doi.org/10.1063/1.2831491).
- [68] S. Gerber and R. J. Wang. “Analysis of the end-effects in magnetic gears and magnetically geared machines”. In: *2014 International Conference on Electrical Machines (ICEM)*. Sept. 2014, pp. 396–402. DOI: [10.1109/ICELMACH.2014.6960211](https://doi.org/10.1109/ICELMACH.2014.6960211).
- [69] S. Niu, N. Chen, S. L. Ho, and W. N. Fu. “Design Optimization of Magnetic Gears Using Mesh Adjustable Finite-Element Algorithm for Improved Torque”. In: *IEEE Transactions on Magnetics* 48.11 (Nov. 2012), pp. 4156–4159. DOI: [10.1109/TMAG.2012.2201920](https://doi.org/10.1109/TMAG.2012.2201920).
- [70] M. Desvaux, R. L. G. Latimier, B. Multon, H. B. Ahmed, and S. Sire. “Design and optimization of magnetic gears with arrangement and mechanical constraints for wind turbine applications”. In: *2016 Eleventh International Conference on Ecological Vehicles and Renewable Energies (EVER)*. Apr. 2016, pp. 1–8. DOI: [10.1109/EVER.2016.7476341](https://doi.org/10.1109/EVER.2016.7476341).
- [71] **M. Filippini** and P. Alotto. “Coaxial Magnetic Gear Design and Optimization”. In: *IEEE Transactions on Industrial Electronics* 64.12 (Dec. 2017), pp. 9934–9942. DOI: [10.1109/TIE.2017.2721918](https://doi.org/10.1109/TIE.2017.2721918).
- [72] N. W. Frank and H. A. Toliyat. “Gearing ratios of a magnetic gear for wind turbines”. In: *2009 IEEE International Electric Machines and Drives Conference*. May 2009, pp. 1224–1230. DOI: [10.1109/IEMDC.2009.5075359](https://doi.org/10.1109/IEMDC.2009.5075359).
- [73] K. Atallah, J. Wang, S. D. Calverley, and S. Duggan. “Design and Operation of a Magnetic Continuously Variable Transmission”. In: *IEEE Transactions on Industry Applications* 48.4 (July 2012), pp. 1288–1295. DOI: [10.1109/TIA.2012.2199451](https://doi.org/10.1109/TIA.2012.2199451).
- [74] L. Shah, A. Cruden, and B. W. Williams. “A Variable Speed Magnetic Gear Box Using Contra-Rotating Input Shafts”. In: *IEEE Transactions on Magnetics* 47.2 (Feb. 2011), pp. 431–438. DOI: [10.1109/TMAG.2010.2097273](https://doi.org/10.1109/TMAG.2010.2097273).
- [75] M. Chen, K. T. Chau, W. Li, C. Liu, and C. Qiu. “Design and Analysis of a New Magnetic Gear With Multiple Gear Ratios”. In: *IEEE Transactions on Applied Superconductivity* 24.3 (June 2014), pp. 1–4. DOI: [10.1109/TASC.2013.2291972](https://doi.org/10.1109/TASC.2013.2291972).
- [76] C. Liu and K.T. Chau. “Electromagnetic Design of a New Electrically Controlled Magnetic Variable Speed Gearing Machine”. In: *MDPI Energies* 7 (2014), pp. 1539–1554.
- [77] H. Rashidi and D. Pishdad. “Integrated Multispeed Magnetic Gears: A Novel Approach to Design of Magnetic Transmission Systems”. In: *IEEE Transactions on Magnetics* 51.4 (Apr. 2015), pp. 1–8. DOI: [10.1109/TMAG.2014.2359639](https://doi.org/10.1109/TMAG.2014.2359639).
- [78] J. Dae Kyu and C. Jung Hwan. “Effect of Stationary Pole Pieces with Bridges on Electromagnetic and Mechanical Performance of a Coaxial Magnetic Gear”. In: *Journal of Magnetics* 18.2 (2013), pp. 207–211. DOI: [10.4283/JMAG.2013.18.2.207](https://doi.org/10.4283/JMAG.2013.18.2.207).
- [79] S. Gerber and R. J. Wang. “Evaluation of a prototype magnetic gear”. In: *2013 IEEE International Conference on Industrial Technology (ICIT)*. Feb. 2013, pp. 319–324. DOI: [10.1109/ICIT.2013.6505692](https://doi.org/10.1109/ICIT.2013.6505692).
- [80] Y. Tian, G. Liu, W. Zhao, and J. Ji. “Design and Analysis of Coaxial Magnetic Gears Considering Rotor Losses”. In: *IEEE Transactions on Magnetics* 51.11 (Nov. 2015), pp. 1–4. DOI: [10.1109/TMAG.2015.2435253](https://doi.org/10.1109/TMAG.2015.2435253).
- [81] Melaine Desvaux, Bernard Multon, Stéphane Sire, and Hamid Ben Ahmed. “Analytical iron loss model for the optimization of magnetic gear”. In: *IEEE International Electric Machines and Drives Conference (IEMDC), 2017*. Miami, United States, May 2017, pp. 1–8. DOI: [10.1109/IEMDC.2017.8002255](https://doi.org/10.1109/IEMDC.2017.8002255).

- [82] R. Zanis, A. Borisavljevic, J. W. Jansen, and E. A. Lomonova. “Iron loss investigation of miniaturized magnetic gears having solid cores”. In: *2014 17th International Conference on Electrical Machines and Systems (ICEMS)*. Oct. 2014, pp. 3078–3082. DOI: 10.1109/ICEMS.2014.7014023.
- [83] J. Liu, W. Zhao, J. Ji, J. Zheng, and Z. Liu. “Comparison of coaxial magnetic gears with parallel and series magnetic circuits”. In: *2016 Eleventh International Conference on Ecological Vehicles and Renewable Energies (EVER)*. Apr. 2016, pp. 1–5. DOI: 10.1109/EVER.2016.7476382.
- [84] **M. Filippini**, P. Alotto, E. Bonisoli, C. Ragusa, M. Repetto, and A. Vigliani. “Magnetic Power Loss Estimation in Coaxial Magnetic Gears”. In: *2017 International CAE Conference*. 2017. URL: [http://www.compumag.org/CMAG2017/\[PB-A6-13\]\\_404.pdf](http://www.compumag.org/CMAG2017/[PB-A6-13]_404.pdf).
- [85] N. Niguchi and K. Hirata. “Cogging Torque Analysis of Magnetic Gear”. In: *IEEE Transactions on Industrial Electronics* 59.5 (May 2012), pp. 2189–2197. DOI: 10.1109/TIE.2011.2159357.
- [86] Z. Q. Zhu and D. Howe. “Influence of design parameters on cogging torque in permanent magnet machines”. In: *IEEE Transactions on Energy Conversion* 15.4 (Dec. 2000), pp. 407–412. ISSN: 0885-8969. DOI: 10.1109/60.900501.
- [87] H. Zaytoon, A. S. Abdel-Khalik, S. Ahmed, and A. Massoud. “Torque ripple alleviation of a radial magnetic gearbox using step skewing approach”. In: *2014 International Conference on Electrical Machines (ICEM)*. Sept. 2014, pp. 648–653. DOI: 10.1109/ICELMACH.2014.6960249.
- [88] Y. Akcay, T. Cox, and A. Costabeber. “Improving magnetic gear overload torque with cage rotor bars”. In: *2017 20th International Conference on Electrical Machines and Systems (ICEMS)*. Aug. 2017, pp. 1–5. DOI: 10.1109/ICEMS.2017.8056295.
- [89] T. Lubin, S. Mezani, and A. Rezzoug. “Experimental and Theoretical Analyses of Axial Magnetic Coupling Under Steady-State and Transient Operations”. In: *IEEE Transactions on Industrial Electronics* 61.8 (Aug. 2014), pp. 4356–4365. DOI: 10.1109/TIE.2013.2266087.
- [90] O. Bottauscio, M. Chiampi, C. Ragusa, L. Rege, and M. Repetto. “A test case for validation of magnetic field analysis with vector hysteresis”. In: *IEEE Transactions on Magnetics* 38.2 (Mar. 2002), pp. 893–896. ISSN: 0018-9464. DOI: 10.1109/20.996230.
- [91] **M. Filippini** and P. Alotto. “An optimization tool for coaxial magnetic gears”. In: *COMPEL - The international journal for computation and mathematics in electrical and electronic engineering* 36.5 (2017), pp. 1526–1539. DOI: 10.1108/COMPEL-02-2017-0068. eprint: <https://doi.org/10.1108/COMPEL-02-2017-0068>. URL: <https://doi.org/10.1108/COMPEL-02-2017-0068>.
- [92] **M. Filippini**, P. Alotto, g. Glehn, and K. Hameyer. “Magnetic transmission gear finite element simulation with iron pole hysteresis”. In: 16 (1 2018), pp. 105–110. DOI: 10.1515/phys-2018-0017.
- [93] G. Bavendiek, K. Hameyer, **M. Filippini**, and P. Alotto. “Analysis of impulse-magnetization in rare-earth permanent magnets”. In: *International Journal of Applied Electromagnetics and Mechanics* 57.S1 (2018), pp. 23–31. DOI: 10.3233/JAE-182301.
- [94] *COMSOL Multiphysics Reference Manual, version 5.3*. Tech. rep. COMSOL Inc, <http://www.comsol.com>, accessed June 2017.
- [95] Jeff Bezanson, Alan Edelman, Stefan Karpinski, and Viral B. Shah. “Julia: A Fresh Approach to Numerical Computing”. In: *CoRR* abs/1411.1607 (2014). arXiv: 1411.1607. URL: <http://arxiv.org/abs/1411.1607>.
- [96] *Julia website*. <https://julialang.org/>. Accessed February, 2018.
- [97] Peter Hunter. *FEM/BEM Notes*. <http://ft-sipil.unila.ac.id/dbooks/FEM%20and%20BEM%20notes.pdf>. Accessed February, 2017. 1998.

- [98] N. Sadowski, Y. Lefevre, M. Lajoie-Mazenc, and J. Cros. “Finite element torque calculation in electrical machines while considering the movement”. In: *IEEE Transactions on Magnetism* 28.2 (Mar. 1992), pp. 1410–1413. ISSN: 0018-9464. DOI: 10.1109/20.123957.
- [99] Francois Henrotte, Geoffrey Deliege, and Kay Hameyer. “The eggshell approach for the computation of electromagnetic forces in 2D and 3D”. In: *COMPEL - The international journal for computation and mathematics in electrical and electronic engineering* 23.4 (2004), pp. 996–1005. DOI: 10.1108/03321640410553427.
- [100] Ole Østerby. “Five Ways of Reducing the Crank–Nicolson Oscillations”. In: *BIT Numerical Mathematics* 43.4 (Nov. 2003), pp. 811–822. ISSN: 1572-9125. DOI: 10.1023/B:BITN.0000009942.00540.94. URL: <https://doi.org/10.1023/B:BITN.0000009942.00540.94>.
- [101] Alex Townsend. *FastGaussQuadrature.jl*. <https://github.com/ajt60gaibb/FastGaussQuadrature.jl>. Accessed August, 2017.
- [102] *WriteVTK.jl*. <https://github.com/jipolanco/WriteVTK.jl>. Accessed August, 2018.
- [103] *Dierckx.jl*. <https://github.com/kbarbary/Dierckx.jl>. Accessed August, 2017.
- [104] *Pardiso.jl*. <https://github.com/JuliaSparse/Pardiso.jl>. Accessed August, 2018.
- [105] Peter Deuffhard. *Newton Methods for Nonlinear Problems: Affine Invariance and Adaptive Algorithms*. Springer Publishing Company, Incorporated, 2011. ISBN: 364223898X, 9783642238987.
- [106] R Saigal and Michael J Todd. “Efficient acceleration techniques for fixed point algorithms”. In: *SIAM Journal on Numerical Analysis* 15.5 (1978), pp. 997–1007. DOI: 10.1137/0715065.
- [107] Donald G. Anderson. “Iterative Procedures for Nonlinear Integral Equations”. In: *J. ACM* 12.4 (Oct. 1965), pp. 547–560. ISSN: 0004-5411. DOI: 10.1145/321296.321305.
- [108] F. I. Hantila, G. Preda, and M. Vasiliu. “Polarization method for static fields”. In: *IEEE Transactions on Magnetism* 36.4 (July 2000), pp. 672–675. ISSN: 0018-9464. DOI: 10.1109/20.877538.
- [109] E. Dlala and A. Arkkio. “Analysis of the Convergence of the Fixed-Point Method Used for Solving Nonlinear Rotational Magnetic Field Problems”. In: *IEEE Transactions on Magnetism* 44.4 (Apr. 2008), pp. 473–478. ISSN: 0018-9464. DOI: 10.1109/TMAG.2007.914888.
- [110] G. Koczka, S. Auberhofer, O. Biro, and K. Preis. “Optimal Convergence of the Fixed-Point Method for Nonlinear Eddy Current Problems”. In: *IEEE Transactions on Magnetism* 45.3 (Mar. 2009), pp. 948–951. ISSN: 0018-9464. DOI: 10.1109/TMAG.2009.2012477.
- [111] S. Auberhofer, O. Biro, and K. Preis. “A Strategy to Improve the Convergence of the Fixed-Point Method for Nonlinear Eddy Current Problems”. In: *IEEE Transactions on Magnetism* 44.6 (June 2008), pp. 1282–1285. ISSN: 0018-9464. DOI: 10.1109/TMAG.2007.916012.
- [112] Ioan R. Ciric, Florea I. Hantila, and Mihai Maricaru. “Convergence acceleration in the polarization method for nonlinear periodic fields”. In: *COMPEL - The international journal for computation and mathematics in electrical and electronic engineering* 30.6 (2011), pp. 1688–1700. DOI: 10.1108/03321641111168020.
- [113] H. Walker and P. Ni. “Anderson Acceleration for Fixed-Point Iterations”. In: *SIAM Journal on Numerical Analysis* 49.4 (2011), pp. 1715–1735. DOI: 10.1137/10078356X.
- [114] Haw-ren Fang and Yousef Saad. “Two classes of multisecond methods for nonlinear acceleration”. In: *Numerical Linear Algebra with Applications* 16.3 (2009), pp. 197–221. DOI: 10.1002/nla.617.
- [115] Phanisri P. Pratapa and Phanish Suryanarayana. “Restarted Pulay mixing for efficient and robust acceleration of fixed-point iterations”. In: *Chemical Physics Letters* 635 (2015), pp. 69–74. ISSN: 0009-2614. DOI: <https://doi.org/10.1016/j.cpllett.2015.06.029>. URL: <http://www.sciencedirect.com/science/article/pii/S0009261415004480>.

- [116] A. Toth and C. Kelley. “Convergence Analysis for Anderson Acceleration”. In: *SIAM Journal on Numerical Analysis* 53.2 (2015), pp. 805–819. DOI: 10.1137/130919398.
- [117] Oszkár Bíró, Gergely Koczka, and Kurt Preis. “Finite element solution of nonlinear eddy current problems with periodic excitation and its industrial applications”. In: *Applied Numerical Mathematics* 79 (2014). Workshop on Numerical Electromagnetics and Industrial Applications (NELIA 2011), pp. 3–17. ISSN: 0168-9274. DOI: <https://doi.org/10.1016/j.apnum.2013.04.007>.
- [118] C. Krüttgen, S. Steentjes, G. Glehn, and K. Hameyer. “Parametric Homogenized Model for Inclusion of Eddy Currents and Hysteresis in 2-D Finite-Element Simulation of Electrical Machines”. In: *IEEE Transactions on Magnetism* 53.6 (June 2017), pp. 1–4. ISSN: 0018-9464. DOI: 10.1109/TMAG.2017.2660460.
- [119] Y. B. Li, S. Niu, S. L. Ho, Y. Li, and W. N. Fu. “Hysteresis Effects of Laminated Steel Materials on Detent Torque in Permanent Magnet Motors”. In: *IEEE Transactions on Magnetism* 47.10 (Oct. 2011), pp. 3594–3597. ISSN: 0018-9464. DOI: 10.1109/TMAG.2011.2155633.
- [120] E. Dlala, A. Belahcen, J. Pippuri, and A. Arkkio. “Interdependence of Hysteresis and Eddy-Current Losses in Laminated Magnetic Cores of Electrical Machines”. In: *IEEE Transactions on Magnetism* 46.2 (Feb. 2010), pp. 306–309. ISSN: 0018-9464. DOI: 10.1109/TMAG.2009.2032930.
- [121] F. Henrotte, S. Steentjes, K. Hameyer, and C. Geuzaine. “Pragmatic two-step homogenisation technique for ferromagnetic laminated cores”. In: *IET Science, Measurement Technology* 9.2 (2015), pp. 152–159. ISSN: 1751-8822. DOI: 10.1049/iet-smt.2014.0201.
- [122] D. Eggers, S. Steentjes, and K. Hameyer. “Advanced Iron-Loss Estimation for Nonlinear Material Behavior”. In: *IEEE Transactions on Magnetism* 48.11 (Nov. 2012), pp. 3021–3024. ISSN: 0018-9464. DOI: 10.1109/TMAG.2012.2208944.
- [123] D. Lin, P. Zhou, W. N. Fu, Z. Badics, and Z. J. Cendes. “A dynamic core loss model for soft ferromagnetic and power ferrite materials in transient finite element analysis”. In: *IEEE Transactions on Magnetism* 40.2 (Mar. 2004), pp. 1318–1321. ISSN: 0018-9464. DOI: 10.1109/TMAG.2004.825025.
- [124] E. Barbisio, F. Fiorillo, and C. Ragusa. “Predicting loss in magnetic steels under arbitrary induction waveform and with minor hysteresis loops”. In: *IEEE Transactions on Magnetism* 40.4 (July 2004), pp. 1810–1819. ISSN: 0018-9464. DOI: 10.1109/TMAG.2004.830510.
- [125] M. Reinlein, T. Hubert, A. Hoffmann, and A. Kremser. “Optimization of analytical iron loss approaches for electrical machines”. In: *2013 3rd International Electric Drives Production Conference (EDPC)*. Oct. 2013, pp. 1–7. DOI: 10.1109/EDPC.2013.6689759.
- [126] P. Zhou, D. Lin, Y. Xiao, N. Lambert, and M. A. Rahman. “Temperature-Dependent Demagnetization Model of Permanent Magnets for Finite Element Analysis”. In: *IEEE Transactions on Magnetism* 48.2 (Feb. 2012), pp. 1031–1034. ISSN: 0018-9464. DOI: 10.1109/TMAG.2011.2172395.
- [127] M. Rosu, J. Saitz, and A. Arkkio. “Hysteresis model for finite-element analysis of permanent-magnet demagnetization in a large synchronous motor under a fault condition”. In: *IEEE Transactions on Magnetism* 41.6 (June 2005), pp. 2118–2123. ISSN: 0018-9464. DOI: 10.1109/TMAG.2005.848319.
- [128] Gyu-Hong Kang, Jin Hur, Hyuk Nam, Jung-Pyo Hong, and Gyu-Tak Kim. “Analysis of irreversible magnet demagnetization in line-start motors based on the finite-element method”. In: *IEEE Transactions on Magnetism* 39.3 (May 2003), pp. 1488–1491. ISSN: 0018-9464. DOI: 10.1109/TMAG.2003.810330.
- [129] W. N. Fu and S. L. Ho. “Dynamic Demagnetization Computation of Permanent Magnet Motors Using Finite Element Method With Normal Magnetization Curves”. In: *IEEE Transactions on Applied Superconductivity* 20.3 (2010), pp. 851–855. ISSN: 1051-8223. DOI: 10.1109/TASC.2009.2039787.

- [130] Yuriy Zhilichev, Peter Campbell, and David Miller. “In situ magnetization of isotropic permanent magnets”. In: *IEEE transactions on magnetics* 38.5 (2002), pp. 2988–2990. DOI: 10.1109/TMAG.2002.803195.
- [131] M. F. Hsieh, C. K. Lin, D. G. Dorrell, and P. Wung. “Modeling and effects of in-situ magnetization of isotropic ferrite magnet motors”. In: *2011 IEEE Energy Conversion Congress and Exposition*. Sept. 2011, pp. 3278–3284. DOI: 10.1109/ECCE.2011.6064211.
- [132] K. S. Kim, M. R. Park, H. J. Kim, S. H. Chai, and J. P. Hong. “Estimation of Rotor Type Using Ferrite Magnet Considering the Magnetization Process”. In: *IEEE Transactions on Magnetism* 52.3 (Mar. 2016), pp. 1–4. ISSN: 0018-9464. DOI: 10.1109/TMAG.2015.2490281.
- [133] S. Ruoho, E. Dlala, and A. Arkkio. “Comparison of Demagnetization Models for Finite-Element Analysis of Permanent-Magnet Synchronous Machines”. In: *IEEE Transactions on Magnetism* 43.11 (Nov. 2007), pp. 3964–3968. ISSN: 0018-9464. DOI: 10.1109/TMAG.2007.906749.
- [134] P. Alotto and P. Molfino. “A 2D Finite Element Procedure for Magnetic Analysis Involving Non-Linear and Hysteretic Materials”. In: *IEEE Transactions on Magnetism* 30.5 (1994), pp. 3379–3382. DOI: 10.1109/20.312663.
- [135] D. Xie, W. Zhang, B. Bai, L. Zeng, and L. Wang. “Finite Element Analysis of Permanent Magnet Assembly With High Field Strength Using Preisach Theory”. In: *IEEE Transactions on Magnetism* 43.4 (Apr. 2007), pp. 1393–1396. ISSN: 0018-9464. DOI: 10.1109/TMAG.2006.891035.
- [136] S. E. Zirka, Y. I. Moroz, P. Marketos, and A. J. Moses. “Congruency-based hysteresis models for transient simulation”. In: *IEEE Transactions on Magnetism* 40.2 (Mar. 2004), pp. 390–399. ISSN: 0018-9464. DOI: 10.1109/TMAG.2004.824137.
- [137] M. Kuczmann. “Nonlinear finite element method in magnetism”. In: *Pollack Periodica* 4.2 (2009), pp. 13–24. DOI: 10.1556/Pollack.4.2009.2.2.
- [138] J. Saitz. “Newton-Raphson method and fixed-point technique in finite element computation of magnetic field problems in media with hysteresis”. In: *IEEE Transactions on Magnetism* 35.3 (May 1999), pp. 1398–1401. ISSN: 0018-9464. DOI: 10.1109/20.767225.
- [139] J. Gyselinck, P. Dular, N. Sadowski, J. Leite, and J.P.A. Bastos. “Incorporation of a Jiles-Atherton vector hysteresis model in 2D FE magnetic field computations: Application of the Newton-Raphson method”. In: *COMPEL - The international journal for computation and mathematics in electrical and electronic engineering* 23.3 (2004), pp. 685–693. DOI: 10.1108/03321640410540601.
- [140] D. Vanoost, H. De Gersem, J. Peuteman, G. Gielen, and D. Pissort. “Nonlinear Magnetostatic Finite-Element Formulation for Models With Radial Symmetry”. In: *IEEE Transactions on Magnetism* 50.2 (Feb. 2014), pp. 85–88. ISSN: 0018-9464. DOI: 10.1109/TMAG.2013.2279114.
- [141] Przybylski Marek, Kapelski Dariusz, Ślusarek Barbara, and Wiak Sławomir. “Impulse Magnetization of Nd-Fe-B Sintered Magnets for Sensors”. In: 16 (2016), pp. 1–14. DOI: 10.3390/s16040569.
- [142] M. F. Hsieh, Y. M. Lien, and D. G. Dorrell. “Post-Assembly Magnetization of Rare-Earth Fractional-Slot Surface Permanent-Magnet Machines Using a Two-Shot Method”. In: *IEEE Transactions on Industry Applications* 47.6 (Nov. 2011), pp. 2478–2486. ISSN: 0093-9994. DOI: 10.1109/TIA.2011.2168933.
- [143] J. Klötzl, M. Pyc, and D. Gerling. “Permanent magnet loss reduction in PM-machines using analytical and FEM calculation”. In: *SPEEDAM 2010*. June 2010, pp. 98–100. DOI: 10.1109/SPEEDAM.2010.5544964.
- [144] Wan-Ying Huang, Adel Bettayeb, Robert Kaczmarek, and Jean-Claude Vannier. “Optimization of Magnet Segmentation for Reduction of Eddy-Current Losses in Permanent Magnet Synchronous Machine”. In: *IEEE Transactions on Energy Conversion* 25.2 (June 2010), pp. 381–387. DOI: 10.1109/tec.2009.2036250.

- [145] C. Dinca, A. Stockli, E. Ramezani, D. Schwarzer, Y. Cat, P. Korneluk, and U. Schäfer. “Characterization of a 7KJ magnetizing pulsed circuit for online quality control of permanent magnets”. In: *2015 IEEE Pulsed Power Conference (PPC)*. May 2015, pp. 1–8. DOI: 10.1109/PPC.2015.7296911.
- [146] Y. Kawase, T. Yamaguchi, N. Mimura, M. Igata, and K. Ida. “Analysis of magnetizing process using discharge current of capacitor by 3-D finite-element method”. In: *IEEE Transactions on Magnetics* 38.2 (Mar. 2002), pp. 1145–1148. ISSN: 0018-9464. DOI: 10.1109/20.996293.
- [147] F. Fiorillo, C. Beatrice, O. Bottauscio, and E. Patroi. “Measuring the Hysteresis Loop of Permanent Magnets With the Pulsed Field Magnetometer”. In: *IEEE Transactions on Magnetics* 43.7 (July 2007), pp. 3159–3164. ISSN: 0018-9464. DOI: 10.1109/TMAG.2007.893536.
- [148] Chang Seop Koh and Sun-Ki Hong. “Finite element analysis of magnetizer using Preisach model”. In: *IEEE Transactions on Magnetics* 35.3 (May 1999), pp. 1227–1230. ISSN: 0018-9464. DOI: 10.1109/20.767171.
- [149] D. Zhang, H. J. Kim, W. Li, and C. S. Koh. “Analysis of Magnetizing Process of a New Anisotropic Bonded NdFeB Permanent Magnet Using FEM Combined With Jiles-Atherton Hysteresis Model”. In: *IEEE Transactions on Magnetics* 49.5 (May 2013), pp. 2221–2224. ISSN: 0018-9464. DOI: 10.1109/TMAG.2013.2245499.
- [150] Gerald Jungmayr, Jens Loeffler, Bjoern Winter, Frank Jeske, and Wolfgang Amrhein. “Magnetic Gear: Radial Force, Cogging Torque, Skewing, and Optimization”. In: *IEEE Transactions on Industry Applications* 52.5 (Sept. 2016), pp. 3822–3830. DOI: 10.1109/tia.2016.2571267.
- [151] J. Druant, H. Vansompel, F. De Belie, and P. Sergeant. “Loss Identification in a Double Rotor Electrical Variable Transmission”. In: *IEEE Transactions on Industrial Electronics* 64.10 (Oct. 2017), pp. 7731–7740. ISSN: 0278-0046. DOI: 10.1109/TIE.2017.2698362.
- [152] M. Kowol, J. Kolodziej, M. Jagiela, and M. Lukaniszyn. “Impact of modulator designs and materials on efficiency and losses in radial passive magnetic gear”. In: *IEEE Transactions on Energy Conversion* (2018), pp. 1–1. ISSN: 0885-8969. DOI: 10.1109/TEC.2018.2862462.
- [153] Sung-Jin Kim, Eui-Jong Park, Sang-Yong Jung, and Yong-Jae Kim. “Torque transfer efficiency estimation of the magnetic gear considering eddy current loss”. In: *2016 IEEE Transportation Electrification Conference and Expo, Asia-Pacific (ITEC Asia-Pacific)*. June 2016, pp. 338–341. DOI: 10.1109/ITEC-AP.2016.7512974.
- [154] Andreas Krings and Juliette Soulard. “Overview and Comparison of Iron Loss Models for Electrical Machines”. In: *Journal of Electrical Engineering* 10.3 (2010), pp. 162–169.
- [155] C. A. Hernandez-Aramburo, T. C. Green, and A. C. Smith. “Estimating rotational iron losses in an induction machine”. In: *IEEE Transactions on Magnetics* 39.6 (Nov. 2003), pp. 3527–3533. DOI: 10.1109/TMAG.2003.819451.
- [156] *Electrical Steel – Altogether more powerful*. Tech. rep. cogent, <https://cogent-power.com/products/non-oriented-electrical-steel>, accessed Jan. 2016.
- [157] Carlo Appino, C Ragusa, and F Fiorillo. “Can rotational magnetization be theoretically assessed?” In: *International Journal of Applied Electromagnetics and Mechanics* 44.3, 4 (2014), pp. 355–370. DOI: 10.3233/JAE-141798.
- [158] C Ragusa, C Appino, and F Fiorillo. “Magnetic losses under two-dimensional flux loci in Fe–Si laminations”. In: *Journal of magnetism and magnetic materials* 316.2 (2007), pp. 454–457. DOI: 10.1016/j.jmmm.2007.03.170.
- [159] C. Appino, M. Khan, O. de la Barrière, C. Ragusa, and F. Fiorillo. “Alternating and Rotational Losses Up to Magnetic Saturation in Non-Oriented Steel Sheets”. In: *IEEE Transactions on Magnetics* 52.5 (May 2016), pp. 1–4. ISSN: 0018-9464. DOI: 10.1109/TMAG.2016.2528338.



- [160] F. Brailsford. “Alternating Hysteresis Loss in Electrical Sheet Steels”. In: *Electrical Engineers, Journal of the Institution of* 84.507 (Mar. 1939), pp. 399–407. DOI: 10.1049/jiee-1.1939.0060.
- [161] J. Pyrhönen, S. Ruoho, J. Nerg, M. Paju, S. Tuominen, H. Kankaanpää, R. Stern, A. Boglietti, and N. Uzhegov. “Hysteresis Losses in Sintered NdFeB Permanent Magnets in Rotating Electrical Machines”. In: *IEEE Transactions on Industrial Electronics* 62.2 (Feb. 2015), pp. 857–865. ISSN: 0278-0046. DOI: 10.1109/TIE.2014.2354597.
- [162] M. Van Der Giet, C. Schlensok, B. Schmulling, and K. Hameyer. “Comparison of 2-D and 3-D Coupled Electromagnetic and Structure-Dynamic Simulation of Electrical Machines”. In: *IEEE Transactions on Magnetics* 44.6 (June 2008), pp. 1594–1597. ISSN: 0018-9464. DOI: 10.1109/TMAG.2007.916121.
- [163] F. Henrotte and K. Hameyer. “A dynamical vector hysteresis model based on an energy approach”. In: *IEEE Transactions on Magnetics* 42.4 (Apr. 2006), pp. 899–902. ISSN: 0018-9464. DOI: 10.1109/TMAG.2006.872473.
- [164] D. Gerada, A. Mebarki, N. L. Brown, C. Gerada, A. Cavagnino, and A. Boglietti. “High-Speed Electrical Machines: Technologies, Trends, and Developments”. In: *IEEE Transactions on Industrial Electronics* 61.6 (June 2014), pp. 2946–2959. ISSN: 0278-0046. DOI: 10.1109/TIE.2013.2286777.
- [165] Lucas FM Da Silva and RD Adams. “Measurement of the mechanical properties of structural adhesives in tension and shear over a wide range of temperatures”. In: *Journal of Adhesion Science and Technology* 19.2 (2005), pp. 109–141. DOI: 10.1163/1568561053148449.
- [166] Aleksandar Borisavljevic. “High-speed PM machines: Applications, trends and limits”. In: *Limits, Modeling and Design of High-Speed Permanent Magnet Machines*. Springer, 2013, pp. 13–27. DOI: 10.1007/978-3-642-33457-3\_2.
- [167] J. D. Ede, Z. Q. Zhu, and D. Howe. “Rotor resonances of high-speed permanent-magnet brushless machines”. In: *IEEE Transactions on Industry Applications* 38.6 (Nov. 2002), pp. 1542–1548. DOI: 10.1109/TIA.2002.804765.
- [168] J. Lee and J. Chang. “Analysis of the Vibration Characteristics of Coaxial Magnetic Gear”. In: *IEEE Transactions on Magnetics* 53.6 (June 2017), pp. 1–4. ISSN: 0018-9464. DOI: 10.1109/TMAG.2017.2665660.
- [169] Ji Young Lee and Jung Hwan Chang. “Vibration and noise characteristics of coaxial magnetic gear according to low-speed rotor structure”. In: *Journal of Mechanical Science and Technology* 31.6 (June 2017), pp. 2723–2728. ISSN: 1976-3824. DOI: 10.1007/s12206-017-0515-4. URL: <https://doi.org/10.1007/s12206-017-0515-4>.
- [170] H.M. Shin and J.H. Chang. “Analysis of Coaxial Magnetic Gear with Low Gear Ratios for Application in Counter Rotating Systems”. In: *Journal of Magnetics* 20.2 (June 2015), pp. 186–192. DOI: 10.4283/jmag.2015.20.2.186.
- [171] M. A. Grande, L. Ferraris, F. Franchini, and E. Pošković. “New SMC Materials for Small Electrical Machine With Very Good Mechanical Properties”. In: *IEEE Transactions on Industry Applications* 54.1 (Jan. 2018), pp. 195–203. ISSN: 0093-9994. DOI: 10.1109/TIA.2017.2756593.
- [172] C F Colebrook. “Turbulent flow in pipes, with particular reference to the transition region between the smooth and rough pipe laws”. In: *Journal of the Institution of Civil Engineers* 11.4 (1939), pp. 133–156. DOI: 10.1680/ijoti.1939.13150. URL: <https://doi.org/10.1680/ijoti.1939.13150>.
- [173] Jukka Kiijarvi. “Darcy friction factor formulae in turbulent pipe flow”. In: *Lunowa Fluid Mechanics Paper 110727* (2011). URL: [http://www.kolumbus.fi/jukka.kiijarvi/clunowa/fluid\\_mechanics/pdf\\_articles/darcy\\_friction\\_factor.pdf](http://www.kolumbus.fi/jukka.kiijarvi/clunowa/fluid_mechanics/pdf_articles/darcy_friction_factor.pdf).
- [174] YC Chong, DA Staton, MA Mueller, and J Chick. “Pressure loss measurement in rotor-stator gap of radial flux electrical machines”. In: *Electrical Machines (ICEM), 2014 International Conference on*. IEEE, 2014, pp. 2172–2178. DOI: 10.1109/ICELMACH.2014.6960485.

- [175] Md Lokman Hosain, Rebei Bel Fdhila, and Kristian Rönnerberg. “Taylor-Couette flow and transient heat transfer inside the annulus air-gap of rotating electrical machines”. In: *Applied Energy* 207 (2017). Transformative Innovations for a Sustainable Future – Part II, pp. 624–633. ISSN: 0306-2619. DOI: <https://doi.org/10.1016/j.apenergy.2017.07.011>. URL: <http://www.sciencedirect.com/science/article/pii/S0306261917308711>.
- [176] J. Nerg, M. Rilla, and J. Pyrhonen. “Thermal Analysis of Radial-Flux Electrical Machines With a High Power Density”. In: *IEEE Transactions on Industrial Electronics* 55.10 (Oct. 2008), pp. 3543–3554. ISSN: 0278-0046. DOI: 10.1109/TIE.2008.927403.
- [177] D. A. Howey, P. R. N. Childs, and A. S. Holmes. “Air-Gap Convection in Rotating Electrical Machines”. In: *IEEE Transactions on Industrial Electronics* 59.3 (Mar. 2012), pp. 1367–1375. ISSN: 0278-0046. DOI: 10.1109/TIE.2010.2100337.
- [178] **M. Filippini** and P. Alotto. “Multi-objective optimization of coaxial magnetic gears”. In: *International Journal of Applied Electromagnetics and Mechanics* 56.S1 (2018). DOI: 10.3233/JAE-172280.
- [179] **M. Filippini** and P. Alotto. “Coaxial magnetic gear design”. In: *2016 IEEE Conference on Electromagnetic Field Computation (CEFC)*. Nov. 2016, pp. 1–1. DOI: 10.1109/CEFC.2016.7815939.
- [180] Y. Wang, **M. Filippini**, G. Bacco, and N. Bianchi. “Parametric Design and Optimization of Magnetic Gears with Differential Evolution Method”. In: *2018 XIII International Conference on Electrical Machines (ICEM)*. Sept. 2018, pp. 919–925. DOI: 10.1109/ICELMACH.2018.8507160.
- [181] Mung Chiang. “Nonconvex optimization for communication networks”. In: *Advances in Applied Mathematics and Global Optimization*. Springer, 2009, pp. 137–196. DOI: 10.1007/978-0-387-75714-8\_5.
- [182] Pietro S. Oliveto, Jun He, and Xin Yao. “Time complexity of evolutionary algorithms for combinatorial optimization: A decade of results”. In: *International Journal of Automation and Computing* 4.3 (July 2007), pp. 281–293. ISSN: 1751-8520. DOI: 10.1007/s11633-007-0281-3.
- [183] R. Storn and K. Price. “Differential Evolution - A Simple and Efficient Heuristic for Global Optimization over Continuous Spaces”. In: *Journal of Global Optimization* 11.4 (1997), pp. 341–359. DOI: 10.1023/A:1008202821328.
- [184] Daniela Zaharie. “Critical values for the control parameters of differential evolution algorithms”. In: *Proceedings of MENDEL*. Vol. 2. 2002, p. 6267.
- [185] Piergiorgio Alotto. “A hybrid multiobjective differential evolution method for electromagnetic device optimization”. In: *COMPEL - The international journal for computation and mathematics in electrical and electronic engineering* 30.6 (Nov. 2011), pp. 1815–1828. DOI: 10.1108/033216411111168129.
- [186] Qingfu Zhang, Aimin Zhou, Shizheng Zhao, Ponnuthurai Nagarathnam Suganthan, Wudong Liu, and Santosh Tiwari. “Multiobjective optimization test instances for the CEC 2009 special session and competition”. In: *University of Essex, Colchester, UK and Nanyang technological University, Singapore, special session on performance assessment of multi-objective optimization algorithms, technical report* 264 (2008).
- [187] M. Gardner, M. Johnson, and H. A. Toliyat. “Analysis of High Gear Ratio Capabilities for Single-Stage, Series Multistage, and Compound Differential Coaxial Magnetic Gears”. In: *IEEE Transactions on Energy Conversion* (2018), pp. 1–1. ISSN: 0885-8969. DOI: 10.1109/TEC.2018.2868730.
- [188] *Hydro-Mec Coaxial Gear catalogue*. Tech. rep. Hydro-Mec, <http://hydromec.com/download/product/metric/catalogue/coaxial.pdf>, accessed Aug. 2017.
- [189] R. G. Montague, C. M. Bingham, and K. Atallah. “Magnetic gear overload detection and remedial strategies for servo-drive systems”. In: *SPEEDAM 2010*. June 2010, pp. 523–528. DOI: 10.1109/SPEEDAM.2010.5544957.

- 
- [190] S. Niu, K. T. Chau, J. Li, and W. Li. “Eddy-Current Analysis of Double-Stator Inset-Type Permanent Magnet Brushless Machines”. In: *IEEE Transactions on Applied Superconductivity* 20.3 (June 2010), pp. 1097–1101. ISSN: 1051-8223. DOI: 10.1109/TASC.2009.2039782.
- [191] *QRUpdate Fortran Library*. <https://sourceforge.net/projects/qrupdate/files/>, available library on SourceForge. Accessed February, 2018. 2012.